Modeling Dislocation Density Evolution in Continuum Crystal Plasticity

by

Athanasios Arsenlis

B.S., Cornell University (1997)

Submitted to the Department of Mechanical Engineering
in partial fulfillment of the requirements for the degree of

Doctor of Philosophy

at the

MASSACHUSETTS INSTITUTE OF TECHNOLOGY

February 2001

Author .....
Department of Mechanical Engineering
February 2, 2001

Certified by .....
David M. Parks
Professor of Mechanical Engineering
Thesis Supervisor

Accepted by .....
Ain Sonin
Chairman, Department Committee on Graduate Students

Modeling Dislocation Density Evolution in Continuum Crystal Plasticity

by

Athanasios Arsenlis

Submitted to the Department of Mechanical Engineering
on February 2, 2001, in partial fulfillment of the
requirements for the degree of
Doctor of Philosophy

Abstract

Dislocations are the singly most important material defects in crystal plasticity, and although dislocation mechanics has long been understood as the underlying physical basis for continuum crystal plasticity formulations, explicit consideration of crystallographic dislocation mechanics has been largely absent in working constitutive models. In light of recent theoretical developments in dislocation dynamics, and the introduction of geometrically necessary dislocation (GND) density in continuum formulations through plastic strain gradients, a single crystal plasticity model based on dislocation density state variables is developed. The density state variables evolve from initial conditions according to equations based on fundamental concepts in dislocation mechanics such as the conservation of Burgers vector in multiplication and annihilation processes. Along with those processes that account for bulk statistical dislocation evolution, the evolving polarity due to dislocation species flux divergences may be included to detail the length-scale dependence of mechanical properties on the micron level. The full dislocation density description of plasticity allows a simple evaluation of the role of GND density in non-homogeneously deforming bodies.

A local version of the constitutive model, which captures the bulk processes of dislocation multiplication and annihilation during plastic deformation, is implemented within a finite element framework to investigate the poly-slip behavior of aluminum single crystals under tension. A non-local version of the constitutive model using an idealized planar double slip system geometry is implemented within a finite element framework to investigate the length-scale dependence observed in the bending of thin single crystal beams. The results not only capture the mechanical stress/strain response of the material, but also detail the development of underlying dislocation structure responsible for the plastic behavior of the crystal.

Thesis Supervisor: David M. Parks
Title: Professor of Mechanical Engineering

Acknowledgments

As with any large body of work, there are many people that influenced and helped to shape this thesis. First and foremost, I have to acknowledge the support and strength of my family. My parents have always encouraged me to strive for high goals, and have instilled in me the hard work ethic and determination that is needed to achieve them. My sisters have always helped push me to succeed in countless ways in every aspect of life. I am forever indebted to my family.

I am deeply grateful for the contributions of my thesis advisor Professor David M. Parks. He has had the most direct influence in my work and my maturation as a student. Reflecting back at my MIT experience, I can't imagine having worked with any other professor at any other institution. At the same time, Professor Parks sparked my imagination on the topic, and grounded me to solve the task at hand. He allowed me the freedom to work with other researchers in the field and helped me synthesize and formalize all of the ideas into a working theory. He has been an invaluable resource to me and, in my mind, the ideal thesis advisor.

I must thank Professor Ali Argon and Professor Sidney Yip for serving on my thesis committee. I also must thank Professor Lallit Anand for teaching me the mathematical rigor associated with plasticity. All of the faculty in the Mechanics and Materials group have been a great resource for different aspects of my research.

I must thank the scientists in the Chemistry and Materials Science Directorate at Lawrence Livermore National Laboratory involved with the Multi-scale Modeling Program, especially Dr. Vasily Bulatov, for their input during my short tenure at Livermore. I thank my colleagues in the mechanics and materials group who helped me along the way with everyday issues. I thank Ray and Una for helping me out whenever I needed them. Lastly, many thanks to my friends in Boston that helped to keep me sane during the whole experience.

Finally, I'd like to thank the United States Department of Defense for funding me for the majority of my time at MIT through the National Defense Science and Engineering Graduate Fellowship.

Contents

List of Figures

List of Tables

Chapter 1

Introduction

1.1 Physics of Crystal Plasticity

Crystalline materials are distinguished from other materials by the arrangement of atoms into a periodic lattice. The ideal shear strength of a perfect crystal is theorized to be one thirtieth of the shear modulus of the material. Such high levels of strength are rarely seen in engineering materials, with the exception of thin crystalline whiskers. The observed yield strength of crystalline solids is usually two to four orders of magnitude below this theoretical level. The conflict between observed behavior and theoretical predictions was resolved with the concept that dislocations, line defects in the crystal lattice, were responsible for the discrepancy.

The mathematical description of a dislocation was developed at the beginning of the twentieth century (Volterra, 1907), but it wasn't until the 1930's that the dislocations were theorized to exist in crystalline solids, in explaining the yield strength discrepancy (Orowan, 1934; Polanyi, 1934; Taylor, 1934; Taylor, 1938). Dislocations are line defects in the crystal lattice of a material where there is a local misregistration. The strength of the defect is contained in the Burgers vector, a lattice vector that quantifies both the direction and magnitude of the misregistration. The ideal strength of the crystal was calculated by assuming that all of the atoms in a shear plane move together to accommodate a given plastic deformation. The dislocations in the lattice enable only sections of the slip planes to shear, leaving other parts in

their original configurations, and the dislocation line itself can be considered as the shear front. Dislocations are the carriers of plasticity due to slip, and relationships have been developed between the motion of dislocation densities and the resulting crystallographic shear observed macroscopically (Orowan, 1940).

Dislocations remained theoretical constructs until the 1950's. In that time, their existence in crystals became widely accepted, and a theory of dislocations and their properties became established (Hirth and Lothe, 1982). It was no surprise when direct evidence of their existence was first found in crystal growth and etch pit experiments. With the invention of transmission electron microscopy, images of individual dislocations could be seen in thin crystalline foils (Amelinckx, 1964). Today, there are countless publications on the experimental observation of dislocations, and new techniques such as Orientation Imaging Microscopy are being developed to probe the geometric aspects of dislocation densities (Adams et al., 1993; Sun et al., 2000).

Along with the role that dislocations play in accommodating plastic deformation in crystalline materials, their evolution with plastic deformation and the interactions between dislocations have been used to explain work hardening. During plastic deformation, dislocations multiply from initial densities, defined as line length per unit volume, of $\rho \leq 10^{12}$ m^{-2} for annealed crystals to saturation levels of $\rho \approx 10^{16}$ m^{-2}, spanning four orders of magnitude (Basinski and Basinski, 1979). At the saturation values, density recovery mechanisms become more prominent as the likelihood of annihilation increases as the distance between dislocations decreases. The evolution of density has been used to describe to the physical processes responsible for the four stages of hardening in single crystals (Argon, 1996).

Dislocation interactions are responsible for much of the intrinsic strength in crystalline solids. The evolving density impedes the motion of gliding dislocations, leading to strain hardening with plastic deformation. Certain dislocations reactions are anticipated to lead to either strong junctions like the famous Lomer-Cotrell lock (Lomer, 1951), or weaker junctions such as the Hirth lock (Hirth. 1961), depending on the geometry of the interacting dislocations. The rates of production of such junctions and other dislocation forest interactions affect the work hardening of crystalline mate-

rials. In polycrystalline materials, the kinematic constraints that neighboring grains impose on the deformation in each crystal require that many slip systems activate. In polycrystals, the hardening rate is composed of the rates of production of all of the different junctions, and the influence of one specific junction cannot be distinguished from the others. In single crystals, the deformation is not as constrained as in the polycrystalline case; therefore, the effects of each different dislocation interaction can be considered individually. In developing a predictive model for single crystals, the influence of particular dislocation interactions must be considered when investigating the orientation-dependence of the stress/strain evolution.

1.2 Dislocation Dynamics

Over the past decade, dislocation dynamics has emerged as a powerful simulation tool in investigating the evolution of dislocation density on the micron scale. The technique tracks the motion and evolution of discrete dislocation lines in response to local stresses from the externally applied loads and the elastic interactions of the rest of the density. Depending of the level of detail that is carried in the simulation, different aspects of dislocation interactions may be investigated.

The most highly resolved simulations have been conducted by Shenoy et al. (2000). They allow for the separation of perfect dislocations into partial dislocations separated by a stacking fault. Using the technique, they have investigated the interaction of these dissociated dislocations in forming strong dislocation junctions. Due to the high resolution used, no more than a few dislocations may be considered in a single simulation. Less resolved simulations have been conducted by Schwarz (1999) that discretize perfect, undissociated, dislocation lines by a series of nodes, and then calculate the forces on the nodes and corresponding reaction of the line. The technique has been used to investigate the multiplication of dislocations in Frank-Read sources, and short-range dislocation interactions (Wickham et al., 1999). The two techniques both discretize the dislocation lines into a series of nodes with differing levels of resolution. The increased resolution has a computational cost associated with it, and

fewer dislocation lines may be represented.

Two other groups have modeled dislocation lines as collections of interconnected straight dislocation line segments. Zbib et al. (1998) have discretized lines into short segments and calculated the forces and moments on the segments to determine their motion. In their discretization, the dislocation segments may have any tangent direction. The coarsest dislocation dynamics technique discretizes dislocation lines into short segments of pure edge and pure screw dislocations (Kubin et al., 1992; Kubin et al., 1998). These coarser representations of the discrete dislocations can simulate greater densities of dislocations, $\rho \approx 10^{14}\text{m}^{-2}$ and may reach plastic strains of $\epsilon \approx 10^{-3}$. The density levels in the coarsest simulations are roughly two orders of magnitude below dislocation densities that are typically found in work hardened crystals (Basinski and Basinski, 1979), and the strain level is between one and two orders of magnitude below typical experimentally-applied strains. A better description of the scale of dislocation dynamics simulations in comparison to engineering length scales is to use the total dislocation line length in a simulation, since the simulation cell size can be changed to arbitrarily set the dislocation density level. The total dislocation line length in the most refined calculations of Shenoy et al. (2000) is on the order of 100 nm. The total dislocation line length that can be achieved by the coarsest calculations of Kubin et al. (1998) are on the order of 10 cm, while the length of dislocation line in engineering structures that have been plastically worked may reach 1×10^{13} m. Furthermore, dislocation dynamics simulations thus far have been limited to simple boundary conditions (periodic and mirror symmetric) and single crystals. Grain boundaries have not been successfully modeled with the technique.

Despite all of the shortcomings and limitations of the dislocation dynamics, it remains a powerful tool in investigating the multiplication and generation of dislocations, the annihilation of dislocations, the reactions between different dislocations, and the evolution of organized dislocation structures. A main focus of the dislocation dynamics community in general has been to capture the stress/strain curve of the simulated material. The statistical results available from many-body dislocation dynamics simulations have largely been under-exploited in terms of the evolution of

the dislocation density, the mean mobility of the density, and the mean properties of the dislocation population over the history of deformation. Furthermore, it is not clear how such information, even if extracted, could be incorporated into strength-based constitutive models of continuum crystal plasticity, and virtually none of the advances in dislocation dynamics have translated into continuum crystal plasticity formulations that reflect the results obtained by the discrete simulations. A dislocation density internal state variable model has the potential to connect the results of the discrete simulations to continuum plasticity by capturing the evolution of the density and its mean properties. The continuum models would be able to simulate the levels of dislocation density and plastic strain in laboratory experiments, which is not yet possible with dislocation dynamics.

1.3 Geometrically-Necessary Dislocations and Scale-Dependent Material Behavior

In his landmark paper, Ashby considered a general dislocation density state of a crystalline material to be composed of two different populations of densities (Ashby, 1970). I will focus this discussion around that article because it has served as the inspiration behind many of the physical arguments in length-scale-dependent plasticity theories. Statistically-stored dislocations (SSD's) were dislocations that were generated during the homogeneous plastic deformation of crystals due to random trapping processes. These were the dislocations associated with bulk deformation processes that resulted in work hardening. Another class was named geometrically-necessary dislocations (GND's) which resulted from local non-homogeneous plastic deformation. The magnitude of the GND population could be related to plastic strain gradients from the work of Kröner (Kröner, 1962) and resulted in curvature of the crystal lattice (Nye, 1953). This dislocation population was indeed "necessary" because it was required to maintain lattice continuity.

The role of SSD's in work hardening was already established from years of analysis

of stress/strain curves for different crystalline materials and corresponding dislocation density images at different stages of deformation. Statistically-stored dislocations acted as forest obstacles to mobile dislocations. Ashby argued that the GND population would act in the same manner as the SSD population. In a homogeneously deforming body, there were no plastic strain gradients, and therefore no GND density. In a non-homogeneously deforming body, all of the dislocation density associated with the homogeneous deformation would still be present, but along with those dislocations, additional dislocations in the form of GND's would exist due to the geometric constraints. The additional geometric density would act in the same manner as the SSD density in creating forest obstacles to dislocation motion and increase the slip resistance as compared to the homogeneously deforming body. The dislocation population, SSD or GND, that numerically dominated the total dislocation density level controlled the stress/strain curve of the material.

The argument for treating the GND's as forest obstacles is subtle in nature. On the individual dislocation level, every dislocation line can be viewed as geometrically necessary. Each dislocation locally accommodates a plastic strain gradient and leads to local lattice curvature, but the SSD and GND measures are really based on the properties of a population of dislocations within a certain volume. If a very small volume ($V = 1 \times 10^{-25}$ m^3) is considered, it is likely that every dislocation within it will be geometrically necessary. If a very large volume ($V = 1 \times 10^{-12}$ m^3) is considered, it is likely that the overwhelming majority of the density will be statistical in nature. The volume in which these densities are defined is important. Since the two measures apply to populations of dislocations rather than to individual dislocations, it is impossible to determine in which group any one dislocation within a given volume belongs. A gliding dislocation would definitely not be able to distinguish an encountered individual dislocation from the two populations; therefore, the GND and SSD populations would both act as forest obstacles to dislocation motion.

A competing theory on the role of the GND's in non-homogeneously deforming crystals is that the GND's pile up and create internal stresses within the material that resist further plastic deformation (Hall, 1951; Petch, 1953; Cottrell, 1958; Nakanishi

and Suzuki, 1974; Weertman, 1996). The arguments are based on the fact that GND's consist of a population of dislocations with the same Burgers vector and tangent line direction. The behavior of such dislocations is analogous to the behavior of charged species. Like charges within a population repel each other, and an electrostatic force must be applied to keep a density of them together. Likewise, dislocations of the same type repel each other, unless they form certain minimum energy structures, and stresses are needed to keep them together. The GND density may organize by piling-up to establish internal stresses that oppose the applied stress and increase the resistance to dislocation motion.

Both theories associate an increase in the resistance to dislocation motion associated with the presence of GND's, but the ideology driving their arguments is quite different. The work-hardening arguments consider GND's to be additive to the background SSD population, and therefore to increase the total dislocation resistance by acting as additional obstacles. The pile-up arguments attribute to the GND's a different behavior than the SSD's, in that the GND's are assumed to create internal stresses that resist the applied stress, instead of behaving just like forest obstacles. The debate about how the GND density affects the plastic behavior is ongoing. In strength-based internal state variables models of crystal plasticity, the influence of the GND population is assumed to either add to obstacle density or to lead to internal stresses within the framework of the model. By developing a dislocation density based internal state variable model for crystal plasticity, one could investigate the question directly by considering the co-evolution of SSD and GND density and the latter's internal stresses.

The effects of a polar dislocation population, a dislocation distribution with net lattice-geometric consequences, have been investigated in several experiments conducted on the micron scale. The classic example of scale-dependent material behavior and its association to polar density is the grain size dependence of yield in polycrystals. The yield strength is observed to increase as the grain size decreases (Hall, 1951; Petch, 1953). The polar density is needed to accommodate the plastic strain incompatibility between neighboring grains, and the magnitude of the polar

density per unit volume increases as the grain dimension decreases, leading to the observed phenomenon (Dai, 1997). Micro-indentation experiments have shown a similar length-scale-dependence in the plastic response of crystalline materials. The measured hardness of a crystal is observed to increase as the indentation depth decreases (Stelmashenko et al., 1993; Ma and Clarke, 1995; Nix and Gao, 1998). Again, the steeper plastic strain gradients are associated with the shallower indentations, and the polar density scales proportionally with the strain gradient, leading to the length-scale-dependent phenomenon observed. Similar results have been observed in the torsion of thin wires ($d = 12\ \mu\text{m} - 170\ \mu\text{m}$) and in the bending of thin beams ($h = 12\ \mu\text{m} - 50\ \mu\text{m}$) (Fleck et al., 1994; Stölken and Evans, 1998). The normalized torsional strength is observed to increase as the radius of the wire decreases, and the normalized bending moment is greater in the thinner beams than in the thicker beams. In each case the normalization is applied such that if no scale dependence was observed, the nominal stress/strain curves would fall on the same line. In the torsion experiments, the GND density scales with the plastic strain gradient from the center of the wire to the surface, and in the bending experiments, the GND density scales with the radius of curvature of the beam. For a given amount of surface strain, the gradients increase in both cases for smaller geometries, and as a result, greater densities of polar dislocations are anticipated in those geometries. The general trend from all of the phenomena is that smaller is stronger due to the presence of greater GND density, and in all of the experiments, the scale of interest is on the order of tens of microns and below.

1.4 Continuum Crystal Plasticity Theories

Although the physical basis for all crystal plasticity formulations is rooted in dislocation mechanics, dislocations, in the form of densities, rarely appear explicitly in working continuum models. The most powerful class of continuum crystal plasticity constitutive models is commonly found in the form of an internal state variable model, where the material "state" is represented by a set of variables which deter-

mine the current plastic response of the material subject to applied loading. In crystal plasticity, material state is most often described by a set of parameters representing slip-system-based deformation resistance (strength), rather than by dislocation density (structure). Currently there are two classes of continuum theories for crystal plasticity: local theories and non-local theories. The local theories have been used to simulate the macroscopic deformation of single crystals and polycrystals, and have no material length scale dependence in their formulations. The non-local theories have been developed in the past decade to incorporate the influence of GND's at microscopic length scales to simulate the material length-scale-dependence observed in the experiments described in the previous section.

1.4.1 Local Macroscopic Theories

The vast majority of continuum crystal plasticity models evolve strength-based internal state variables according to phenomenological hardening rules. Much of crystal plasticity research has focused on developing better phenomenological hardening rules to describe the plastic behavior of crystals (Franciosi and Zaoui, 1982; Follansbee and Kocks, 1988; Bassani and Wu, 1991; Qin and Bassani, 1992; Kothari and Anand, 1998; Marin and Dawson, 1998; Nemat-Nasser et al., 1998a; Nemat-Nasser et al., 1998b; Balasubramanian and Anand, 2000). All of the models increment the crystallographic strengths with an equation of the form:

$$\dot{s}^a = \sum_b h^{ab}\dot{\gamma}^b \ , \tag{1.1}$$

where s^a is the strength on slip system a, h^{ab} is a hardening matrix, and $\dot{\gamma}^b$ are the crystallographic plastic shearing rates on all of the slip systems. The hardening matrix h^{ab} is typically taken to be a function of the current strength state and material constants. The crystallographic plastic shearing rate on each slip system is typically a function of the local stress state and the strength of the slip system. Given the complex non-linear relations between dislocation structure and deformation resistance, it is not surprising that the successes of traditional approaches to the development of

phenomenological relations describing the evolution of deformation resistances have been circumscribed.

Strength-based constitutive models have been successful in predicting the stress/strain response and the texture evolution of polycrystals for a wide range of strain rates and temperatures (Mathur and Dawson, 1989; Bronkhorst et al., 1992; Beaudoin et al., 1994; Nemat-Nasser et al., 1998a; Nemat-Nasser et al., 1998b; Kumar and Dawson, 1998). However, in detailed inspections of simulation results, the predictions of the strength-based crystal plasticity models have failed to capture the local plastic response of crystalline materials (Becker and Panchanadeeswaran, 1995). They have been mostly unsuccessful in capturing the orientation dependence of the stress/strain behavior of single crystals (Kumar and Yang, 1999). Also, the material state as quantified by crystallographic strengths cannot be directly observed, and it has been difficult to reconcile with experimental observations, often requiring experimental data that is difficult to obtain (Kocks and Brown, 1966; Bassani and Wu, 1991).

Beneath all of the phenomenology associated with the strength-based internal state variable models there are dislocation processes that govern the evolution of the strength variables. The crystallographic strengths quantify the resistance that gliding dislocations encounter due to their local and non-local interactions with the rest of the dislocation density and other barriers as they move across slip planes. The evolution of this resistance is determined by the net generation and annihilation of dislocation density during plastic deformation. A few constitutive models have been proposed which use dislocation densities as internal state variables (Cuitiño and Ortiz, 1992; Cuitiño and Ortiz, 1993). These models have successfully captured the orientation-dependence of the stress/strain behavior in copper and $L1_2$ intermetallic single crystals; however, the evolution of the dislocation state variables again follows phenomenological constitutive laws similar to those developed for strength-based internal state variable formulations. Furthermore, only one scalar density is quantified for each slip system, and the geometric aspects of the dislocation density on that system are not captured.

1.4.2 Non-Local Microscopic Theories

Experiments performed over the past decade investigating the scale dependence of crystal plasticity have inspired a variety of non-local crystal plasticity theories that can incorporate an internal material length scale. The theories, as a group, have been referred to as strain-gradient plasticity theory because the material length-scale-dependence is usually incorporated by a constitutive response that is a function of gradients in the plastic strain of a material. Ideologically, "strain-gradient plasticity" does not fit properly within the internal state variable framework. The plastic strain of a material does not quantify the state of a material because it can not be determined without knowing the processing history of a material. Furthermore, plastic strain does not contain any information about the current (dislocation) structure of the crystal. Likewise, the strain gradients in a material do not quantify the material state for the same reasons. More appropriate descriptions have been suggested such as "lattice-incompatibility plasticity" or"strain-incompatibility plasticity"; these alternatives try to capture the underlying idea that the dislocation structure is responsible for the length-scale-dependent material behavior.

The first non-local theories were constructed and implemented to model the size of shear bands formed during the deformation of polycrystalline specimens (Zbib and Aifantis, 1989; Mühlhaus and Aifantis, 1991). Conventional local theories could not specify a finite shear band width, and finite element implementations of the those theories would predict shear bands that were dependent on the element size and mesh geometry. The non-local models that were developed could predict a finite width of shear bands by associating a strain energy with the second gradient of deformation, but the models were not crystallographic in nature and made no attempt to relate the behavior to the presence of GND's.

Fleck and Hutchinson (1993, 1997) (Fleck et al., 1994) developed a phenomenological theory that incorporated higher order strain gradients and couple stresses to predict the strain gradient dependence of strength. Along with the couple stresses, higher-order boundary conditions needed to be specified to complete the formalism.

The theory was inspired by concepts in dislocation mechanics, but the formal theory developed phenomenological relationships between the strength of a material and the invariants of the strain gradients without any direct dislocation or lattice considerations. Initially, the theory was isotropic and did not carry the crystalline geometry, but the theory has been refined recently to extend the formalism to crystallographic systems (Shu and Fleck, 1998; Shu and Fleck, 1999). Also, new theories have been developed within the Fleck and Hutchinson framework that attempt to tie the phenomenological theory to its dislocation underpinnings (Nix and Gao, 1998; Gao et al., 1999; Huang et al., 2000). These models have been used to investigate the grain size dependence of yield in polycrystals (Smyshlyaev and Fleck, 1996), torsion of thin wires (Fleck et al., 1994), micro-indentation (Nix and Gao, 1998; Shu and Fleck, 1998), and bi-crystal interfaces (Shu and Fleck, 1999). The original theory and all of its extensions have used the small strain assumptions in their deformation kinematics.

To my knowledge, a finite deformation constitutive theory following the Fleck and Hutchinson framework has never been developed. New frameworks for scale dependent plasticity have been suggested that associate an internal energy with the lattice incompatibility (Gurtin, 2000; Menzel and Steinmann, 2000). They are similar in structure to the Fleck and Hutchinson approach in that they also add higher-order boundary conditions. Menzel and Steinmann's framework still carries the small strain assumption while Gurtin's framework is established for finite deformations, but neither of the models develop constitutive equations.

Another set of theories has been developed for finite deformations that attempt to establish more direct connections to the underlying dislocation structure. The multiplicative decomposition of the total deformation gradient into its plastic and elastic parts is exploited to evaluate the lattice-incompatibility associated with non-homogeneous plastic deformation. The measure can be directly related to certain aspects of the underlying dislocation structure in the material. This measure yields a second-order dislocation tensor that is then incorporated into existing local strength-based internal variable models forming strength dislocation hybrid models that can capture the length scale dependence in the mechanical behavior observed. Some

models have been developed whereby the dislocation tensor is directly incorporated into the constitutive behavior (Acharya and Bassani, 2000; Acharya and Beaudoin, 2000). Models have also been developed which quantify the polar dislocation density crystallographically that add to the total dislocation density in the crystal (Dai, 1997; Arsenlis and Parks, 2000). These methods are computationally simpler than the Fleck and Hutchinson forms because they do not add higher order boundary conditions and do not employ couple stresses, and they are based on proper state variables of strength and dislocation density rather than relying on strain and strain gradients. The drawback of the hybrid models is that the nature of the GND populations calculated through the lattice incompatibility is assumed to be additive to that of the SSD population, sessile, and the interaction of the GND population with the strength-based state variables must be prescribed.

A non-local theory of plasticity has been developed where the material state is entirely described by dislocation densities (Sluys and Estrin, 2000). The dislocation density model is based on the local dislocation model of Cuitiño and Ortiz (1992), and non-local features are included through the addition of diffusion-like equations for the evolution of dislocation density. As in the Cuitiño and Ortiz model, the density has no geometric character associated with it other than the slip-system on which they reside. Moreover, the non-local model doesn't track the GND population, and all of the dislocations are considered statistical in nature. This model is distinct from the other models described above in that it is able to simulate the material length-scale-dependence in shear banding without relying on any notion of polar dislocations and strain gradients. It is not clear whether it would be successful in predicting the length-scale dependencies found in the other observed phenomena where the behavior has been shown to be strongly dependent on the magnitude of the plastic strain gradients.

1.5 Outline of Thesis

This work will focus on the role of dislocations, in the form of densities, in the evolution of the mechanical behavior of crystalline materials. The evolution of the material

(dislocation density) state and that state's response to applied loads will be the bases for understanding the behavior observed during deformation processes. Chapter 2 will focus on the geometry of dislocation densities by investigating the properties of the GND and SSD densities on a crystallographic basis. The geometry of each crystallographic dislocation density ξ will be quantified by its line length per unit volume, ρ^{ξ}; its Burgers vector, $\mathbf{b}^{\xi}$; and its tangent line direction, $\mathbf{t}^{\xi}$. The following question is considered: If all that is known about the dislocation density state is the Nye tensor, $\mathbf{A}$, what, if anything, can be said about the crystallographic dislocation density state? The geometrical analysis will show that the two categories of dislocation density (SSD and GND) can be described through arrangements of crystallographic dislocation densities. Certain arrangements of crystallographic density will pierce surface of the volume in which they are contained and have a net Burgers vector and tangent line direction. These arrangements will be referred to as GND densities. Other arrangements do not pierce the surface of the volume, but instead self-terminate, forming complex loop structures. These arrangements will be referred to as SSD densities. If Nye's tensor is known, then the space of crystallographic dislocation densities is restricted so that the lattice incompatibility as quantified by Nye's tensor is accommodated by the crystallographic density.

Armed with geometric properties of crystallographic dislocation densities considered in Chapter 2, the evolution of crystallographic dislocation density in a plastically deforming crystal will be the focus of Chapter 3. The polar accumulation/loss of crystallographic density associated with the non-homogeneous plastic deformation leading to Nye's tensor will depend on the flux divergence of crystallographic dislocation densities. The kinematics associated with this process quantifies the change in the polarity of the crystallographic density completely, and no constitutive equations need to be developed. The evolution of the statistical density is not as easily quantified; however, the general closed-loop structure of the SSD's provides a principal upon which to build a consistent set of evolution equations. On the individual dislocation level, the conservation of Burgers vector requires that moving dislocation lines be connected. On the density level, the conservation of Nye's tensor acts in a similar

fashion. A mobile edge dislocation density must create a trail of screw density, and a mobile screw density must leave a trail of edge density because all of line dislocation lines in the density must be connected through a nodal network that conserves Nye's tensor, as was discovered in Chapter 2. The edge and screw density trails come in the form of dipole pairs that increase the total dislocation density level without affecting Nye's tensor. Pair-wise annihilation reactions act to eliminate statistical dislocation density. The frequency of reaction is based on the frequency that a given crystallographic species comes within a critical distance of its polar opposite. Again, density is removed in dipole pairs without affecting Nye's tensor. The kinematics of density generation by loop expansion and of density reduction by pair-wise annihilation introduce three internal constitutive functions that must be described to complete the model: the average dislocation segment length, the capture radius of annihilation, and the average dislocation velocity for each crystallographic density considered.

In Chapter 4, a "local" version of the model will be implemented into a finite element algorithm to investigate the orientation dependence of the stress/strain behavior of aluminum single crystals under simple tension. The local version will consider only the evolution of the dipole density, but not the accumulation/loss of density due to species flux divergence. A set of constitutive functions will be developed based on the activated slip theory of Kocks et al. (1975) and simple scaling arguments. The ability of aluminum to cross-slip will be handled by including two different types of dislocation densities in the model: Screw dislocation density that will be free to cross-slip on two slip planes, and edge dislocation density that will not be able to do so. Based on the results of the simulations performed on aluminum, explanations for the differences in the experimentally observed mechanical behaviors of aluminum and copper will be offered based on observations of dislocation density evolution in the aluminum simulations. Also, the importance of the Hirth-lock in controlling the deformation of aluminum in the $< 100 >$-orientation will be discussed.

In Chapter 5, a "non-local" version of the model will be implemented on an idealized two dimensional double slip geometry. Unlike the "local" model, the "non-local" model will include the polar accumulation/loss equations in the total evolution of

the crystallographic dislocation density. A deeper analysis of the crystallographic dislocation density evolution equations than the analysis conducted in Chapter 3 will show that the length-scale-dependence observed in crystal plasticity is most likely due to internal stresses related to the polar density, and not due to any polar density effects on forest obstacle mechanisms. Simulations of thin beam bending will show that the polarity of the dislocation density increases as the beam thickness decreases at the same level of total strain, but that the total dislocation density remains mostly unchanged as the beam thickness decreases at the same level of total strain. Furthermore, the polar dislocation density will only account for 1% of the total density, but the stresses associated with the polarity will lead to a 16% increase in strength. The relatively large affect by a relatively small fraction of the polarized density is supported by experimental evidence and could not be credibly accounted for by obstacle-based theories of length-scale-dependence.

In Chapter 6, the results of the thesis will be reviewed, and directions for future inquiry will be proposed. In its current state, the "non-locality" of the model appears only in the evolution of density. There are no non-local forces in the model. Incorporation of non-local dependencies in the constitutive functions of the model is potentially the most promising generalization for developing a system of equations with enough complexity to capture the organization of dislocation density into cellular structures. A list of mathematical symbols commonly found in the thesis is given in Table 1.1

Table 1.1: Commonly used symbols.

$\mathbf{F}$	Total Deformation Gradient ($\partial\mathbf{x}/\partial\mathbf{X}$)
$\mathbf{F}^{\mathrm{e}}$	Elastic Deformation Gradient
$\mathbf{F}^{\mathrm{p}}$	Plastic Deformation Gradient
$\mathbf{L}^{\mathrm{p}}$	Plastic Flow Rate ($\dot{\mathbf{F}}^{\mathrm{p}}\mathbf{F}^{\mathrm{p}-1}$)
$\mathbf{T}$	Cauchy Stress Tensor
$\bar{\mathbf{T}}$	Second Piola-Kirchhoff Stress Tensor w.r.t the isoclinic configuration
$\mathbf{E}^{\mathrm{e}}$	Cauchy-Green Elastic Strain w.r.t. the isoclinic configuration
$\mathcal{L}$	Anisotropic Elastic Stiffness Tensor
μ	Shear modulus
ν	Poisson's Ratio
$\boldsymbol{\alpha}$	Nye's Dislocation Tensor (small strains)
$\mathbf{A}$	Nye's Dislocation Tensor (large strains)
∇	Gradient Operator ($\partial/\partial\mathbf{X}$)
$\dot{\gamma}^a$	Plastic Strain Rate on Slip-System a
τ^a	Resolved Shear Stress on Slip-System a
$\mathbf{m}_0^a$	Slip Direction of Slip-System a in the reference configuration
$\mathbf{n}_0^a$	Slip Plane Normal of Slip-System a in the reference configuration
$\mathbf{p}_0^a$	In-Plane Normal Direction of Slip-System a in the reference configuration
ρ^ξ	Crystallographic Dislocation Density of Index ξ
$\mathbf{b}_0^\xi$	Burgers Vector of Density Index ξ in the reference configuration
$\mathbf{t}_0^\xi$	Tangent Line Direction of Density Index ξ in the reference configuration
$\bar{v}^\xi$	Average Velocity of Density Index ξ
$\bar{l}^\xi$	Average Segment Length of Density Index ξ
$G^{\xi\zeta}$	Forest Strength Interaction Matrix
$H^{\xi\zeta}$	Average Segment Length Interaction Matrix
ρ_{e+}^a	Positive Edge Dislocation Density on Slip-System a
ρ_{e-}^a	Negative Edge Dislocation Density on Slip-System a
ρ_{s+}^a	Positive Screw Dislocation Density on Slip-System a
ρ_{s-}^a	Negative Screw Dislocation Density on Slip-System a
$\bar{\rho}_e^a$	Mean Density of Edge Dislocations on Slip-System a
$\bar{\rho}_s^a$	Mean Density of Screw Dislocations on Slip-System a
$\rho_{e\pm}^a$	Polarity of Edge Dislocation Density on Slip-System a
$\rho_{s\pm}^a$	Polarity of Screw Dislocation Density on Slip-System a
R_e, R_s	Edge and Screw Capture Radii of Annihilation, respectively

Chapter 2

Crystallographic Aspects of Geometrically-Necessary and Statistically-Stored Dislocation Density

2.1 Crystallographic Dislocations from Strain Gradients

Gradients in the plastic strain within crystalline materials give rise to dislocations in order to maintain continuity in the crystal. Furthermore, with knowledge of the crystalline orientation in relation to the strain gradient, the type of dislocation needed to maintain lattice continuity is also specified. The graphical arguments for the existence of these dislocations presented in this section are based on the two-dimensional constructs of Ashby (Ashby, 1970), but have been extended to three-dimensions.

Consider the schematic in Figure 2-1(a-e) of a simple crystal undergoing single slip on slip system "a". The coordinate reference frame is set such that $\mathbf{m}^a$ is a unit vector in the slip direction, $\mathbf{n}^a$ is the slip-plane unit normal, and $\mathbf{p}^a = \mathbf{m}^a \times \mathbf{n}^a$. Imagine that the material can be separated into three sections, and each section can be deformed

independently of the others. Through expanding dislocation loops, the respective sections are plastically deformed such that the plastic strain increases linearly in the slip direction. When the dislocation loops reach the boundaries of each section, the screw portions reach free boundaries and exit the material, but the edge portions of the loops encounter fictitious internal boundaries and remain as dipoles spread to either side of each section. The sections are then forced back together, and there are negative edge dislocations which do not annihilate, but remain in the material, leading to lattice curvature.

Mathematically, the relationship between the plastic strain gradient $\nabla\gamma^a$ on a slip system a and the edge dislocation density takes the following form:

$$\rho^a_{GN(e)}|\mathbf{b}| = -\nabla\gamma^a \cdot \mathbf{m}^a = -\gamma^a_{,k} m^a_k \ , \tag{2.1}$$

where $\rho^a_{GN(e)}$ is the geometrically-necessary positive edge dislocation density and $\mathbf{b}$ is the Burgers vector.

A similar construction can be created to illustrate the presence of screw dislocations due to strain gradients. The schematic in Figure 2-2(a-e) shows the same single slip system material as in Figure 2-1(a-e). In this figure, the material is again separated into three sections, and each section is deformed independently of the other. Through expanding dislocation loops, the sections are plastically deformed such that the plastic strain increases linearly in the $\mathbf{p}^a$-direction. When the dislocation loops reach the boundaries of each section, the edge portions reach free boundaries and exit the material, but the screw segments encounter fictitious internal boundaries and remain as dipoles spread to either side of each section. In the figure shown, the negative screw dislocations are illustrated, but there are also an equal number of positive screw dislocations, not shown, on the back (hidden) side of each section. When the sections are forced back together, there are positive screw dislocations which do not annihilate, remaining in the material and causing the lattice to warp.

The relationship between the plastic strain gradient $\nabla\gamma^a$ on a slip system a and

the screw dislocation density takes the following form:

$$\rho^a_{GN(s)}|\mathbf{b}| = \nabla\gamma^a \cdot \mathbf{p}^a = \gamma^a_{,k} p^a_k \ , \tag{2.2}$$

where $\rho^a_{GN(s)}$ is the geometrically-necessary positive screw dislocation density and $\mathbf{b}$ is the Burgers vector.

These developments clearly show that gradients of plastic strain lead to the presence of dislocations with same polarity. Furthermore, depending on the direction of the gradients in relation to the crystalline geometry, the type of dislocations needed to maintain lattice continuity can be specified, independent of the mechanism which caused the strain gradient. The plastic deformation in each example was accomplished through expanding dislocation loops, but the gradients of the plastic deformation were in different directions, leading to the accumulation of either geometrically-necessary edge or screw dislocations. The existence of the dislocations was necessary to maintain lattice continuity, and led to distortions of the the crystal lattice. Generally, the dislocation state associated with lattice distortion can be described in terms of a second-order tensor, to be discussed in the next section.

2.2 Nye's Tensor and Continuously-Distributed Dislocation Density

In 1953, Nye introduced a dislocation tensor quantifying the state of dislocation of a lattice (Nye, 1953). Nye's tensor, α_{ij}, is a representation of dislocations with Burgers vector i and line vector j. Considering continuously-distributed dislocations, Nye's tensor quantifies a special set of dislocations whose geometric properties are not canceled by other dislocations in the crystal. Consider the volume element shown in Figure 2-3, which is a section of a crystal containing two edge dislocations threading through the volume. The most rigorous manner to describe the dislocation state in the volume would be to characterize the lines by two Dirac delta functions of strength b in space; however, such a quantification of dislocation density becomes overwhelming

given the densities involved in plastic deformation processes ($\rho \approx 10^{16} m^{-2}$) (Basinski and Basinski, 1979). Allowing such point densities to become continuously-distributed within a volume creates a more compact way of describing dislocations in space, but a result of this process is that the spatial correlation of the individual dislocation lines within the volume is lost.

If the reference volume element over which dislocation properties will be continuously-distributed is taken to be the entire volume in Figure 2-3, the net Nye's tensor of the element is zero because the dislocation density, as drawn, consists of two dislocations with common tangent line vector but opposite Burgers vector: these form a dislocation dipole. When the properties of each dislocation segment are distributed uniformly over the entire volume, the exact positions of the original dislocations are no longer relevant. In terms of Nye's tensor, an equivalent form would be to place the two dislocations on top of one another, allowing them to annihilate, leaving behind no dislocation density in the element. In any continuously-distributed dislocation formulation, individual dislocation dipoles, planar dislocation loops, and other three-dimensional self-terminating dislocation structures fully contained within the reference volume make no net contribution to Nye's tensor. The three-dimensional self-terminating dislocation structures mentioned here will be further developed in later sections. These redundant structures, which make no contribution to Nye's tensor, are considered statistically-stored dislocations (SSD's), and are believed to result from plastic deformation processes (Ashby, 1970). Once individual dislocation segments are considered to be uniformly distributed within a reference volume, Nye's tensor measures the non-redundant dislocation density within the volume. These non-redundant dislocations are believed to result from plastic strain gradient fields, as demonstrated in the previous section, and have geometric consequences on the crystal lattices. As a result, they are commonly referred to as geometrically-necessary dislocation (GND) density.

Nye's tensor can easily be calculated for a volume element by a line integral over all dislocations within the volume. If $\mathbf{b}$ is the Burgers vector of a dislocation with

local unit tangent line direction $\mathbf{t}$, Nye's tensor, α_{ij}, can be defined as

$$\alpha_{ij} \equiv \frac{1}{V} \int_L b_i t_j ds \ , \tag{2.3}$$

where V is the reference volume, ds in an element of arc length along the dislocation line, and L is the total length of dislocation line within V. Nye's tensor becomes a summation of the integrated properties of all the individual dislocation line segments in the volume. This integral relation also has the property of averaging the dislocation properties within the volume, thus converting clearly distinct dislocation lines into a uniformly distributed property within the volume. If each of the dislocation line segments is considered as a separate entity with constant Burgers vector, the definition of Nye's tensor can be rewritten as

$$\alpha_{ij} \equiv \frac{1}{V} \sum_{\xi} b_i^{\xi} \int_l \bar{t}_j^{\xi} ds^{\xi} \ , \tag{2.4}$$

where l is the length of a dislocation segment of type ξ. Inspection of this summation of integrals immediately shows global properties of Nye's tensor. Consider Figure 2-4 of a dislocation threading though a reference volume element used to define Nye's tensor. If Eq. 2.4 is used to evaluate Nye's tensor for this element, the result becomes

$$\alpha_{ij} = \frac{1}{V} b_i \left(x_j^+ - x_j^- \right) \ , \tag{2.5}$$

where $\mathbf{x}^-$ and $\mathbf{x}^+$ are the positions of the starting and stopping points of the dislocation line segment, respectively. Equation 2.5 states that the only information from each dislocation line segment needed to calculate its contribution to Nye's tensor is its Burgers vector and two endpoints. The path that the dislocation line makes between these two points has no effect on the evaluation of Nye's tensor. Returning to Figure 2-4, for the purpose of evaluating Nye's tensor, the curved dislocation line could be replaced by the dashed straight dislocation line having the same geometric properties. Equation 2.5 may be rewritten to reflect this substitution, with the result that it is the average tangent vector, $\bar{\mathbf{t}}$, and the secant length, $\bar{l}^{\xi}$, which are needed

to calculate α_{ij}:

$$\alpha_{ij} = \frac{1}{V} \sum_{\xi} \bar{l}^{\xi}_{GN} \; b^{\xi}_{i} \; \bar{t}^{\xi}_{j} \; , \tag{2.6}$$

where

$$\bar{t}^{\xi}_{j} = \frac{\left(x^{+}_{j} - x^{-}_{j}\right)}{\sqrt{\left(x^{+}_{k} - x^{-}_{k}\right)\left(x^{+}_{k} - x^{-}_{k}\right)}} \tag{2.7}$$

and

$$\bar{l}^{\xi}_{GN} = \sqrt{\left(x^{+}_{k} - x^{-}_{k}\right)\left(x^{+}_{k} - x^{-}_{k}\right)} \; . \tag{2.8}$$

Using the description of dislocation density as line length in a volume, the summation of geometric dislocation lengths, $\bar{l}^{\xi}$, in a reference volume, V, can be replaced by a summation of geometric dislocation density, ρ^{ξ}_{GN}, in the volume

$$\alpha_{ij} = \sum_{\xi} \rho^{\xi}_{GN} b^{\xi}_{i} \bar{t}^{\xi}_{j} \; , \tag{2.9}$$

where

$$\rho^{\xi}_{GN} \equiv \frac{\bar{l}^{\xi}_{GN}}{V} \; . \tag{2.10}$$

Of course, the dislocation density described in Eq. 2.9 is not the total dislocation density of any arbitrary dislocation line segment, but it is the portion of the total dislocation density which has geometric consequences. The remaining density of the total line, which has no geometric consequence, must be considered statistical in character. For an arbitrary dislocation line segment, ξ, with a total density in a reference volume, V, defined by

$$\rho^{\xi} \equiv \frac{1}{V} \int_{l} ds^{\xi} \; , \tag{2.11}$$

the portion of the total density which has no geometric consequence, and which would therefore be statistical in nature, would be

$$\rho^{\xi}_{SS} \equiv \rho^{\xi} - \rho^{\xi}_{GN} \; , \tag{2.12}$$

where the subscript SS denotes that the dislocation density is considered statistically-stored. With this decomposition of total dislocation density, an arbitrary line threading through a reference volume element as in Figure 2-4 may be separated into that portion of the total density which has geometric effects, ρ_{GN}, and the portion of the total density which does not, ρ_{SS}.

Another result of the definition of Nye's tensor which becomes immediately apparent through Eq. 2.5 is that closed dislocation loops of constant Burgers vector have no net geometric consequence; i.e.,

$$\alpha_{ij} = \frac{1}{V} b_i \oint_l t_j ds = 0_{ij} \ . \tag{2.13}$$

As a generalization of this property, any dislocation network structure which is topologically closed and is entirely contained within the reference volume also has no net contribution to Nye's tensor.

In this formulation of Nye's tensor, the size of the reference volume element over which the density is averaged plays a crucial role in defining the tensor. Consider again Figure 2-3 of the dislocation dipole. If the reference volume elements were taken to be smaller than the entire volume shown, such that both dislocations did not populate the same element, Nye's tensor within each sub-volume would change, becoming non-zero. In the limit as the volume elements used to define the dislocation state become differential, Nye's tensor tends toward two delta functions that exactly describe the dislocation state. Selection of an appropriate reference volume element must take into account the scale of the geometric effects to be captured. A volume element that is too large with respect to the geometric constraints may miss the existence of important geometrically-derived dislocations in one portion of the element that, when averaged with other dislocations in the same element, create no net Nye's tensor. Conversely, a volume element which is too small may become too computationally intensive (too numerous) to manage, and may begin to reach length scales where dislocation density can no longer be considered continuously-distributed, so that discrete dislocation mechanics must be adopted.

The definition of Nye's tensor proposed here is based on the description of dislocation density as line length in a reference volume. In Nye's original formulation of the dislocation tensor, dislocation density was described as a number density of lines piercing a plane. He defined the tensor in the following manner

$$\alpha_{ij} = nb_i t_j \ , \tag{2.14}$$

where n was the number density of dislocation lines with Burgers vector, $\mathbf{b}$, crossing a unit area normal to their unit tangent line vector, $\mathbf{t}$. This expression closely resembles the definition of the tensor in Eq. 2.9. In the procedure by which Nye described the dislocation tensor, the dislocations which constituted it were considered to be continuously-distributed, and the tangent line vectors were implicitly constant. The discrete case, in which a material is segmented into volume elements, was not considered in the original formulation. The expression proposed here is a generalization which can be applied to arbitrary dislocation arrangements, and the two definitions are equivalent because the dislocations which contribute to the geometric density in the bulk must pierce the surface that encloses the reference volume, as a consequence of Eq. 2.13. Consider Figure 2-5a, which represents a relatively simple dislocation arrangement containing two dislocation junctions threading through the volume. By applying Eq. 2.3 to the system, it can be shown that a geometrically equivalent dislocation arrangement would be a single straight dislocation segment as shown in Figure 2-5b. This results from the property that Burgers vector is conserved through line segments and their junctions. Applying both Eq. 2.3 and Eq. 2.14 to the simplified structure in Figure 2-5b yields the same value for Nye's tensor. The definitions are equivalent because of the stereological relationship between the two descriptions of dislocation density.

2.3 Lattice-Geometric Consequences of Nye's Tensor

Certain plastic strain gradients necessarily lead to the existence of dislocations in crystalline materials to maintain lattice continuity. Nye's tensor provides a measure of these geometrically-derived dislocations, and a non-zero Nye's tensor leads to lattice curvature, neglecting elastic strain gradients in the material. Introduction of dislocations of the same type into a crystal causes the lattice to curve and generally warp, and a tensor quantifying such lattice curvature must be closely related to Nye's tensor. The curvature tensor, κ_{ij}, is defined as a small right-handed lattice rotation of magnitude $\delta\vartheta$ about the i-axis for a unit change of position of magnitude δx in the j-direction:

$$\delta\vartheta_i = \kappa_{ij}\delta x_j \ . \tag{2.15}$$

Nye's tensor relates the GND density to lattice curvature in the following manner:

$$\kappa_{ij} = -\alpha_{ji} + \frac{1}{2}\delta_{ji}\alpha_{kk} \ , \tag{2.16}$$

which is the same result that Nye derived, but with a different sign convention (Nye, 1953). There is also a contribution from elastic strain gradients to the total lattice curvature. A complete and rigorous derivation of the relationship between strain gradients, curvature, and the new definition of Nye's tensor is presented in this section.

The following derivation closely mirrors a previous analysis by Fleck and Hutchinson (Fleck and Hutchinson, 1997). The equations are developed for small deformations for simplicity to illustrate the properties of Nye's tensor. In the next chapter, the geometry associated with large deformations will be used; however, many of the physical insights remain the same. The displacement gradient, $u_{i,j}$, can be additively decomposed into the plastic slip tensor, γ_{ij}, the skew lattice rotation tensor, ϕ_{ij}, and the symmetric elastic strain tensor, $\epsilon^{\mathrm{el}}_{ij}$, as shown in Eq. 2.17:

$$u_{i,k} = \gamma_{ik} + \phi_{ik} + \epsilon^{\mathrm{el}}_{ik} \ . \tag{2.17}$$

The curl of the displacement gradient vanishes because of the symmetry of the second gradient; this also implies that deformation occurs in such a way that the body remains simply connected. Such a procedure, when performed on Eq. 2.17, produces:

$$e_{pjk}u_{i,kj} = e_{pjk}\gamma_{ik,j} + e_{pjk}\phi_{ik,j} + e_{pjk}\epsilon^{\mathrm{el}}_{ik,j} = 0_{pi} \ , \tag{2.18}$$

where e_{pjk} are the cartesian components of the alternating tensor. The components of the lattice rotation tensor, ϕ_{ik}, can be written in terms of the lattice rotation vector, ϑ_l, according to

$$\phi_{ik} = e_{ilk}\vartheta_l \ . \tag{2.19}$$

Substitution of Eq. 2.19 into Eq. 2.18 gives

$$e_{pjk}\gamma_{ik,j} + e_{pjk}e_{ilk}\vartheta_{l,j} + e_{pjk}\epsilon^{\mathrm{el}}_{ik,j} = 0_{pi} \ . \tag{2.20}$$

Using the definition of $\kappa_{lj} = \vartheta_{l,j}$ implied by Eq. 2.15, inversion of Eq. 2.20 gives

$$\kappa_{pi} = e_{pjk}\gamma_{ik,j} - \frac{1}{2}\delta_{pi}e_{sjk}\gamma_{sk,j} + e_{pjk}\epsilon^{\mathrm{el}}_{ik,j} \ . \tag{2.21}$$

Since plastic deformation is a result of the slip on crystallographic planes, γ_{ij} can be written as a sum of crystallographic shears such that

$$\gamma_{ik} = \sum_a \gamma^a \ m^a_i \ n^a_k \ , \tag{2.22}$$

where $\mathbf{m}^a$ is the slip direction and $\mathbf{n}^a$ is the slip-plane normal direction of slip-system a on which a plastic shear, γ^a, has occurred. Applying the curl operation inside the summation yields

$$e_{pjk}\gamma_{ik,j} = \sum_a e_{pjk}\gamma^a_{,j}m^a_i n^a_k = \sum_a \gamma^a_{,j}m^a_i(m^a_j p^a_p - p^a_j m^a_p) \ , \tag{2.23}$$

where the last step follows from the definition $\mathbf{p}^a = \mathbf{m}^a \times \mathbf{n}^a$. Using Eq. 2.1 and

Eq. 2.2, the right side of Eq. 2.23 can be replaced by dislocation densities:

$$e_{pjk}\gamma_{ik,j} = \sum_a -\rho^a_{GN(e)}\ b^a\ m^a_i\ p^a_p - \rho^a_{GN(s)}\ b^a\ m^a_i\ m^a_p\ . \tag{2.24}$$

Dislocation densities are considered to be defined as length of line in a reference volume, which allows for a substitution of variables in Eq. 2.24, leading to

$$e_{pjk}\gamma_{ik,j} = -\sum_a \rho^a_{GN}\ b^a\ m^a_i\ \bar{t}^a_p\ , \tag{2.25}$$

where

$$\rho^a_{GN} \equiv \sqrt{\left(\rho^a_{GN(e)}\right)^2 + \left(\rho^a_{GN(s)}\right)^2} \tag{2.26}$$

and

$$\bar{t}^a_p \equiv \frac{\rho^a_{GN(e)}p^a_p + \rho^a_{GN(s)}m^a_p}{\rho^a_{GN}}\ . \tag{2.27}$$

The right-hand side of Eq. 2.25 is the expression used to define Nye's tensor in Eq. 2.9 relating the gradient of plastic slip to Nye's tensor. Substitution of Eq. 2.25 into Eq. 2.21 using the definition of Nye's tensor in Eq. 2.9 yields

$$\kappa_{pi} = -\alpha_{ip} + \frac{1}{2}\delta_{pi}\alpha_{kk} + e_{pjk}\epsilon^{\mathrm{el}}_{ik,j}\ , \tag{2.28}$$

which is the same expression as Eq. 2.16 in the absence of elastic strain gradients.

The relationships among plastic slip gradients, geometrically-necessary dislocation density, Nye's tensor, and lattice curvature presented thus far are general and apply to any crystal lattice. In the next section, the presence of GND density in crystals with a high degree of symmetry is considered. The symmetry allows for multiple dislocation configurations to have the same total geometric properties. Therefore, the crystallographic dislocation state resultant from the geometric constraints is indeterminate. The indeterminacy can be resolved using two methods, as proposed in the next section.

2.4 Unique Description of GND's in Redundant Crystals

The most rigorous manner to describe crystallographic dislocation density would be to develop initial conditions and evolution laws for their densities and their interactions. The geometrical properties of such dislocation distributions would just be a consequence of the evolving state. Nye's tensor would be a simple result of the density at any instant, and plastic strain would result from the motion of density through the volume. Such evolution equations will be the focus of Chapter 3. However, the plastic slip-gradient field alone imposes geometric constraints on the dislocation density state which disallows many crystallographic dislocation distributions.

In crystals with a high degree of symmetry, the geometric constraints can be satisfied with many different dislocation configurations due to their redundancy, much the same as a given plastic deformation can be performed by different combinations of slip on individual systems. In such redundant crystals, the number of distinct dislocation "types", each with its own geometric properties, exceeds the nine independent values in Nye's tensor, but the concept of geometrically-necessary dislocations implies a minimization of density. Consider again Figure 2-4 of the dislocation threading through a reference volume. It was shown that its total dislocation density could be decomposed into a geometrically-necessary part and a statistically-stored part. The geometrically-necessary part was the minimum dislocation density needed to span the two endpoints of the dislocation line segment. If the only information from which crystallographic dislocation densities are to be determined results from geometric constraints, then the crystallographic dislocation density derived from the constraints must be a minimum density. Anything above the geometric minimum necessary would (necessarily!) incorporate some statistical character which cannot be determined through geometric arguments. By considering different density normalizations and minimizing the dislocation density with respect those normalizations, a unique description of crystallographic GND's can be found.

The first step in finding the GND configuration on a crystallographic basis is to

discretize the dislocation space of a crystal. The Burgers vectors in a crystal are already discrete, but the tangent line vector of a dislocation is free to occupy any direction on the slip plane (If dislocations are allowed to climb, even this restrictive condition no longer holds!). The tangent line vectors must be discretized in such a fashion that the discretized space is well representative of the actual dislocation space. The discretized Burgers vector, $\mathbf{b}$, and tangent line vectors, $\mathbf{t}$, form n-pairs of geometric dislocation properties. Nye's tensor, $\boldsymbol{\alpha}$, can be written as a summation of dislocation dyadics, $\mathbf{d}_i$, premultiplied by a scalar dislocation density, ρ_i, as follows:

$$\boldsymbol{\alpha} = \sum_{i=1}^{n} \rho_i \mathbf{d}_i \ , \tag{2.29}$$

where the dislocation dyadic is given by

$$\mathbf{d}_i = \mathbf{b}^i \otimes \mathbf{t}^i \ . \tag{2.30}$$

The relationship (2.29) can be rewritten such that Nye's tensor, represented as a nine-dimensional column vector Λ containing the components of $\boldsymbol{\alpha}$, is the result of a linear operator, $\mathbf{D}$, acting on the n-dimensional crystallographic dislocation density vector, ρ, as shown:

$$\mathbf{D}\rho = \Lambda \ . \tag{2.31}$$

The null space of operator $\mathbf{D}$ yields those combinations of crystallographic dislocation density which have no geometric consequence; thus these combinations can be considered as statistically-stored. Such dislocation density groups are placed in a subspace of the n-dimensional ρ-space, ρ_{SS}; the dimension of the statistically-stored dislocation density subspace is $n - 9$.

In considering GND's, there are two minimizations which can be considered. One minimization, L^2, is geometrically motivated through Eq. 2.26 and minimizes the sum of the squares of the resulting dislocation densities. The discretization of the dislocation space only allows certain dislocations on the slip plane to exist, and the L^2 minimization takes this into account by being able to combine dislocation line

lengths into a single dislocation line length which may not exist within the original discretization. The other minimizing technique, L^1, is energetically motivated. By considering dislocation density as line length through a volume, the total dislocation line energy can be minimized by finding the dislocation configuration with the smallest total line length.

Mathematically, the L^2 minimization is the easier of the two methods to compute. The functional, $C(\rho, y)$, to be minimized takes the form

$$C(\rho, y) = \rho^T \rho + y^T(\mathbf{D}\rho - \Lambda) \ , \tag{2.32}$$

where the nine-dimensional vector y contains the Lagrange multipliers. The solution can be found explicitly because it follows from singular value decomposition, having the following mathematical form:

$$\rho_{GN} = \left(\mathbf{D}^T\mathbf{D}\right)^{-1}\mathbf{D}^T\Lambda \equiv \mathbf{B}\Lambda \ , \tag{2.33}$$

which gives an explicit formula for the crystallographic GND density, ρ_{GN}, for any given value of Nye's tensor. Furthermore, ρ_{GN} calculated in this manner describes a dislocation density subspace which is orthogonal to ρ_{SS} such that $(\rho_{GN})^T\rho_{SS} = 0$, and the two subspaces span the total n-dimensional space of crystallographic dislocation densities.

There is no explicit formula for determining ρ_{GN} from Nye's tensor with respect to the L^1 minimum. Using this technique, the functional, $E(\rho, y)$, to be minimized takes the form

$$E(\rho, y) = \sum_{i=1}^{n} |\rho_i| + y^T(\mathbf{D}\rho - \Lambda) \ , \tag{2.34}$$

where the nine-dimensional vector y contains the Lagrange multipliers. A linear simplex method is implemented to calculate ρ_{GN} for each different value of Nye's tensor. The resultant crystallographic dislocation density vector doesn't lie outside the ρ_{SS} subspace, as is possible for the one obtained using the L^2 minimization. The two techniques are demonstrated on a face-centered cubic (FCC) crystal in the

following sections to illustrate the properties of each normalization, and the null space of $\mathbf{D}$ is also analyzed to determine the properties of ρ_{SS} in redundant crystals.

2.5 Geometrically-Necessary Dislocations in FCC Crystals

Face-centered cubic crystals have slip systems in which the slip-planes are of $\{111\}$ type and the slip-directions are of $< 110 >$ type. Although any discrete basis of dislocations which exist in the crystal may be considered, a natural choice is to limit the dislocations to only pure edge and pure screw types as Kubin et al. (1992) have done in their dislocation simulations. Adopting this discretization, there are a total of eighteen different dislocation types: twelve edge and six screw dislocations. The dislocations and their line properties are given in Table 2.1. Crystallographic dislocation density is described by an eighteen-dimensional vector in which each distinct dislocation type receives its own index, and ρ_i is the density of the ith dislocation type. The densities in the vector may be positive or negative in sign, and the interpretation of the sign of a density will be discussed. Nye's tensor has only nine independent components; therefore, when describing the dislocation state in terms of crystallographic dislocation densities, the problem is under-defined, much like the indeterminacy of apportioning slip on crystallographic planes based on a known plastic deformation.

The geometric properties of the crystallographic dislocation densities were mapped onto the FCC unit cell using Eq. 2.9, and the indices of Nye's tensor became the three orthonormal directions of the FCC unit cell. A set of nine vectors were found which led to no contribution in Nye's tensor. These null vectors can be considered as the redundant or SSD's and will be discussed in detail in the next section. The GND density was calculated using the two different techniques outlined in the previous section, and the resultant GND distributions from the L^2 and L^1 minimizations will be presented independently and compared at the end of this section.

Using the singular value decomposition described above, a set of nine crystallographic dislocation vectors were obtained which minimized the sum of the squares of the densities and satisfied the geometric requirements of Nye's tensor. Table 2.2 shows the matrix which can be used to compute a general crystallographic dislocation distribution from GND density using L^2 minimization and the SSD density with $< 100 >$ directions as the basis vectors of Nye's tensor. The first nine columns of this matrix make up the matrix, $\mathbf{B}$, in Eq. 2.33. Note that there are negative crystallographic dislocation densities in the GND vectors. The negative densities appear as a result of the discrete dislocation basis chosen. The basis defines the right-handed edge and screw dislocations as being positive densities, and left-handed edge and screw dislocation densities are considered negative. The L^1 formulation employs an expanded basis, and the necessity to interpret negative densities is eliminated.

Upon inspection of the nine GND vectors, there are only two distinct dislocation arrangements which are formed: one which exhibits the same properties as a $< 100 >$ $< 100 >$ screw dislocation, and one which exhibits the same properties as a $< 100 >$ $< 010 >$ edge dislocation on the FCC unit cell. The other seven density vectors are just orthogonal transformations of these two GND vectors. In FCC materials, dislocations with Burgers vectors of $< 100 >$ type are not preferred, but an arrangement of crystallographic dislocations can be formed which has the same geometric properties as a $< 100 >$ type dislocation. This arrangement for a screw dislocation is mathematically described by the first density vector (column 1) in Table 2.2, and is graphically presented in Figure 2-6 by interpreting the densities as line lengths within a volume described by Eq. 2.9. Figure 2-6 shows the resulting double-helical structure, with screw dislocations around the perimeter of the structure and a mix of edge and screw dislocations in the center. The global geometric properties of this dislocation structure are the same as those of a [100] type screw dislocation. It is periodic in the direction of the dislocation line vector, [100], and there is a discrete rotational symmetry about the [100] axis, much as a [100] [100] screw dislocation would have, if it existed in FCC crystals.

A similar arrangement can be created to describe a resultant $< 100 >$ $< 010 >$

edge dislocation in FCC materials. This arrangement is mathematically described by the second vector (column 2) in Table 2.2, and is graphically shown in Figure 2-7. It is made up of twelve edge dislocations, and two screw dislocations which cross at the center of the structure. The structure is again periodic in the line direction, and it has the same global geometric properties as the $< 100 > < 010 >$ edge dislocation. The structure also has a mirror symmetry on either side of the virtual extra atomic half plane. With these nine vectors, a lattice dislocated with an arbitrary Burgers vector and line direction can be described as a periodic structure made up of the eighteen crystallographic dislocation densities in FCC materials.

To implement the L^1 minimization of GND's using the linear simplex method, the discretization employed for the L^2 minimization had to be altered such that only positive densities were considered. This was accomplished by giving the left-handed screw and edge dislocations their own index, i, and requiring all densities to be non-negative. The size of the discrete dislocation basis doubled, introducing eighteen more SSD vectors. The new SSD vectors introduced through this discretization represent dislocation dipoles formed by right and left-handed dislocations of equal length. Dislocation dipoles are what are classically thought to result from plastic deformation, and are the most common example of SSD's, and although they were not accounted for in the discretized space employed in the L^2 formulation, they do appear in this expanded space.

To calculate the GND density using the linear simplex method, a feasible solution was found through row reduction of the matrix $\mathbf{D}$ from Eq. 2.31 and back substitution. The minimal L^1 density was found through an iterative process, and had to be conducted for each different value of Nye's tensor. In order to compare the results of L^1 and L^2 minimizations, the dislocation structures for the $< 100 > < 100 >$ screw dislocations and the $< 100 > < 010 >$ edge dislocations were also found using the L^1 minimization technique. The crystallographic dislocation structure for a [100] [100] screw dislocation using the L^1 minimization technique is depicted in Figure 2-8. The structure consists of two separate dislocation lines with Burgers vectors [110] and $[1\bar{1}0]$, respectively, and the same average tangent line vector [100], and each thread-

ing dislocation line consists of three dislocation line segments. The crystallographic dislocation structure for the L^1 minimal [100] [010] edge dislocation found is shown in Figure 2-9. It also is made up two separate dislocation lines with Burgers vectors [110] and $[1\bar{1}0]$, respectively, and the same average tangent line vector [010], and each threading dislocation line consists of two dislocation line segments.

The purpose of this exercise in crystallographic GND's was to find a method to best represent the actual GND dislocation arrangements in crystals. Both of the methods found periodic dislocation arrangements which threaded through the reference volume and had the same global geometric effects. Comparing the screw and edge dislocation arrangements obtained with the two different techniques, the L^1 minimization appears to be a more promising technique than the L^2 technique for determining GND's. In each case, the L^1 method created dislocation structures which were composed of two separate dislocation lines with constant Burgers vectors threading through the volume; the arrangements created by the L^2 method were much more complicated in the sense that they contained more dislocation segments in their structures and also required the formation of intricate junctions. The total dislocation line length needed to describe the [100] [010] edge dislocation with the L^2 minimization was a factor of 1.25 greater than the corresponding L^1 minimization. The total line length needed to describe the [100] [100] screw dislocation with the L^2 minimization was a factor of 1.01 greater than the L^1 minimization. Note that this particular crystalline orientation required the longest total dislocation line length to represent a geometrically-necessary screw dislocation calculated using the L^1 minimization. All other crystalline orientations required shorter total dislocation line lengths. The disadvantage of employing the L^1 method over the L^2 method is that there is no explicit formulation using the linear simplex method to determine ρ_{GN} from Nye's tensor, whereas the singular value decomposition does provide an explicit relation for the L^2 minimum configuration.

2.6 Statistically-Stored Dislocations in FCC Crystals

Classically, statistically-stored dislocation density has been considered to be comprised of dislocation dipoles and planar dislocation loops. In the formalism used to find ρ_{GN} with the L^1 minimization, a total of twenty-seven SSD density vectors were found: only eighteen of these were common dislocation dipoles. In the analysis of the null space of the linear operator $\mathbf{D}$ in Eq. 2.31, nine other SSD structures were found which are neither simple dislocation dipoles nor simple planar loops. These higher-order closed structures are mathematically represented by the space spanned by the last nine vectors of the matrix in Table 2.2. An infinite number of SSD structures can be created by different combinations of the twenty-seven null vectors found, but to illustrate the properties of higher-order SSD structures, the simplest in terms of fewest number of lines and highest symmetry have been found.

The simplest structure consists of five dislocation line segments and is mathematically represented, in varying orientations, by the last eight null vectors in Table 2.2. Interpreting the densities as dislocation line lengths as before, the vectors can be graphically represented. The basic structure corresponding to the last eight null vectors is shown in Figure 2-10. The structure consists of a central edge dislocation that splits into two dislocations which loop around and connect back to the original center dislocation. The Burgers vectors of the three dislocation lines which compose this structure are different, and this structure could be created by the intersection of two expanding dislocation loops with different Burgers vectors on the slip plane. The result would be a dislocation arrangement like the one depicted. Note, however, that the two dislocations are not required to initially be on the same slip plane because, through cross-slipping, an intersection may also occur. There are two linearly-independent planar dislocation structures such as the one depicted in Figure 2-10 on each of the four slip systems leading to the eight null vectors in Table 2.2.

The remaining SSD arrangement described by column 10 in Table 2.2 is made

up of six edge dislocations in the three-dimensional structure shown in Figure 2-11. Three of the dislocations are on the same slip plane with the other three lying, respectively, in the other three slip planes of the FCC crystal lattice. This structure is unique in that it contains a three-dimensional stacking fault whose boundaries are the edge dislocations shown in the figure. Since the extra half planes of atoms are fully contained within the structure, there is no geometric consequence over the volume containing the structure. Linear combinations of this vector with the other eight can create other, more complicated, three-dimensional SSD's. Figure 2-12 depicts a three-dimensional structure consisting of four screw dislocations on the perimeter of the structure and four edge dislocations in the interior of the structure, but as these three-dimensional structures become more complicated, it becomes harder to imagine their occurrence in real crystals.

In general, the higher-order dislocation structures in FCC crystals primarily consist of dislocation loop segments which terminate at planar junctions. The total structure self-terminates, which is to say that the Burgers vector is conserved at each junction in the structure. The closed structures do not thread through the volume as do the crystallographic GND's; furthermore, they don't create any dislocations which pierce the surface of the reference volume.

A general dislocation state for FCC crystals in this basis of thirty-six linearly independent density vectors (nine crystallographic GND vectors, eighteen dislocation dipole vectors, and nine higher-order SSD vectors) can be constructed by any linear combination of the twenty-seven SSD vectors and the particular combination of GND vectors dictated by the value of Nye's tensor. This geometrically-allowable dislocation (GAD) density would conform to the geometric constraints, but would not restrict the total crystallographic dislocation density to any minimum principle. These vectors span the space of all glissile dislocations in FCC crystals, within the discrete dislocation basis. Such a discrete basis could be used to model observed dislocation density arrangements. Also, there may be other crystalline kinetic constraints which may suppress the population of dislocations on certain planes. In Chapter 3, evolution equations for crystallographic dislocation density will be developed such that the

SSD and GND populations can be individually tracked during plastic deformation, and minimization techniques that were presented in this chapter to determine the geometric density will not be necessary. In Chapter 4, a statistical density model evolving the eighteen dislocation dipole vectors will be implemented to simulate the behavior of aluminum single crystals subject to tension.

2.7 Geometrically-Necessary Dislocations in Polycrystalline Aggregates

Parallels have been suggested between the determination of active slip systems from the plastic deformation tensor and the determination of crystallographic GND's from Nye's tensor. In fact, the method used to determine ρ_{GN} using the L^1 minimization is analogous to the method employed by Taylor in the determination of the active slip systems in plastic deformation (Taylor, 1934; Taylor, 1938). Taylor's method was based on the principle of maximum work. The active slip systems were determined to be those which required the least cumulative shearing to accomplish the desired deformation. The L^1 minimization of ρ_{GN} employs a similar energy principle because it produces the dislocation configuration with the smallest total line energy (assuming the constant line energy model), which satisfies Nye's tensor.

Continuing with this analogy, there is a geometric relationship between the yield strength of a polycrystal and the critical resolved shear strength of a slip system. There should be a corresponding relationship between Nye's tensor averaged over a polycrystal and the crystallographic GND density in a single crystal. The Taylor factor, $\overline{m}$, relating the tensile yield strength, σ_y, to the critical resolved shear strength for slip, τ_{CRSS}, acts as an isotropic manifestation of the crystalline anisotropy at the continuum level, and is defined as

$$\sigma_y = \overline{m}\tau_{CRSS} \ . \tag{2.35}$$

The Taylor factor, $\overline{m}$, was successfully derived by Bishop and Hill, and for FCC

polycrystals, $\overline{m}$ was found to be 3.06 (Bishop and Hill, 1951b; Bishop and Hill, 1951a).

A similar factor may be considered for macroscopic strain gradient fields in polycrystals. Of course, GND's arise locally in polycrystals in which macroscopic strain gradients are not present. Local interactions between neighboring grains give rise to GND's leading to the grain-size dependence of strain hardening (Dai et al., 2000). Apart from this local GND density, macroscopic strain gradient fields lead to a macroscopic Nye's tensor which must be interpreted on a continuum level. Using the information at the single crystal level, a corresponding Nye factor, $\overline{r}$, may be introduced to reflect the scalar measure of GND density, P_{GN}, resultant from macroscopic plastic strain gradients.

The simplest macroscopic description of plastic strain gradient fields, which can be described by single-parameter Nye's tensors, are found in plane strain bending and torsion. In the calculation of $\overline{r}$ for each of these cases, Nye's tensor, α_{ij} was taken to be uniform across the polycrystal, but the dislocation density was not continuous across the polycrystal. These conditions ensured intra-grain lattice continuity, but allowed dislocation lines to terminate at grain boundaries. The Nye factor was calculated with the following equation:

$$\overline{r} = \frac{1}{nb} \sum_{i=1}^{n} |\rho_{GN}(\alpha_{ij}; \phi, \theta, \omega)|^i \ , \tag{2.36}$$

where b is the magnitude of the Burgers vector and ϕ, θ, and ω are the Euler angles defining the orientation of crystal i, and n is the number of grains in the sample. The crystallographic GND dislocation density, ρ_{GN}, was calculated using the linear simplex method for each orientation, and the isotropic measure, $\overline{r}$, of the GND density was the total dislocation line length in each grain. The calculation was conducted for FCC polycrystals in bending and torsion. In the case of bending, the Nye factor was found to be $\overline{r} = 1.85$ such that

$$\mathrm{P}_{GN(e)} b = 1.85 |\alpha_{12}| \ , \tag{2.37}$$

and in the case of torsion, the Nye factor was found to be $\overline{r} = 1.93$ such that

$$\mathrm{P}_{GN(s)}b = 1.93|\alpha_{11}| \ , \tag{2.38}$$

where the (e) and (s) subscripts denote the isotropic edge and screw density respectively.

The Nye factor accounts for the underlying crystalline anisotropy in this continuum measure of GND's. Current isotropic continuum models (Fleck and Hutchinson, 1997; Gao et al., 1999) of strain-gradient plasticity use invariants of the curvature tensor, which is closely related to Nye's tensor through Eq. 2.28, as a measure of GND density, but the value of Nye's tensor on a continuum material point of a polycrystal is not a sufficient measure of the GND's present. The actual dislocation density based on crystallographic considerations for the case of plane strain bending and torsion is almost twice that which would be predicted by the use of Nye's tensor alone. Since the dependence of the plastic resistance on the dislocation density is most often a function of the square root of the dislocation density, the increased resistance due to the presence of GND density is underestimated if the scalar measure of the GND density is not magnified by a Nye factor.

The dislocation density descriptions in this chapter were static. Only the geometric relationships between the GND's and SSD's were considered, with no attention as to how such density structures could evolve with plastic deformation. There were clues uncovered in Section 2.1 that could possibly lead to evolution equations for the GND density. The evolution of the SSD density is much more complex, and both the generation and annihilation of such density must be considered if a general dislocation state variable for plasticity is to be formulated. However, the analysis in this chapter shows that the evolution equations of the SSD density must conserve Nye's tensor.

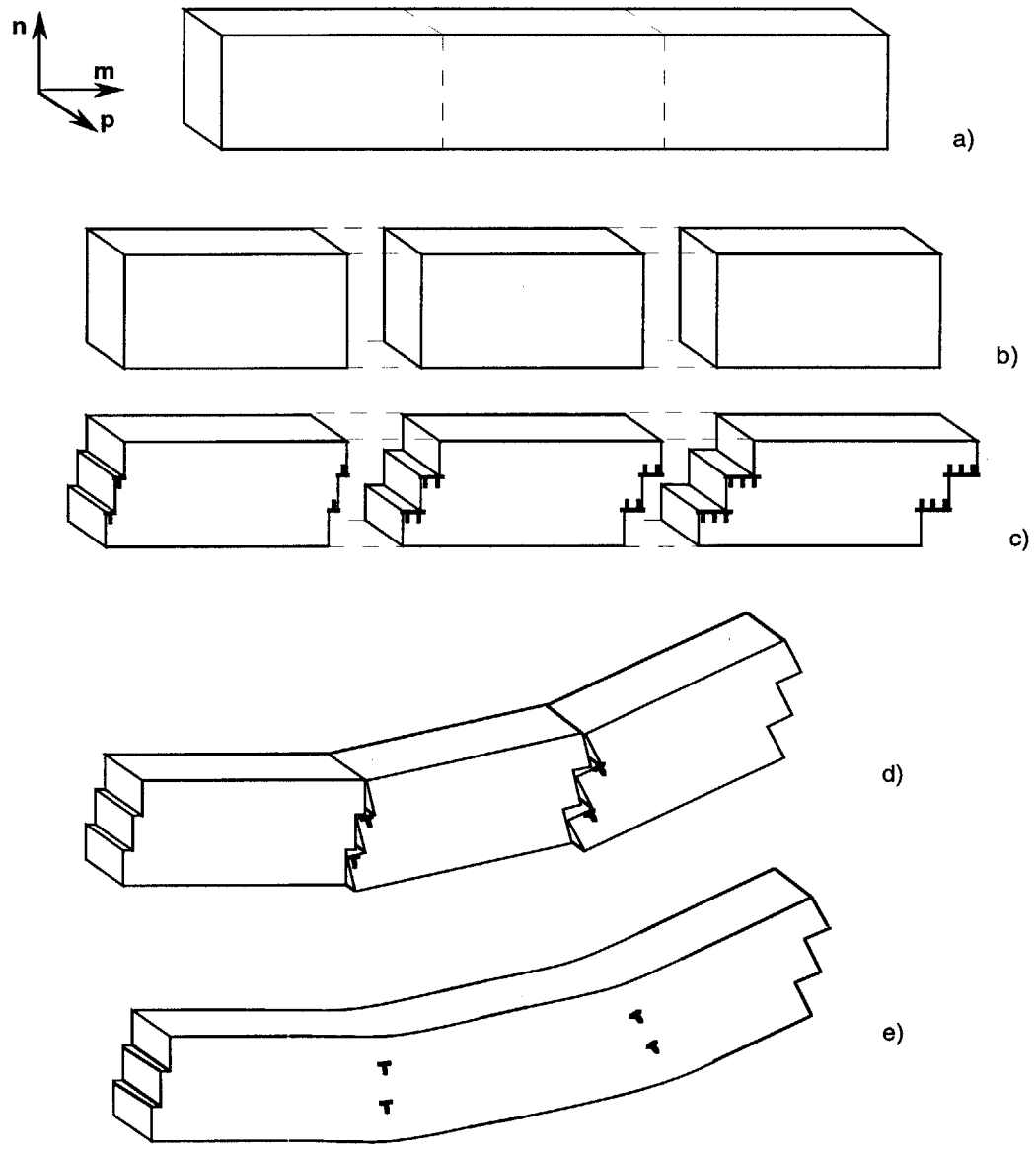

Figure 2-1: Schematic process (a-e) through which geometrically-necessary edge dislocations accumulate.

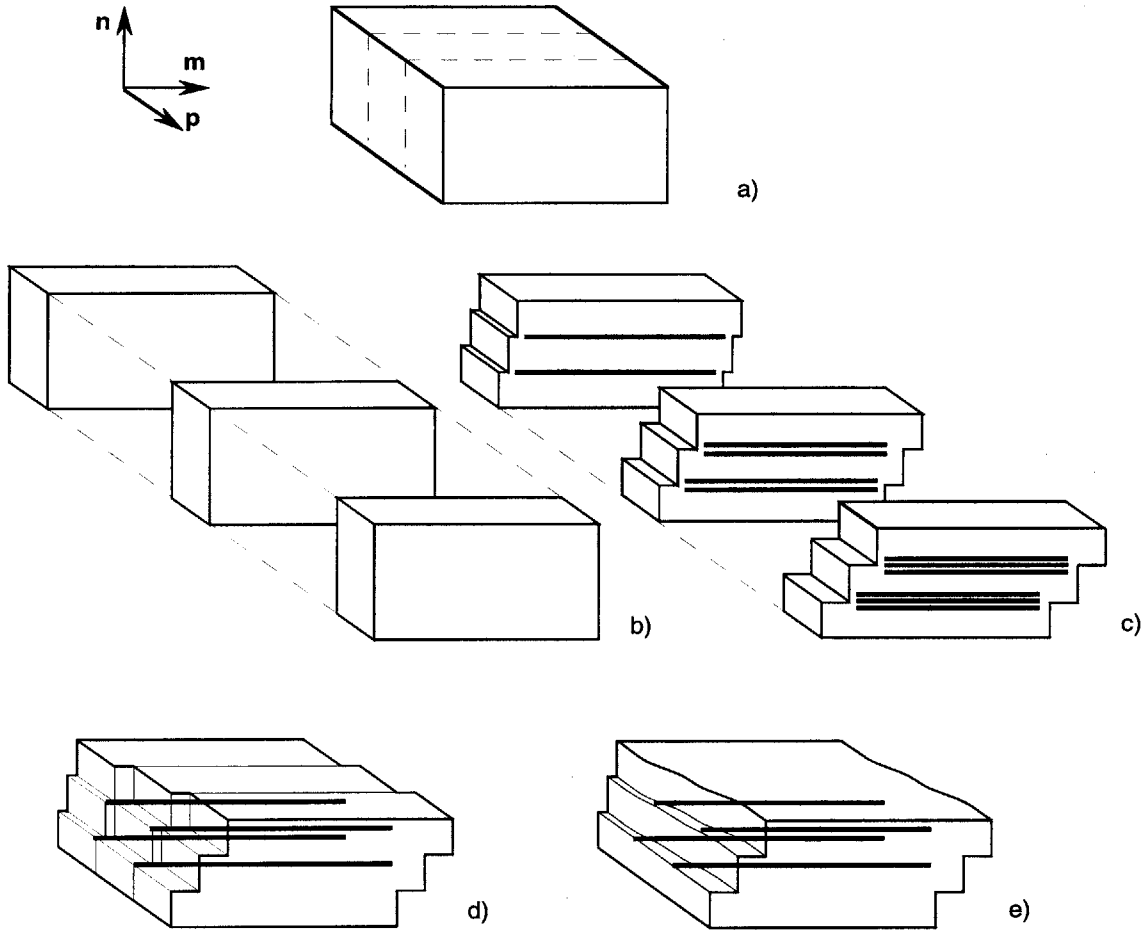

Figure 2-2: Schematic process (a-e) through which geometrically-necessary screw dislocations accumulate.

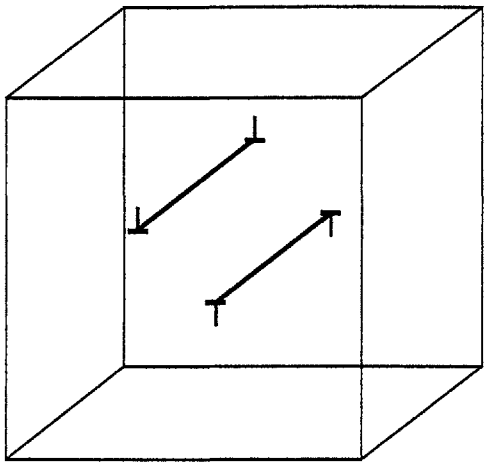

Figure 2-3: An edge dislocation dipole in a volume element used to define Nye's tensor.

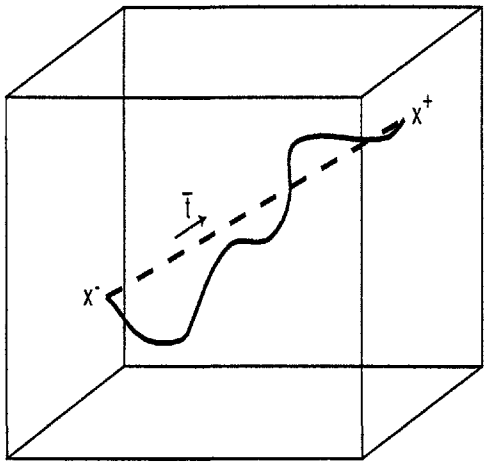

Figure 2-4: A dislocation line threading through a reference volume element used to define Nye's tensor.

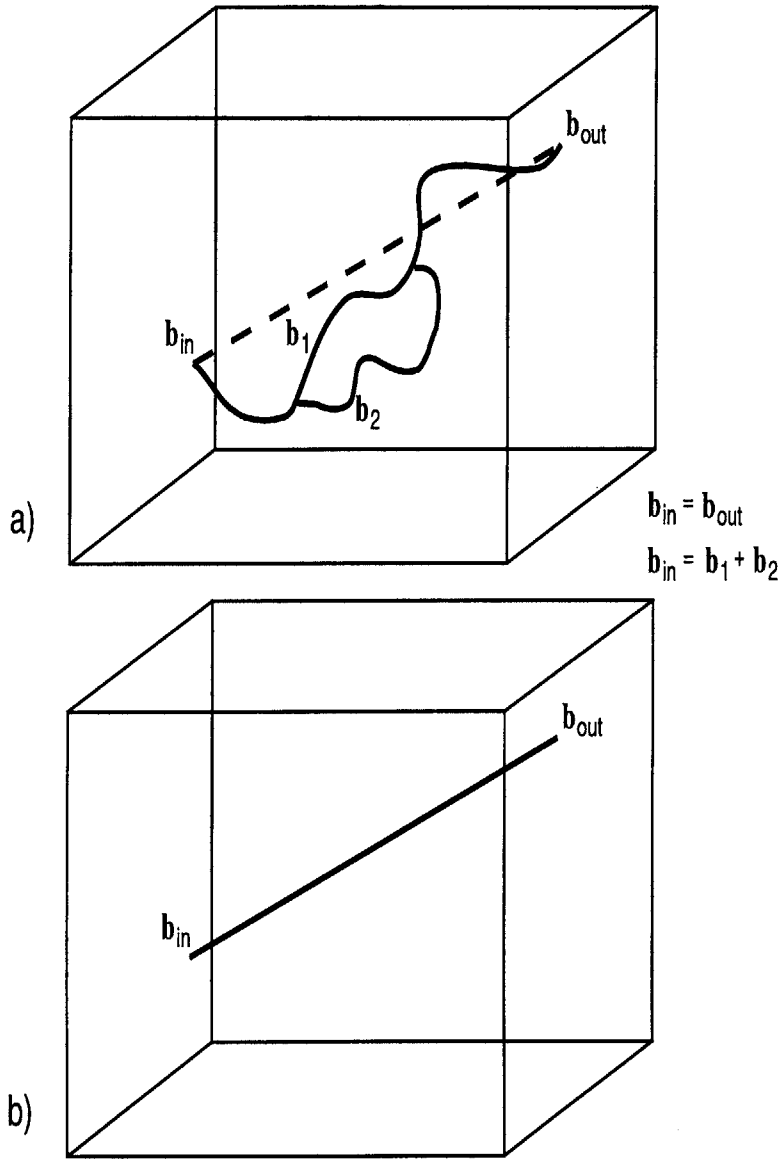

Figure 2-5: A simple dislocation network with two junctions threading through a reference volume element used to define Nye's tensor (a), and its corresponding geometric fingerprint (b).

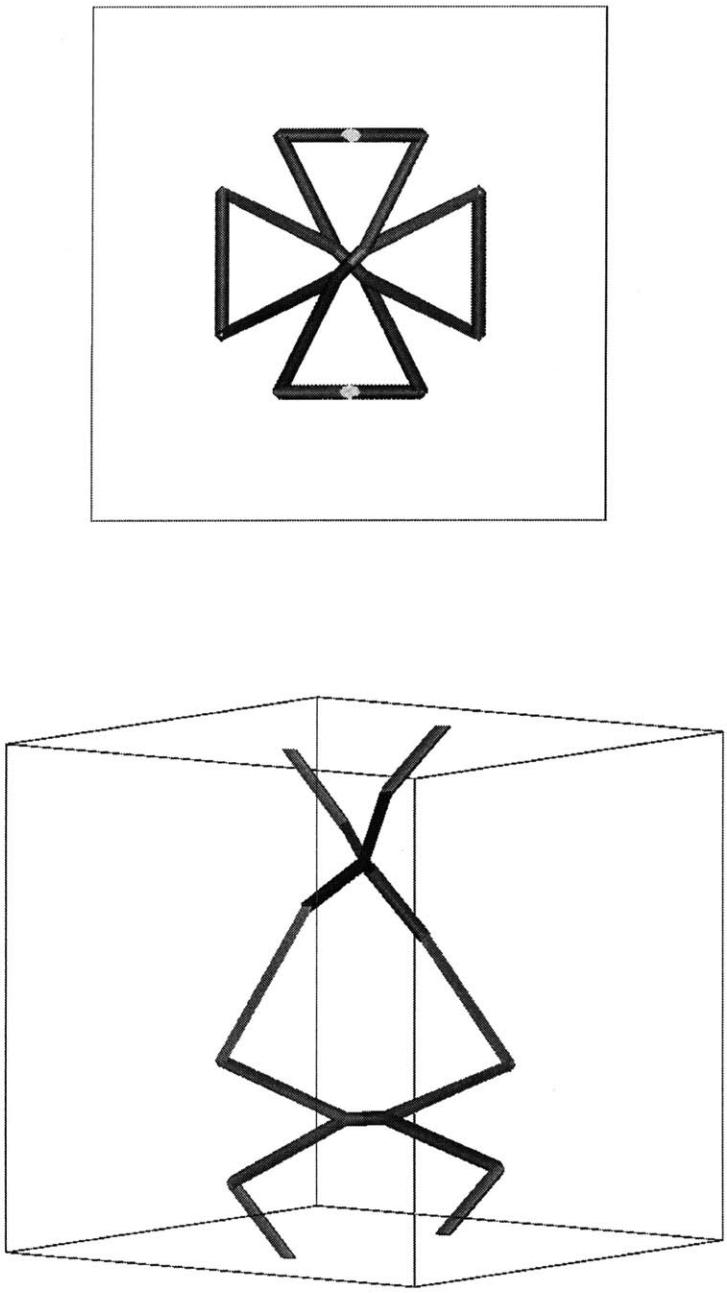

Figure 2-6: A periodic dislocation network derived through the L^2 minimization scheme which has the same geometric properties as a $< 100 > < 100 >$ positive screw dislocation.

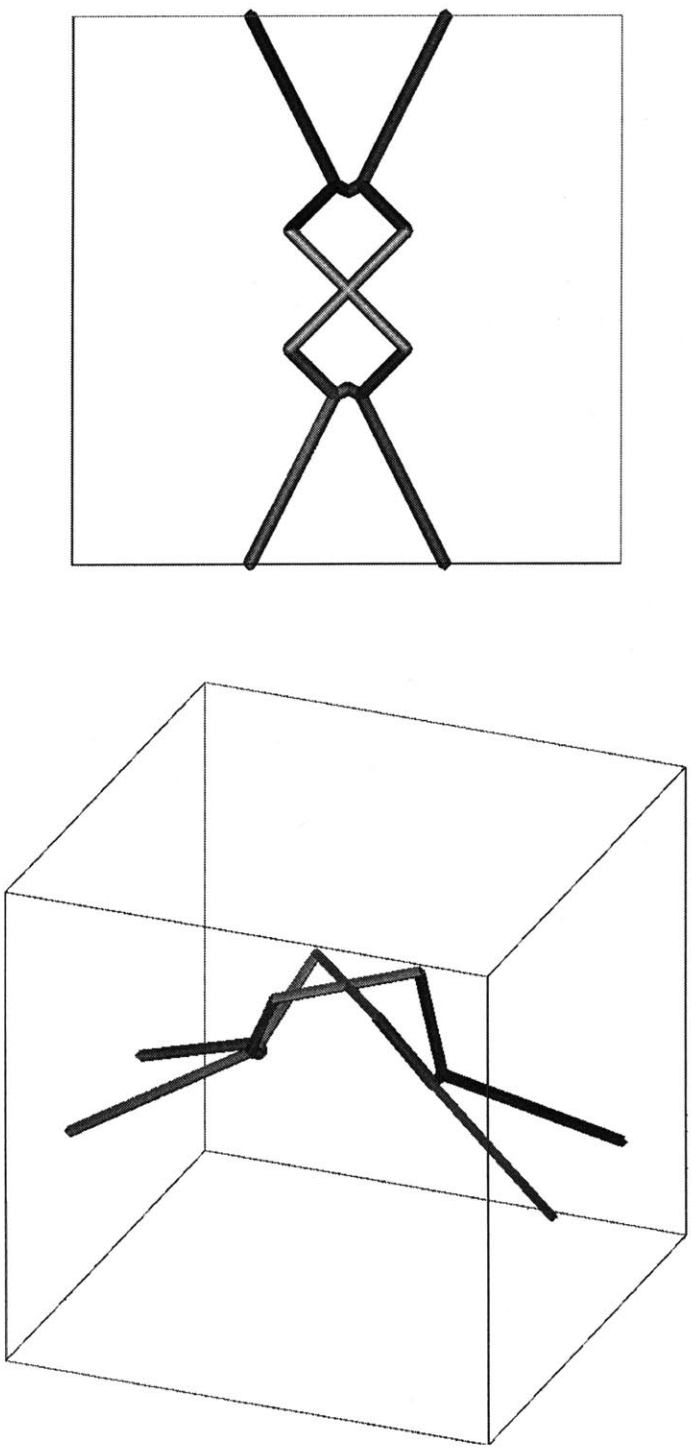

Figure 2-7: A periodic dislocation network derived through the L^2 minimization scheme which has the same geometric properties as a $< 100 > < 010 >$ positive edge dislocation.

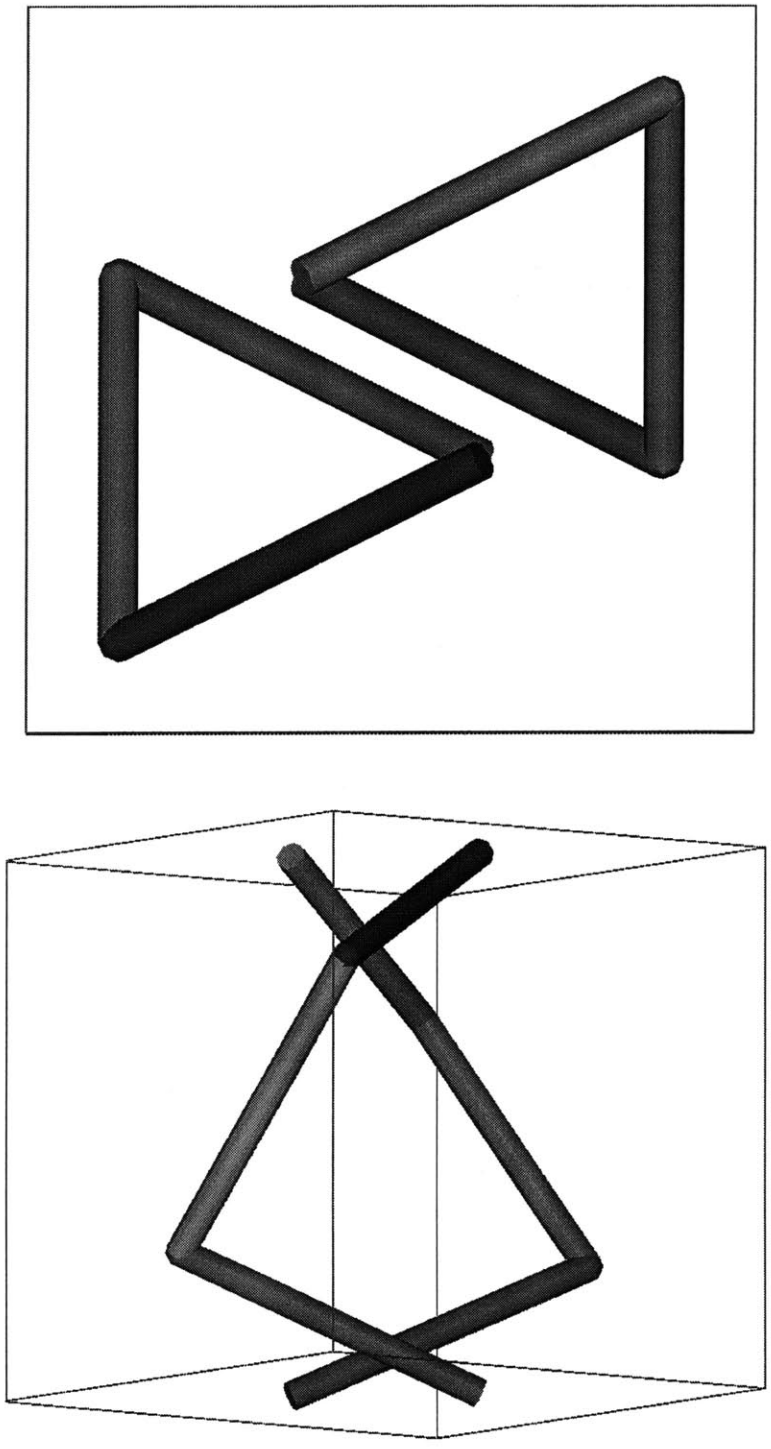

Figure 2-8: A periodic dislocation network derived through the L^1 minimization scheme which has the same geometric properties as a $< 100 > < 100 >$ positive screw dislocation.

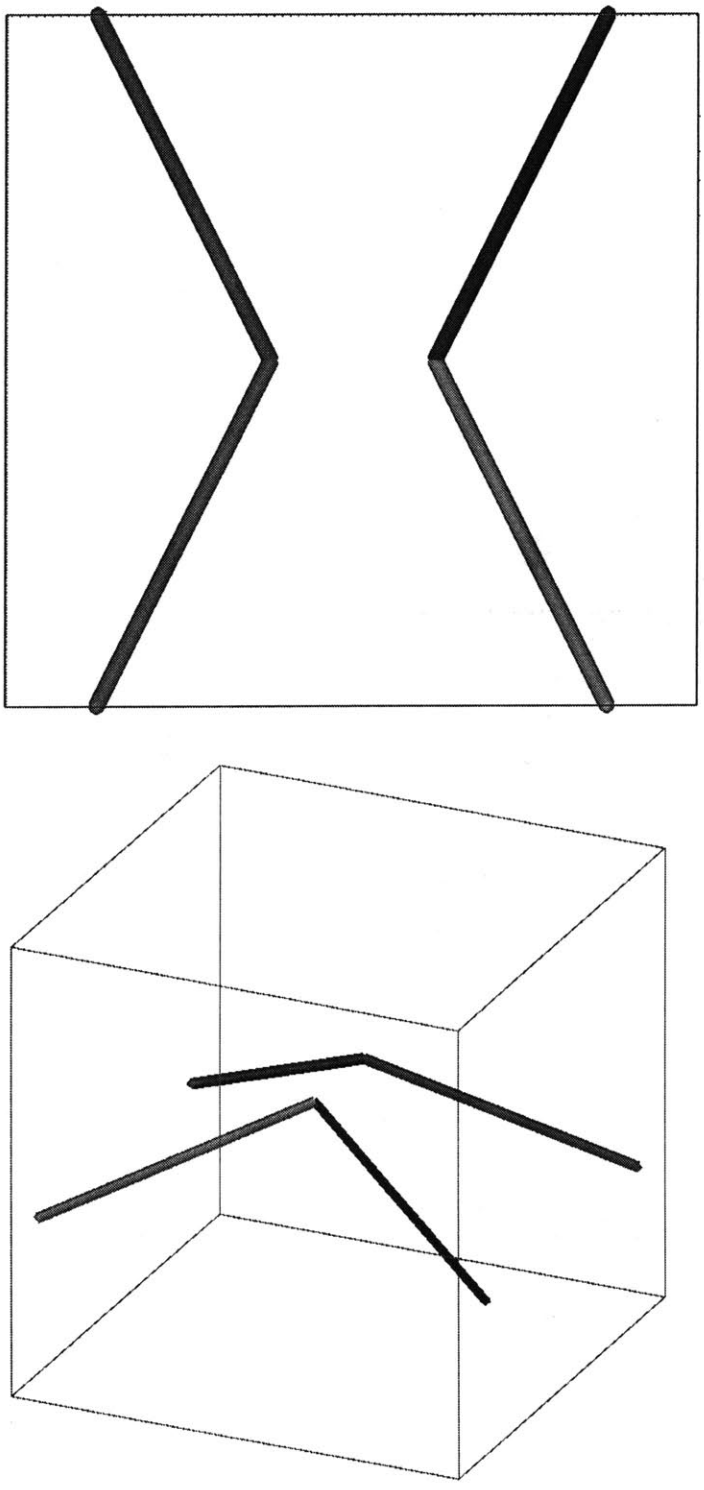

Figure 2-9: A periodic dislocation network derived through the L^1 minimization scheme which has the same geometric properties as a $< 100 > < 010 >$ positive edge dislocation.

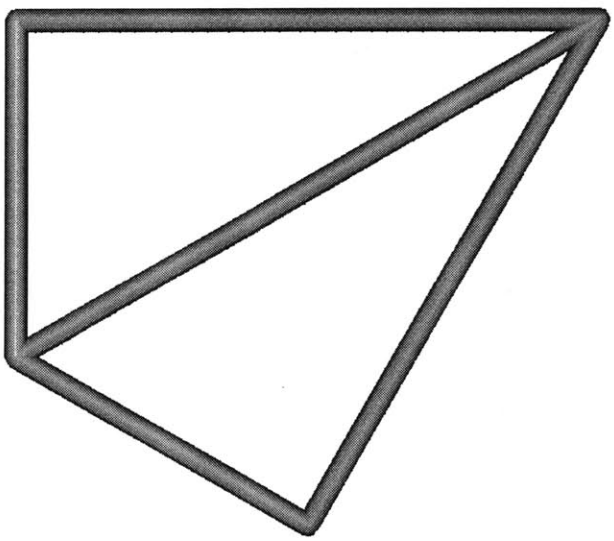

Figure 2-10: A discrete planar dislocation structure representing the intersection of two dislocation loops with different Burgers vectors.

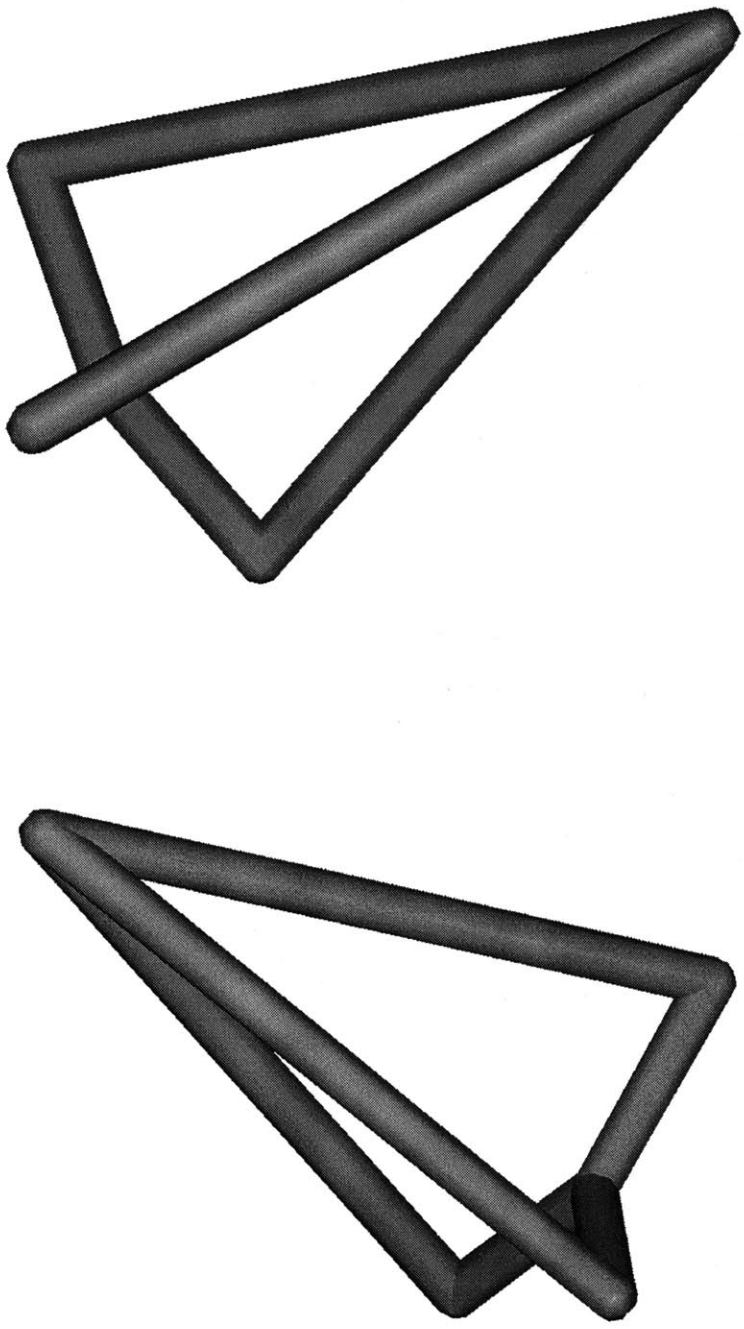

Figure 2-11: A three-dimensional dislocation structure composed of six edge dislocations which self terminates and has no geometric consequence.

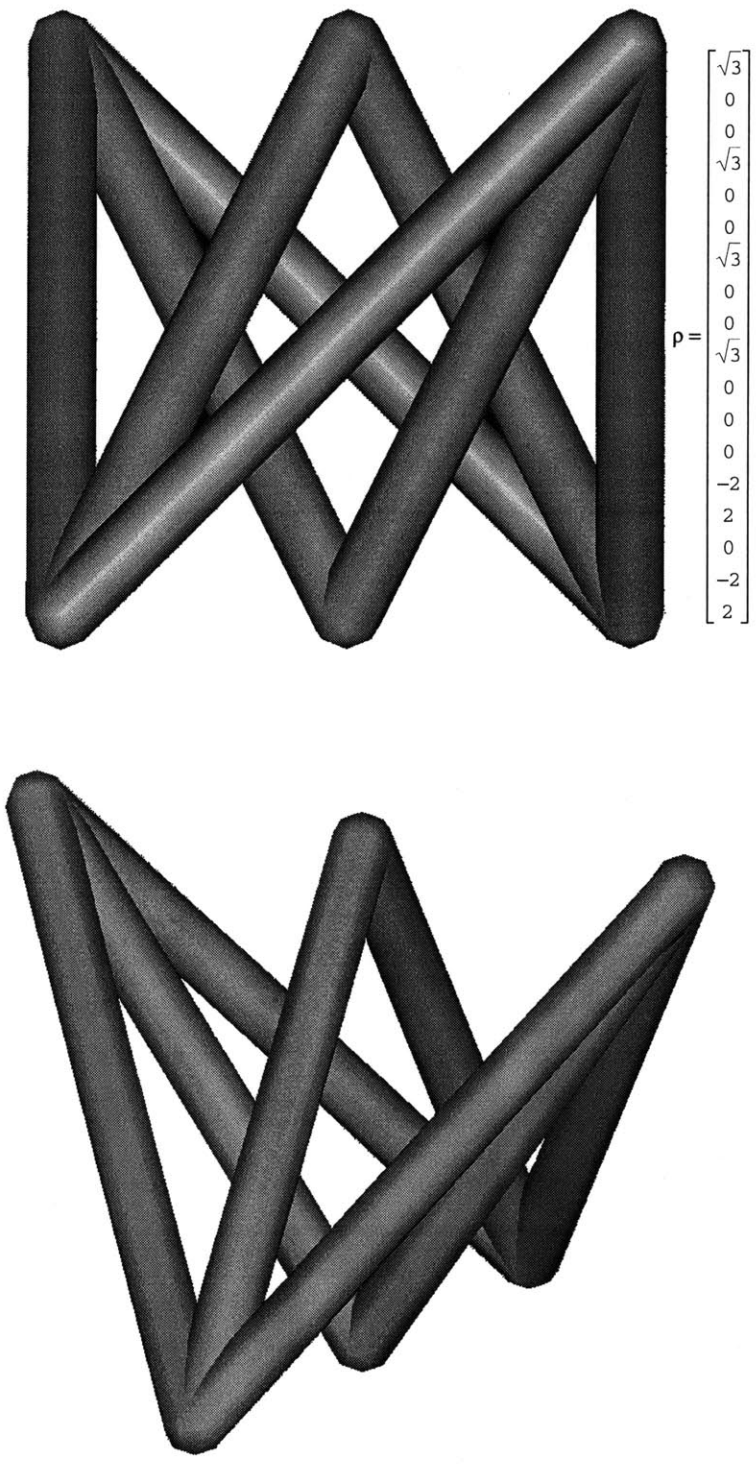

Figure 2-12: A three-dimensional dislocation structure composed of four edge and four screw dislocations which self terminates and has no geometric consequence.

Table 2.1: The dislocation basis used to describe the dislocation state in FCC crystals. The dislocation densities are indexed with respect to their Burgers vector direction, $\hat{\mathbf{b}} = \mathbf{b}/\|\mathbf{b}\|$; tangent line direction, $\mathbf{t}$; and resident slip plane, $\mathbf{n}$.

Density	$\hat{\mathbf{b}}$	$\mathbf{t}$	$\mathbf{n}$
ρ_1	$\frac{1}{\sqrt{2}}[\bar{1}10]$	$\frac{1}{\sqrt{6}}[\bar{1}\bar{1}2]$	$\frac{1}{\sqrt{3}}[111]$
ρ_2	$\frac{1}{\sqrt{2}}[10\bar{1}]$	$\frac{1}{\sqrt{6}}[\bar{1}2\bar{1}]$	$\frac{1}{\sqrt{3}}[111]$
ρ_3	$\frac{1}{\sqrt{2}}[0\bar{1}1]$	$\frac{1}{\sqrt{6}}[\bar{1}\bar{1}2]$	$\frac{1}{\sqrt{3}}[111]$
ρ_4	$\frac{1}{\sqrt{2}}[\bar{1}\bar{1}0]$	$\frac{1}{\sqrt{6}}[\bar{1}1\bar{2}]$	$\frac{1}{\sqrt{3}}[1\bar{1}\bar{1}]$
ρ_5	$\frac{1}{\sqrt{2}}[101]$	$\frac{1}{\sqrt{6}}[\bar{1}\bar{2}1]$	$\frac{1}{\sqrt{3}}[1\bar{1}\bar{1}]$
ρ_6	$\frac{1}{\sqrt{2}}[01\bar{1}]$	$\frac{1}{\sqrt{6}}[211]$	$\frac{1}{\sqrt{3}}[1\bar{1}\bar{1}]$
ρ_7	$\frac{1}{\sqrt{2}}[110]$	$\frac{1}{\sqrt{6}}[1\bar{1}\bar{2}]$	$\frac{1}{\sqrt{3}}[\bar{1}1\bar{1}]$
ρ_8	$\frac{1}{\sqrt{2}}[\bar{1}01]$	$\frac{1}{\sqrt{6}}[121]$	$\frac{1}{\sqrt{3}}[\bar{1}1\bar{1}]$
ρ_9	$\frac{1}{\sqrt{2}}[0\bar{1}\bar{1}]$	$\frac{1}{\sqrt{6}}[\bar{2}\bar{1}1]$	$\frac{1}{\sqrt{3}}[\bar{1}1\bar{1}]$
ρ_{10}	$\frac{1}{\sqrt{2}}[1\bar{1}0]$	$\frac{1}{\sqrt{6}}[112]$	$\frac{1}{\sqrt{3}}[\bar{1}\bar{1}1]$
ρ_{11}	$\frac{1}{\sqrt{2}}[\bar{1}0\bar{1}]$	$\frac{1}{\sqrt{6}}[1\bar{2}\bar{1}]$	$\frac{1}{\sqrt{3}}[\bar{1}\bar{1}1]$
ρ_{12}	$\frac{1}{\sqrt{2}}[011]$	$\frac{1}{\sqrt{6}}[\bar{2}1\bar{1}]$	$\frac{1}{\sqrt{3}}[\bar{1}\bar{1}1]$
ρ_{13}	$\frac{1}{\sqrt{2}}[110]$	$\frac{1}{\sqrt{2}}[110]$	$\frac{1}{\sqrt{3}}[1\bar{1}\bar{1}]$ or $\frac{1}{\sqrt{3}}[\bar{1}1\bar{1}]$
ρ_{14}	$\frac{1}{\sqrt{2}}[101]$	$\frac{1}{\sqrt{2}}[101]$	$\frac{1}{\sqrt{3}}[1\bar{1}\bar{1}]$ or $\frac{1}{\sqrt{3}}[\bar{1}\bar{1}1]$
ρ_{15}	$\frac{1}{\sqrt{2}}[011]$	$\frac{1}{\sqrt{2}}[011]$	$\frac{1}{\sqrt{3}}[\bar{1}\bar{1}1]$ or $\frac{1}{\sqrt{3}}[\bar{1}1\bar{1}]$
ρ_{16}	$\frac{1}{\sqrt{2}}[\bar{1}10]$	$\frac{1}{\sqrt{2}}[\bar{1}10]$	$\frac{1}{\sqrt{3}}[111]$ or $\frac{1}{\sqrt{3}}[\bar{1}\bar{1}1]$
ρ_{17}	$\frac{1}{\sqrt{2}}[10\bar{1}]$	$\frac{1}{\sqrt{2}}[10\bar{1}]$	$\frac{1}{\sqrt{3}}[111]$ or $\frac{1}{\sqrt{3}}[\bar{1}1\bar{1}]$
ρ_{18}	$\frac{1}{\sqrt{2}}[0\bar{1}1]$	$\frac{1}{\sqrt{2}}[0\bar{1}1]$	$\frac{1}{\sqrt{3}}[1\bar{1}\bar{1}]$ or $\frac{1}{\sqrt{3}}[111]$

$$
\begin{bmatrix} \rho_1 \\ \rho_2 \\ \rho_3 \\ \rho_4 \\ \rho_5 \\ \rho_6 \\ \rho_7 \\ \rho_8 \\ \rho_9 \\ \rho_{10} \\ \rho_{11} \\ \rho_{12} \\ \rho_{13} \\ \rho_{14} \\ \rho_{15} \\ \rho_{16} \\ \rho_{17} \\ \rho_{18} \end{bmatrix} b = \begin{bmatrix} a & 7c & -13c & -7c & -a & 13c & c & -c & 0 & 3 & 1 & 1 & 0 & 0 & 0 & 0 & 0 & 0 \\ -a & 13c & -7c & -c & 0 & c & 7c & -13c & a & 0 & -2 & 1 & 0 & 0 & 0 & 0 & 0 & 0 \\ 0 & c & -c & -13c & a & 7c & 13c & -7c & -a & 0 & 1 & -2 & 0 & 0 & 0 & 0 & 0 & 0 \\ a & -7c & 13c & 7c & -a & 13c & -c & -c & 0 & 0 & 0 & 0 & 1 & 1 & 0 & 0 & 0 & 0 \\ -a & -13c & 7c & c & 0 & c & -7c & -13c & a & 3 & 0 & 0 & -2 & 1 & 0 & 0 & 0 & 0 \\ 0 & -c & c & 13c & a & 7c & -13c & -7c & -a & 0 & 0 & 0 & 1 & -2 & 0 & 0 & 0 & 0 \\ a & -7c & -13c & 7c & -a & -13c & c & c & 0 & 0 & 0 & 0 & 0 & 0 & 1 & 1 & 0 & 0 \\ -a & -13c & -7c & c & 0 & -c & 7c & 13c & a & 0 & 0 & 0 & 0 & 0 & -2 & 1 & 0 & 0 \\ 0 & -c & -c & 13c & a & -7c & 13c & 7c & -a & 3 & 0 & 0 & 0 & 0 & 1 & -2 & 0 & 0 \\ a & 7c & 13c & -7c & -a & -13c & -c & c & 0 & 1 & 0 & 0 & 0 & 0 & 0 & 0 & 1 & 1 \\ -a & 13c & 7c & -c & 0 & -c & -7c & 13c & -a & 1 & 0 & 0 & 0 & 0 & 0 & 0 & -2 & 1 \\ 0 & c & c & -13c & a & -7c & -13c & 7c & -a & 1 & 0 & 0 & 0 & 0 & 0 & 0 & 1 & -2 \\ 5d & e & 0 & e & 5d & 0 & 0 & 0 & -d & 0 & 0 & 0 & -\sqrt{3} & \sqrt{3} & -\sqrt{3} & \sqrt{3} & 0 & 0 \\ 5d & 0 & e & 0 & -d & 0 & e & 0 & 5d & 0 & 0 & 0 & 0 & -\sqrt{3} & 0 & 0 & 0 & -\sqrt{3} \\ -d & 0 & 0 & 0 & 5d & e & 0 & e & 5d & 0 & 0 & 0 & 0 & 0 & \sqrt{3} & 0 & \sqrt{3} & 0 \\ 5d & -e & 0 & -e & 5d & 0 & 0 & 0 & -d & 0 & -\sqrt{3} & \sqrt{3} & 0 & 0 & 0 & 0 & -\sqrt{3} & \sqrt{3} \\ 5d & 0 & -e & 0 & -d & 0 & -e & 0 & 5d & 0 & 0 & -\sqrt{3} & 0 & 0 & 0 & -\sqrt{3} & 0 & 0 \\ -d & 0 & 0 & 0 & 5d & -e & 0 & -e & 5d & 0 & \sqrt{3} & 0 & \sqrt{3} & 0 & 0 & 0 & 0 & 0 \end{bmatrix} \begin{bmatrix} \alpha_{11} \\ \alpha_{12} \\ \alpha_{13} \\ \alpha_{21} \\ \alpha_{22} \\ \alpha_{23} \\ \alpha_{31} \\ \alpha_{32} \\ \alpha_{33} \\ \lambda_1 \\ \lambda_2 \\ \lambda_3 \\ \lambda_4 \\ \lambda_5 \\ \lambda_6 \\ \lambda_7 \\ \lambda_8 \\ \lambda_9 \end{bmatrix}
$$

where $a = \frac{\sqrt{3}}{9}$ $c = \frac{\sqrt{3}}{84}$ $d = \frac{1}{18}$ $e = \frac{3}{14}$

Table 2.2: The linear operator used to create geometrically allowed dislocation density from Nye's tensor and statistically stored dislocation density. The first nine columns form the matrix **B** in Eq. 2.33 weighted by the components of Nye's tensor with $< 100 >$ basis vectors. The last nine columns represent non-dipole components of the statistically-stored dislocation density, weighted by the parameters λ_i independent of Nye's tensor.

Chapter 3

Dislocation Density-Based State Variable Model for Continuum Crystal Plasticity

The dislocation density state variable formulation may conceptually be separated into two parts: the kinematics associated with crystallographic slip, resulting plastic deformation, and lattice reorientation; and the kinematics associated with evolution of the dislocation density state in the crystal. The two parts are intimately related. The dislocation state affects the plastic response of the crystal, and the plastic response of the crystal determines the evolution of the dislocation state. In this section, kinematic relationships for crystallographic slip and dislocation density evolution, as well as the links between them, will be developed.

3.1 Single Crystal Kinematics

The single crystal kinematics described below is based on the developments of Asaro and Rice (1977). The total deformation gradient, $\mathbf{F}$, mapping a reference configuration of the material to the final configuration, may be multiplicatively decomposed into an elastic deformation gradient, $\mathbf{F}^e$, and a plastic deformation gradient, $\mathbf{F}^p$, such

that

$$\mathbf{F} = \mathbf{F}^{\mathrm{e}}\mathbf{F}^{\mathrm{p}} \ , \tag{3.1}$$

where $\mathbf{F}^{\mathrm{p}}$ maps the original configuration of a body to an intermediate configuration describing the effects of plastic deformation on an unrotated and undeformed crystal lattice, and $\mathbf{F}^{\mathrm{e}}$ maps the intermediate configuration to the final deformed configuration. Typically, $\mathbf{F}^{\mathrm{e}}$ is associated with small elastic stretches and arbitrary rigid-body rotations. The plastic deformation gradient evolves according to the flow rule

$$\dot{\mathbf{F}}^{\mathrm{p}} = \mathbf{L}^{\mathrm{p}}\mathbf{F}^{\mathrm{p}} \ , \tag{3.2}$$

where $\mathbf{L}^{\mathrm{p}}$ is the plastic flow rate. In crystals, $\mathbf{L}^{\mathrm{p}}$ is comprised of the superposition of the resolved crystallographic plastic shear rates, $\dot{\gamma}^a$, such that

$$\mathbf{L}^{\mathrm{p}} = \sum_a \dot{\gamma}^a \mathbf{m}_0^a \otimes \mathbf{n}_0^{\mathrm{a}} \ , \tag{3.3}$$

where $\mathbf{m}_0^a$ and $\mathbf{n}_0^a$ are unit lattice vectors in the undeformed configuration corresponding to the slip direction and the slip plane normal direction, respectively, for a given slip system a. During plastic deformation, the crystal lattice may stretch and rotate, and in the deformed configuration, the slip direction and slip plane normal become $\mathbf{m}_*^a$ and $\mathbf{n}_*^a$, respectively, which can be related to the initial lattice directions through the following transformations:

$$\mathbf{m}_*^a = \mathbf{F}^{\mathrm{e}}\mathbf{m}_0^a \ ; \quad \mathbf{n}_*^a = \mathbf{F}^{\mathrm{e}-\mathrm{T}}\mathbf{n}_0^a \ . \tag{3.4}$$

An elastic strain measure, $\mathbf{E}^{\mathrm{e}}$, corresponding to the Cauchy-Green strain with respect to the intermediate configuration, is defined as

$$\mathbf{E}^{\mathrm{e}} \equiv \frac{1}{2}\{\mathbf{F}^{\mathrm{e}\mathrm{T}}\mathbf{F}^{\mathrm{e}} - \mathbf{I}_2\} \ , \tag{3.5}$$

where $\mathbf{I}_2$ is the second-order identity tensor. The work-conjugate stress measure, $\bar{\mathbf{T}}$, corresponding to the second Piola-Kirchhoff stress tensor with respect to the in-

termediate configuration, is related to the Cauchy stress, $\mathbf{T}$, through the following transformation:

$$\bar{\mathbf{T}} = \det\left(\mathbf{F}^{e}\right)\mathbf{F}^{e-1}\mathbf{T}\mathbf{F}^{e-T} \ . \tag{3.6}$$

The work-conjugate stress measure is related to the Cauchy-Green elastic strain tensor through the anisotropic elastic coefficients of the crystalline material. The functional form of this relationship is taken to be

$$\bar{\mathbf{T}} = \mathcal{L}\left[\mathbf{E}^{e}\right] \ , \tag{3.7}$$

where $\mathcal{L}$ is a fourth-order tensor containing the anisotropic elastic coefficients of the crystal.

The connections between the single crystal kinematics and dislocation density state variables are made by relating the conservative glide motion of the crystallographic densities to the plastic shear rates in Eq. 3.3 through the Orowan relation (Orowan, 1940). The evolution of the dislocation density state in turn depends on the current material state, the stress $\bar{\mathbf{T}}$, and the crystal orientation. The stress state is a function of the current elastic deformation gradient, which can be considered as the residual of the total deformation gradient modulo the plastic deformation gradient. Therefore, the evolution of stress, strain, and dislocation state with loading history are strongly coupled.

3.2 Dislocation Density Kinematics

With the exception of Eq. 3.7, the mathematical relationships in the previous section were all based on the configurational geometry of a plastically deforming body. Geometric considerations simplified the constitutive response from a general, and *a priori*, unstructured relationship connecting the histories of stress and the total deformation gradient, to a simple linear relationship between the second Piola-Kirchhoff stress and the Cauchy-Green elastic strain, both referred to the intermediate configuration. The remaining complexity of the model lies in predicting the resolved plastic shearing

rates, $\dot{\gamma}^a$, for representative values of stress and material state.

Internal state variables, a set of variables quantifying the properties of the current material state that control the material response being investigated, have proven to be powerful tools in capturing the plastic evolution of solids. The most widely used state variables in continuum crystal plasticity represent crystallographic slip-system strengths. Evolution of "strength" state variables has been inferred from phenomenological hardening equations relating changes in the crystallographic strengths to the slip-system activity. The ability of these models to predict accurately the plastic behavior of the materials is directly related to the phenomenological complexity in the model (Kumar and Yang, 1999). Complex phenomenology is needed because there is typically no underlying geometric structure to connect the slip-system resistance to the slip-system activity. As before, where use of geometric essentials associated with the single crystal kinematics enabled constitutive simplification, the geometry associated with dislocation density kinematics presented in Chapter 1 provides a structural framework for development of a simple set of constitutive equations for the plastic evolution of crystals.

The arrangement of dislocation lines in the crystal is not arbitrary. The conservation of Burgers vector and the continuity of the dislocation line must be maintained. Dislocation lines cannot terminate within an otherwise perfect crystal. They must end either on a free surface, a grain boundary, another set of dislocations, or some other type of defect. If the dislocation ends on another set of dislocations at a node, then the combined Burgers vector of the set, be it one line or many, must have the same Burgers vector as the first dislocation, thereby conserving the total Burgers vector.

A density of dislocation lines, defined as the total length of dislocation line (as a function of Burgers vector and tangent line vector) within a unit volume, must follow the same physical laws that govern the individual lines. In representing a group of dislocation lines as a density, information about the actual spatial correlation of the lines within the volume is lost. However, the concept of conservation of Burgers vector can be extended to apply to a density of dislocations, thus restricting the spatial

variation of dislocation density fields. Within the current internal state variable framework, this conservation principle will become the basis of the density evolution equations developed.

The evolution of the dislocation density at macroscopic length scales can be considered as controlled by two physical processes: the generation of new density, and the annihilation of existing density. Both processes rely on the motion of dislocations through the crystal: in a static crystal the dislocation density doesn't change. With the consideration of the accumulation or loss of density due to the dislocation flux divergence of each species, the macroscopic model may be extended to capture the scale-dependent material behavior observed at microscopic length scales.

The generation of density can be considered in two parts: nucleation and growth. The nucleation of density is controlled by the presence of discrete sources such as the famous Frank-Read source (and other such configurations), whereby planar dislocation loops are nucleated. As stated before, dislocation density doesn't capture the spatial correlation of the dislocation lines within the volume; therefore, it also doesn't correlate with whether or not the configurations associated with the various specific sources exist within the volume. The assumption is made that such sources do exist, providing a non-zero dislocation density is found within the volume. The expansion of these (previously) nucleated planar loops by dislocation glide will be primarily responsible for the increase of the total dislocation line length within the volume and for the corresponding crystallographic shear resulting from their collective motion. The annihilation of density will be primarily controlled by encounters of dislocation line segments with the opposite polarity and the same character. If two dislocation lines of the same character but opposite polarity occupy the same lattice space, there is no way to distinguish them from the perfect crystal. The line defects are eliminated, causing a reduction in the total density. This density recovery mechanism, in which mobile species of the same character but opposite polarity encounter each other with some frequency, and eliminate their respective lengths, will be the basis for the annihilation of density in the model. The flux divergence contribution to the dislocation density accumulation/loss will follow from the plastic strain gradient considerations

in Chapter 2, but instead of relying on a minimization scheme to determine uniquely the polar density on a crystallographic basis from the plastic strain gradients, the flux divergence of the individual species of dislocation density will be used to determine uniquely the polarity of the crystallographic dislocation state.

3.2.1 Generation of New Density

During crystallographic slip, dislocations move across the slip planes to accomplish the plastic deformation, but in doing so, they must increase the total dislocation line length to maintain line continuity and conservation of Burgers vector. The simplest illustrative example of this may be found in the expansion of a planar dislocation loop. Consider the expanding dislocation loop shown in Figure 3-1. The dislocation line marks the boundary between the regions in the plane that have slipped (gray) and the regions that have not (white). The change in the plastic shear $\delta\gamma$ due to the expansion of the loop is given by

$$\delta\gamma = \frac{\delta A_s |\mathbf{b}|}{V} , \tag{3.8}$$

where δA_s is the change in the slipped area, and V is the volume of the region. Along with the increase in area of the slipped region, the length of the boundary has also increased, and the process has thus generated more dislocation density, or line length within the volume. The change in the length of the dislocation line cannot be quantified by considering only the change in the slipped area because different configurations of the boundary can contain equal areas (but unequal perimeters). However, if the outward displacement of the dislocation line were known as a function of its Burgers vector and tangent line, then not only would the change in the slipped area be known, but the increase of the dislocation length, as a function of Burgers vector and tangent line, would also be known.

The continuous space that a dislocation tangent line vector may occupy makes such a general description difficult. If the tangent line space is restricted to a set of discrete values, the topology of the dislocation loops within the crystal becomes

fixed, and the increase of the discrete dislocation density due to expanding planar loops becomes tractable. If the dislocation loop shown in Figure 3-1 is idealized to be composed of discrete dislocation line segments of known geometry, then evolution equations may be written to quantify exactly the generation of the density due to slip.

Consider the idealized expanding dislocation loop in Figure 3-2. The loop in Figure 3-1 has been idealized to be composed of discrete segments of pure edge and screw dislocations. Of course, this discretization is by no means the only possible discretization of the dislocation loop in Figure 3-1, but it is the simplest discrete loop geometry needed to establish the dislocation evolution equations. The discretized loop is composed of a positive edge dislocation, negative edge dislocation, positive screw dislocation, and negative screw dislocation segments arranged so that they form a closed loop. The same density discretization has been previously described (Lardner, 1974); however, the density evolution equations developed by Lardner from the same schematic are significantly different than the equations developed here. From the simple schematic, it is immediately evident that an outward motion of the screw dislocation segments leads to increased line length of the edge dislocation segments, and an outward motion of the edge dislocations leads to increased line length of the screw dislocations. The increased length is needed to maintain the continuity of the dislocation loop in the crystal. For this simple case, the time rate of change for the dislocation line lengths l becomes

$$\dot{l}_{e+} = \dot{l}_{e-} = v_{s+} + v_{s-} \tag{3.9}$$

$$\dot{l}_{s+} = \dot{l}_{s-} = v_{e+} + v_{e-} \ , \tag{3.10}$$

where v is the outward velocity of the dislocation loop relative to the lattice, the subscripts e and s denote dislocation character (edge, screw), and the "+" and "−" denote dislocation polarity, (right-, left-handed). Note that the generation of dislocation lines conserves Burgers vector because equal line lengths of positive and negative dislocations are created, and that the rate of generation is independent of the length

of the moving dislocation lines. The time rate of change of the slipped area A_s is quantified by

$$\dot{A}_s = l_{e+}v_{e+} + l_{e-}v_{e-} + l_{s+}v_{s+} + l_{s-}v_{s-} \ , \tag{3.11}$$

and is related to the plastic shear rate in the body through Eq. 3.8.

The results of the simple model involving a single dislocation loop may be generalized and applied to populations of discrete dislocation segments in a material. If dislocation density ρ is defined to be the dislocation line length per unit volume of the crystal, then the kinematic evolution equations for the generation of dislocation density become

$$\dot{\rho}^a_{s+(gen)} = \dot{\rho}^a_{s-(gen)} = \frac{\rho^a_{e-}\bar{v}^a_{e-}}{\bar{l}^a_{e-}} + \frac{\rho^a_{e+}\bar{v}^a_{e+}}{\bar{l}^a_{e+}} \tag{3.12}$$

$$\dot{\rho}^a_{e+(gen)} = \dot{\rho}^a_{e-(gen)} = \frac{\rho^a_{s-}\bar{v}^a_{s-}}{\bar{l}^a_{s-}} + \frac{\rho^a_{s+}\bar{v}^a_{s+}}{\bar{l}^a_{s+}} \ , \tag{3.13}$$

where $\bar{v}$ is the average velocity of the dislocation population, $\bar{l}$ is the average segment length of the dislocation density, and the superscript a denotes the crystal slip-system. The sign convention implied in the equations requires that all densities, average velocities, and average lengths be positive. The ratio $\rho/\bar{l}$ yields the number density of dislocations per unit volume, and, as in the simple example, the rate of generation of dislocation density is independent of the total length of the dislocations. Also, the Burgers vector is again conserved, with equal values of positive and negative density being created. The configuration used to introduce the dislocation generation equations was a planar loop, but the geometry need not be so simple. The main assumption is that the mobile segments terminate within the crystal at dislocation nodes. Motion of a dislocation segment away from those nodes would again require that the moving segment leave a dislocation dipole trail extending to the nodes. The planar loop example used to motivate the generation of density is just the simplest type of node a dislocation segment would encounter.

The discretization chosen here leads to the evolution equations found in this section. A different discretization of the dislocation tangent line space would lead to

similar, but different, evolution equations. The main requirement in choosing an appropriate discretization is to choose a set such that closed planar loops can be described by the discrete space of tangent lines. The evolution equations for a different set could again be motivated by the expansion of a single loop, while maintaining line continuity.

The dependence of the plastic shear rate on the dislocation density flux can be easily found by combining Eq. 3.11 and a rate form of Eq. 3.8, providing

$$\dot{\gamma}^a = \left(\rho^a_{e+}\bar{v}^a_{e+} + \rho^a_{e-}\bar{v}^a_{e-} + \rho^a_{s+}\bar{v}^a_{s+} + \rho^a_{s-}\bar{v}^a_{s-}\right)|\mathbf{b}|sign(\tau^a) \ , \tag{3.14}$$

where τ^a is the resolved shear stress on slip system a. This result is equivalent to the classical result obtained by Orowan (1940). Even in this simplest case, it is impossible to determine the rate of dislocation generation from the plastic strain rate because the plastic strain rate doesn't contain enough information to determine uniquely the velocities of each of the participating densities.

3.2.2 Annihilation of Existing Density

Along with the generation of new density in the crystal, the annihilation of dislocation density occurs simultaneously. At relatively low densities, the generation of density dominates the dislocation density evolution, but as density increases, annihilation processes become more prevalent. Many dislocation reaction processes can reduce the dislocation density. In modeling dislocation annihilation within the discrete dislocation density basis considered, the annihilation of each discrete density must be considered.

Many dislocation reactions can be considered as a means of reducing the total density. The simplest reaction that can be conceived is between two dislocations, having the same tangent line direction but opposite Burgers vectors, that encounter one another, leaving from their reaction no resultant contribution to their respective densities. A more general "annihilation" reaction could be considered in which, for example, two dislocations with different Burgers vectors and tangent lines combine to

form a dislocation with lower total energy than the energy contained in the two initial dislocations. All such possible reactions could be considered, but just as the evolution equations for generation required the conservation of Burgers vector, the total Burgers vector must again be conserved. This restriction is most generally enforced by using the dislocation tensor. The dislocation density tensor $\boldsymbol{\alpha}$ was defined in the previous chapter as:

$$\boldsymbol{\alpha} \equiv \sum_{\xi} \mathbf{b}_0^{\xi} \otimes \int_{l} \mathbf{t}_0^{\xi} d\rho^{\xi} \ , \tag{3.15}$$

where $d\rho$ is a differential length per unit volume of a dislocation line with Burgers vector $\mathbf{b}_0$ and unit tangent $\mathbf{t}_0$ for all dislocation segments ξ contained in the volume. For a discrete dislocation basis, the line integral became a simple summation of the form:

$$\boldsymbol{\alpha} = \sum_{\xi} \rho^{\xi} \ \mathbf{b}_0^{\xi} \otimes \mathbf{t}_0^{\xi} \ . \tag{3.16}$$

A general set of density generation and annihilation evolution equations must satisfy the condition that the net change in the dislocation density tensor must be zero, such that they only generate and annihilate the SSD density of the crystal. The generation equations previously discussed satisfied this condition implicitly by creating dipole density that does not contribute to the dislocation tensor. Self-annihilation likewise is concerned with the interaction of dipoles that have no net dislocation tensor. All allowable annihilation reactions conserve the dislocation tensor and lead to a decrease in the free energy in the crystal. In the current formulation, the assumption is made that the dislocation reaction responsible for the majority of density reduction is controlled by self-annihilation, in which dislocations with the same character but different polarity react, leaving behind no contribution to the resultant density.

Consider a single negative dislocation moving with a velocity, v_{rel}, relative to a field of positive dislocations of density ρ_+. If the positive field is randomly distributed, then the negative dislocation passes within a certain distance, R, of a positive dislocation at a frequency f given by

$$f = \rho_+ R v_{rel} \ . \tag{3.17}$$

If there are $N\_/V$ negative dislocations per unit volume moving through the positive field, and an average segment length of $\bar{l}\_$ is eliminated every time one of the dislocations passes within the distance above, then the rate of annihilation of the negative density becomes

$$\dot{\rho}\_ = -\frac{N\_\bar{l}\_}{V}\rho_+ R v_{rel} \ . \tag{3.18}$$

In Eq. 3.18, $N\_\bar{l}\_/V$ is equivalent to the density of negative dislocations $\rho\_$. Also, the annihilation rate of the negative density must be equal to the annihilation rate of the positive density of the same character. The annihilation rates must be applied to all of the dislocation indices introduced in the generation evolution equations. For the pure edge and pure screw dislocation density discretization considered, the annihilation rates become

$$\dot{\rho}^a_{e+(ann)} = \dot{\rho}^a_{e-(ann)} = -\rho^a_{e+}\rho^a_{e-}R_e\left(\bar{v}^a_{e+} + \bar{v}^a_{e-}\right) \tag{3.19}$$

$$\dot{\rho}^a_{s+(ann)} = \dot{\rho}^a_{s-(ann)} = -\rho^a_{s+}\rho^a_{s-}R_s\left(\bar{v}^a_{s+} + \bar{v}^a_{s-}\right) \ . \tag{3.20}$$

Without screw cross-slip or edge climb, the annihilating dislocations would have to lie in the same slip plane. Although cross-slip and climb motion may not be addressed explicitly within the present model , the relative magnitudes of capture radii account for both processes implicitly. From Eq.'s 3.12, 3.13, 3.19, and 3.20, it is clear that the generation depends linearly on the density, and the annihilation depends quadratically on the density. Furthermore, if there is no net polarity of the dislocation density in the initial state and $\rho_+|_{(t=0)} = \rho\_|_{(t=0)}$, polar densities of the same character will be equal for all time as determined through the generation and annihilation processes; therefore, the internal variable space may be reduced by defining

$$\rho^a_e = \rho^a_{e+} + \rho^a_{e-} = 2\rho^a_{e+} = 2\rho^a_{e-} \tag{3.21}$$

$$\rho^a_s = \rho^a_{s+} + \rho^a_{s-} = 2\rho^a_{s+} = 2\rho^a_{s-} \ , \tag{3.22}$$

and

$$\bar{l}_e^a = \bar{l}_{e+}^a = \bar{l}_{e-}^a \tag{3.23}$$

$$\bar{l}_s^a = \bar{l}_{s+}^a = \bar{l}_{s-}^a \, . \tag{3.24}$$

3.2.3 The Accumulation/Loss of Polar Density

The role of non-homogeneous deformation and the observed length-scale dependent material response has been linked to the polarity of dislocation density. A more common name for this density is geometrically-necessary dislocation density (Ashby, 1970) because the net polarity of a dislocation density has geometric consequences on the crystal lattice. The GND/SSD classification of dislocation density has evolved to the extent that these two populations are sometimes considered as separate entities and treated differently. The polar dislocation density exists within a sea of statistical density, and it is impossible to associate any one particular dislocation with either population.

There are two extreme viewpoints in the decomposition of the dislocation density: every dislocation is geometrically necessary, and every dislocation is statistically-stored. Both statements can be correct, depending on the length scale of observation. As discussed in Chapter 2, the definition of these quantities (GND/SSD) depends on the size of the representative volume element (RVE) under consideration. El-Azab (2000) considers nano-scopic RVE's in an attempt to describe discrete dislocation dynamics within a continuum framework in which every dislocation is geometrically necessary. The other extreme considers a macroscopic RVE in which geometrically-necessary dislocations exist only if the body experiences large macroscopic strain gradients (Gao et al., 1999). Although no one claims that deformation in crystals is locally homogeneous everywhere, the simplifying assumption is made in some models to describe the behavior of large RVE's. A key part of the concepts of geometrically-necessary and statistically-stored dislocation density is the RVE over which they are measured. The RVE used in any analysis must be smaller than the geometric features

that are being investigated so that their influence can be clearly resolved.

The SSD/GND decomposition of dislocation density is useful in thinking about the geometric consequences (or the lack thereof, as the case may be) of the total density; however, a more natural description of a general dislocation population is to describe the density by its mean and its polarity (Lardner, 1974). The mean density for each character on slip-system a is given by

$$\bar{\rho}_e^a = \frac{1}{2}\left(\rho_{e+}^a + \rho_{e-}^a\right) \tag{3.25}$$

$$\bar{\rho}_s^a = \frac{1}{2}\left(\rho_{s+}^a + \rho_{s-}^a\right) , \tag{3.26}$$

and the polarity of a dislocation density is given by

$$\rho_{e\pm}^a = \rho_{e+}^a - \rho_{e-}^a \tag{3.27}$$

$$\rho_{s\pm}^a = \rho_{s+}^a - \rho_{s-}^a , \tag{3.28}$$

for each crystallographic density in the discrete set. Note, however that the dislocation polarity, thus defined, may be positive or negative, depending on the magnitudes of the positive and negative species. This mean/polarity classification describes the same density state as the SSD/GND decomposition, but ideologically, there is a difference in the two measures.

The SSD/GND decomposition implies an additive relationship between the GND's and the SSD's, whereas the mean/polarity decomposition has no such implication. Both the GND and SSD densities are taken to quantify real densities, and not the absence of density, in a volume; decomposition of a general dislocation density distribution into an SSD and a GND density leads to two non-negative measures of density. In chapter 2, the SSD/GND decomposition was used to analyze dislocation distributions in FCC crystals, and any negative crystallographic densities that were found through the minimization techniques were interpreted as positive densities of negative species, and not as an absence of positive species. Both positive and negative crystallographic GND densities were interpreted as additional dislocation density,

above a norm of statistical dislocation density.

The mean/polarity decomposition of density employs a different metric. The density mean quantifies the total dislocation density of a given dislocation character; the mean is calculated as half of the total density of the same character on a given slip system. The polarity of the dislocation density is the difference between the positive and negative species of the same character. The mean is always positive and is a count of the total number of dislocations in a volume. The polarity can be either positive or negative, and a negative polarity can equally well be interpreted as an "absence" of density instead of the "presence" of density of a particular sign. The polarity and the mean are independent measures of the total dislocation density of a given character. In the GND/SSD decomposition of density, the two measures, being both positive, sum to the total density, but it is not clear what happens to the level of SSD density in a crystal under non-homogeneous deformation, compared to the homogeneously deforming crystal at the same level of plastic strain. Most often the SSD density is assumed to be the same in both cases, leading to an implicit addition of density due to the species flux divergence contribution in non-homogeneously deforming crystals. The polarity of the density has no implication on the total level of density because it quantifies the difference between two species.

The polar accumulation and/or loss of the individual species will first be considered in a small deformation analysis building upon the results of Chapter 2. The small strain analysis will be used to build intuition as to dislocation processes involved. Then a large deformation analysis will be conducted based on the finite deformation kinematics in Section 3.1.

Small Deformation Analysis

Equations 2.1 and 2.2 may be rewritten in rate form in terms of the dislocation polarity such that

$$\dot{\rho}^a_{e\pm} = -\frac{1}{|\mathbf{b}|}\nabla\dot{\gamma}^a \cdot \mathbf{m}^a_0, \tag{3.29}$$

$$\dot{\rho}^a_{s\pm} \;=\; \frac{1}{|\mathbf{b}|}\nabla\dot{\gamma}^a \cdot \mathbf{p}^a_0 \,. \tag{3.30}$$

The directional derivatives of the crystallographic plastic strain rates lead to a change in polarity of the dislocation densities on that slip system. If the change in the polarity is positive, the strain rate relationship doesn't specify whether the change is due to an excess accumulation of positive density, an excess loss of negative density, or some combination of both. All that Eq.'s 3.29 & 3.30 specify is the change in the net difference between the two densities.

The ambiguity of the relationship between strain rate gradient and the changes in the density of individual dislocation species can be overcome by substituting the Orowan relation in Eq. 3.14 for the strain rate in Eq.'s 3.29 & 3.30. By tracing the dislocation flux divergence for each species, a unique set of polar accumulation/loss equations for dislocation density due to non-homogeneous plastic deformation may be written, but simple substitution of Eq. 3.14 into Eq.'s 3.29 & 3.30 does not solve the ambiguity problem alone. An appeal must be made to the physics behind the process. Surely, a flux divergence of positive edge dislocations cannot directly affect the evolution rate of negative edge dislocation density. The flux of positive edge dislocations definitely affects the population of negative edge dislocations through the annihilation evolution equations, but the flux divergence is a rate measure of the difference in the number of dislocations of a given type entering and leaving a material point within the crystal. Likewise, the flux divergence of the negative edge density should not directly affect the rate of change of the density of positive edge dislocations at a material point. The same arguments may be applied to the flux divergences of the screw densities, and they, too, may be thought to operate independent of one another in affecting the dislocation polarity at a material point.

Another physical consideration has to be offered to discuss the cross accumulation/loss terms, due to the discrete dislocation density basis used. Substitution of the Orowan relation into Eq. 3.30 leads to terms wherein the gradient of the flux of edge density, dotted with the $\mathbf{p}^a_0$-direction, leads to a change in the polarity of the screw density. There seem to be no good arguments as to whether such a contribution

should lead to accumulation of one of the screw densities or to a loss of the other. Luckily, the cross terms become smaller and smaller as the dimension of the discrete dislocation density space increases because the cross effect may be spread among more dislocation densities. Lardner (1974) assumed that the cross terms would be additive because a slight screw character was being added to an otherwise pure edge dislocation line, but the "pure edge" densities and "pure screw" densities that are used in the discretization should be regarded as terms of real densities they represent. The "pure edge" density should not be literally interpreted but should perhaps be understood as representing the portion of the density that behaves more like edge dislocations than screw dislocations. In the aluminum study conducted in the next chapter, the distinction can be made easily, based on the ability of the dislocation density to cross-slip (screw) or not (edge). Perfectly straight dislocations are only model constructs for actual curved dislocations in the material. Since it is ambiguous as to whether a flux divergence of the edge density will lead to an accumulation or loss of density of respective screw species, the assumption is made that it leads to both symmetrically. The same reasoning can be applied to screw density flux in Eq. 3.29.

With the physical considerations applied to the individual density fluxes, the following expressions quantifying the accumulation/loss of dislocation density of a given species due to dislocation flux divergence may be written as

$$\dot{\rho}^a_{e+(flux)} = -\left[\nabla\left(\rho^a_{e+}\bar{v}^a_{e+}\right) + \frac{1}{2}\nabla\left(\rho^a_{s+}\bar{v}^a_{s+}\right) + \frac{1}{2}\nabla\left(\rho^a_{s-}\bar{v}^a_{s-}\right)\right]\cdot \mathbf{m}^a_0 sign\left(\tau^a\right) \quad (3.31)$$

$$\dot{\rho}^a_{e-(flux)} = \left[\nabla\left(\rho^a_{e-}\bar{v}^a_{e-}\right) + \frac{1}{2}\nabla\left(\rho^a_{s+}\bar{v}^a_{s+}\right) + \frac{1}{2}\nabla\left(\rho^a_{s-}\bar{v}^a_{s-}\right)\right]\cdot \mathbf{m}^a_0 sign\left(\tau^a\right) \quad (3.32)$$

$$\dot{\rho}^a_{s+(flux)} = \left[\nabla\left(\rho^a_{s+}\bar{v}^a_{s+}\right) + \frac{1}{2}\nabla\left(\rho^a_{e+}\bar{v}^a_{e+}\right) + \frac{1}{2}\nabla\left(\rho^a_{e-}\bar{v}^a_{e-}\right)\right]\cdot \mathbf{p}^a_0 sign\left(\tau^a\right) \quad (3.33)$$

$$\dot{\rho}^a_{s-(flux)} = -\left[\nabla\left(\rho^a_{s-}\bar{v}^a_{s-}\right) + \frac{1}{2}\nabla\left(\rho^a_{e+}\bar{v}^a_{e+}\right) + \frac{1}{2}\nabla\left(\rho^a_{e-}\bar{v}^a_{e-}\right)\right]\cdot \mathbf{p}^a_0 sign\left(\tau^a\right) \quad (3.34)$$

Inspection of Eq's 3.31-3.34 gives insight into how the crystallographic densities change due to non-homogeneous plastic deformation; the gradients in the plastic strain rate alone are not able to provide such insight. Suppose that the dislocation density everywhere in the crystal has no initial polarity such that $\rho^a_{e\pm} = 0$ and $\rho^a_{s\pm} = 0$,

and that the average velocity of each dislocation species, locally, is only a function of the local density state and stress. A property of the average velocity for crystals in this case is that

$$\begin{aligned}
\hat{\bar{v}}^a_{e+}\left(\rho^b_{e+},\rho^b_{e-},\rho^b_{s+},\rho^b_{s-}\right) &= \hat{\bar{v}}^a_{e+}\left(\rho^b_{e-},\rho^b_{e+},\rho^b_{s+},\rho^b_{s-}\right) \\
&= \hat{\bar{v}}^a_{e+}\left(\rho^b_{e+},\rho^b_{e-},\rho^b_{s-},\rho^b_{s+}\right) \\
&= \hat{\bar{v}}^a_{e+}\left(\rho^b_{e-},\rho^b_{e+},\rho^b_{s-},\rho^b_{s+}\right) \\
&= \hat{\bar{v}}^a_{e-}\left(\rho^b_{e-},\rho^b_{e+},\rho^b_{s-},\rho^b_{s+}\right)
\end{aligned}$$

because

$$\rho^b_{e+} = \rho^b_{e-} \quad \text{and} \quad \rho^b_{s+} = \rho^b_{s-}$$

and the crystal contains enough symmetry for the stress to equally activate both positive and negative dislocation densities. Therefore, the positive edge density flux at any material point will be the same as the negative edge density flux at that same material point, and the same relationship can be derived between the positive and negative screw dislocation densities. If this equality between the positive and negative species is true everywhere in the crystal, but the level of density is allowed to vary spatially in the crystal, then as the crystal begins to deform non-homogeneously, due to the non-homogeneous distribution of statistical density, a polarity in the density will arise locally from the previously unpolarized crystal. Furthermore, with the positive and negative dislocation density flux the same at every point $\mathbf{X}$, according to

$$\begin{aligned}
\rho^a_{e-}(\mathbf{X})\,\bar{v}^a_{e-}(\mathbf{X}) &= \rho^a_{e+}(\mathbf{X})\,\bar{v}^a_{e+}(\mathbf{X}) \\
\rho^a_{s-}(\mathbf{X})\,\bar{v}^a_{s-}(\mathbf{X}) &= \rho^a_{s+}(\mathbf{X})\,\bar{v}^a_{s+}(\mathbf{X}) \ ,
\end{aligned}$$

the change in the dislocation density species must have the following relationship at

every point $\mathbf{X}$ for small strains

$$\dot{\rho}^a_{e+(flux)}(\mathbf{X}) = -\dot{\rho}^a_{e-(flux)}(\mathbf{X}) \quad \text{and} \quad \dot{\rho}^a_{s+(flux)}(\mathbf{X}) = -\dot{\rho}^a_{s-(flux)}(\mathbf{X}) \tag{3.35}$$

based on Eq.'s 3.31-3.34, solely.

In this special case, the flux divergence equations lead to an increase in the positive edge density and to an equal loss of negative edge density, and the mean density remains unaffected. The mean density most definitely will be affected by the statistical processes of generation and annihilation that occur with homogeneous plastic deformation. Furthermore, if the density polarity is small compared to the mean density of a certain character on a slip-system, the accumulation/loss of density due to further dislocation flux divergence will not significantly affect the total dislocation density. In general, the flux divergence contribution to the dislocation density evolution can augment or lessen the total dislocation density of a given character depending on its current polarity and flux divergence. Instances in which the species flux divergence increases the existing polarity can lead to an increase in the total dislocation density as well, and in cases where the species flux divergence decreases the existing polarity, the total dislocation density can decrease as a result. In either instance, the change in the total density due to the species flux divergence is only a fraction of the change in the polarity of the density. In fact, the change in the mean density due to the flux divergence of density takes the following form

$$\dot{\bar{\rho}}^a_{e(flux)} = \frac{1}{2}\left[\nabla\left(\rho^a_{e-}\bar{v}^a_{e-}\right) - \nabla\left(\rho^a_{e+}\bar{v}^a_{e+}\right)\right]\cdot \mathbf{m}^a_0 sign\left(\tau^a\right) \tag{3.36}$$

$$\dot{\bar{\rho}}^a_{s(flux)} = \frac{1}{2}\left[\nabla\left(\rho^a_{s+}\bar{v}^a_{s+}\right) - \nabla\left(\rho^a_{s-}\bar{v}^a_{s-}\right)\right]\cdot \mathbf{p}^a_0 sign\left(\tau^a\right)\ . \tag{3.37}$$

The fact that non-homogeneous plastic deformation can lessen as well as augment the total dislocation density, compared to the density levels in homogeneously deforming crystals, contradicts the physical arguments of Ashby (1970). Instead of additional dislocations being required to satisfy lattice incompatibility, as compared to the homogeneously deforming body as Ashby envisioned, the density merely de-

velops a polarity sufficient to accommodate the geometric constraints. According to the physical arguments presented above, the total density in both the homogeneously and non-homogeneously deforming bodies may be different at the same level of plastic strain, but there is some ambiguity as to which crystal would contain more density. Interpreted within the additive SSD/GND density framework, the presence of a GND density may lead to a reduction of the SSD density such that the total density is increased or decreased. The change in the total density between the two states will be only a fraction of the polarity in the crystal. In Ashby's model, the augmented density led to a higher density of forest obstacles and greater strength in the non-homogeneously deforming body than in the homogeneously deforming body. Since the total density isn't necessarily augmented according to the physical arguments presented the difference in the obstacle-generated strength in the two cases will not be as great as anticipated. In instances where the density mean numerically dominates the polarity, the contribution of the flux divergence to the evolution of the mean will be insignificant compared to the generation and annihilation evolution equations, leading to no measurable change in the forest resistance. Further discussion as to the role of the polar density in leading to the experimentally-observed length-scale dependent phenomena will be deferred until a set of non-local constitutive equations are developed in Chapter 5.

Large Deformation Analysis

The small strain analysis assumed that there was no geometry change, no initial lattice curvature, and no geometric character to the initial density. In the large deformation analysis these assumptions will be relaxed so that the current geometry, the initial dislocation state, and the initial lattice curvature crystal are considered. The results of the small strain analysis in determining whether the polar dislocation density is accumulated or lost will again be used in this discussion.

In Chapter 2, the incompatibility of the plastic strain was related to Nye's dislocation tensor in Eq. 2.25 in the small strain analysis. The result was generalized by

Dai (1997) for finite deformations in the form

$$\mathbf{A} = -\left(\nabla \times \mathbf{F}^{\mathrm{p}\mathrm{T}}\right)^{\mathrm{T}} , \tag{3.38}$$

where $\mathbf{A}$ is the dislocation tensor due to lattice incompatibility for finite deformations. The notation in Eq. 3.38 is confusing as to how the derivatives are taken with all of the matrix transposes that are performed; therefore, the indicial notation will be used to evaluate the components of the tensors involved in the expressions to develop the accumulation or loss of each dislocation species due to the flux divergence of dislocation density. In indicial notation, Eq. 3.38 takes the form

$$\mathrm{A}_{iq} = -e_{qjk}\mathrm{F}^{\mathrm{p}}_{ik,j} , \tag{3.39}$$

where e_{qjk} is the alternating tensor and "$,j$" denotes "$\partial/\partial \mathrm{X}_j$" with respect to the reference configuration. This definition of Nye's tensor is incomplete because it doesn't account for the initial dislocation state of the crystal. Formally, with the initial plastic deformation gradient equal to identity at every point $\mathbf{X}$ within the body according to

$$\mathbf{F}^{\mathrm{p}}\left(\mathbf{X}, t = 0\right) \equiv \mathbf{I}_2,$$

then

$$\mathbf{A}\left(\mathbf{X}, t = 0\right) = \mathbf{0}$$

according to Eq. 3.38. In the reference configuration, the plastic deformation gradient is identity everywhere in the body since there is considered to be no plastic deformation in the initial state. Strain is not a measure of material state. Equation 3.38 would require that there be no polarity in the initial dislocation density state. In general, this cannot be true; therefore. Eq. 3.38 must be generalized to allow for an

initial polarity in the reference configuration leading to

$$\mathrm{A}_{iq} \equiv \mathrm{A}_{0(iq)} - e_{qjk}\mathrm{F}^{\mathrm{p}}_{ik,j} \ , \tag{3.40}$$

where $\mathbf{A}_0$ is the Nye's tensor in the reference configuration. This is the definition of the dislocation tensor in the deformed configuration that will be used in the analysis. In rate form, Eq. 3.40 becomes

$$\dot{\mathrm{A}}_{iq} = -e_{qjk}\dot{\mathrm{F}}^{\mathrm{p}}_{ik,j} \ . \tag{3.41}$$

Eq. 3.41 is a complete expression for the change in the dislocation density tensor in the reference configuration due to the changes in the plastic deformation gradient. In fact, it is the basis for the relationship that will be used to increment the polar dislocation density in the non-local model presented in Chapter 5; however, it does not contain much insight into the dislocation mechanics responsible for the changes. By considering each of the components that contribute to $\dot{\mathbf{A}}$ separately, a better understanding of the underlying phenomena responsible for the change in the geometric character of the dislocation density can be discovered.

Substitution of the flow rule in Eq.3.2 for $\dot{\mathbf{F}}^{\mathrm{p}}$ leads to

$$\dot{\mathrm{A}}_{iq} = -e_{qjk}\left(\mathrm{L}^{\mathrm{p}}_{il}\mathrm{F}^{\mathrm{p}}_{lk}\right)_{,j} \ . \tag{3.42}$$

The product rule of differentiation leads to

$$\dot{\mathrm{A}}_{iq} = -e_{qjk}\left(\mathrm{L}^{\mathrm{p}}_{il,j}\mathrm{F}^{\mathrm{p}}_{lk} + \mathrm{L}^{\mathrm{p}}_{il}\mathrm{F}^{\mathrm{p}}_{lk,j}\right) \ . \tag{3.43}$$

Substitution of Eq. 3.3 and Eq. 3.40 into Eq. 3.43 yields

$$\begin{aligned} \dot{\mathrm{A}}_{iq} \ = \ & -e_{qjk}\sum_{a}\left(\dot{\gamma}^{a}_{,j}\mathrm{m}^{a}_{(0)i}\mathrm{n}^{a}_{(0)l} + \dot{\gamma}^{a}\mathrm{m}^{a}_{(0)i,j}\mathrm{n}^{a}_{(0)l} + \dot{\gamma}^{a}\mathrm{m}^{a}_{(0)i}\mathrm{n}^{a}_{(0)l,j}\right)\mathrm{F}^{\mathrm{p}}_{lk} \\ & +\mathrm{L}^{\mathrm{p}}_{il}\left(\mathrm{A}_{lq} - \mathrm{A}_{(0)lq}\right) \ . \end{aligned} \tag{3.44}$$

In Section 2.3, it was shown that Nye's tensor could be related to lattice curvature. In the general case considered in this derivation, an initial value of Nye's tensor in the reference configuration must correspond to a lattice curvature in the reference configuration. Neglecting the lattice curvature associated with small elastic deformation gradients, the change in the lattice directions due to an initial distribution of polar density can be written for small strains as

$$\begin{aligned} \mathrm{m}^a_{(0)i,j} &\doteq \mathrm{p}^a_{(0)i}\mathrm{A}_{(0)_{jl}}\mathrm{n}^a_{(0)l} - \mathrm{n}^a_{(0)i}\mathrm{A}_{(0)_{jl}}\mathrm{p}^a_{(0)l} \\ &\quad +\frac{1}{2}\mathrm{A}_{(0)_{kk}}\left(\mathrm{n}^a_{(0)i}\mathrm{p}^a_{(0)j} - \mathrm{p}^a_{(0)i}\mathrm{n}^a_{(0)j}\right) \end{aligned} \tag{3.45}$$

$$\begin{aligned} \mathrm{n}^a_{(0)i,j} &\doteq \mathrm{m}^a_{(0)i}\mathrm{A}_{(0)_{jl}}\mathrm{p}^a_{(0)l} - \mathrm{p}^a_{(0)i}\mathrm{A}_{(0)_{jl}}\mathrm{m}^a_{(0)l} \\ &\quad +\frac{1}{2}\mathrm{A}_{(0)_{kk}}\left(\mathrm{p}^a_{(0)i}\mathrm{m}^a_{(0)j} - \mathrm{m}^a_{(0)i}\mathrm{p}^a_{(0)j}\right) . \end{aligned} \tag{3.46}$$

Substitution into Eq 3.44 leads to the final result

$$\begin{aligned} \dot{\mathbf{A}} &\doteq \sum_a \mathbf{m}^a_0 \otimes \left(\mathbf{F}^{\mathrm{p}\mathrm{T}}\mathbf{n}^a_0 \times \nabla\dot{\gamma}^a\right) \\ &+ \sum_a \dot{\gamma}^a \mathbf{p}^a_0 \otimes \left[\mathbf{F}^{\mathrm{p}\mathrm{T}}\mathbf{n}^a_0 \times \left(\mathbf{A}_0\mathbf{n}^a_0 - \frac{1}{2}tr(\mathbf{A}_0)\mathbf{n}^a_0\right)\right] \\ &- \sum_a \dot{\gamma}^a \mathbf{n}^a_0 \otimes \left[\mathbf{F}^{\mathrm{p}\mathrm{T}}\mathbf{n}^a_0 \times \left(\mathbf{A}_0\mathbf{p}^a_0 - \frac{1}{2}tr(\mathbf{A}_0)\mathbf{p}^a_0\right)\right] \\ &+ \sum_a \dot{\gamma}^a \mathbf{m}^a_0 \otimes \left[\mathbf{F}^{\mathrm{p}\mathrm{T}}\mathbf{m}^a_0 \times \left(\mathbf{A}_0\mathbf{p}^a_0 - \frac{1}{2}tr(\mathbf{A}_0)\mathbf{p}^a_0\right)\right] \\ &- \sum_a \dot{\gamma}^a \mathbf{m}^a_0 \otimes \left[\mathbf{F}^{\mathrm{p}\mathrm{T}}\mathbf{p}^a_0 \times \left(\mathbf{A}_0\mathbf{m}^a_0 - \frac{1}{2}tr(\mathbf{A}_0)\mathbf{m}^a_0\right)\right] \\ &+ \mathbf{L}^{\mathrm{p}}\left(\mathbf{A} - \mathbf{A}_0\right) . \end{aligned} \tag{3.47}$$

The first line on the right-hand side of Eq. 3.47 can be understood as the large deformation generalization of the small strain relationship between the non-homogeneous shearing rate and the dislocation tensor in Eq. 2.25. The rest of terms, which did not appear in the small strain analysis, result from deformation on a curved crystal lattice. The expressions on the second and third lines of Eq. 3.47 result from a lattice Burgers vector that changes direction with respect to the material coordinates in which the reference lattice configuration is defined. The expressions on the fourth

and fifth lines of Eq. 3.47 result from a slip-plane normal vector that changes direction with respect to the material coordinates in which the reference configuration is defined. The last line of Eq. 3.47 results from a constant dislocation flux through a crystal whose geometric density is changing. According to the results of Eq. 3.47, flux of a single dislocation species across a crystal with an initially curved lattice can lead to the accumulation/loss of polar density with the same Burgers vector, and can also lead to the accumulation/loss of polar densities with different Burgers vectors, due to curvature in the slip plane.

The most general description of the plastic deformation of an initially curved lattice has been considered. However, the initial lattice curvature compared to the final lattice curvature at the end of a typical plastic strain gradient experiment (e.g. thin-beam bending or thin-wire torsion) is small, given that the dislocation polarity at the end of one these experiments is two orders of magnitude ($\rho_{\pm} \approx 10^{14} m^{-2}$) larger than the total initial dislocation density of the crystal ($\rho \approx 10^{12} m^{-2}$). Therefore, the simplifying assumption can be made that $\mathbf{A}_0 \approx \mathbf{0}$. Although not as rigorous as the general case, this assumption results in great simplification in the time rate of change of Nye's tensor:

$$\dot{\mathbf{A}} \doteq \sum_a \mathbf{m}_0^a \otimes \left(\mathbf{F}^{\mathrm{p}\mathrm{T}} \mathbf{n}_0^a \times \nabla \dot{\gamma}^a \right) + \mathbf{L}^{\mathrm{p}} \mathbf{A} \, . \tag{3.48}$$

Whereas in the more general case with $\mathbf{A}_0 \neq \mathbf{0}$ a material circuit and a lattice circuit drawn around the initial dislocation state in the reference configuration led to two different areas, the lattice and material circuits drawn around the initial dislocation state with $\mathbf{A}_0 = \mathbf{0}$ correspond to the same closed loops. Since in Eq. 3.40 Nye's tensor is calculated with respect to the reference configuration during the deformation of the crystal, material circuits used to calculate the change in the Nye's tensor due to non-homogeneous plastic deformation are equivalent to lattice circuits for $\mathbf{A}_0 = \mathbf{0}$

As in the small strain case, the change in the dislocation tensor viewed in this form doesn't uniquely specify the change in the crystallographic density. A minimization technique could be implemented as done in Section 2.4 to find a reasonable crystallographic distribution, but considering each dislocation density flux individually leads

to a unique description of the crystallographic dislocation density state. The plastic flow rate $\mathbf{L}^{p\xi}$, due to the density flux of a single species ξ, is defined as

$$\mathbf{L}^{p\xi} \equiv \rho^{\xi}\bar{v}^{\xi}\mathbf{b}_0^{\xi} \otimes \mathbf{n}_0^{\xi} sign\left(\tau^{\xi}\right) \ . \tag{3.49}$$

Likewise, the time rate of change of the dislocation tensor $\dot{\mathbf{A}}^{\xi}$, due to the density flux of a single species ξ, is defined as

$$\begin{aligned} \dot{\mathbf{A}}^{\xi} \ \equiv \ & \mathbf{b}_0^{\xi} \otimes \left[\mathbf{F}^{p\mathrm{T}}\mathbf{n}_0^{\xi} \times \nabla\left(\rho^{\xi}\bar{v}^{\xi}\right)\right] sign\left(\tau^{\xi}\right) \\ & + \left(\rho^{\xi}\bar{v}^{\xi}\right)\mathbf{b}_0^{\xi} \otimes \mathbf{A}^{\mathrm{T}}\mathbf{n}_0^{\xi} sign\left(\tau^{\xi}\right) \ , \end{aligned} \tag{3.50}$$

with the assumption that $\mathbf{A}_0 \approx \mathbf{0}$, and the total rate of change of the dislocation tensor becomes

$$\dot{\mathbf{A}} = \sum_{\xi} \dot{\mathbf{A}}^{\xi} \ . \tag{3.51}$$

From Eq. 3.50, it is clear that the flux divergence of a dislocation density with Burgers vector $\mathbf{b}_0$ will affect only dislocation densities with the same Burgers vector. As in the small strain case, the non-homogeneous flux of edge dislocations will affect the screw dislocation polarity and vice-versa. However, unlike the small strain case, a non-homogeneous flux of edge or screw density could affect the polarity of dislocation density with tangent directions not contained in the slip plane. The change in the dislocation tensor, due to the flux of a single species ξ that contributes to the plastic shear associated with slip-system a, can be decomposed into three rates of dislocation density accumulation/loss such that

$$\dot{\rho}_{e\pm}^{a}\mathbf{b}_0^{\xi} \otimes \mathbf{p}_0^{a} + \dot{\rho}_{s\pm}^{a}\mathbf{b}_0^{\xi} \otimes \mathbf{m}_0^{a} + \dot{\rho}_{j\pm}^{a}\mathbf{b}_0^{\xi} \otimes \mathbf{n}_0^{a} = \dot{\mathbf{A}}^{\xi} \ , \tag{3.52}$$

where

$$\dot{\rho}_{e\pm}^{a} \ = \ \frac{1}{\left|\mathbf{b}_0^{\xi}\right|^2}\mathbf{b}_0^{\xi} \cdot \dot{\mathbf{A}}^{\xi}\mathbf{p}_0^{a}, \tag{3.53}$$

$$\dot{\rho}^a_{s\pm} = \frac{1}{\left|\mathbf{b}^\xi_0\right|^2}\mathbf{b}^\xi_0 \cdot \dot{\mathbf{A}}^\xi \mathbf{m}^a_0, \tag{3.54}$$

$$\text{and } \dot{\rho}^a_{j\pm} = \frac{1}{\left|\mathbf{b}^\xi_0\right|^2}\mathbf{b}^\xi_0 \cdot \dot{\mathbf{A}}^\xi \mathbf{n}^a_0 \ . \tag{3.55}$$

The $\dot{\rho}_\pm$ terms in Eq. 3.52 should be read as "the time rate of change of the polarity of the dislocation density", and the subscript j indicates a density of dislocation jogs with tangent line direction parallel to the the slip plane normal $\mathbf{n}^a_0$. In the generation and annihilation evolution equations, dislocation jogs were not explicitly introduced, although jog density would have to be produced in order for edge dislocations to climb and self-annihilate. For highly symmetric crystals, FCC and BCC crystals for example, the dislocation density space does not necessarily need to be expanded to explicitly account for jogs because the jog density can be represented by a combination of edge density on a cross-slip plane and in-plane edge density.

Consider Figure 3-3 of a jogged edge dislocation line. The jog with a tangent line parallel to the slip plane normal could be represented by addition of edge density on the cross-slip plane and a reduction of edge density in the primary plane. The change in the two edge dislocation densities to account for the polar jog density is

$$\dot{\rho}^b_{e\pm} = \dot{\rho}^a_{j\pm}\left(\frac{\mathbf{m}^a_0 \cdot \mathbf{m}^b_0}{\mathbf{n}^a_0 \cdot \mathbf{p}^b_0}\right) \tag{3.56}$$

$$\dot{\rho}^a_{e\pm} = -\dot{\rho}^b_{e\pm}\left(\frac{\mathbf{p}^a_0 \cdot \mathbf{p}^b_0}{\mathbf{m}^a_0 \cdot \mathbf{m}^b_0}\right) \tag{3.57}$$

$$\text{for} \qquad \mathbf{m}^a_0 \times \mathbf{m}^b_0 = \mathbf{0} \ ,$$

where $\rho^b_{e\pm}$ is the edge dislocation polarity on the cross-slip plane, $\mathbf{p}^b_0$ is the tangent line direction of a positive edge dislocation on the cross-slip plane (also the in-plane bi-normal direction), and $\mathbf{p}^a_0$ is the tangent line direction of a positive edge dislocation on the primary slip plane. By using such a transformation for dislocation jogs that arise due to the geometric constraints, the basis of pure edge and screw dislocations does not have to be expanded to explicitly include jog densities for highly symmetric crystals.

Using the same arguments as in the small strain case, in which a non-homogeneous flux of positive edge dislocation affected only the positive edge density and both screw dislocation densities, and a non-homogeneous flux of positive screw density affected only the positive screw density and both edge dislocation densities, a unique set of equations can be written for the change in the polar dislocation densities due to the geometric constraints for large deformations. The equations take the form:

$$\dot{\rho}^a_{e+(flux)} = |\mathbf{b}^a_0|^{-2}\,\mathbf{b}^a_0 \cdot \left(\dot{\mathbf{A}}^a_{e+} + \frac{1}{2}\dot{\mathbf{A}}^a_{s+} + \frac{1}{2}\dot{\mathbf{A}}^a_{s-}\right)\mathbf{p}^a_0 \tag{3.58}$$

$$\dot{\rho}^a_{e-(flux)} = -|\mathbf{b}^a_0|^{-2}\,\mathbf{b}^a_0 \cdot \left(\dot{\mathbf{A}}^a_{e-} + \frac{1}{2}\dot{\mathbf{A}}^a_{s+} + \frac{1}{2}\dot{\mathbf{A}}^a_{s-}\right)\mathbf{p}^a_0 \tag{3.59}$$

$$\dot{\rho}^a_{s+(flux)} = |\mathbf{b}^a_0|^{-2}\,\mathbf{b}^a_0 \cdot \left(\dot{\mathbf{A}}^a_{s+} + \frac{1}{2}\dot{\mathbf{A}}^a_{e+} + \frac{1}{2}\dot{\mathbf{A}}^a_{e-}\right)\mathbf{m}^a_0 \tag{3.60}$$

$$\dot{\rho}^a_{s-(flux)} = -|\mathbf{b}^a_0|^{-2}\,\mathbf{b}^a_0 \cdot \left(\dot{\mathbf{A}}^a_{s-} + \frac{1}{2}\dot{\mathbf{A}}^a_{e+} + \frac{1}{2}\dot{\mathbf{A}}^a_{e-}\right)\mathbf{m}^a_0 \tag{3.61}$$

$$\dot{\rho}^a_{j\pm} = |\mathbf{b}^a_0|^{-2}\,\mathbf{b}^a_0 \cdot \left(\dot{\mathbf{A}}^a_{e+} + \dot{\mathbf{A}}^a_{e-} + \dot{\mathbf{A}}^a_{s+} + \dot{\mathbf{A}}^a_{s-}\right)\mathbf{n}^a_0 \tag{3.62}$$

where $\dot{\mathbf{A}}^a_{e+}$ is the time rate of change of the dislocation tensor due to a non-homogeneous flux of positive edge dislocations on slip-system a. Likewise, $\dot{\mathbf{A}}^a_{e-}$ is the change in the dislocation tensor due to negative edge dislocations, $\dot{\mathbf{A}}^a_{s+}$ is associated with positive screw dislocations, and $\dot{\mathbf{A}}^a_{s-}$ is associated with negative screw dislocations. The total change in Nye's tensor due to dislocation flux divergence on slip system a can be written in the form

$$\dot{\mathbf{A}}^a = \dot{\mathbf{A}}^a_{e+} + \dot{\mathbf{A}}^a_{e-} + \dot{\mathbf{A}}^a_{s+} + \dot{\mathbf{A}}^a_{s-}\ , \tag{3.63}$$

and is simply the sum of the individual contributions of each density species on that slip system. The jog density can be treated explicitly or converted into a combination of edge densities in the primary slip plane and the cross-slip plane, as discussed earlier.

3.3 Constitutive Equations

The evolution equations of the generation and annihilation of crystallographic dislocation density, as well as the accumulation/loss equations due to non-homogeneous

dislocation glide, have been based on kinematic relationships. The total dislocation density evolution is found by combining the three parts such that

$$\dot{\rho}^{\xi} = \dot{\rho}^{\xi}_{(gen)} + \dot{\rho}^{\xi}_{(ann)} + \dot{\rho}^{\xi}_{(flux)} \tag{3.64}$$

No constitutive equations were introduced to capture any material-specific properties and the evolution of those properties with deformation history. However, the evolution equations introduced three internal modeling functions: the average dislocation velocity $\bar{v}^{\xi}$, the average dislocation length $\bar{l}^{\xi}$, and the capture radius R^{ξ} for each dislocation density of index ξ. The material-specific behavior is introduced through the forms of these three internal functions that in general may depend on the dislocation density state, applied stress, crystal geometry, and temperature such that

$$\bar{v}^{\xi} = \hat{\bar{v}}^{\xi}\left(\rho^{\varsigma}, \bar{\mathbf{T}}, \mathbf{b}_0^{\varsigma}, \mathbf{t}_0^{\varsigma}, \mathbf{n}_0^{\varsigma}, \theta\right) \tag{3.65}$$

$$\bar{l}^{\xi} = \hat{\bar{l}}^{\xi}\left(\rho^{\varsigma}, \bar{\mathbf{T}}, \mathbf{b}_0^{\varsigma}, \mathbf{t}_0^{\varsigma}, \mathbf{n}_0^{\varsigma}, \theta\right) \tag{3.66}$$

$$R^{\xi} = \hat{R}^{\xi}\left(\rho^{\varsigma}, \bar{\mathbf{T}}, \mathbf{b}_0^{\varsigma}, \mathbf{t}_0^{\varsigma}, \mathbf{n}_0^{\varsigma}, \theta\right) \ , \tag{3.67}$$

where θ is absolute temperature. Along with the geometry of the dislocation contained in $\mathbf{b}_0^{\varsigma}$ and $\mathbf{t}_0^{\varsigma}$, another direction, $\mathbf{n}_0^{\varsigma}$, which specifies the unit normal of the area swept by a moving dislocation, is included as part of the dislocation geometry.

The average dislocation velocity is most directly related to the strengthening of the crystal. For a material to strain harden, the average velocity must decrease with increasing density faster than the density increases. The strain rate is the resultant of a product between the dislocation density and the average velocity. Therefore, to maintain a constant strain rate as the density increases, the average velocity necessarily decreases. If the velocity were independent of the density and only a function of the applied stress, strain softening would be observed. To strain harden a material, the dislocation mobility must decrease with increasing density, such that increasingly larger stresses must be applied to sustain the same level of plastic activity in the material.

The average segment lengths most directly control the growth of dislocation density. They are used to quantify the increment in density for an increment in dislocation flux. The capture radii most directly control the annihilation rate of density. The average segment lengths, along with the capture radii, dictate the evolution profile of the dislocation density with plastic deformation and determine the saturation level of density. Explicit forms of the three constitutive functions will be developed to model behavior of aluminum single crystals in tension and the bending of thin beams.

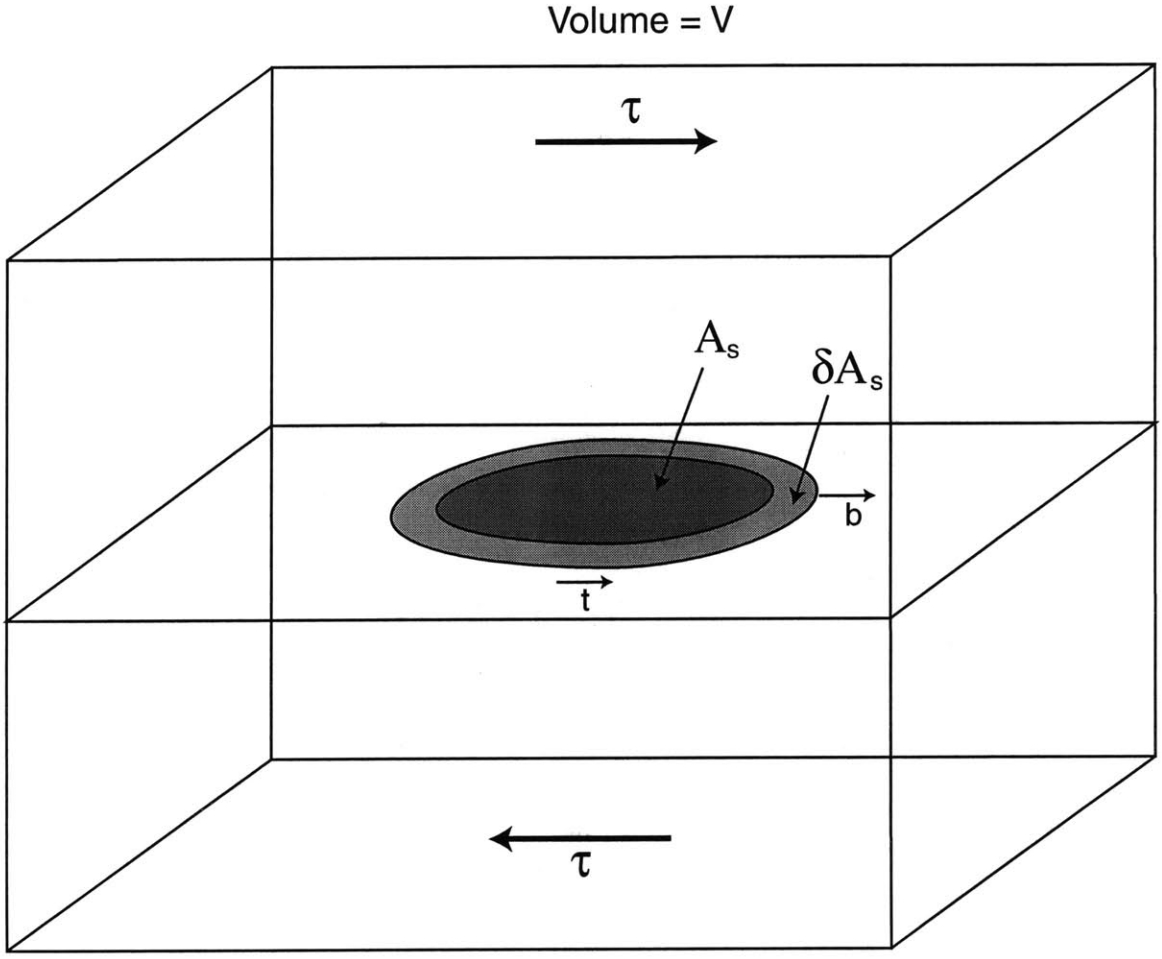

Figure 3-1: Schematic of an expanding dislocation loop during crystallographic slip leading to the generation of dislocation density and plastic shear.

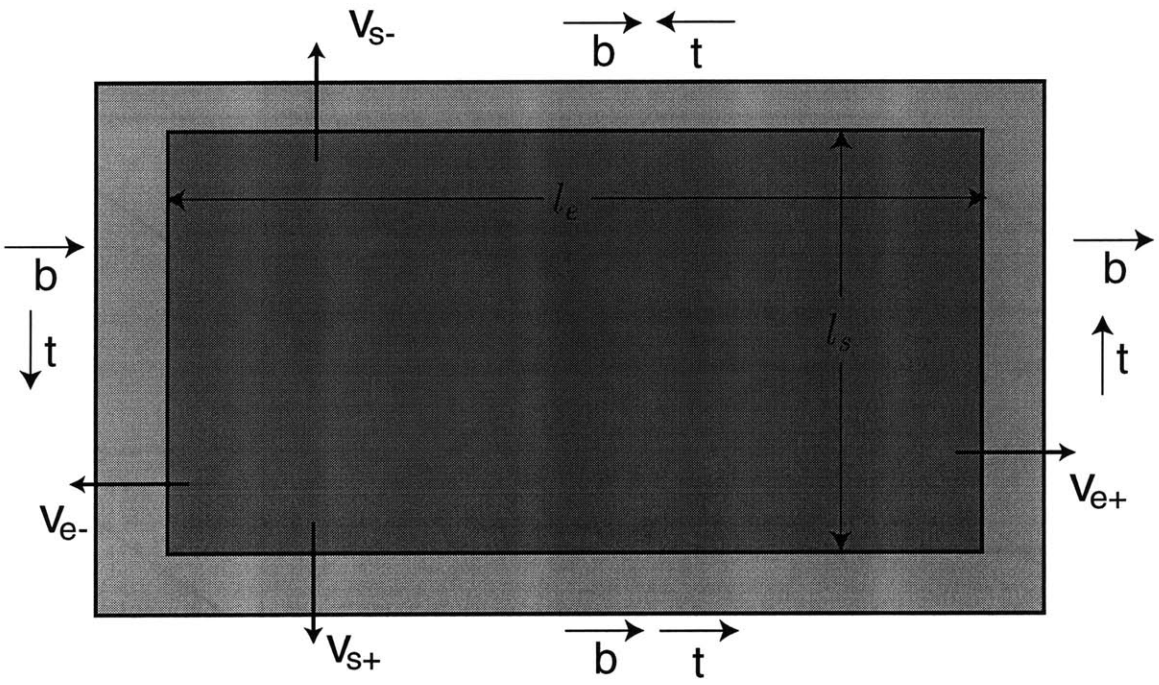

Figure 3-2: Schematic of an expanding dislocation loop idealized as a composition of discrete line segments forming a closed loop.

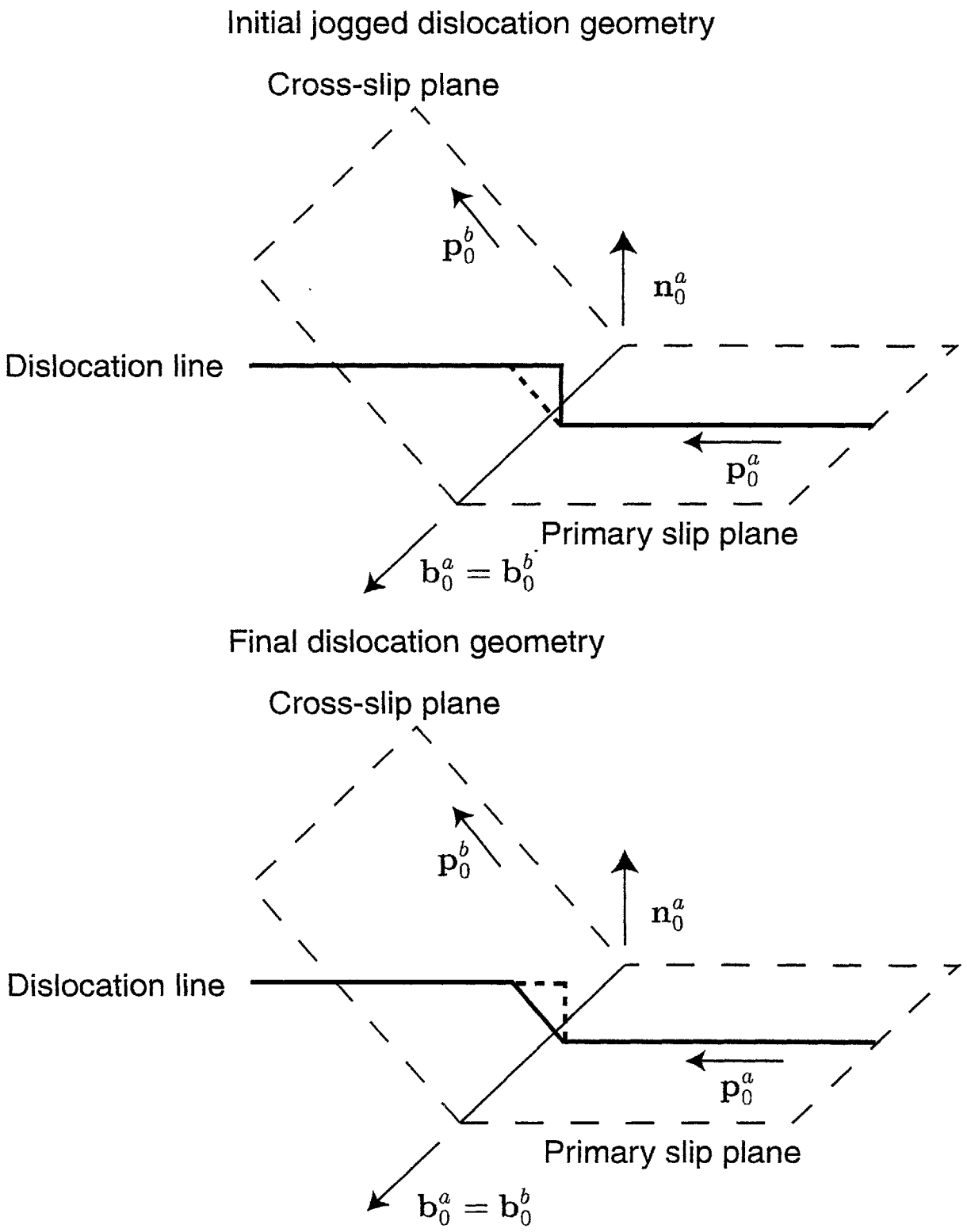

Figure 3-3: Schematic of a jogged edge dislocation which can be represented as combination of edge dislocations on the primary and cross-slip planes.

Chapter 4

Application of Local Model to Anisotropic Behavior of Aluminum Single Crystals

The "local" model will consider only the dislocation evolution equations associated with the generation of new density and the annihilation of old density. The polar accumulation/loss equations associated with non-homogeneous deformation will not be considered as part of the simulation. The adjective "local" refers to the property of the model that allows the behavior at a single material point to be calculated independently of the behavior at the material points around it. This is in contrast to the "non-local" models in which the behavior of a single material point is dependent on the behavior of material points around it. Inclusion of the polar accumulation/loss equations leads to a "non-local" model because the change in the dislocation polarity is a function of the dislocation flux divergence, and calculation of the flux divergence depends on the activity of multiple material points.

Since the local constitutive model doesn't include the changes in the dislocation polarity due to non-homogeneous plastic deformation, the model will not capture the length-scale dependent material behavior observed. During bulk deformation processes the total dislocation density can be orders of magnitude larger than the polarity of the density; therefore, the local model will be able to capture the evolution

of bulk material properties at macroscopic length scales. The model will be applied to investigate the plastic anisotropy of aluminum single crystal in tension, where the effects of microscopic plastic inhomogeneities and resulting dislocation density should be negligible compared to the bulk generation and annihilation of dislocation density in determining the plastic evolution of the crystals.

4.1 Selection of Discrete Dislocation Basis

Single crystal aluminum was chosen as the model material on which to test the density-based internal state variable model. The material was chosen because it has a highly symmetric crystal structure (FCC) leading to geometrically similar dislocation densities, and because pure aluminum and its alloys are widely used in engineering applications. Continuum simulations of FCC single crystals have been concerned mainly with the plastic response of copper (Cuitiño and Ortiz, 1992; Bassani and Wu, 1991), and to our knowledge, there has been no successful continuum simulation of the plastic behavior of single crystal aluminum with existing continuum crystal plasticity models. The mechanical behavior of single crystal aluminum is quite different from that of copper. For reasons that will be discussed in Section 4.6, single crystal copper turns out to be a relatively "easy" crystal material to simulate, but it is much more difficult to capture the mechanical behavior of aluminum single crystals.

The first step in modeling a crystalline material in this dislocation density framework is to choose a dislocation density discretization. Since the model will be applied to capture the plastic response of single crystal aluminum at room temperature, where aluminum is known to cross-slip readily due to its high stacking fault energy, a total of eighteen distinct dislocation densities in the reduced basis will be used. The Burgers vectors, as well as the tangent line directions, are given in Table 4.1. Of the eighteen dislocations, there are twelve pure edge dislocations, one for each $< 110 > \{111\}$ slip-system, and there are six pure screw dislocations, one for each $< 110 >$ Burgers vector, that are permitted to slip freely on both of the glide planes in which they reside. More generally, the total density may be considered to be composed of two

populations of dislocations. The screw densities represent the fraction of the population that may cross-slip, and edge densities represent the fraction of the population that cannot cross-slip.

4.2 Selection of Constitutive Functions

In developing the internal modeling functions, each geometrically similar dislocation density will have the same functional form and material constants for dislocation mobility, average length, and capture radius. The motion of individual dislocations during plastic deformation may be viewed as a percolation process in which dislocation lines follow the path of least resistance, subject to the local stresses applied to the line. Most of the time the lines are immobile, pinned by forest dislocations. With sufficient activation such an obstacle can be overcome, thereby allowing the dislocation to move rapidly to the next set of obstacles. Assuming that the average dislocation velocity can be written for the density of lines in an explicit form, the dislocation density mobility will be described by an activated glide model first proposed by Kocks et. al. (1975). The average density mobility will take the following functional form:

$$\bar{v}_e^a = v_{e0} \exp\left[-\frac{\Delta F_e}{k\theta}\left(1-\left(\frac{|\tau^a|}{s_{ep}+s_{ed}}\right)^{p_e}\right)^{q_e}\right] \tag{4.1}$$

$$\bar{v}_s^a = v_{s0} \exp\left[-\frac{\Delta F_s}{k\theta}\left(1-\left(\frac{|\tau^a|}{s_{sp}+s_{sd}}\right)^{p_s}\right)^{q_s}\right], \tag{4.2}$$

where the subscripts e and s denote edge and screw, respectively. In Eq.'s 4.1 and 4.2, v_0 is a reference velocity, ΔF is the activation energy required to overcome the obstacles to dislocation motion, k is Boltzmann's constant, τ is the resolved shear stress on the dislocation density glide plane, s_p is the intrinsic lattice resistance, s_d is the resistance due to interactions with forest dislocations, and the parameters p and q determine the influence of the applied stress on the activation energy. The resolved shear stress τ^a is a function of the applied stress and crystal geometry. For

dislocation densities in slip-system a, the resolved shear stress is approximated by

$$\tau^a \doteq \left(\bar{\mathbf{T}}\right) \cdot \left(\mathbf{m}_0^a \otimes \mathbf{n}_0^a\right) \ , \tag{4.3}$$

following Bronkhorst et al. (1992).

The dislocation resistance s_d is a non-linear function of the dislocation density state. Dislocations may impede the motion of gliding dislocations either by piling up on the glide planes, or by piercing the glide plane as a forest that the mobile density must cut. The dislocation resistance will be modeled as though it is primarily due to forest dislocation density interactions; however, reactions between the glide dislocations and other dislocations that lie in parallel glide planes will also be taken into account. Although these dislocations do not pierce the glide plane, statistical densities of dislocations parallel to the glide planes have been observed to increase the resistance to slip (Argon, 1969). The strength will take the following functional form:

$$s_d^{\xi} = \mu \left|\mathbf{b}\right| \sqrt{\sum_{\zeta} G^{\xi\zeta} \rho^{\zeta}} \ , \tag{4.4}$$

where s_d^{ξ} is the resistance encountered by dislocation density of index ξ, μ is the shear modulus, and $G^{\xi\zeta}$ is a matrix detailing the strength of interactions between dislocations of index ξ and ζ. By considering the symmetry of the FCC crystal, and the types of junctions known to form between different dislocations, $G^{\xi\zeta}$ can be filled with six independent coefficients $G_0 - G_5$ (Lomer, 1951; Kocks, 1959; Franciosi and Zaoui, 1982).

The first two coefficients, G_0 and G_1, account for in-plane interactions, and the other four coefficients, $G_2 - G_5$, account for out-of-plane interactions. The G_0 coefficient describes the interaction between dislocations with the same Burgers vector and parallel slip planes (self-interaction); however, there is no resistance between edge and screw dislocations with the same Burgers vector on parallel slip planes. The G_1 coefficient describes the interaction between dislocations on parallel slip planes, but with different Burgers vectors. The other four interaction coefficients contain dislocation

densities that pierce the planes of the gliding density.

The crystallographic densities have been defined as line length per unit volume, but a totally equivalent definition may be used in which the density is defined as a number density piercing a unit area with a normal direction parallel to the dislocation tangent direction. The two measures of dislocation density yield the same magnitude of density. The piercing density of dislocation density ρ^ζ with tangent line direction $\mathbf{t}_0^\zeta$ on a plane with a unit normal $\mathbf{n}_0^\xi$ becomes $|\mathbf{n}_0^\xi \cdot \mathbf{t}_0^\zeta|\rho^\zeta$. The four interaction coefficients describing interaction between the out-of-plane forest density and the glide dislocations must account for not only the strength of the interaction, but also the piercing density on the glide plane.

The interaction coefficient G_2 describes the interaction between dislocation densities with the same Burgers vector, but on a different slip plane (cross-slip interaction) given by $G_2 = g_2|\mathbf{n}_0^\xi \cdot \mathbf{t}_0^\zeta|$, where g_2 accounts for the strength of the interaction and $|\mathbf{n}_0^\xi \cdot \mathbf{t}_0^\zeta|$ accounts for the piercing density. Likewise, the coefficient $G_3 = g_3|\mathbf{n}_0^\xi \cdot \mathbf{t}_0^\zeta|$ describes the interaction between dislocation densities that result in a junction with a $< 110 >$ Burgers vector in either of the slip planes of the dislocations involved (glissile junction). Finally, the remaining two coefficients represent dislocation interactions that form sessile junctions. The weaker of the two, the Hirth lock, is described by $G_4 = g_4|\mathbf{n}_0^\xi \cdot \mathbf{t}_0^\zeta|$, and the stronger of the two, the Lomer-Cottrell lock, is described by $G_5 = g_5|\mathbf{n}_0^\xi \cdot \mathbf{t}_0^\zeta|$. The six coefficients fill the strength interaction matrix according to the types of interactions anticipated between the gliding density and the forest density. Table 4.6.2 shows the arrangement of the six interaction coefficients in the strength sub-matrix for the edge dislocation interactions.

A simple functional form for the dislocation capture radii R^ξ will be considered. Two constant distances, R_e and R_s, will be considered; they describe the critical distance necessary for annihilation between edge and screw dislocations, respectively. Two distances are necessary because the ability of screw dislocations to cross-slip dictates that the screw density should have a larger capture radius than edge dislocations that cannot cross-slip. The edge capture radius is based on the ability for edge dislocations on parallel planes to climb short distances toward one another.

Perhaps the average dislocation segment length is the most difficult constitutive function to understand and physically motivate. Consider again the "generation" evolution equations, found in Eq.'s 3.12 and 3.13, and their relationship with the plastic strain rate, found in Eq. 3.14. The average dislocation segment length relates an increment of the density flux associated with a particular species to an increment in density due to its glide motion. The scale of the average segment length is on the order of the diameter of the average dislocation loop. The motion of kinks on dislocation lines contributes to the plastic strain rate on a slip system, but does not contribute to the increase in dislocation density on that system. The length scales representative of kink motion are much smaller than the magnitude of the average segment length in these constitutive functions. The functional form of the average segment length could in theory be directly determined by analyzing dislocation dynamics simulations from the viewpoint of this kinematic framework. The simulations conducted by Kubin and co-workers (Kubin et al., 1992; Kubin et al., 1998) are probably the most applicable. In their simulations, the dislocation lines are discretized as a series of small edge and screw dislocation segments. Since the same discretization is used in this density model, analysis of the dislocation evolution in their discrete simulations could lead to a functional form of the "average segment length." To our knowledge, dislocation dynamics researchers have not published such an analysis of dislocation evolution; therefore a simple functional form of the average segment length will be used.

The average dislocation segment length $\bar{l}^{\xi}$ will be assumed to be solely a function of the dislocation density state of the material. Dislocation segments may get trapped in certain sections of the crystal where the forest density is considerably greater than in the majority of the crystal. As the forest density increases, more sections of the dislocation loops may get trapped, and the average length of a dislocation segment decreases. The following functional form will be used to model $\bar{l}^{\xi}$:

$$\bar{l}^{\xi} = \frac{1}{\sqrt{\sum_{\varsigma} H^{\xi\varsigma}\rho^{\varsigma}}} , \tag{4.5}$$

where $H^{\xi\varsigma}$ is the average segment length interaction matrix. The $H^{\xi\varsigma}$ matrix will be

assumed to be composed of six coefficients $H_0 - H_5$ that follow the same convention as the coefficients in the $G^{\xi\zeta}$ matrix, and are based on the type of interactions anticipated between the gliding dislocation and the forest density. Because the H_0 and H_1 coefficients detail the interaction between dislocations in parallel planes, we will ignore the these contributions to $\bar{l}$, by setting $H_0 = H_1 = 0$. The coefficients $H_2 - H_5$ detail the interactions with dislocations that pierce the slip plane. The out-of-plane coefficients are determined by the formula $H_{i=2,5} = h_i \left|\mathbf{n}^{\xi} \cdot \mathbf{t}^{\zeta}\right|$, where h_i quantifies the strength of interaction and $\left|\mathbf{n}^{\xi} \cdot \mathbf{t}^{\zeta}\right|$ quantifies the dislocation piercing on the slip plane. The values of $H^{\xi\zeta}$ are, in principal, independent of the values in the strength interaction matrix, $G^{\xi\zeta}$, but the $H^{\xi\zeta}$ matrix takes the same form.

4.3 Finite Element Implementation of Local Constitutive Model

The constitutive model for single crystals aluminum was implemented into a the commercially available FEM package ABAQUS/Standard as a user-defined material (UMAT) (Hibbitt et al., 1998) and was used with first-order brick (C3D8) elements to simulate the orientation dependence of the stress/strain behavior of aluminum single crystals subject to uniaxial tension at ambient temperature. The ABAQUS/Standard UMAT is part of an implicit algorithm that enforces nodal equilibrium at every time increment. The inputs to the UMAT interface are the total deformation gradient at time t, $\mathbf{F}(t)$; the Cauchy stress at time t, $\mathbf{T}(t)$; an estimate as to the total deformation gradient at time $\tau = t + \Delta t$, $\mathbf{F}(\tau)$; and a set of state-dependent variables at time t. The state-dependent variables in this formulation are the crystallographic dislocation densities, ρ^{ξ}, and the plastic deformation gradient, $\mathbf{F}^{\mathrm{p}}$, with respect to the reference configuration. Although the plastic deformation isn't a true state variable (it is a hereditary integral of the plastic deformation rate in the material), it allows for the conceptual separation of the total deformation gradient into the plastic and elastic deformation gradients. Along with these two state variables, the time rate of change

of the dislocation density at time t, $\dot{\rho}^{\xi}(t)$, and the time rate of change of the second Piola-Kirchhoff stress at time t, $\dot{\bar{\mathbf{T}}}(t)$, are also given to aid in the calculation.

Given the input variables to the UMAT interface, the subroutine is responsible for calculating the Cauchy stress at time τ, $\mathbf{T}(\tau)$; the plastic deformation gradient at time τ, $\mathbf{F}^{\mathrm{p}}(\tau)$; the crystallographic dislocation density at time τ, $\rho^{\xi}(\tau)$; and the material jacobian at time τ, $\mathcal{C}(\tau)$. The material jacobian is defined as

$$\mathcal{C} \equiv \frac{\partial \mathbf{T}(\tau)}{\partial \mathbf{E}_t(\tau)} , \tag{4.6}$$

where $\mathbf{E}_t(\tau)$ is the relative strain tensor. It is defined by

$$\mathbf{E}_t(\tau) \equiv ln\left(\mathbf{U}_t(\tau)\right) , \tag{4.7}$$

where $\mathbf{U}_t(\tau)$ is the relative stretch tensor. The relative stretch tensor is evaluated from the polar decomposition of the relative deformation gradient, $\mathbf{F}_t(\tau)$, such that

$$\mathbf{F}_t(\tau) = \mathbf{R}_t(\tau)\,\mathbf{U}_t(\tau) . \tag{4.8}$$

The relative deformation gradient is determined by the following expression

$$\mathbf{F}_t(\tau) = \mathbf{F}(\tau)\,\mathbf{F}^{-1}(t) . \tag{4.9}$$

4.3.1 Time Integration Procedure

The determination of the state at time τ from the inputs to the UMAT subroutine employs a backward Newton solving algorithm. This section will develop the relevant equations that are iterated to solve for the state at the new time increment.

The constitutive equation found Eq. 3.7 may be combined with Eq. 3.1 to form

$$\bar{\mathbf{T}}(\tau) = \frac{1}{2}\mathcal{L}\left[\mathbf{F}^{\mathrm{p}-\mathrm{T}}(\tau)\,\mathbf{F}^{\mathrm{T}}(\tau)\,\mathbf{F}(\tau)\,\mathbf{F}^{\mathrm{p}-1}(\tau) - \mathbf{I}_2\right] . \tag{4.10}$$

Assuming that $\mathbf{L}^{\mathrm{p}}$ is constant over the time increment, time integration of the plastic

flow rule in Eq. 3.2 leads to

$$\mathbf{F}^{\mathrm{p}}(\tau) = exp\left[\Delta t \mathbf{L}^{\mathrm{p}}(\tau)\right] \mathbf{F}^{\mathrm{p}}(t) \ . \tag{4.11}$$

The time increments taken during the course of the deformation are typically small, allowing for the exponential in Eq. 4.11 to be approximated by a Taylor series to give

$$\mathbf{F}^{\mathrm{p}}(\tau) \doteq \left[\mathbf{I}_2 + \Delta t \mathbf{L}^{\mathrm{p}}(\tau)\right] \mathbf{F}^{\mathrm{p}}(t) \tag{4.12}$$

Inversion of Eq. 4.12 to the same level of accuracy with the substitution of the crystallographic slip rates for the plastic velocity gradient from Eq. 3.3 leads to

$$\mathbf{F}^{\mathrm{p}-1}(\tau) \doteq \mathbf{F}^{\mathrm{p}-1}(t) \left[\mathbf{I}_2 - \Delta t \sum_a \dot{\gamma}^a(\tau) \mathbf{S}_0^a\right] \tag{4.13}$$

where

$$\mathbf{S}_0^a \equiv \mathbf{m}_0^a \otimes \mathbf{n}_0^a \tag{4.14}$$

and

$$\dot{\gamma}^a(\tau) = \dot{\gamma}^a\left(\bar{\mathbf{T}}(\tau), \rho^{\varsigma}(\tau)\right) \ . \tag{4.15}$$

The crystallographic strain rates are also functions of the crystalline geometry, but for notational simplicity the geometry dependence is not explicitly included in this section. Substitution of Eq. 4.13 into Eq. 4.10 leads to the following relationship:

$$\bar{\mathbf{T}}(\tau) \doteq \bar{\mathbf{T}}^{tr} - \Delta t \sum_a \dot{\gamma}^a\left(\bar{\mathbf{T}}(\tau), \rho^{\varsigma}(\tau)\right) \mathbf{C}^a \ , \tag{4.16}$$

where

$$\bar{\mathbf{T}}^{tr} = \frac{1}{2}\mathcal{L}\left[\mathbf{B} - \mathbf{I}_2\right] \ , \tag{4.17}$$

$$\mathbf{B} = \mathbf{F}^{\mathrm{p}-\mathrm{T}}(t) \mathbf{F}^{\mathrm{T}}(\tau) \mathbf{F}(\tau) \mathbf{F}^{\mathrm{p}-1}(t) \ , \tag{4.18}$$

$$\mathbf{C}^a = \frac{1}{2}\mathcal{L}\left[\mathbf{K}^a\right] \ , \tag{4.19}$$

$$\mathbf{K}^a = \mathbf{B}\mathbf{S}_0^a + \mathbf{S}_0^{a\mathrm{T}}\mathbf{B} \ . \tag{4.20}$$

All of the quantities in Eq.'s 4.17-4.20 are known. In Eq. 4.16, the second Piola-Kirchhoff stress has been written as a function of itself and the crystallographic dislocation density at time τ.

The dislocation density at time τ can be written in the following form

$$\rho^{\xi}(\tau) = \rho^{\xi}(t) + \Delta t \dot{\rho}^{\xi}\left(\bar{\mathbf{T}}(\tau), \rho^{\zeta}(\tau)\right) \tag{4.21}$$

The time rate of change of the dislocation density is taken as constant over the time increment with the value at the the end of the increment. The portions of the dislocation density evolution equations that are considered here are the generation and annihilation contributions, but not the polar accumulation/loss contributions, and, similar to the crystallographic strain rates, the dislocation density time rate of change is also a function of the crystal geometry, although it is not explicitly included in the notation.

Equations 4.16 and 4.21 have $\bar{\mathbf{T}}(\tau)$ and $\rho^{\xi}(\tau)$ posed in such a way that they are functions of $\bar{\mathbf{T}}(\tau)$ and $\rho^{\xi}(\tau)$ and known quantities. Therefore, they can be iteratively solved to find solution at the next time increment. In strength-based crystal plasticity models, the crystallographic strengths are most often updated explicitly because they are found to change very little over the time increment. This allows for a large improvement of the computational performance of the analysis. In contrast, the dislocation density state variables grow exponentially and, therefore, must be included in the Newton iteration when solving for the state at time τ.

A column vector, $\mathbf{Z}$, is created by combining the second Piola-Kirchhoff stress tensor as a six-dimensional vector and the 18-dimensional crystallographic dislocation density vector in the following manner:

$$\mathbf{Z} = \begin{bmatrix} \bar{\mathrm{T}}_{11}(\tau) \\ \bar{\mathrm{T}}_{22}(\tau) \\ \bar{\mathrm{T}}_{33}(\tau) \\ \bar{\mathrm{T}}_{12}(\tau) \\ \bar{\mathrm{T}}_{23}(\tau) \\ \bar{\mathrm{T}}_{31}(\tau) \\ \rho_1(\tau) \\ \rho_2(\tau) \\ \vdots \\ \rho_{18}(\tau) \end{bmatrix} = \begin{bmatrix} \bar{\mathrm{T}}_1(\tau) \\ \bar{\mathrm{T}}_2(\tau) \\ \bar{\mathrm{T}}_3(\tau) \\ \bar{\mathrm{T}}_4(\tau) \\ \bar{\mathrm{T}}_5(\tau) \\ \bar{\mathrm{T}}_6(\tau) \\ \rho_1(\tau) \\ \rho_2(\tau) \\ \vdots \\ \rho_{18}(\tau) \end{bmatrix} . \tag{4.22}$$

The solution of the stress and dislocation density state after the nth iteration of the Newton method is given by

$$\mathbf{Z}_{n+1} = \mathbf{Z}_n - \mathcal{F}_n^{-1}\left[\mathbf{W}_n\right] , \tag{4.23}$$

where

$$\mathbf{W}_n = \begin{bmatrix} \bar{\mathbf{T}}_n(\tau) - \bar{\mathbf{T}}^{tr} + \Delta t \sum_a \dot{\gamma}^a \left(\bar{\mathbf{T}}_n(\tau), \rho_n^\zeta(\tau)\right) \mathbf{C}^a \\ \rho_n^\xi(\tau) - \rho^\xi(t) - \Delta t \dot{\rho}^\xi \left(\bar{\mathbf{T}}_n(\tau), \rho_n^\zeta(\tau)\right) \end{bmatrix} , \tag{4.24}$$

and

$$\mathcal{F} = \mathcal{I} + \Delta t \begin{bmatrix} \sum_a \mathbf{C}^a \otimes \frac{\partial \dot{\gamma}^a\left(\bar{\mathbf{T}}_n(\tau), \rho_n^\zeta(\tau)\right)}{\partial \bar{\mathbf{T}}_n(\tau)} & \sum_a \mathbf{C}^a \otimes \frac{\partial \dot{\gamma}^a\left(\bar{\mathbf{T}}_n(\tau), \rho_n^\zeta(\tau)\right)}{\partial \rho^\zeta(\tau)} \\ -\frac{\partial \dot{\rho}^\xi\left(\bar{\mathbf{T}}_n(\tau), \rho_n^\zeta(\tau)\right)}{\partial \bar{\mathbf{T}}_n(\tau)} & -\frac{\partial \dot{\rho}^\xi\left(\bar{\mathbf{T}}_n(\tau), \rho_n^\zeta(\tau)\right)}{\partial \rho_n^\zeta(\tau)} \end{bmatrix} , \tag{4.25}$$

where $\mathcal{I}$ is 24x24 square matrix with unity on the diagonal and zeros everywhere else. In Eq. 4.24, the $\mathbf{W}_n$ column vector has the same format as the $\mathbf{Z}$ vector, and in Eq. 4.25, the tensors $\bar{\mathbf{T}}_n$, $\bar{\mathbf{T}}^{tr}$, and $\mathbf{C}^a$ are written as column vectors also. The initial guess as to the stress and dislocation density state at time τ is done through

an explicit calculation where

$$\bar{\mathbf{T}}_{n=0}(\tau) = \bar{\mathbf{T}}(t) + \Delta t \dot{\bar{\mathbf{T}}}(t) \tag{4.26}$$

and

$$\rho^{\xi}_{n=0}(\tau) = \rho^{\xi}(t) + \Delta t \dot{\rho}^{\xi}(t) \ , \tag{4.27}$$

where $\dot{\bar{\mathbf{T}}}(t)$ is approximated by

$$\dot{\bar{\mathbf{T}}}(t) \doteq \frac{\bar{\mathbf{T}}(t) - \bar{\mathbf{T}}(t - \Delta t)}{\Delta t} \ ,$$

and

$$\dot{\rho}^{\xi}(t) = \dot{\rho}^{\xi}\left(\bar{\mathbf{T}}(t), \rho^{\zeta}(t)\right) \ .$$

After the iterative solution is found to within a small tolerance for the set of non-linear equations, the state is updated. The plastic deformation gradient at time τ is updated using Eq. 4.12, and the elastic deformation gradient is calculated by using Eq. 3.1 and inverting the plastic deformation gradient. Once the elastic deformation gradient at time τ is obtained, the Cauchy stress at time τ is calculated through Eq. 3.6, and the crystallographic orientations are updated through Eq. 3.4.

4.3.2 Calculation of the Material Jacobian

For small changes in the deformation gradient over the time increment, the relationship between $\mathbf{E}_t(\tau)$ and $\mathbf{U}_t(\tau)$ can be approximated by

$$\mathbf{E}_t(\tau) \doteq \mathbf{U}_t(\tau) - \mathbf{I}_2 \ . \tag{4.28}$$

Differentiating this equation, the following result is obtained

$$d\mathbf{E}_t(\tau) \doteq d\mathbf{U}_t(\tau) \ . \tag{4.29}$$

Therefore, the material jacobian can be approximated by

$$\mathcal{C} \doteq \frac{\partial \mathbf{T}\left(\tau\right)}{\partial \mathbf{U}_{t}\left(\tau\right)} \ . \tag{4.30}$$

For simplicity, indicial notation will be used to develop the equations associated with the derivation of the material jacobian. Inversion of Eq. 3.6 takes the form

$$\mathrm{T}_{ij} = \left[det\left(\mathbf{F}^{\mathrm{e}}\right)\right]^{-1}\left(\mathrm{F}^{\mathrm{e}}_{im}\bar{\mathrm{T}}_{mn}\mathrm{F}^{\mathrm{e}}_{jn}\right) \ . \tag{4.31}$$

Taking the partial derivative of the Cauchy stress with respect to the relative stretch tensor leads to

$$\begin{aligned}\frac{\partial \mathrm{T}_{ij}}{\partial \mathrm{U}_{t(kl)}} &= \left[det\left(\mathbf{F}^{\mathrm{e}}\right)\right]^{-1}\left[\mathcal{S}_{imkl}\bar{\mathrm{T}}_{mn}\mathrm{F}^{\mathrm{e}}_{jn} + \mathrm{F}^{\mathrm{e}}_{im}\mathcal{Q}_{mnkl}\mathrm{F}^{\mathrm{e}}_{jn}\right. \\ &\quad \left. + \mathrm{F}^{\mathrm{e}}_{im}\bar{\mathrm{T}}_{mn}\mathcal{S}_{jnkl} - \mathrm{F}^{\mathrm{e}}_{im}\bar{\mathrm{T}}_{mn}\mathrm{F}^{\mathrm{e}}_{jn}\left(\mathrm{F}^{\mathrm{e}-1}_{qp}\mathcal{S}_{pqkl}\right)\right] \ , \end{aligned} \tag{4.32}$$

where

$$\mathcal{S}_{ijkl} \equiv \frac{\partial \mathrm{F}^{\mathrm{e}}_{ij}}{\mathrm{U}_{t(kl)}} \ , \tag{4.33}$$

$$\mathcal{Q}_{ijkl} \equiv \frac{\partial \bar{\mathrm{T}}_{ij}}{\partial \mathrm{U}_{t(kl)}} \ . \tag{4.34}$$

From a combination of Eq.'s 3.1, 4.8, 4.9, and 4.13, the elastic deformation is approximated by the following expression

$$\mathrm{F}^{\mathrm{e}}_{ij}\left(\tau\right) \doteq \mathrm{R}_{t(ik)}\left(\tau\right)\mathrm{U}_{t(kl)}\left(\tau\right)\mathrm{F}^{\mathrm{e}}_{lm}\left(t\right)\left[\delta_{mj} - \sum_{a}\dot{\gamma}^{a}\left(\tau\right)\Delta t\mathrm{S}^{a}_{0(mj)}\right] \ . \tag{4.35}$$

Differentiation of Eq. 4.35 with respect to the relative stretch tensor yields

$$\begin{aligned}\mathcal{S}_{ijkl} &\doteq \mathrm{R}_{t(ik)}\left(\tau\right)\mathrm{F}^{\mathrm{e}}_{lj}\left(t\right) - \mathrm{R}_{t(ik)}\left(\tau\right)\mathrm{F}^{\mathrm{e}}_{lm}\left(t\right)\sum_{a}\dot{\gamma}^{a}\left(\tau\right)\Delta t\mathrm{S}^{a}_{0(mj)} \\ &\quad - \mathrm{R}_{t(in)}\left(\tau\right)\mathrm{U}_{t(np)}\left(\tau\right)\mathrm{F}^{\mathrm{e}}_{pm}\left(t\right)\sum_{a}\mathrm{J}^{a}_{kl}\Delta t\mathrm{S}^{a}_{0(mj)} \end{aligned} \tag{4.36}$$

where

$$\mathbf{J}^a \equiv \frac{\partial \dot{\gamma}^a(\tau)}{\partial \mathbf{U}_t(\tau)} \ . \tag{4.37}$$

The partial derivative of the second Piola-Kirchhoff stress with respect to the relative stretch tensor can be found by differentiating Eq. 4.16. The result that operation is

$$\mathcal{Q}_{ijkl} = \mathcal{D}_{ijkl} - \Delta t \sum_a \mathrm{C}^a_{ij} \mathrm{J}^a_{kl} - \Delta t \sum_a \dot{\gamma}^a \mathcal{J}^a_{ijkl} \ , \tag{4.38}$$

where

$$\mathcal{D}_{ijkl} = \frac{1}{2} \mathcal{L}_{ijmn} \mathcal{E}_{mnkl} \ , \tag{4.39}$$

$$\mathcal{J}_{ijkl} = \frac{1}{2} \mathcal{L}_{ijmn} \left[\mathcal{E}_{mpkl} \mathrm{S}^a_{0(pn)} + \mathcal{E}_{pnkl} \mathrm{S}^a_{0(pm)} \right] \tag{4.40}$$

with

$$\mathcal{E}_{ijkl} = \mathrm{F}^{\mathrm{e}}_{ki}(t) \, \mathrm{U}_{t(lm)} \mathrm{F}^{\mathrm{e}}_{mj}(t) + \mathrm{F}^{\mathrm{e}}_{mi}(t) \, \mathrm{U}_{t(mk)} \mathrm{F}^{\mathrm{e}}_{lj}(t) \ . \tag{4.41}$$

To complete the set of equations necessary to determine the material jacobian an analytical form for $\mathbf{J}^a$ must be found. The crystallographically resolved plastic strain rate is a function of the second Piola-Kirchhoff stress and the crystallographic dislocation density state; therefore, $\mathbf{J}^a$ can be written as

$$\mathrm{J}^a_{ij} = \frac{\partial \dot{\gamma}^a}{\partial \bar{\mathrm{T}}_{kl}} \frac{\partial \bar{\mathrm{T}}_{kl}}{\partial \mathrm{U}_{t(ij)}} + \frac{\partial \dot{\gamma}^a}{\partial \rho^\varsigma} \frac{\partial \rho^\varsigma}{\partial \mathrm{U}_{t(ij)}} \ . \tag{4.42}$$

By differentiating Eq. 4.21 it can be shown that

$$\frac{\partial \rho^\varsigma}{\partial \mathrm{U}_{t(ij)}} = \left[\delta^{\xi\varsigma} - \Delta t \frac{\partial \dot{\rho}^\xi}{\partial \rho^\varsigma} \right]^{-1} \frac{\partial \dot{\rho}^\xi \Delta t}{\partial \bar{\mathrm{T}}_{kl}} \frac{\partial \bar{\mathrm{T}}_{kl}}{\partial \mathrm{U}_{t(ij)}} \ . \tag{4.43}$$

Substitution into Eq. 4.42 yields

$$\mathrm{J}^a_{ij} = \mathrm{M}^a_{kl} \mathcal{Q}_{klij} \ , \tag{4.44}$$

where

$$\mathrm{M}^a_{kl} \equiv \frac{\partial \dot{\gamma}^a}{\partial \bar{\mathrm{T}}_{kl}} + \left[\delta^{\xi\zeta} - \Delta t \frac{\partial \dot{\rho}^\xi}{\partial \rho^\zeta}\right]^{-1} \frac{\partial \dot{\rho}^\xi \Delta t}{\partial \bar{\mathrm{T}}_{kl}} \,. \tag{4.45}$$

Substitution of this result into Eq. 4.38 and solving for $\mathcal{Q}_{ijkl}$ leads to the final expression

$$\mathcal{Q}_{ijkl} = \left[\delta_{im}\delta_{jn} + \Delta t \sum_a \mathrm{M}^a_{mn} \mathrm{C}^a_{ij}\right]^{-1} \left[\mathcal{D}_{mnkl} - \Delta t \sum_a \dot{\gamma}^a \mathcal{J}^a_{mnkl}\right] \,. \tag{4.46}$$

The analytical expression for the material jacobian is an approximate solution, but the level of error is the same as the level of error in calculating the Cauchy stress and the dislocation density state at time τ as a result of the Taylor expansions that were used to simplify the calculation. Note, the material jacobian derived here is non-symmetric, with $\mathcal{C}_{ijkl} \neq \mathcal{C}_{klij}$. The analytical jacobian is much faster to calculate than a jacobian calculated through perturbation techniques; furthermore, an accurate jacobian reduces the number of iterations that the implicit finite element algorithm must perform to obtain an equilibrium solution and provides a good prediction as to the deformation gradient at the next time step.

4.4 Selection of Material Constants

Along with the anisotropic elastic constants (Huntington, 1958) needed in Eq. 3.7, the constants introduced in the three constitutive functions for the dislocation mobility, average segment lengths, and capture radii contain the material-specific properties needed to model the evolution of the dislocation density state and stress/strain response for any loading history. The parameter space introduced by the constitutive functions is quite large, and able to provide a rich description of the material.

Most of the material constants may occupy only a limited range of values. Kocks et al. (1975) suggest that the activation energy ΔF should lie in the range

$$0.05 \leq \frac{\Delta F}{\mu b^3} \leq 2 \,. \tag{4.47}$$

Likewise, the exponents p and q also typically lie in the following ranges:

$$0 \leq p \leq 1 \ , \text{ and } 1 \leq q \leq 2 \ . \tag{4.48}$$

The strength interaction coefficients $G_0 - G_5$ are related to forest interactions and the amount that a dislocation line bows before it can cut through an obstacle; therefore, the interaction coefficients G_0, G_1, and $g_2 - g_5$ should all be less than unity. Furthermore, latent hardening experiments have shown that the out-of-plane interactions should be stronger than the in-plane interactions, and a strength interaction scale has been suggested by Franciosi and Zaoui (1982). The segment length interaction coefficients $H_0 - H_5$ should also have a limited range of numerical values related to the strength interaction coefficients. A general guideline is that $H_i \leq G_i$ for all interactions.

Using the rough guidelines, values of the strength and average segment length interaction coefficients were determined by considering the stress/strain response and deformation stability for different crystallographic orientations. Single slip was investigated using the $< 123 >$ orientation. The description "$< 123 >$ orientation" of a crystal in this context means that the $< 123 >$ crystallographic direction was parallel to the tensile axis. In this orientation, only one slip-system was highly active, and the value of the G_0-coefficient could be determined because it dominated the stress/strain behavior. Likewise, the poly-slip orientations considered($< 111 >$, $< 100 >$, and $< 112 >$) were also used to determine values of the coefficients, although their analysis was more complex. With more than one slip-system potentially active during the deformation, sub-matrices including only the active systems could be constructed, and the influence of the different interaction coefficients could be probed by considering the stability of deformation modes to orientation perturbations, as well as the appearance of certain coefficients in some the sub-matrices but not others. For slight misalignments with the tensile axis, all six of the potentially active slip-systems in the $< 111 >$ orientation are observed to contribute to the plastic deformation, while only four of the eight potentially active slips systems in the

misaligned $< 100 >$ orientation are observed to contribute to the plastic deformations. The interaction coefficient associated with the Hirth-lock, G_4, appears in the sub-matrix of active systems for the $< 100 >$ orientation, but not in the sub-matrix for the $< 111 >$ orientations. Taking advantage of such differences in the plastic deformation observed for different orientations, the importance of certain interaction interaction coefficients in some orientations (but not in others), and the stability of deformations modes to misorientations provides a methodology of determining representative values for the model parameters. The values of the strength interaction coefficients and the average segment length coefficients may be found in Table 4.6.2.

To decrease further the parameter space, edge and screw densities were given the same mobility. In the mobility functions, the values of the activation energy, ΔF, and the exponents which control the stress dependence, p and q, were taken from Balasubramanian and Anand (2000), in which the values were determined by considering the temperature-dependence of the rate-dependent yield strength of polycrystalline aluminum. The remaining coefficients were determined by fitting the orientation-dependent stress/strain data of aluminum single crystals at room temperature and by maintaining dislocation densities of the same magnitude as observed in experiments. The remaining values of all the constants used to capture the mechanical properties of aluminum may be found in Table 4.3.

4.5 Simulation Geometry, Boundary Conditions, and Initial State Conditions

The model will be used to simulate single crystal tension experiments conducted by Kocks (1959) and by Hosford et al. (1960). The four crystallographic orientations mentioned in the previous section will be investigated: $< 111 >$, $< 100 >$, $< 112 >$, and $< 123 >$. Both experimental investigations detail the many aspects of the tests that will be included in the simulation geometry, boundary conditions, and initial material state. In the deformation of single crystals, the geometry, boundary conditions,

and initial state are critical in determining the plastic evolution of crystal. Individual crystals in a polycrystalline material are constrained by their neighboring grains, and the anisotropic behavior of each crystal is countered by the anisotropic behavior of its neighbor leading to a more homogeneous deformation mode than observed in single crystals. The ability of the Taylor models to capture the texture evolution of polycrystals is a result of this quasi-homogeneous deformation in polycrystals (Bronkhorst et al., 1992). Due to the strong anisotropy in single crystals, and the unconstrained free surfaces, the details are very important in defining the simulation.

In their experiments, the investigators used similar specimen geometries and boundary conditions, and in this theoretical investigation, the geometry and boundary conditions will closely follow from the experimental conditions documented. The simulation geometry used was square cylinder where the length of the cylinder parallel to the loading direction was nine times greater than the cross-sectional width. The geometry was discretized into 72 first-order brick (C3D8) elements as shown in Figure 4-1, leading to 576 materials points.

The simulation boundary conditions were set to model a finite crystal in tension. The normal direction of the top and bottom surface was fixed to remain parallel to the tensile axis. The top and bottom surfaces were also fixed so that they were unable to rotate relative to one another about the tensile axis, but the surfaces were able to contract in cross-sectional area. The lateral surfaces with normal directions that were initially perpendicular to the tensile axis were left traction-free. Lastly, the whole geometry was required, on average, to remain aligned with the pulling direction. Similar boundary conditions were used in the experimental investigations by using grips on the specimens were not free to rotate during the tests. A specimen-average true tensile strain rate of 10^{-3} s^{-1} was applied to the geometry for 100 s to ultimately reach a 10% strain level in each of the four orientations.

The initial material state conditions that had to be specified were the initial crystallographic orientations, the initial dislocation density state of the material, and temperature. In their experiments, Kocks (1959) and Hosford et al. (1960) both document slight misalignments (within 2°) of the samples with the nominal orientations

tested. The exact orientation of the test crystals was not documented. For reasons that will be discussed in the next section, the initial misalignment of the crystal with the tensile axis has a pronounced effect on the deformation history of single crystals, especially for orientations in which two or more slip-systems are potentially active. A one degree misalignment was included for the three orientations that had more than one equally favored slip-system as an attempt to simulate the real initial condition of the experiments. The exact orientations were chosen so that there was a large difference in the initial Schmid factors on the highly-stressed slip-planes. The Euler angles used to simulate the four nominal orientations may be found in Table 4.4. The three Euler angles θ, ϕ, and ω are used to create a second-order rotation tensor $\mathbf{Q}$ that relates the crystal basis vectors to the global reference frame according to

$$\mathbf{e}_i^{global} = \mathbf{Q}\mathbf{e}_i^{crystal} \,, \tag{4.49}$$

and

$$\mathbf{Q} = \begin{bmatrix} \cos\phi\cos\omega - \sin\phi\sin\omega\cos\theta & \sin\phi\cos\omega - \cos\phi\sin\omega\cos\theta & \sin\omega\sin\theta \\ -\cos\phi\sin\omega - \sin\phi\cos\omega\cos\theta & -\sin\phi\sin\omega + \cos\phi\cos\omega\cos\theta & \cos\omega\sin\theta \\ \sin\phi\sin\theta & -\cos\phi\sin\theta & \cos\theta \end{bmatrix} . \tag{4.50}$$

The initial crystallographic dislocation density was distributed equally among the edge and screw dislocation densities so that half of the density was initially of edge character, and the other half was initially of screw character. The initial dislocation density was set to 4.16×10^{10} m^{-2} for each crystallographic edge dislocation density and 8.33×10^{10} m^{-2} for each crystallographic screw dislocation density, such that the total initial density was $\rho_0 = 1 \times 10^{12}$ m^{-2} ($\rho_0 b^2 = 8.2 \times 10^{-8}$). Although the dislocation density state was not documented in the experiments conducted by the investigators cited earlier, the level of density chosen corresponds to a typical density found in annealed crystals (Basinski and Basinski, 1979). The simulations were conducted at room temperature (298 K), and isothermal conditions were assumed during the deformation history.

4.6 Results and Discussion

4.6.1 Summary of Experimental Observations

In three of the orientations considered, two or more slip-systems are equally stressed if the crystal is perfectly aligned with the tensile axis. The $< 111 >$ orientation has six equally favored slip-systems, while the $< 100 >$ has eight equally-stressed systems. The $< 112 >$ orientation has only two highly-stressed slip-systems. The $< 123 >$ orientation has one highly-stressed slip-system. The orientations of the specimens in the reported experiments deviated from the ideal orientation by no more than two degrees (Kocks, 1959; Hosford et al., 1960); however, the symmetry of the slip-systems with the tensile axis was broken, leading to variations in the resolved stresses on the potentially active slip-systems.

From x-ray and slip-trace analysis, as well as observations of the macroscopic deformation of the tensile specimens, even slight crystallographic misalignment has a pronounced effect on the deformation mode of the oriented crystals. The $< 111 >$-oriented crystals are observed to deform uniformly by activating all six slip-systems, thus maintaining the orientation of the $< 111 >$ direction substantially parallel to the tensile axis. The $< 100 >$ orientation, which has eight potentially active slip-systems, follows a more complicated deformation path. Initially, all eight slip-systems are active, but after a small amount of plastic strain ($\epsilon \approx 0.01$), the specimens are observed to transition from an isotropic deformation to a plane strain deformation, with the predominant crystallographic slip occurring on two pairs of the cross-slip systems. The $< 100 >$ direction maintains its alignment with the tensile axis during the deformation; however, during the plane strain deformation mode, there is significant asterism in the $< 100 >$ pole that is not observed during the initial isotropic deformation of the crystal. The $< 112 >$-oriented crystals are observed to deform plastically in a single-slip mode with secondary slip on the other highly stressed slip-system. The dislocations created during the deformation of $< 112 >$-oriented crystals are known to form Lomer-Cottrell locks, widely considered as the strongest dislocation junctions in FCC crystals; as a result, the $< 112 >$-oriented crystals are observed to have the

greatest plastic resistance among crystal orientations which primarily undergo single slip.

The stress/strain response of the different orientations is most effectively characterized by comparing the responses to the behaviors observed in copper, the most widely tested and simulated FCC crystal. Figure 4-2 depicts the stress/strain behavior of aluminum single crystals as determined by Kocks (1959) and Hosford et al. (1960), while Figure 4-3 depicts the stress/strain behavior of single crystal copper specimens as determined by Takeuchi (1975). The experimental data is compared most effectively if the stress levels measured for the different crystals are normalized by their shear moduli. Both crystals have anisotropic elastic behavior; therefore, a scalar shear modulus is calculated for each crystal by calculating the shear modulus resolved on the slip-planes. The calculation takes the form:

$$\mu = \frac{1}{3}\left(C_{11} - C_{12} + C_{44}\right) \ , \tag{4.51}$$

where C_{11}, C_{12}, and C_{44} are the anisotropic elastic constants with respect to the FCC unit cell, leading to $\mu_{Al} = 25$ GPa and $\mu_{Cu} = 37$ GPa. The normalized stress/strain curves determined from the experimental data for both crystals can be found in Figure 4-4.

As in copper, the $< 111 >$ orientation of aluminum has the highest initial hardening rate and reaches the highest stress levels. The curvature of the stress/strain curve in aluminum is much greater, and the saturation level of stress is reached at lower plastic strains, as compared to copper loaded in the same orientation. The $< 100 >$ orientations of the two crystals have drastically different behaviors. Both aluminum and copper initially have high rates of hardening for small plastic strains. Copper crystals continue along that path and ultimately reach stress levels that are roughly half that of the stress levels reached for the $< 111 >$-oriented crystals. The $< 100 >$-oriented aluminum behaves quite differently. As the material transitions from the isotropic deformation mode to the plane strain deformation mode, the hardening rate transitions from the initial high slope to a very low hardening slope, and

the final stress levels reached are between one-fourth and one-third of the stress levels reached by the $< 111 >$-oriented aluminum crystals. The $< 112 >$ and $< 123 >$ orientations that predominately deform by activating a single slip-system also exhibit different behavior for the two materials. Both crystals initially have a period of Stage I hardening with low hardening rates. Copper crystals transition to Stage II hardening with a high linear hardening rate, and then come to Stage III hardening behavior with falling hardening rates as the rate of dislocation density accumulation begins to fall. The aluminum crystals transition from Stage I directly to Stage III behavior at earlier strain levels than copper, without the appearance of the high linear hardening found in Stage II.

The stress/strain evolution in single crystals has been shown to be very sensitive to the accuracy of the initial orientation, especially for orientations in which two or more systems are equally favored (Davis et al., 1957). Likewise, the exact orientations, with the 1° misalignments, used in the simulations are most likely not the same as in the experiments, but there should be reasonable agreement in the deformation modes observed in the experiments and simulations. The constants in the model were set to approximate closely the stress/strain curves documented in experiments so as to understand the underlying processes and dislocation evolution responsible for the mechanical behavior of the crystal.

4.6.2 Comparison of Simulations and Experiments

The results of the simulations are shown in Figure 4-2, along with the experimentally determined values of the stress/strain behavior for the different orientations. The simulations reasonably capture the stress/strain relationships for the four different orientations considered. Along with the stress/strain profile for each orientation, the evolving dislocation density profile may also be investigated. First, gross measures of the state will be considered, such as the total level of dislocation density and the character, edge or screw, of the whole density during the deformation, then a more detailed analysis of the dislocation structure will be conducted of the two orientations that have the most potentially-active slip-systems. The dislocation profile will be

investigated at a material point in the center of the specimen geometry, away from the constrained ends, because experimental investigators typically look at the center when conducting microscopy of deformed materials.

Consider Figure 4-5 that shows the total dislocation density, defined as the sum of all the crystallographic densities in the material, during the deformation of the material. The dislocation density appears to grow linearly with plastic strain, although the slope is different for each orientation. In experiments this linear relationship is often observed, and it has led to phenomenological expressions of density evolution as linear functions of plastic strain rates (Cuitiño and Ortiz, 1992). The crystal orientation with the most total density ($< 111 >$) is also the strongest, and the crystal orientation with the least density ($< 123 >$) is the also the weakest. Consider Figure 4-6 that shows the ratio of edge dislocation density to the total dislocation density of the crystal. This is a gross measure of the total character of the underlying dislocation state of the material. Initially all of the orientations start out with a ratio of one half as set by the initial conditions of the simulations. The orientations that deform by activating multiple slip-systems ($< 111 >$ and $< 100 >$) reach steady-state ratios around 0.75. The single-slip orientation ($< 123 >$) has a much higher concentration of edge dislocations relative to screw dislocations, showing a ratio of 0.97. In single crystal tension experiments, researchers looking at dislocation microstructures associated with single slip have commented that the dislocation density observed is composed almost completely of edge dislocations (Argon, 1969), as predicted by the simulation. The $< 112 >$ orientation shows a transition behavior. The crystal initially follows the path of the single-slip behavior: then, at 6% strain it undergoes a transition, and the ratio of edge dislocation density to screw dislocation density appears more in line with the orientations that activate multiple slip-systems.

Dislocation models have been proposed that characterize only one scalar density for each slip system (Cuitiño and Ortiz, 1992). A simple distribution of density as a function of in-plane tangent direction is assumed, and effective piercing densities are calculated using that distribution so that the dislocation density resistance may be calculated using an interaction matrix similar to the form adopted in Eq. 4.4.

The results of the current simulations suggest that such an assumption may not accurately describe the density evolution in plastically deforming crystals and that the dislocation density distribution may depend on the mode of plastic deformation.

The sensitivity of the initial misorientation for the crystals with multiple slip-system activation was investigated for the $< 111 >$, $< 100 >$, and $< 112 >$ orientations. The results are shown in Figures 4-7, 4-8, and 4-9, respectively, for orientations ranging from a perfectly-oriented crystal to orientations with a maximum of 2^{o} misalignment. The perfectly-oriented $< 111 >$ simulation traces the experimental data, and for misorientations of one degree or less, the agreement is quite good. The perfectly-oriented $< 100 >$ simulation deviates from the experimental data of aluminum, and qualitatively resembles the behavior of single crystal copper in the same orientation. The $< 100 >$ simulation with 0.5^{o} misorientation closely resembles the behavior of the perfect orientation, but the crystals with misorientations of 1^{o} and 1.5^{o} exhibit different behavior and transition to a lower hardening behavior after starting out on the same initial slope as the perfectly-oriented simulation. At 2^{o} off-axis, both orientations of the crystal experience some degree of single slip. The alignment appears to be less critical in the nominally $< 112 >$-oriented crystal. Except for the perfectly-aligned crystal, there is little variation in the stress/strain behavior of the misoriented crystals with increasing misalignment as compared to the other two orientations.

The deformation modes observed in the experiments are also captured by the simulations. The deformation modes in the $< 111 >$- and $< 100 >$-oriented crystals are the most interesting to compare and contrast because they have the most potentially active slip-systems. The shear rates on the active slip-systems during the history of the deformation of the $< 111 >$- and $< 100 >$-oriented crystals are given in Figures 4-10 and 4-11, respectively. In the figures, the Schmid and Boas notation is used for the twelve slip-systems where the letters A, B, C, and D denote the $(1\bar{1}\bar{1})$, (111), $(\bar{1}\bar{1}1)$, and $(\bar{1}1\bar{1})$ slip planes, respectively; and the numbers 1, 2, 3, 4, 5, and 6 denote the Burgers vectors $[011]$, $[0\bar{1}1]$, $[101]$, $[10\bar{1}]$, $[110]$, and $[\bar{1}10]$, respectively. The initial misorientation in each crystal breaks the symmetry of the potentially active

slip-systems with the tensile axis. In the case of the < 111 >-oriented crystal, the deformation is able to maintain activity on all six slip-systems, and converges toward the symmetric activation on all slip-systems after initially diverging. In the < 111 > orientation, the arrangement of the active slip-systems relative to the tensile axis promotes the symmetric activation of all slip-systems. A non-symmetric deformation mode causes lattice rotation that increases the Schmid factors on the less-active systems and decreases the Schmid factors on the highly-active systems, thus stabilizing the deformation mode. The < 100 >-oriented crystal shows a significantly different behavior. At the start of the deformation history, all eight potentially-active systems contribute to the plastic deformation, but the deformation mode quickly diverges from one in which all eight are active, to one where four of the slip-systems account for the majority of the plastic deformation. The four systems consist of two pairs of slip-systems in which the screw dislocations may cross-slip. As a result, the macroscopic deformation appears isotropic in the early stages, and ends in plane strain after a small amount of tensile elongation. The symmetric activation of the two cross-slip pairs does not cause any lattice rotation of the crystal. The asterism of the pole that is observed in the experiments is due to non-homogeneous deformation on a length scale smaller than the length scale of observation. The cross-slip pairs are not equally active locally, and activation of a single cross-slip pair leads to the deviations in the pole figure that are experimentally observed.

The differences in the dislocation density evolution between the < 111 > and < 100 > orientations detail the misorientation dependence of the stress/strain evolution. The history of the crystallographic dislocation density evolution mirrors the strain-rate history of the crystals. Consider Figures 4-12 and 4-13 that show the accumulation of crystallographic dislocation density during deformation for the < 111 >- and < 100 >-oriented crystals, respectively. The crystallographic dislocation density evolution in the < 111 >-oriented crystal also shows that the dislocation density, which initially diverges due to the crystal misalignment, converges at larger strains toward two values: one for the edge densities, and another for the screw densities. The crystallographic dislocation density evolution in the < 100 >-oriented crystal

significantly differs from that of the < 111 >-oriented crystal. In Figure 4-13, the dislocation density plotted on a log scale shows that the greatest change in the dislocation density occurs in the first few percent of tensile strain, and during the deformation, the dislocation density roughly spans four orders of magnitude. Whereas in the < 111 > orientation, the distribution of dislocation density was converging, the dislocation density in this orientation diverges. The most abundant crystallographic densities are found in the four slip planes that accomplish the majority of the deformation in the plane strain mode described.

Since both the edge and screw dislocation densities are calculated for each slip-system, the general character of the dislocation density can be evaluated. Figure 4-14 and Figure 4-15 show the evolving character of the active dislocation densities during deformation of the < 111 >- and < 100 >-oriented crystals, respectively. The initial condition was set so that half of the initial population was split evenly between edge and screw densities. As the deformation progressed, the edge dislocation densities became roughly three and a half times greater than the screw density with the same Burgers vector. The character in this simulation is a product of the difference in the capture radii of the edge and screw dislocations; however, there are also other methods within the framework to model the character of the evolving density. By manipulating the ratio between the reference velocities, $\bar{v}_0$, in the edge and screw mobility equations, the character of the dislocation density can also be controlled. From the dislocation evolution equations found in Eq.'s 3.12, 3.13, 3.19, and 3.20, it is evident that as the mobility ratio changes, the relative density of the slower species will increase; and as the ratio between the capture radii changes, the relative density of the species with the larger capture radius will decrease. The result is robust and independent of the dislocation density profile set as the initial conditions of the simulation. A more detailed analysis of the influence of different material parameters on the stress/strain behavior and dislocation evolution may be found in Appendix A.

The magnitude of the dislocation density, along with its character, translates into the crystallographic strength of the crystal. Figure 4-16 and Figure 4-17 show the resistance to dislocation motion on the potentially active slip-systems for the < 111 >-

and $< 100 >$-oriented crystals, respectively. The six resistances in the $< 111 >$ orientation increase in a stable manner, just as do the dislocation densities. Initially, the tensile stress and the crystallographic resistances are close in magnitude, while at ten percent elongation, the crystallographic resistances are roughly four and a half times the tensile stress. At ten percent strain, the crystallographic strengths of the crystal are still increasing, while the stress appears to be reaching a saturation level. The separation occurs because as the dislocation density increases, the same plastic strain rates may be attained with lower average velocities as shown in Figure 4-18, enabling the ratio of the applied stress to the crystallographic strength to decrease with increasing density, as shown in Figure 4-19.

The history of the crystallographic strengths in the $< 100 >$ orientation shown in Figure 4-17 again reflects the bifurcation (rapid evolution of a symmetry-breaking initial imperfection) discussed earlier. The weakest systems are those with the most in-plane density, and the systems with the highest strengths are those that become inactive and have the lowest densities. Furthermore, the spread in the strengths also demonstrates the strong off-diagonal dominance of the strength-interaction matrix associated with forest interactions.

The orientation-dependent behavior of single crystal aluminum is quite different from the behavior observed in copper, as discussed earlier. The dislocation density model yields some insight into the underlying reasons for the different behaviors. The ability of screw dislocations in aluminum to cross-slip readily, in contrast to the inability of those in copper to do so, is one major factors in the difference. In the model, the ability of the screw density to cross-slip led to the use of a large capture radius for the screw dislocations in annihilation. The large capture radius in turn led to a high curvature in the $< 111 >$ stress/strain curve, and to the disappearance of Stage II hardening in the $< 112 >$ and $< 123 >$ orientations. The dynamic recovery of dislocation density occurs at much lower density levels in aluminum than in copper. The differences in the behavior of the $< 100 >$-oriented crystals is a much more complicated story.

As misorientations are applied to a nominally $< 100 >$-oriented crystal, the tran-

sition from the activation of eight slip-systems as found in copper to the activation of four slip-systems in aluminum, depends not only on the ability of screw dislocations to cross-slip, but also on the relative weakness of the Hirth lock as compared to the other out-of-plane dislocation interactions. The eight potentially active slip-systems in the $< 100 >$ test appear as four pairs of cross-slip systems. As the misorientation is applied, one of the slip-systems in each cross-slip pair has the higher Schmid factor, while the other of the pair has one of the lower Schmid factors of the eight active systems. As demonstrated earlier, the most active systems show larger dislocation densities. The ability of the screw dislocations to cross-slip, however, increases the mobile density on the system with the lower Schmid factor and promotes the increase of edge dislocations on the other slip-system. Examination of the dislocation density evolution in Figure 4-13 shows this mechanism. The edge dislocation density on the two slip systems with the lower initial Schmid factors is lower than the corresponding screw dislocation density; but as the deformation proceeds, the edge density on these systems eventually exceeds their screw dislocation density, and ultimately it approaches the value of the edge dislocation density on the systems with the higher initial Schmid factors. The transition from the activation of all eight slip-systems to four slip-systems, which is aided by the ability of the screw dislocations to cross-slip, would not be possible if not for the relative weakness of the strength interaction coefficient, g_4, associated with the Hirth lock compared to the other out-of-plane strength interactions: g_2, g_3, and g_5. The forest interactions led to an off-diagonal dominance in the strength interaction matrix $G^{\xi\zeta}$. The weakness of the Hirth lock interaction coefficient enables the plane strain deformation mode to have a lower hardening rate than in the isotropic deformation case. It is not clear how such physical understanding could be incorporated into a phenomenological form that could be used in association with the strength-based internal state variable models of continuum crystal plasticity.

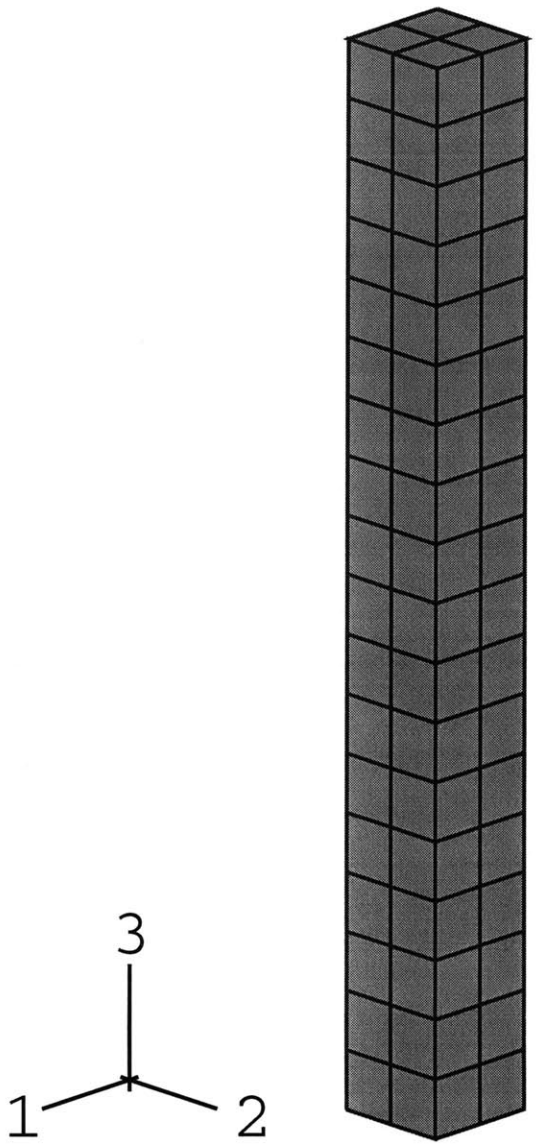

Figure 4-1: The specimen geometry used to simulate the anisotropic plastic deformation of Aluminum single crystals in tension.

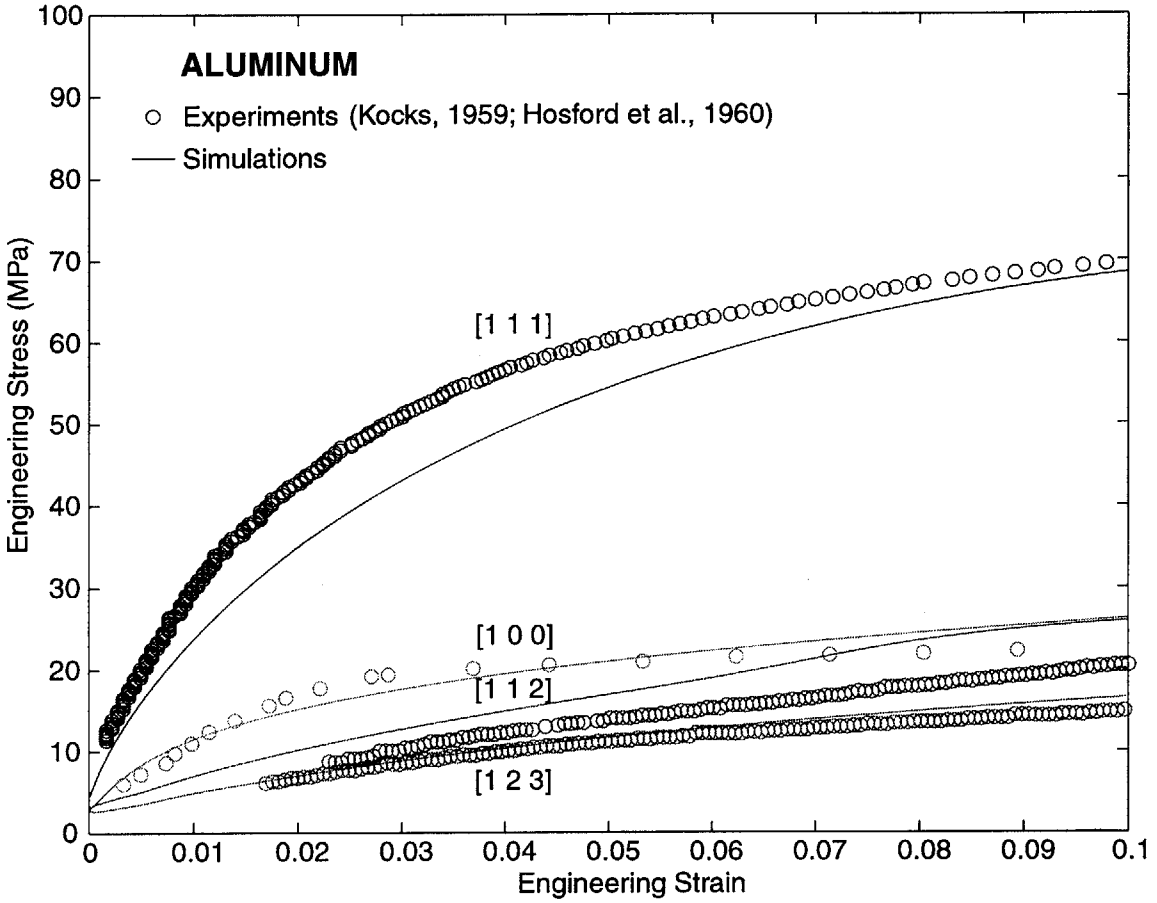

Figure 4-2: Comparison of the orientation dependence of the stress/strain response of single crystal aluminum observed during tensile experiments and calculated by finite element simulations.

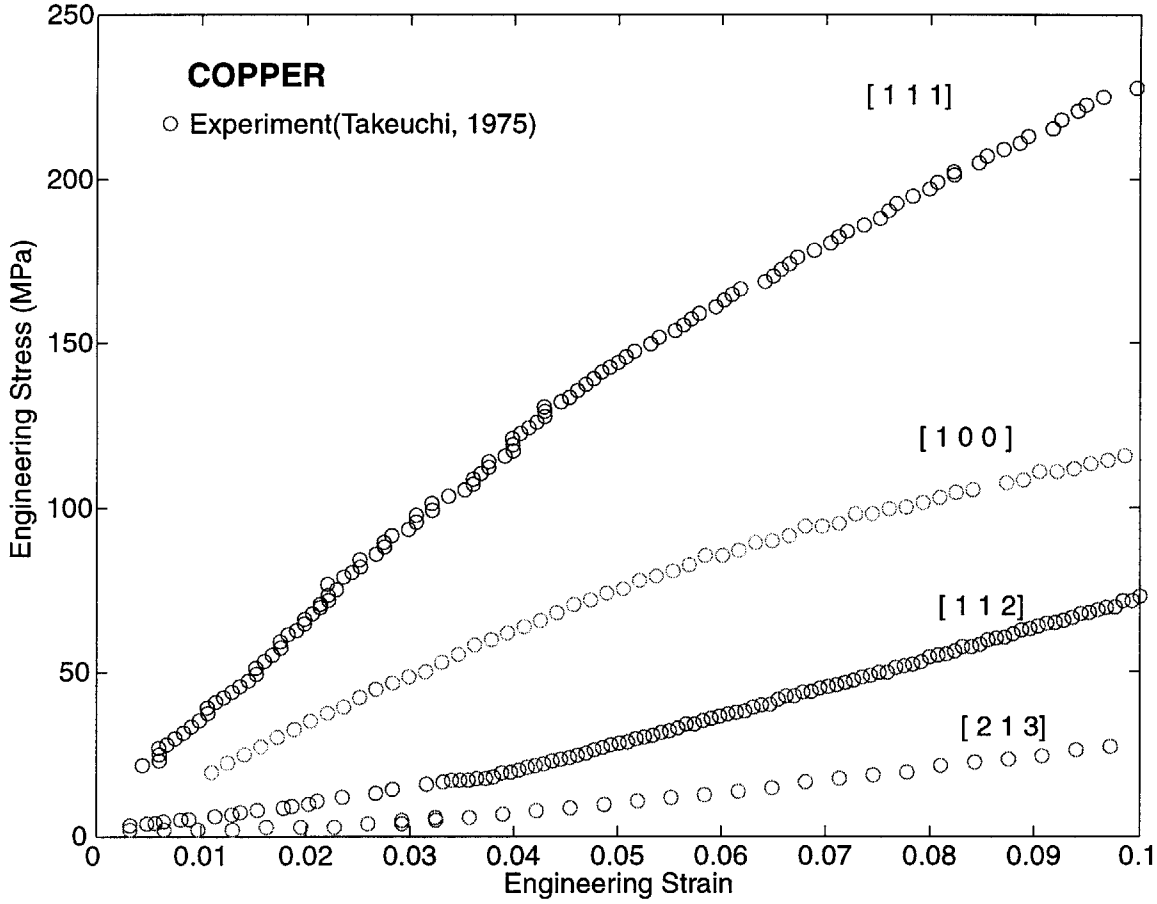

Figure 4-3: The stress/strain response of copper single crystals during simple tension for different orientations relative to the tensile axis.

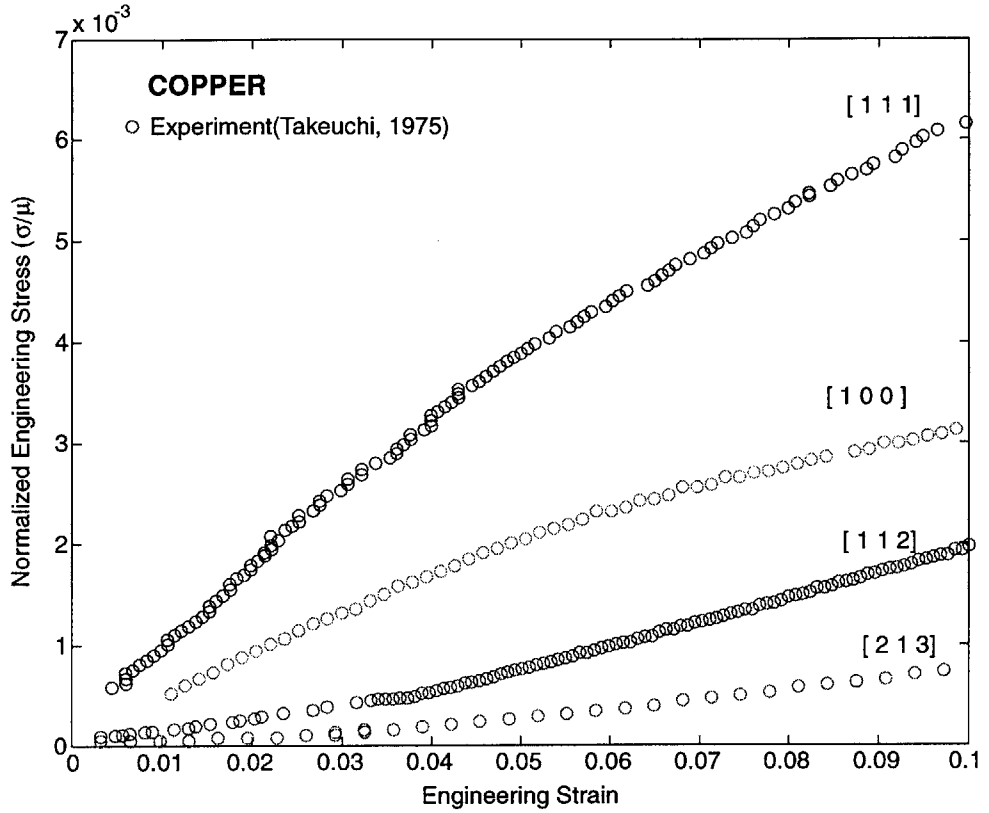

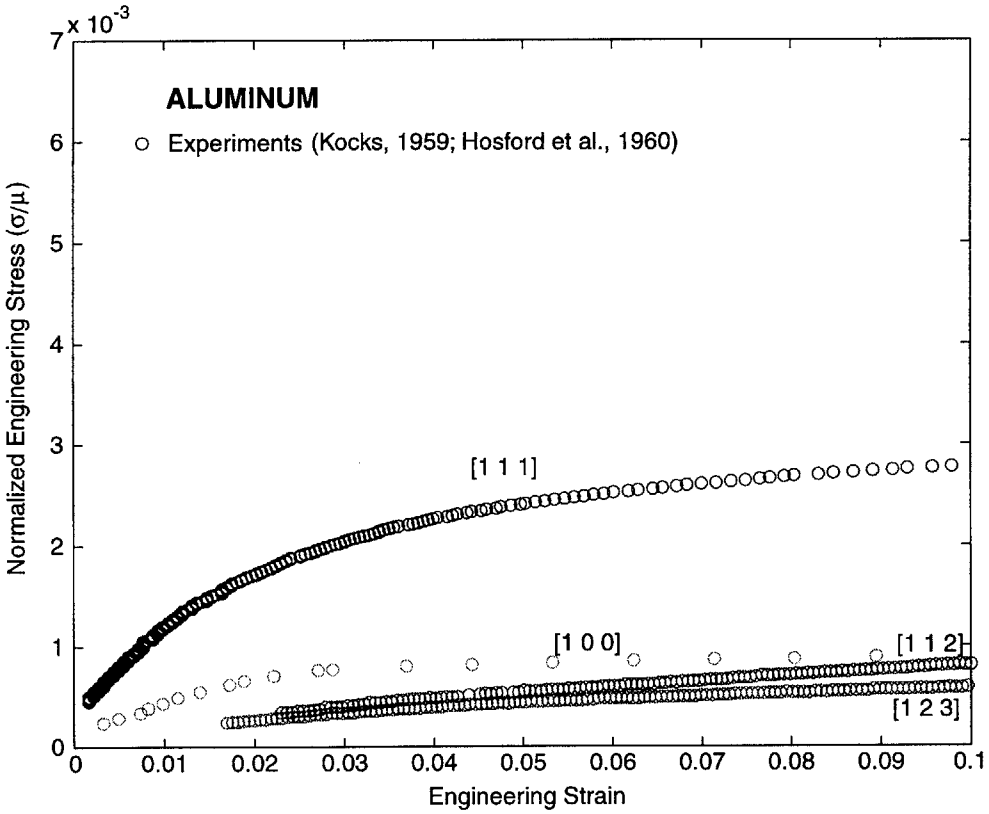

Figure 4-4: The experimentally-determined stress/strain response of copper and aluminum single crystals normalized by the shear modulus of each crystal.

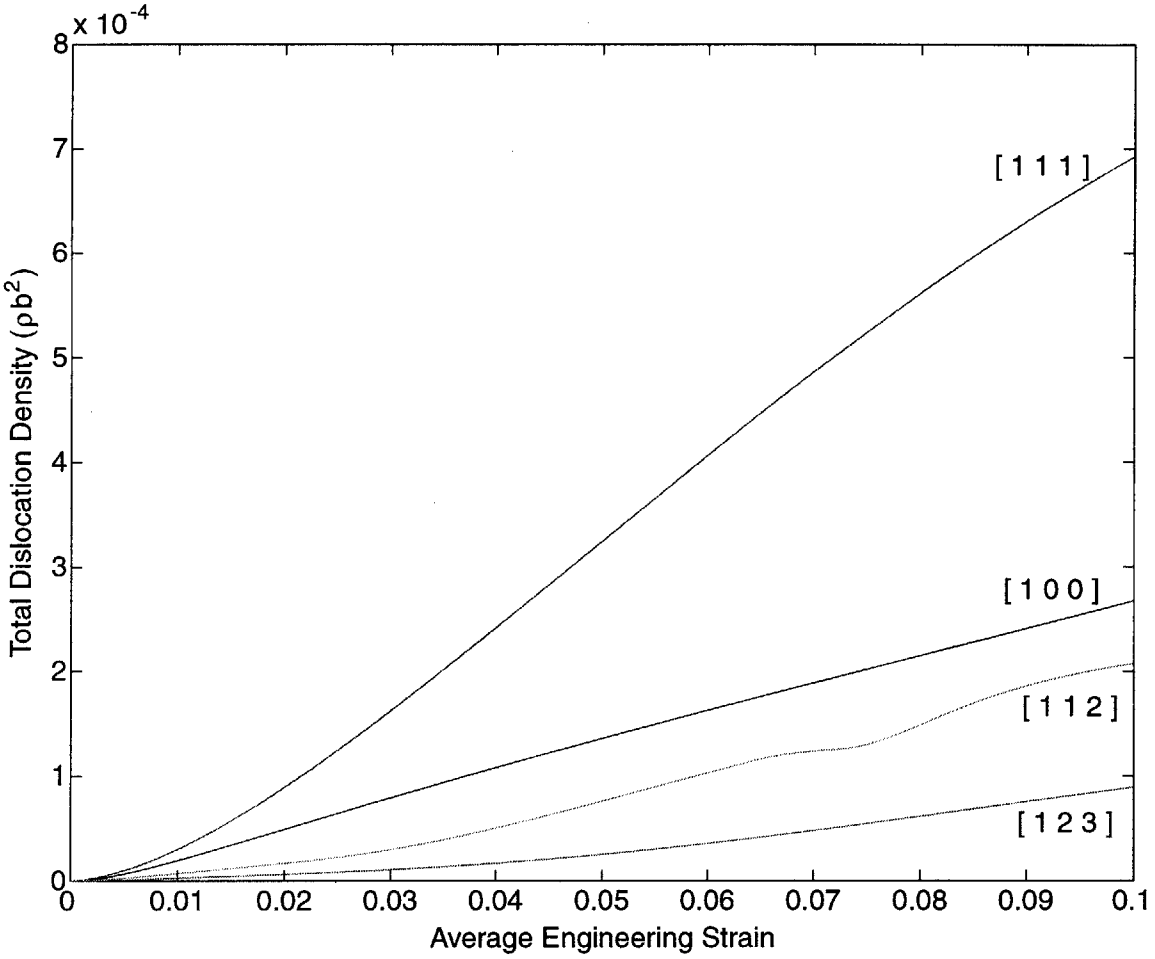

Figure 4-5: Total crystallographic dislocation density evolution during plastic deformation for the four orientations considered.

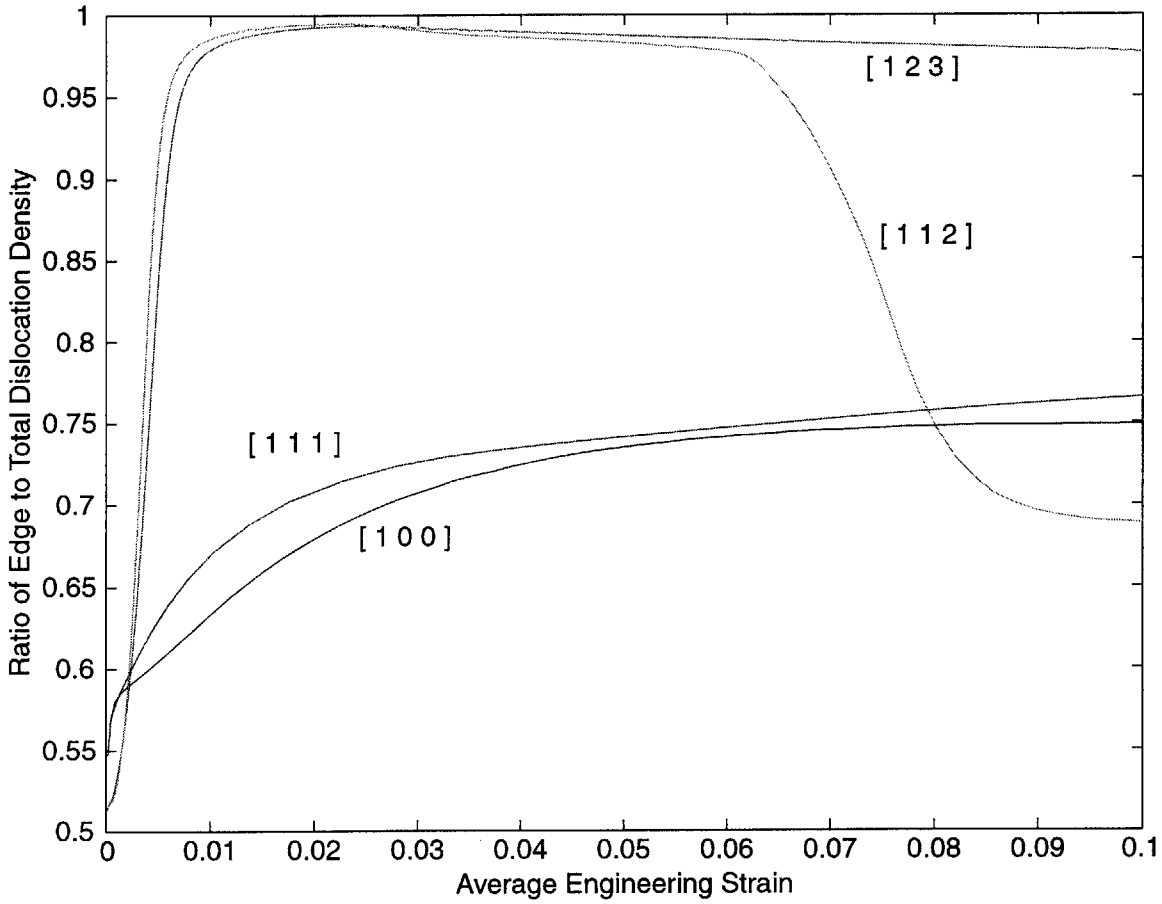

Figure 4-6: Ratio of edge dislocation density to total dislocation density during the plastic deformation for the four orientations considered.

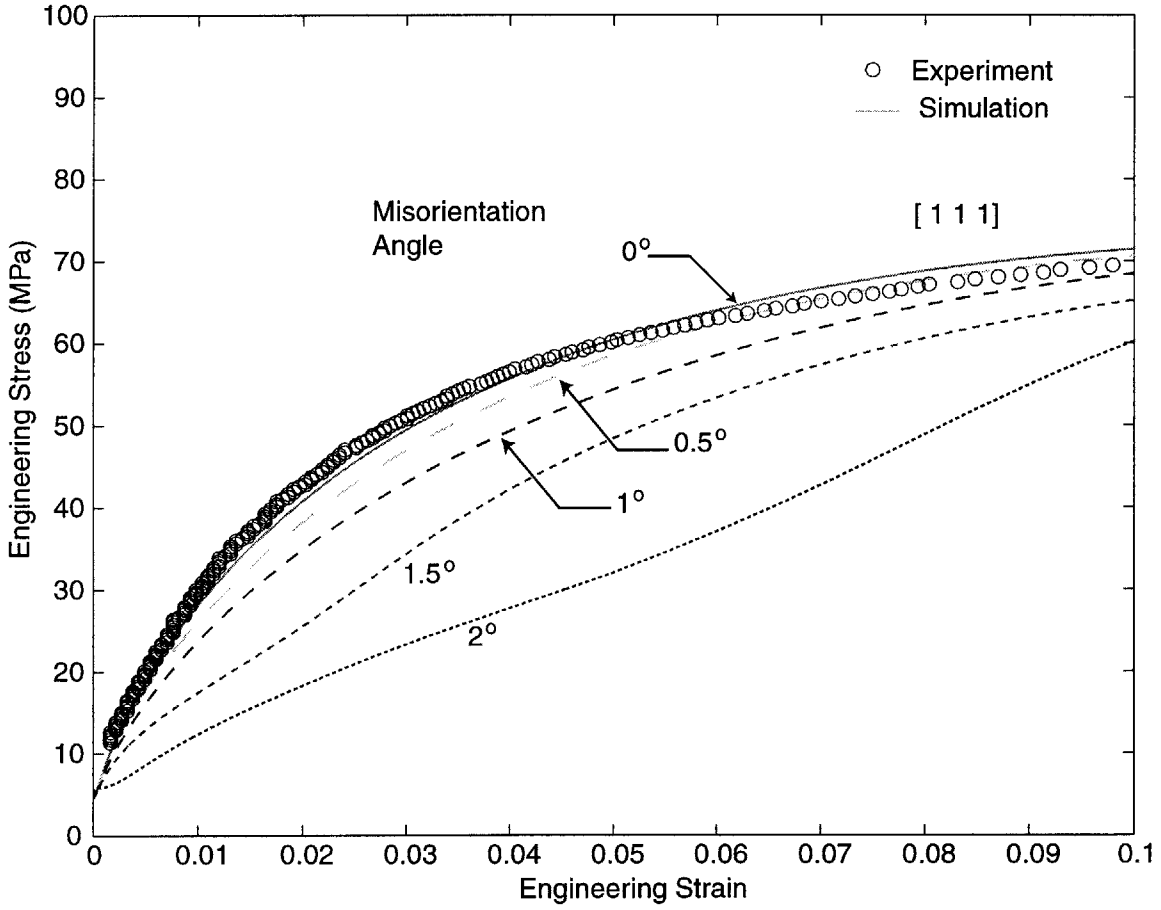

Figure 4-7: Effect of initial misorientation on the stress/strain of a nominally < 111 >-oriented single crystal.

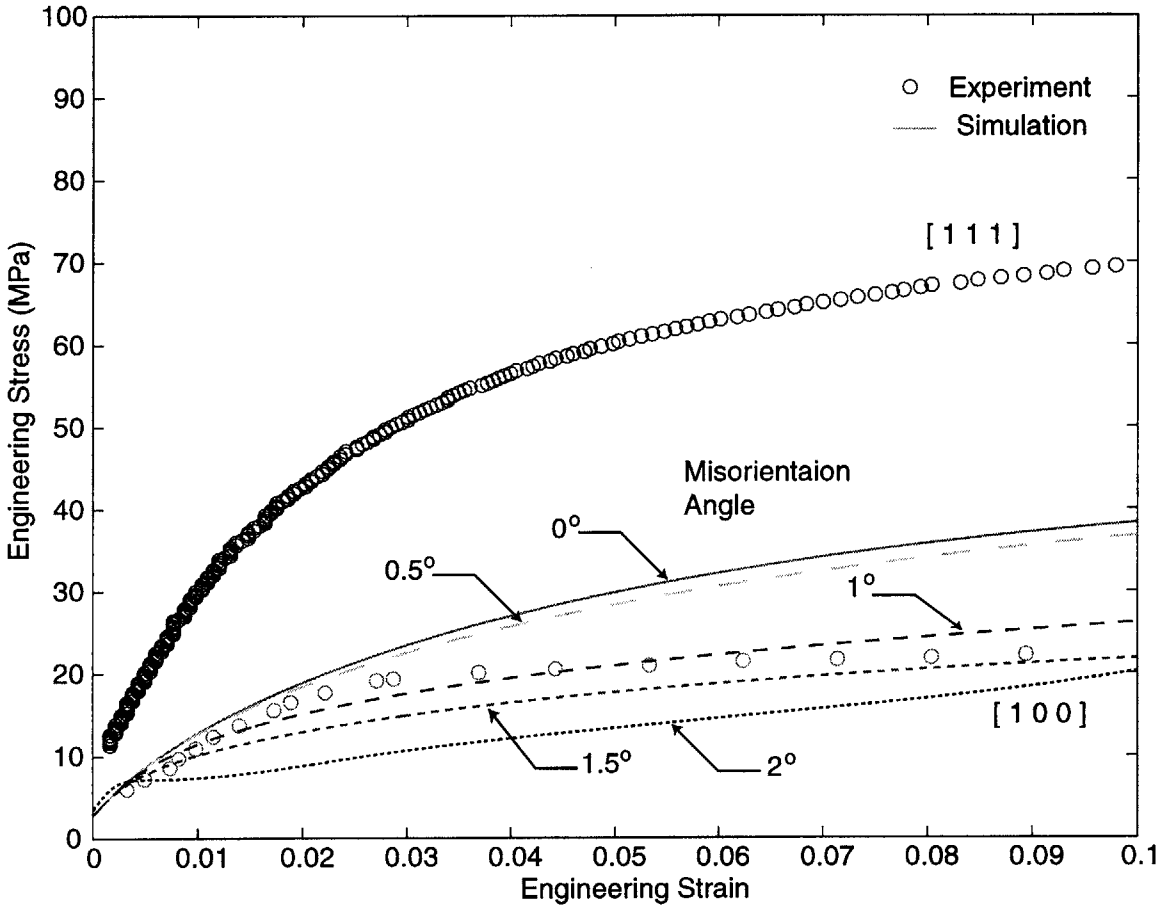

Figure 4-8: Effect of initial misorientation on the stress/strain of a nominally < 100 >-oriented single crystal.

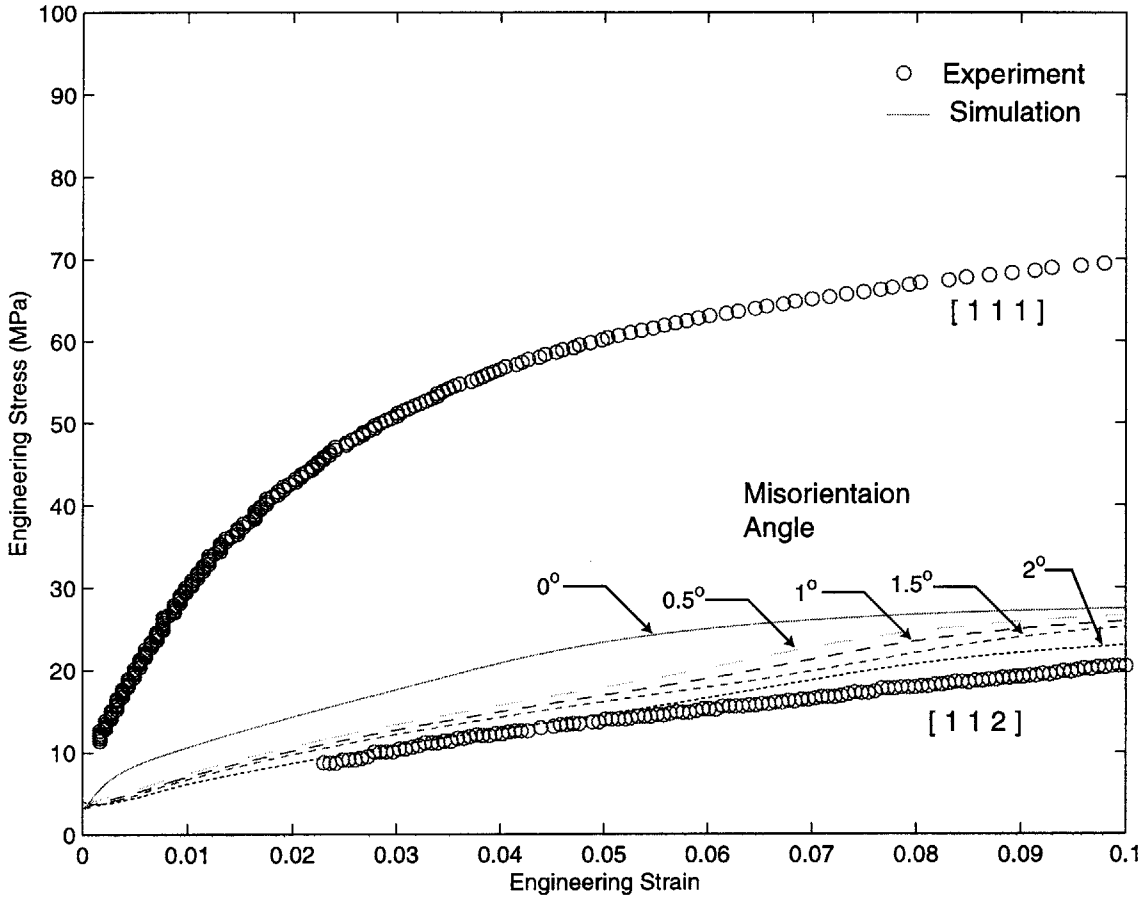

Figure 4-9: Effect of initial misorientation on the stress/strain of a nominally < 112 >-oriented single crystal.

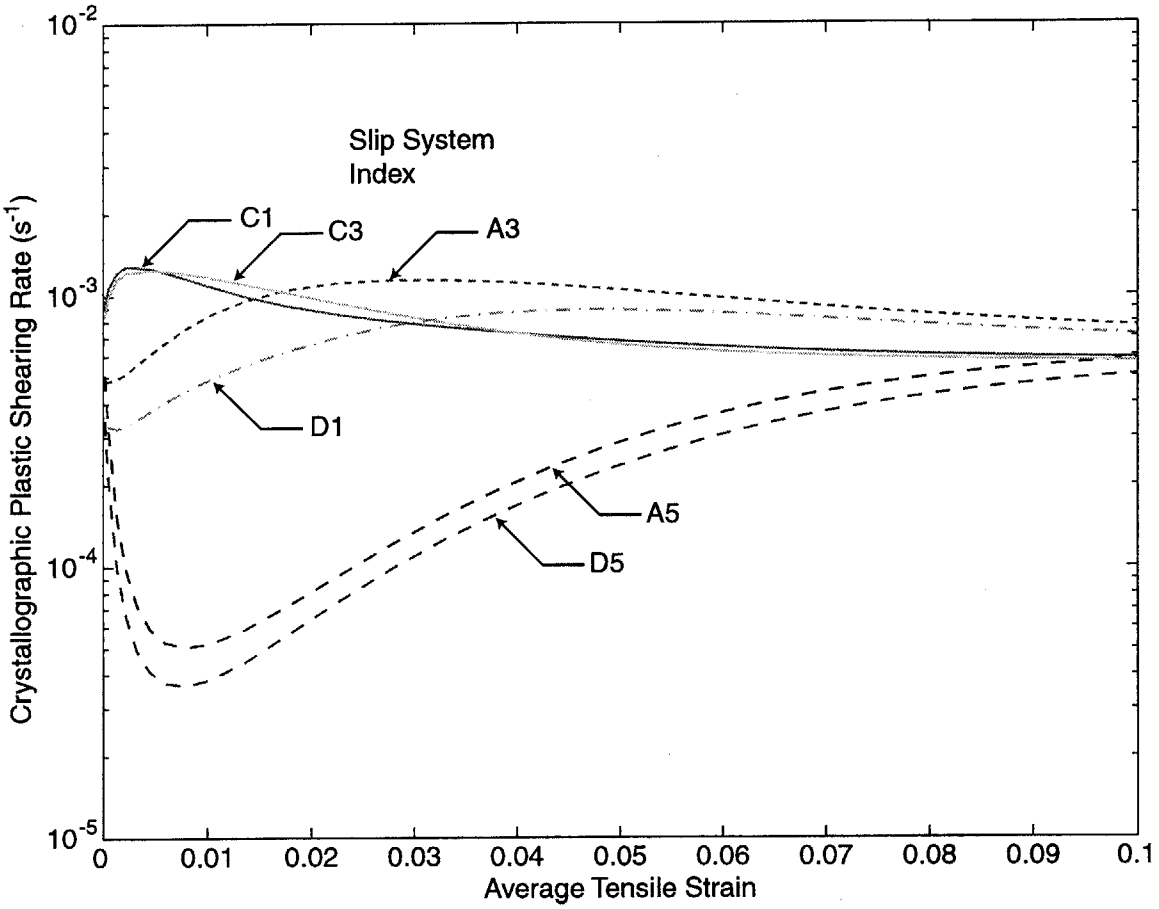

Figure 4-10: A history of the crystallographic plastic strain rates of the six potentially active slip-systems of a $< 111 >$-oriented single crystal. Initial misorientation is 1°.

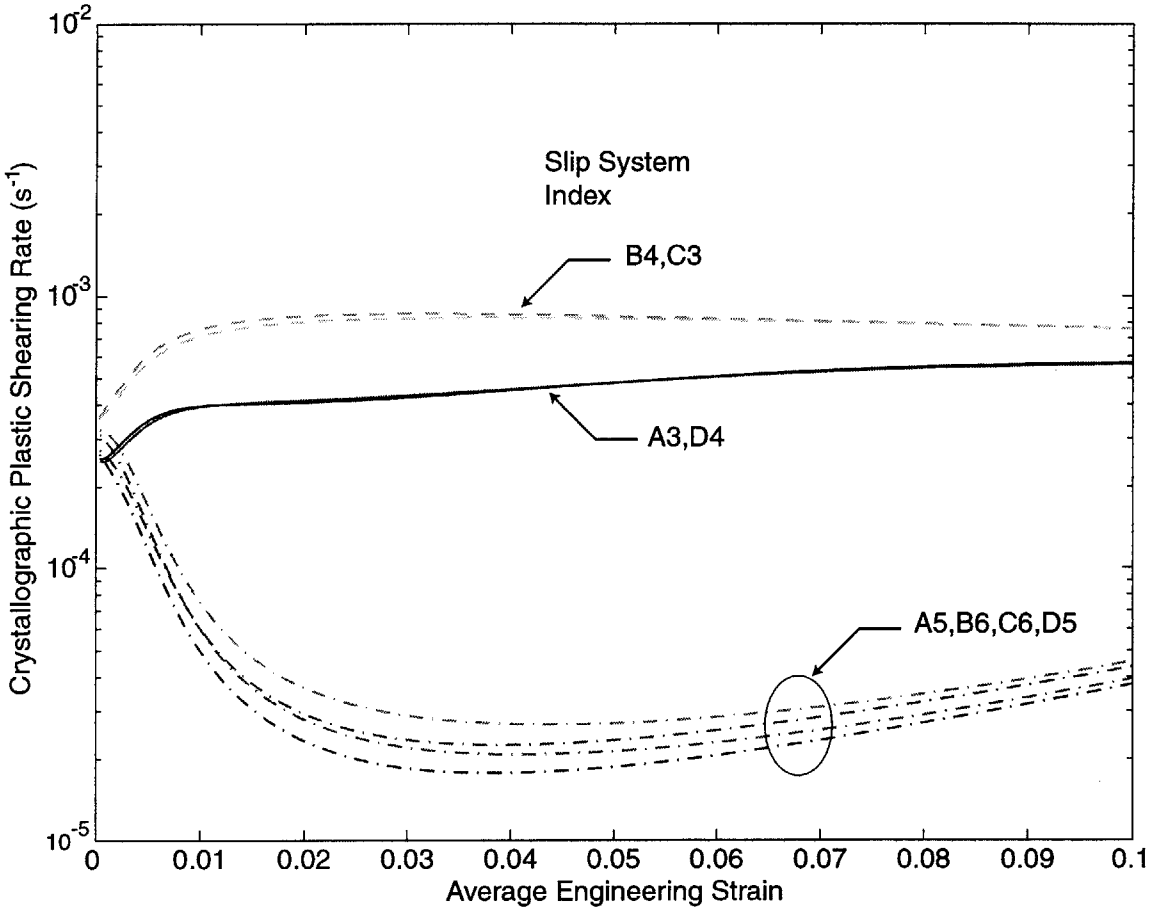

Figure 4-11: A history of the crystallographic plastic strain rates of the eight potentially active slip-systems of a $< 100 >$-oriented single crystal. Initial misorientation is 1°.

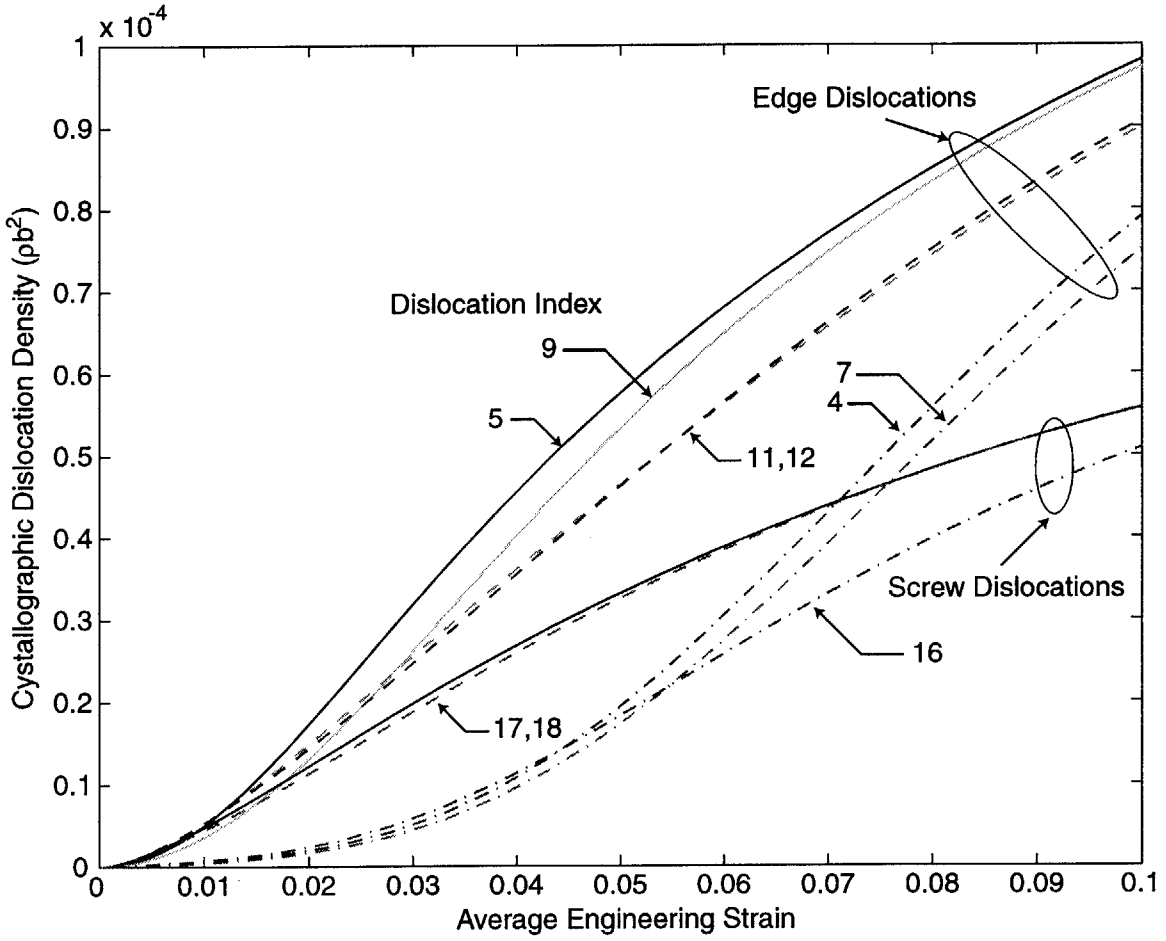

Figure 4-12: A history of the crystallographic dislocation density generated during the tensile elongation of a < 111 >-oriented single crystal. Refer to Table 4.1 for the crystallographic details of each density index.

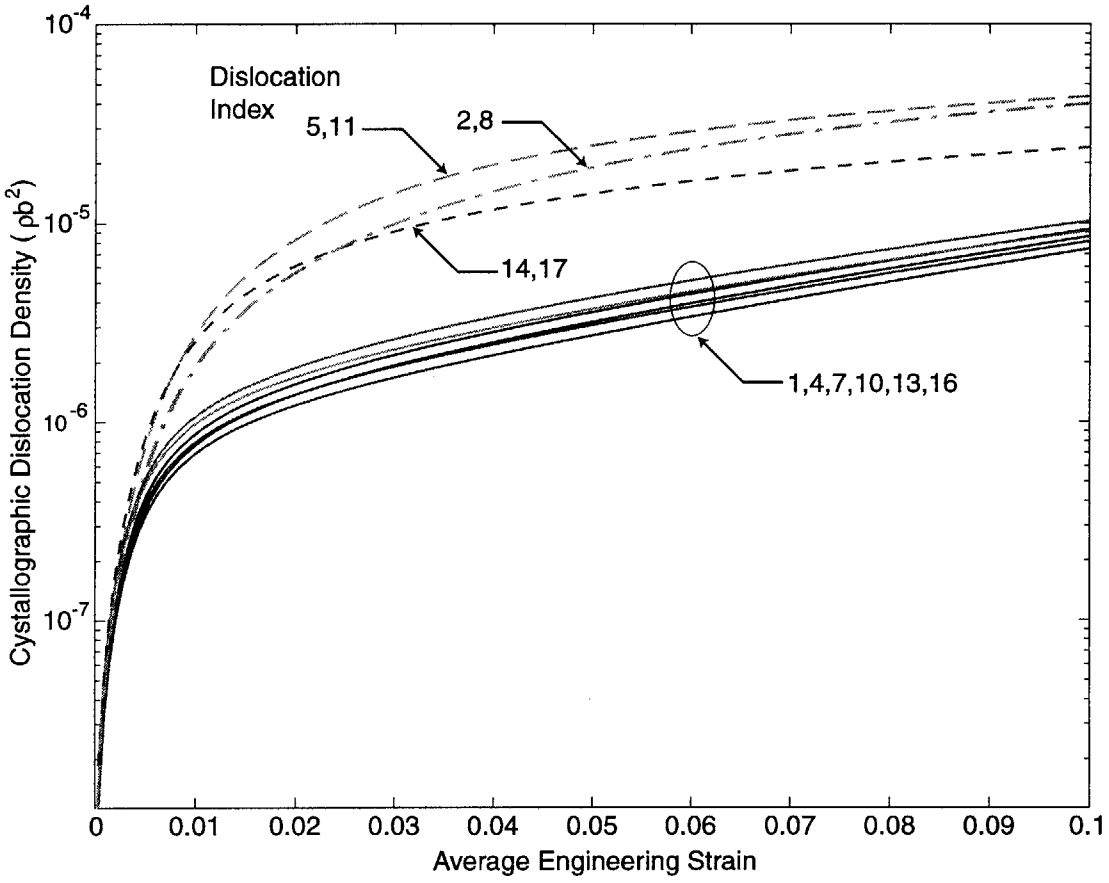

Figure 4-13: A history of the crystallographic dislocation density generated during the tensile elongation of a $< 100 >$-oriented single crystal. Refer to Table 4.1 for the crystallographic details of each density index.

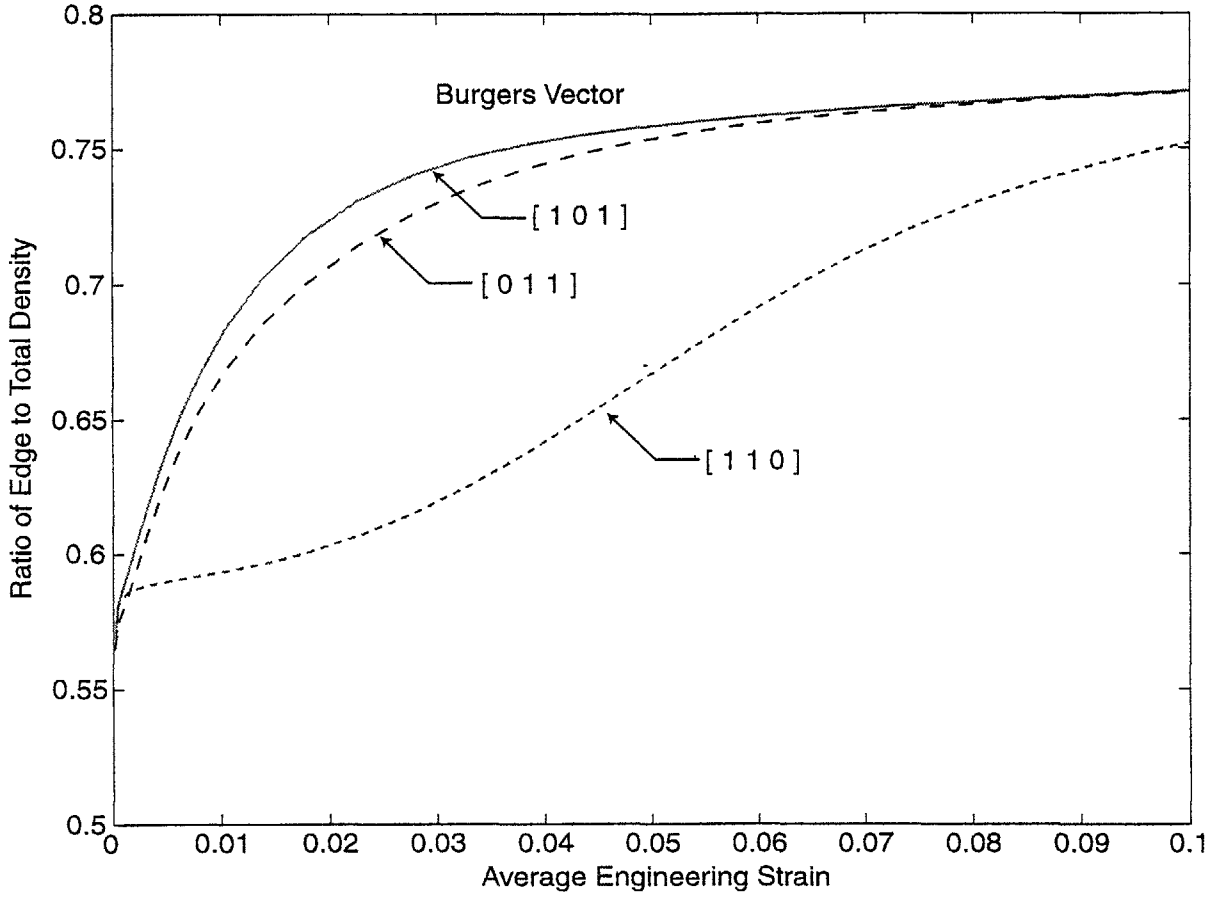

Figure 4-14: The ratio of edge dislocation density to the total density for each active Burgers vector during the tensile elongation of a $< 111 >$-oriented single crystal.

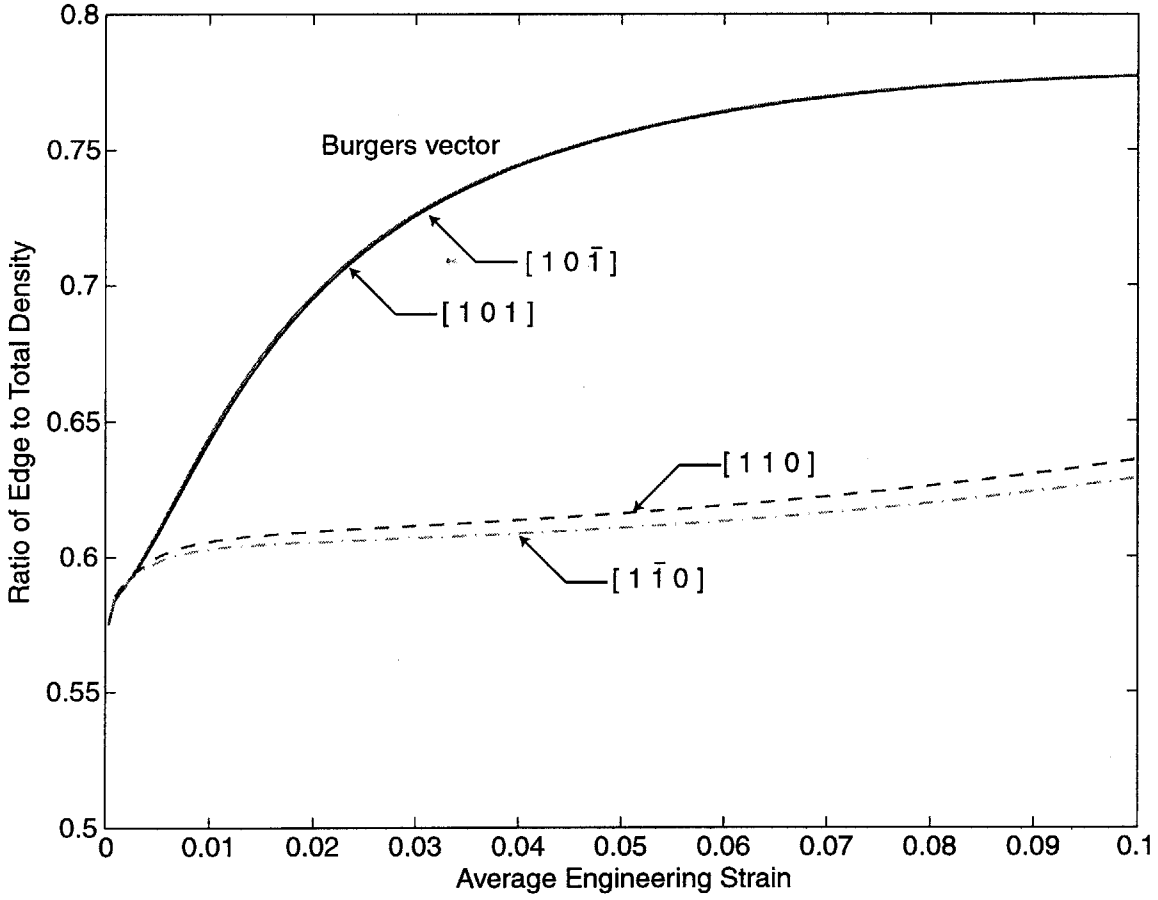

Figure 4-15: The ratio of edge dislocation density to the total density for each active Burgers vector during the tensile elongation of a $< 100 >$-oriented single crystal.

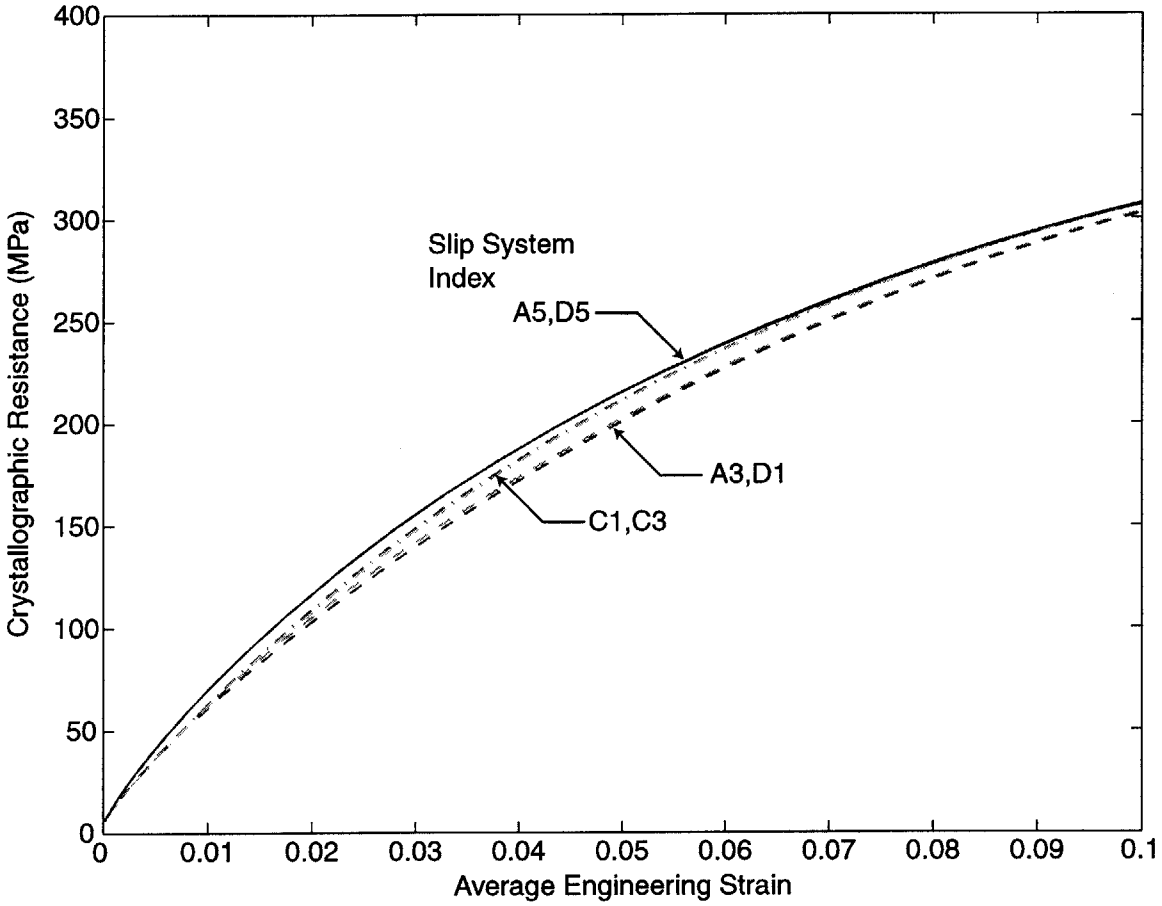

Figure 4-16: A history of the evolution of slip-system strengths in the six potentially active systems during the tensile elongation of a $< 111 >$-oriented single crystal.

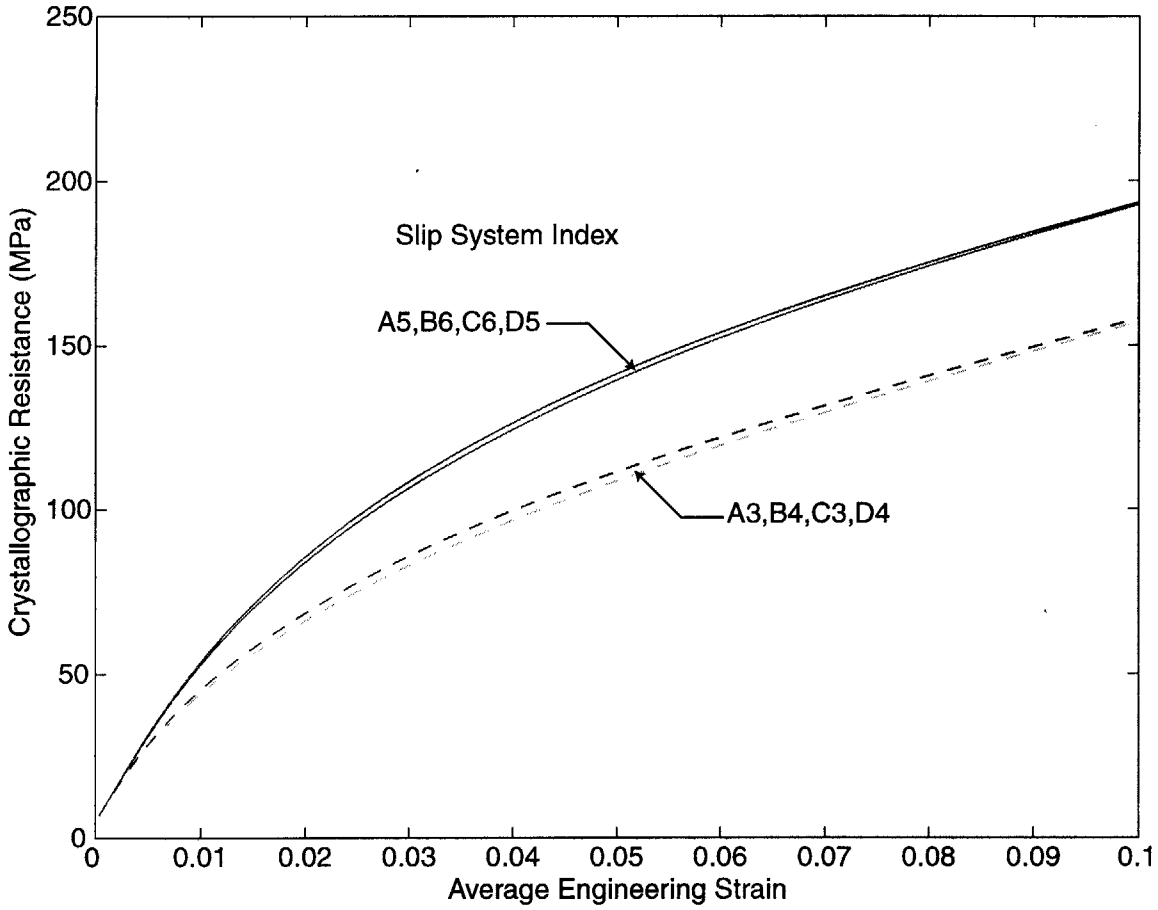

Figure 4-17: A history of the evolution of slip-system strengths in the eight potentially active systems during the tensile elongation of a $< 100 >$-oriented single crystal.

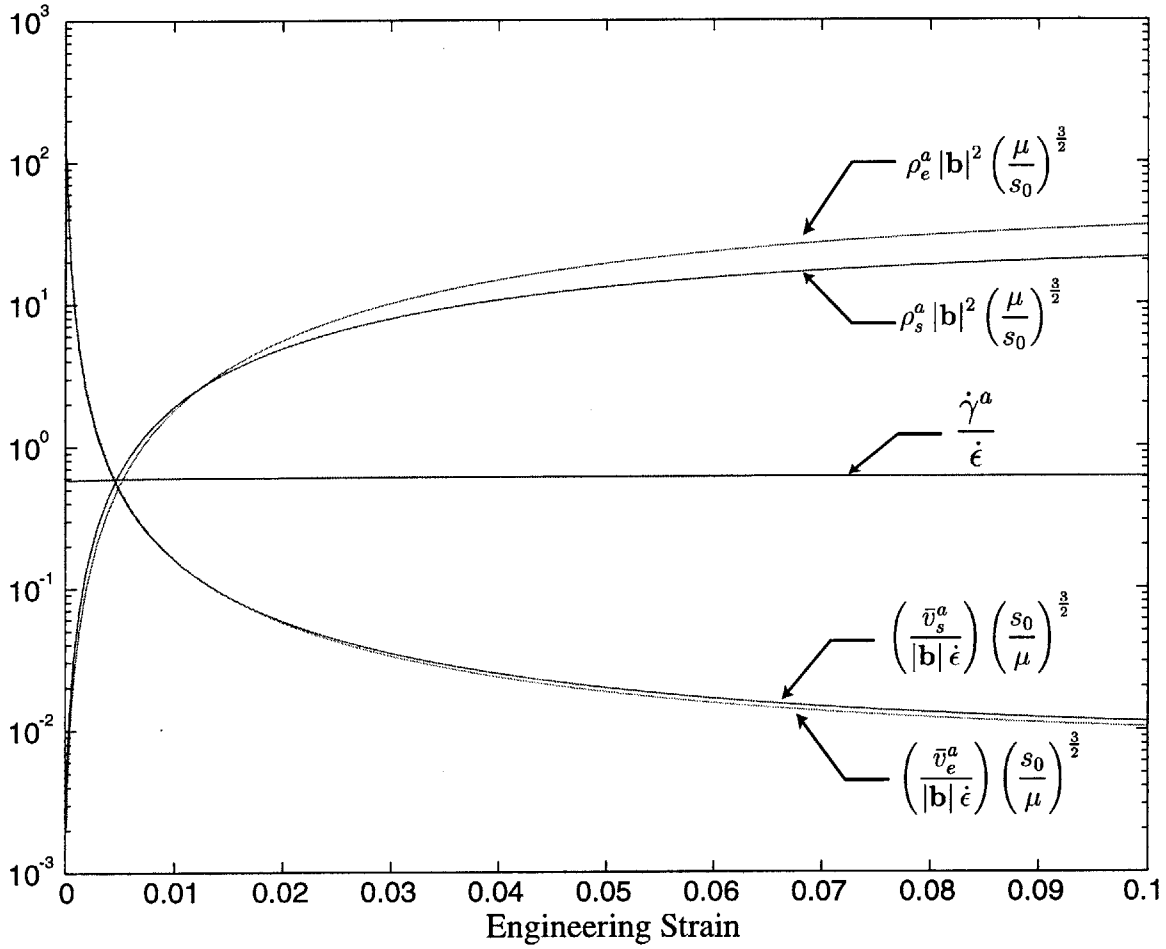

Figure 4-18: Decomposition of the crystallographic strain rate on one of the six equally-active slip-systems for a perfectly-oriented < 111 > crystal into the density on that slip plane, both edge and screw, and their respective average velocities.

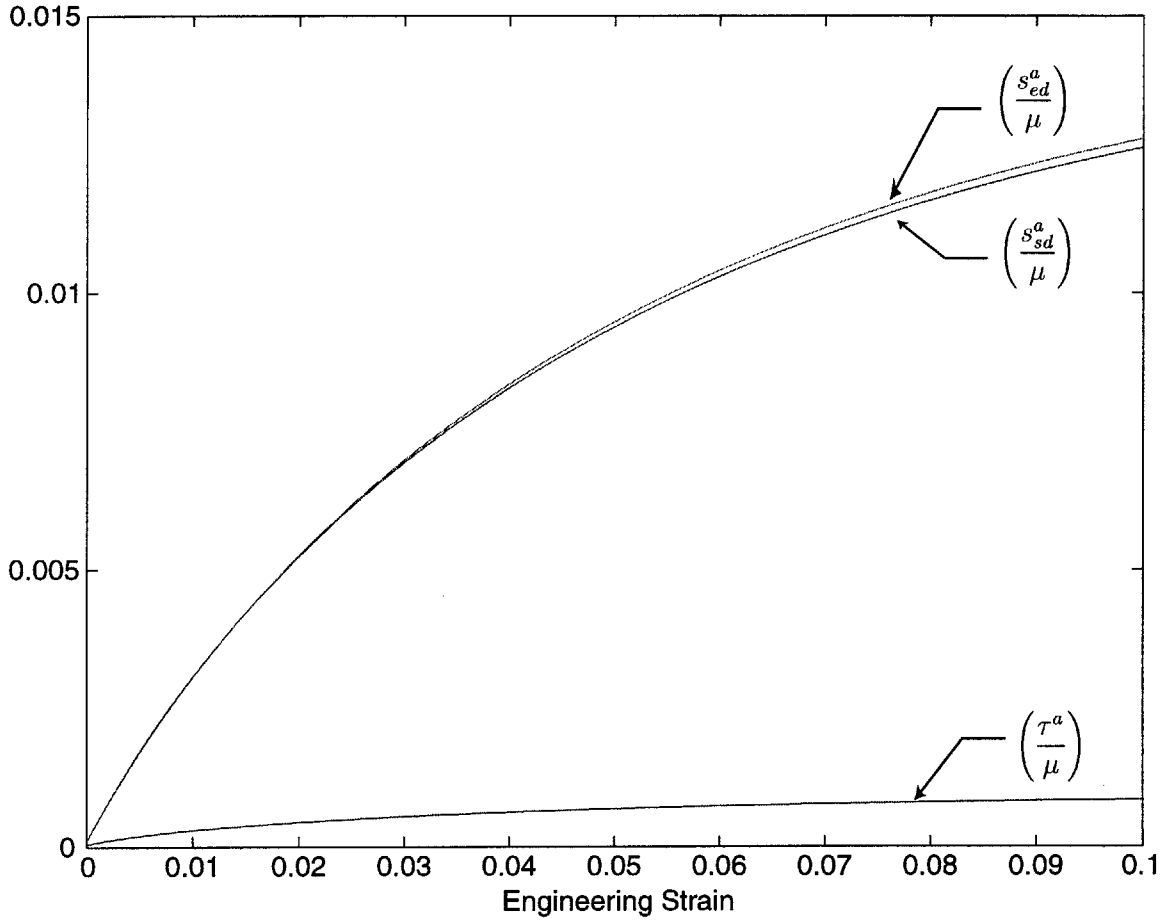

Figure 4-19: Normalized resistance and normalized applied shear stress on one of the six equally-active slip-systems for a perfectly-oriented $< 111 >$ crystal during tensile elongation.

Table 4.1: Geometry of dislocation density discretization used to model aluminum single crystals.

ρ Index	$\hat{\mathbf{b}}_0$	$\mathbf{t}_0$	Slip System
1	$\frac{1}{\sqrt{2}}[1\bar{1}0]$	$\frac{1}{\sqrt{6}}[11\bar{2}]$	B6
2	$\frac{1}{\sqrt{2}}[10\bar{1}]$	$\frac{1}{\sqrt{6}}[1\bar{2}1]$	B4
3	$\frac{1}{\sqrt{2}}[01\bar{1}]$	$\frac{1}{\sqrt{6}}[\bar{2}11]$	B2
4	$\frac{1}{\sqrt{2}}[110]$	$\frac{1}{\sqrt{6}}[1\bar{1}2]$	A5
5	$\frac{1}{\sqrt{2}}[101]$	$\frac{1}{\sqrt{6}}[12\bar{1}]$	A3
6	$\frac{1}{\sqrt{2}}[01\bar{1}]$	$\frac{1}{\sqrt{6}}[211]$	A2
7	$\frac{1}{\sqrt{2}}[110]$	$\frac{1}{\sqrt{6}}[\bar{1}12]$	D5
8	$\frac{1}{\sqrt{2}}[10\bar{1}]$	$\frac{1}{\sqrt{6}}[121]$	D4
9	$\frac{1}{\sqrt{2}}[011]$	$\frac{1}{\sqrt{6}}[21\bar{1}]$	D1
10	$\frac{1}{\sqrt{2}}[1\bar{1}0]$	$\frac{1}{\sqrt{6}}[112]$	C6
11	$\frac{1}{\sqrt{2}}[101]$	$\frac{1}{\sqrt{6}}[\bar{1}21]$	C3
12	$\frac{1}{\sqrt{2}}[011]$	$\frac{1}{\sqrt{6}}[2\bar{1}1]$	C1
13	$\frac{1}{\sqrt{2}}[1\bar{1}0]$	$\frac{1}{\sqrt{2}}[1\bar{1}0]$	B6 & C6
14	$\frac{1}{\sqrt{2}}[10\bar{1}]$	$\frac{1}{\sqrt{2}}[10\bar{1}]$	B4 & D4
15	$\frac{1}{\sqrt{2}}[01\bar{1}]$	$\frac{1}{\sqrt{2}}[01\bar{1}]$	A2 & B2
16	$\frac{1}{\sqrt{2}}[110]$	$\frac{1}{\sqrt{2}}[110]$	A5 & D5
17	$\frac{1}{\sqrt{2}}[101]$	$\frac{1}{\sqrt{2}}[101]$	A3 & C3
18	$\frac{1}{\sqrt{2}}[011]$	$\frac{1}{\sqrt{2}}[011]$	C1 & D1

Table 4.2: Strength interaction sub-matrix, $G^{\xi\zeta}$, for the edge dislocation interactions. The average segment length interaction matrix, $H^{\xi\zeta}$ takes the same form, but with different values. The values used to model single crystal aluminum are given below.

$$\left[G^{\xi\zeta}\right]_{\substack{\xi=1,12\\ \zeta=1,12}} = \begin{bmatrix} G_0 & G_1 & G_1 & G_4 & G_5 & G_3 & G_4 & G_3 & G_5 & G_2 & G_3 & G_3 \\ G_1 & G_0 & G_1 & G_5 & G_4 & G_3 & G_3 & G_2 & G_3 & G_3 & G_4 & G_5 \\ G_1 & G_1 & G_0 & G_3 & G_3 & G_2 & G_5 & G_3 & G_4 & G_3 & G_5 & G_4 \\ G_4 & G_5 & G_3 & G_0 & G_1 & G_1 & G_2 & G_3 & G_3 & G_4 & G_3 & G_5 \\ G_5 & G_4 & G_3 & G_1 & G_0 & G_1 & G_3 & G_4 & G_5 & G_3 & G_2 & G_3 \\ G_3 & G_3 & G_2 & G_1 & G_1 & G_0 & G_3 & G_5 & G_4 & G_5 & G_3 & G_4 \\ G_4 & G_3 & G_5 & G_2 & G_3 & G_3 & G_0 & G_1 & G_1 & G_4 & G_5 & G_3 \\ G_3 & G_2 & G_3 & G_3 & G_4 & G_5 & G_1 & G_0 & G_1 & G_5 & G_4 & G_3 \\ G_5 & G_3 & G_4 & G_3 & G_5 & G_4 & G_1 & G_1 & G_0 & G_3 & G_3 & G_2 \\ G_2 & G_3 & G_3 & G_4 & G_3 & G_5 & G_4 & G_5 & G_3 & G_0 & G_1 & G_1 \\ G_3 & G_4 & G_5 & G_3 & G_2 & G_3 & G_5 & G_4 & G_3 & G_1 & G_0 & G_1 \\ G_3 & G_5 & G_4 & G_5 & G_3 & G_4 & G_3 & G_3 & G_2 & G_1 & G_1 & G_0 \end{bmatrix}$$

Strength interaction coefficients: $G_0 = 0.10,\ G_1 = 0.22,\ G_{i=2,5} = g_i \left|\mathbf{n}^{\xi} \cdot \mathbf{t}^{\zeta}\right|,$
where $g_2 = 0.30,\ g_3 = 0.38,$
$g_4 = 0.16,\ g_5 = 0.45$

Length interaction coefficients: $H_0 = 0.00,\ H_1 = 0.00,\ H_{i=2,5} = h_i \left|\mathbf{n}^{\xi} \cdot \mathbf{t}^{\zeta}\right|,$
where $h_2 = 0.05,\ h_3 = 0.12,$
$h_4 = 0.03,\ h_5 = 0.25$

Table 4.3: Material parameters used for single crystal Aluminum simulations.

Elastic Coefficients	C_{11}	=	108 GPa
	C_{12}	=	61.3 GPa
	C_{44}	=	28.5 GPa
	μ	=	25.0 GPa
Dislocation Mobility Coefficients	$v_{e0} = v_{s0}$	=	1 m/s
	$\Delta F_e = \Delta F_s$	=	3.0×10^{-19} J/atom
	$s_{ep} = s_{sp}$	=	2 MPa
	$p_e = p_s$	=	1.1
	$q_e = q_s$	=	0.141
Capture Radii	R_e	=	18.6 nm
	R_s	=	93.0 nm
Burgers Vector	$\|\mathbf{b}\|$	=	2.863 Å

Table 4.4: Euler angles used to simulate misoriented single crystals with 1° misorientation.

Orientation	θ (°)	ϕ (°)	ω (°)
< 111 >	55.6430	135.5119	0.0000
< 100 >	89.5774	90.9063	45.0000
< 112 >	34.4494	−43.9860	90.0000
< 123 >	36.6992	153.4349	180.0000

Chapter 5

Application of Non-Local Model to Lattice-Incompatibility Plasticity

5.1 Ideal Double-Slip Geometry and Selection of Discrete Dislocation Basis

An idealized crystalline geometry is chosen to investigate the length-scale-dependence of crystal plasticity on the micron scale. The idealization is made to reduce the dimension of the crystallographic dislocation density from 36 densities in the full three-dimensional problem to 8 dislocation densities in the idealized geometry. A three-dimensional non-local model has been developed previously, based on a hybrid crystallographic strength/dislocation state variable formulation (Arsenlis and Parks, 2000), the results of which show the same length-scale-dependence as an idealized two-dimensional model with the same formulation (Dai et al., 2000). Therefore, an idealized crystalline geometry appears to be adequate for investigating the role of the polarity of the dislocation density in crystal plasticity at microscopic length scales.

The idealized geometry that will be used is a planar crystal with two slip-systems. The double-slip geometry, initially proposed by Asaro (1979) and then refined by

Dai (1997) , has been derived from a special orientation of three-dimensional FCC crystals, leading to an effective double-slip geometry. The FCC crystalline orientation which leads to this condition is depicted in Figure 5-1. Plane strain deformations occurring in the plane with a normal direction parallel to the $[\bar{1}10]$ direction can be accomplished by activating a combination of four slip systems on two slip planes. The plane strain condition is enforced by requiring equal activation of the $[\bar{1}01](111)$ slip-system with the $[10\bar{1}](111)$ slip-system and equal activation of the $[101](\bar{1}\bar{1}1)$ slip-system with the $[011](\bar{1}\bar{1}1)$ slip-system. Equal activation of the two pairs of slip systems leads to an effective double-slip geometry, in which the "effective" slip-systems become $[\bar{1}\bar{1}2](111)$ and $[112](\bar{1}\bar{1}1)$. The complex three-dimensional geometry can be simplified into a two-dimensional one described by two angles, ϕ and ψ, as shown in Figure 5-2. Here ϕ is the angle that the symmetry axis makes with the global coordinates, and ψ is the half-angle between the two "effective" slip-systems. The value of ψ that will be used in the analysis is $30°$, which is approximately the angle derived from the FCC geometry.

The crystallographic basis that will be used is of the same type as previously used to model the anisotropic behavior of single crystal aluminum. Four dislocation densities, corresponding to positive and negative edge and screw densities, for each slip-system will be used to characterize the crystal, leading to a total of eight crystallographic dislocation densities. A schematic of the "crystallographic" dislocation density geometries included in the model is shown in Figure 5-3. Although the model considers only plane strain deformations, the dislocation motion is three-dimensional. The motion of the (effective) edge dislocations remains in the plane; however, the contribution of the screw densities to the in-plane plastic deformation results from their motion out of the plane.

Planar dislocation models have been constructed such that only edge dislocations are used to characterize the state of these idealized crystals (Needleman, 1995), but in the context of those models, edge dislocation sources must be included explicitly to evolve the dislocation density state. Furthermore, the edge dislocations in Needleman's idealized crystal do not contribute to dislocation forest hardening since they

do not pierce the other slip-system, and as a result the obstacle resistance does not evolve. Including the screw dislocation densities in the present model removes the necessity to include explicit sources of density, due to the evolution equations introduced in Section 3.2. Also, the forest density can evolve with deformation because the screw dislocations of one system pierce the plane of the other slip-system.

Since all of the plastic deformation occurs in this two-dimensional plane, non-homogeneous plastic slip will cause the lattice planes to bend in the plane, leading to a polarity in the edge dislocation densities only. Polarity in the screw densities would cause the crystal to twist out of the plane, which is not permitted in the plane strain condition. Polarity in the jog density would cause the crystal to bend out of the plane, which is also disallowed by the plane strain boundary condition. The idealized crystal geometry results in a great simplification in the dislocation polarity such that only four of the eight dislocation densities are affected. Since there are only two non-zero components of Nye's tensor to be accommodated through multiple combinations of the four edge densities in the model, the polar accumulation/loss equations developed in Section 3.2.3 will be used to determine the "crystallographic" dislocation profile of the dislocation tensor in this underconstrained system.

5.2 Selection of Constitutive Functions

If the set of functions quantifying the average dislocation velocity, capture radius, and average segment length as described in Section 4.2 were implemented without any modifications to model this idealized crystalline geometry, no length-scale-dependence associated with non-homogeneous plastic deformation would be predicted by the simulations. Even with the evolution of the dislocation polarity included in the general evolution equations for density, the model would not predict a length-scale-dependence. The functional forms found in Eq.'s 4.1, 4.2, and 4.5 all depend on the mean dislocation density, and are independent of the polarity of the dislocation density. The dislocation junction strengths in Eq. 4.4 and the average segment-length-interaction coefficients in Eq. 4.5 were independent of the polarity of the interacting

dislocation densities. The total strength interaction coefficients, $G_0 - G_5$, did depend on the character of the dislocation density to calculate the piercing density, but even the character of the interacting dislocations did not affect the strength of the junctions, $g_2 - g_5$. The analysis of the density accumulation/loss equations associated with the flux divergence of dislocation density in Section 3.2.3, showed that the time rate of change in the total dislocation density due to the flux divergence of the dislocation density was only a fraction of the rate of accumulation of polarity in the density. Furthermore, the difference between the total dislocation density in the non-homogeneously deforming crystal and the homogeneously deforming crystal could be positive or negative for the same level of plastic deformation, depending on the existing polarity and current flux divergence. In situations in which the mean numerically dominated the polarity of the density, the time rate of change in the total density due to the flux divergence was insignificant compared to the time rate of change in the total density due to the statistical processes of generation and annihilation.

Since the change in the total dislocation density including the polar density accumulation/loss equations is most likely small for most plastic deformation histories, the stress/strain behavior of a crystal following the constitutive behavior modeled in Chapter 4 would be largely unaffected by the polarity of the dislocation density. Therefore, the functional forms of the constitutive equations that were used to model single crystal aluminum must be modified to capture the length-scale-dependence observed in experiments both in magnitude and direction. The thin beam bending experiments conducted by Stölken and Evans (1998) showed that the polarity of the dislocation density increased unambiguously the normalized bending strength of the beam. The change of the magnitude of the bending strength due to the polarity of the density is on the order of the tensile strength of the films as shown in Figure 5-4. The magnitude of the polarity of dislocation density in the beam bending experiments scales with curvature multiplied by the Burgers vector. The magnitude of the dislocation polarity in the 12.5 μm thick beam at 10% surface strain is approximately 10^{14} m^2, while the total dislocation density, according to the simulations conducted in Chapter 4, is on the order of 10^{16} m^2, yet the small relative difference in the polarity

($\approx 1\%$) leads to first order effect in the strength. Any modification in the constitutive equations must be able to reproduce the magnitude of the length-scale-dependence observed in experiments.

The constitutive equations can be modified such that the length-scale-dependence is incorporated directly, by modifying Orowan's relation, or indirectly, by modifying the evolution equations for the statistical density. The plastic strain rate on slip-system a can be written as a function of the mean and the polarity of the dislocation density through the following expression:

$$\begin{aligned}\dot{\gamma}^a &= \left[\rho^a_{(m)e+}\left(\bar{\rho}^a_e, \rho^a_{e\pm}\right)\bar{v}^a_{(m)e+}\left(\tau^a, \bar{\rho}^\zeta, \rho^\zeta_\pm\right)\right. \\ &\quad +\rho^a_{(m)e-}\left(\bar{\rho}^a_e, \rho^a_{e\pm}\right)\bar{v}^a_{(m)e-}\left(\tau^a, \bar{\rho}^\zeta, \rho^\zeta_\pm\right) \\ &\quad +\rho^a_{(m)s+}\left(\bar{\rho}^a_s, \rho^a_{s\pm}\right)\bar{v}^a_{(m)s+}\left(\tau^a, \bar{\rho}^\zeta, \rho^\zeta_\pm\right) \\ &\quad \left.+\rho^a_{(m)s-}\left(\bar{\rho}^a_s, \rho^a_{s\pm}\right)\bar{v}^a_{(m)s-}\left(\tau^a, \bar{\rho}^\zeta, \rho^\zeta_\pm\right)\right]|\mathbf{b}|sign\left(\tau^a\right) , \end{aligned} \tag{5.1}$$

where $\rho^a_{(m)}$ denotes the mobile density of each species on slip system a, written as functions of the mean and the polarity of the dislocation density, and $\bar{v}^a_{(m)}$ is the average velocity of the mobile density of each species, written as a function of the resolved shear stress and the mean and polarity of the complete set of dislocation densities. The "direct" modifications change the level of plastic slipping activated for a given resolved stress level by making the mobile density and/or the average dislocation velocity decreasing functions of dislocation polarity.

The statistical evolution of dislocation density (generation and annihilation) can be written as a function of the mean and the polarity of the dislocation density through the following expressions:

$$\begin{aligned}\dot{\rho}^a_{e(stat)} &= \frac{\rho^a_{(m)s+}\left(\bar{\rho}^a_s, \rho^a_{s\pm}\right)\bar{v}^a_{(m)s+}\left(\tau^a, \bar{\rho}^\zeta, \rho^\zeta_\pm\right)}{\bar{l}^a_{(m)s+}\left(\bar{\rho}^\zeta, \rho^\zeta_\pm\right)} + \frac{\rho^a_{(m)s-}\left(\bar{\rho}^a_s, \rho^a_{s\pm}\right)\bar{v}^a_{(m)s-}\left(\tau^a, \bar{\rho}^\zeta, \rho^\zeta_\pm\right)}{\bar{l}^a_{(m)s-}\left(\bar{\rho}^\zeta, \rho^\zeta_\pm\right)} \\ &\quad -\rho^a_{(m)e+}\left(\bar{\rho}^a_e, \rho^a_{e\pm}\right)\rho^a_{(m)e-}R_e\left(\rho^a_{e\pm}\right)\left[\bar{v}^a_{(m)e+}\left(\tau^a, \bar{\rho}^\zeta, \rho^\zeta_\pm\right) + \bar{v}^a_{(m)e-}\left(\tau^a, \bar{\rho}^\zeta, \rho^\zeta_\pm\right)\right] \\ &\quad -\rho^a_{(m)e+}\left(\bar{\rho}^a_e, \rho^a_{e\pm}\right)\rho^a_{(im)e-}R_e\left(\rho^a_{e\pm}\right)\bar{v}^a_{(m)e+}\left(\tau^a, \bar{\rho}^\zeta, \rho^\zeta_\pm\right) \\ &\quad -\rho^a_{(im)e+}\left(\bar{\rho}^a_e, \rho^a_{e\pm}\right)\rho^a_{(m)e-}R_e\left(\rho^a_{e\pm}\right)\bar{v}^a_{(m)e-}\left(\tau^a, \bar{\rho}^\zeta, \rho^\zeta_\pm\right) , \end{aligned} \tag{5.2}$$

$$\dot{\bar{\rho}}^a_{s(stat)} = \frac{\rho^a_{(m)e+}\left(\bar{\rho}^a_e, \rho^a_{e\pm}\right)\bar{v}^a_{(m)e+}\left(\tau^a, \bar{\rho}^\zeta, \rho^\zeta_\pm\right)}{\bar{l}^a_{(m)e+}\left(\bar{\rho}^\zeta, \rho^\zeta_\pm\right)} + \frac{\rho^a_{(m)e-}\left(\bar{\rho}^a_e, \rho^a_{e\pm}\right)\bar{v}^a_{(m)e-}\left(\tau^a, \bar{\rho}^\zeta, \rho^\zeta_\pm\right)}{\bar{l}^a_{(m)e-}\left(\bar{\rho}^\zeta, \rho^\zeta_\pm\right)}$$
$$-\rho^a_{(m)s+}\left(\bar{\rho}^a_s, \rho^a_{s\pm}\right)\rho^a_{(m)s-}R_s\left(\rho^a_{s\pm}\right)\left[\bar{v}^a_{(m)s+}\left(\tau^a, \bar{\rho}^\zeta, \rho^\zeta_\pm\right) + \bar{v}^a_{(m)s-}\left(\tau^a, \bar{\rho}^\zeta, \rho^\zeta_\pm\right)\right]$$
$$-\rho^a_{(m)s+}\left(\bar{\rho}^a_s, \rho^a_{s\pm}\right)\rho^a_{(im)s-}R_s\left(\rho^a_{s\pm}\right)\bar{v}^a_{(m)s+}\left(\tau^a, \bar{\rho}^\zeta, \rho^\zeta_\pm\right)$$
$$-\rho^a_{(im)s+}\left(\bar{\rho}^a_s, \rho^a_{s\pm}\right)\rho^a_{(m)s-}R_s\left(\rho^a_{s\pm}\right)\bar{v}^a_{(m)s-}\left(\tau^a, \bar{\rho}^\zeta, \rho^\zeta_\pm\right) \quad , \tag{5.3}$$

(5.4)

where $\rho^a_{(im)}$ denotes the immobile density of each species on slip system a, written as functions of the mean and polarity of the dislocation density. To effect scale-dependent strengthening, the "indirect" modifications to the evolution equations must increase the rate of change of the density mean by making the average segment length and/or the capture radii decreasing functions of dislocation polarity. Each of these possibilities will be considered individually, and the relative merits of each technique for capturing the length-scale-dependence in crystal plasticity will be discussed.

Consider first the effect of reducing the mobile dislocation density in the presence of density polarity. The functions for the mobile and immobile dislocation densities in Eq.'s 5.1-5.3 that were used in the "local" simulation of aluminum were

$$\rho^a_{(m)e+} = \bar{\rho}^a_e + \frac{1}{2}\rho^a_{e\pm} \tag{5.5}$$

$$\rho^a_{(m)e-} = \bar{\rho}^a_e - \frac{1}{2}\rho^a_{e\pm} \tag{5.6}$$

$$\rho^a_{(m)s+} = \bar{\rho}^a_s + \frac{1}{2}\rho^a_{s\pm} \tag{5.7}$$

$$\rho^a_{(m)s-} = \bar{\rho}^a_s - \frac{1}{2}\rho^a_{s\pm} \tag{5.8}$$

$$\rho^a_{(im)e+} = \rho^a_{(im)e-} = \rho^a_{(im)s+} = \rho^a_{(im)s-} = 0. \tag{5.9}$$

In the local simulations, the polarity was identically zero because the polar accumulation/loss contribution to the evolution of the dislocation density was not included in the simulations. As stated earlier, these functions for the mobile density do not introduce a length-scale-dependence after the polar accumulation/loss equations have been added to the general evolution equations for dislocation density, but the functions can

be altered by considering the polar density to be immobile, yielding a length-scale dependence. Possible modifications of the mobile and immobile dislocation density might take the form

$$\rho^a_{(m)e+} = \rho^a_{(m)e-} = \min\left(\bar{\rho}^a_e + \frac{1}{2}\rho^a_{e\pm}, \bar{\rho}^a_e - \frac{1}{2}\rho^a_{e\pm}\right) \tag{5.10}$$

$$\rho^a_{(m)s+} = \rho^a_{(m)s-} = \min\left(\bar{\rho}^a_s + \frac{1}{2}\rho^a_{s\pm}, \bar{\rho}^a_s - \frac{1}{2}\rho^a_{s\pm}\right) \tag{5.11}$$

$$\rho^a_{(im)e+} = \max\left(0, \rho^a_{e\pm}\right) \tag{5.12}$$

$$\rho^a_{(im)e-} = \max\left(0, -\rho^a_{e\pm}\right) \tag{5.13}$$

$$\rho^a_{(im)s+} = \max\left(0, \rho^a_{s\pm}\right) \tag{5.14}$$

$$\rho^a_{(im)s+} = \max\left(0, -\rho^a_{s\pm}\right) \tag{5.15}$$

In a density state with no polarity, these functional forms yield the same values for the mobile and immobile dislocation density as the previous set of functions. In a polarized density state, the second set of functions lead to a smaller mobile density than the first set of functions by requiring the absolute polar density of each species to be immobile.

Treating the polar density as immobile requires that greater velocities be activated by greater stresses in order to retain the same crystallographic plastic shear rates. This is one of the techniques used implicitly in every existing non-local crystal plasticity model (Fleck and Hutchinson, 1997; Shu and Fleck, 1998; Gao et al., 1999; Dai et al., 2000) because the "effective" polar density calculated in each of these models always increases the inferred dislocation density and is never permitted to contribute to the plastic deformation (e.g. through an Orowan equation), but its presence is assumed to increase the resistance to plastic deformation. The argument for reducing the mobile density follows from the physical arguments of Ashby (1970). In his interpretation, the polar density is viewed as an additional amount of density needed to maintain lattice compatibility, which was not present during "homogeneous" plastic deformation. Since these dislocations were needed to maintain the coherence of the lattice structure, they could perhaps be viewed as not as mobile as the statistical

density, which had no geometric consequence; at the extreme limit, the polar dislocations could be considered sessile. At the dislocation density mechanics level, however, there appears to be no good reason to adopt the underlying assumptions upon which this method is based.

The motion of polar dislocations within a representative volume element (RVE) in a crystal does not affect the dislocation polarity in that RVE. The generation and annihilation evolution equations create and remove dislocation dipoles and other statistical density arrangements whether the participating dislocation densities responsible have a polar character or not. The only method of changing the density polarity within an RVE is by having unequal in-flux and out-flux of polar density, as discussed in Section 3.2.3. Instead of maintaining the local lattice continuity by requiring the absolute polar density be immobile, the model could maintain local lattice continuity merely by having the same number of polar dislocations entering and leaving the volume as required by the zero flux-divergence condition, without imposing a mobility constraint on the density due to the presence of polarity.

Consider the extreme case in which the size of the RVE is chosen so small that only a few dislocation lines were contained within it, and the majority of these dislocations would be considered to be polar within the small RVE. A mobility constraint on the "polar" density within the RVE would, in the limit, lead to an immobile (total) density state globally! The initial dislocation state of a well-annealed crystal most closely resembles this dislocation density state. During the annealing process, dislocation density is principally removed by statistical annihilation, leaving a crystal with an abundance of polar dislocations. The length scale of diffusion associated with the annihilation of statistical density is related to $1/\sqrt{(\bar{\rho})}$, while the length scale of diffusion associated with the polar density is related to the grain size. In most engineering materials, the spacing between dislocations is much smaller than grain diameter, and the mobility constraint does not appear to be valid for such density conditions. At its most basic level, this method of incorporating material length-scale-dependence relies on the ability to distinguish polar dislocations from statistical dislocations, which, in general, is not possible.

The other direct method of including the length-scale-dependence would be to reduce the average dislocation mobility in the presence of polar dislocation field. Within the functional form of the average dislocation velocity selected in Eq. 4.1, there are three ways that the influence of the polarity of the dislocation density could be incorporated. The dislocation strength interaction matrix, $G^{\xi\zeta}$, could be polarized, the forest interactions associated with the polar density could be stronger compared to the interactions with statistical density, or a back stress resulting from the spatial arrangement or polarity could be considered.

The dislocation interaction matrix, $G^{\xi\zeta}$, used to model the anisotropic plastic behavior of aluminum single crystals did not consider the difference in strength interactions between dislocation densities with different polarities and characters. The strength of interaction, g, was based solely on the slip systems of the two interacting densities. The simplification made in the model is not an accurate description of an actual crystal, but should be valid for cases in which the dislocation polarity doesn't influence the behavior. In general, the reactions between dislocations can depend both on the polarity of the dislocations, as well as their character (Wickham et al., 1999).

The possible dependence of the strength interaction matrix on the polarity of the density may be of interest in modeling the length-scale-dependence of crystal plasticity. For simplicity, the discussion will be limited to the forest interaction between a polarized set of edge dislocations on two slip-systems, since these are the only densities which become polar in the present idealized crystal geometry. A polarized strength interaction matrix would lead to two interaction coefficients between the four edge densities: g_{++} $(= g_{--})$, which describes the interaction between dislocations of like sign on the two slip-systems, and g_{+-} $(= g_{-+})$, which describes the interaction between dislocations of opposite sign on the two slip-systems. The average of the of the two polar interaction coefficients, $\bar{g} = 1/2\,(g_{++} + g_{+-})$, is effectively the simplified value that was used in the local model described in Chapter 4, and it corresponds to an effective strength interaction coefficient for models that consider the evolution of statistical densities only.

For the interaction matrix to be considered polarized, one of the two polar coefficients must be greater than $\bar{g}$, and the other must be less than $\bar{g}$. Suppose $g_{++} > g_{+-}$ so that the interaction between densities with like signs is stronger than the interaction between densities with different signs. States of density polarity in which the positive densities outnumber the negative densities on both slip-systems would lead to a greater resistance in mobility of the positive species on the slip systems and to a lesser resistance in the mobility of the the negative species on the slip systems, both compared to the unpolarized dislocation density state with the same mean. Therefore, a given plastic strain rate could be accomplished by the negative densities moving at faster velocities, due to the weaker resistance, and the positive densities moving at slower velocities, due to the stronger resistance, without significantly affecting the level of applied stress needed to maintain the plastic shear rate. Although the polarization of the strength interaction matrix is supported by theoretical findings (Wickham et al., 1999), it doesn't lead to a measurable length-scale-dependence in crystals with polarized dislocation density states compared crystals with unpolarized density states. Polarization of the strength interaction matrix would weaken the resistance for some densities while strengthening the resistance of others simultaneously, leading to a small (if any) net effect. Furthermore, the direction of change in the applied stress level, compared to the homogeneously deforming crystal, is ambiguous and depends on the exact form of the mobility function.

A second potential method of modifying the average dislocation velocity is to attribute a greater strength to the forest interactions of gliding densities with polar forest densities than to their corresponding interactions with statistical forest densities. A possible modification of the dislocation resistance takes the form

$$s_d^{\xi} = \sqrt{G^{\xi\zeta}\left[\left(\bar{\rho}^{\zeta} - \frac{1}{2}|\rho_{\pm}^{\zeta}|\right) + \frac{w}{2}|\rho_{\pm}^{\zeta}|\right]}\,, \tag{5.16}$$

where w is a coefficient greater than one. The term inside the parenthesis is the absolute SSD density, and $|\rho_{\pm}^{\zeta}|$ is the absolute GND density. The increased strength could be attributed to the inability of the polar dislocation density to move, thus creating

stronger obstacles. This method "effectively" increases the total density by $\frac{(w-1)}{2}|\rho_{\pm}^{\zeta}|$ as viewed through the strength contribution in the presence of a density polarity, and would lead to the same type of response as the reduction of the mobile density. In both cases, a larger "effective" density would be used to calculate the dislocation resistance in the average density mobility function than the corresponding density that contributes to the plastic shear through the Orowan relation. This method is the most common manner through which the length-scale-dependence is introduced into non-local plasticity models (Fleck and Hutchinson, 1997; Shu and Fleck, 1998; Gao et al., 1999; Dai et al., 2000). The magnitude of the statistical dislocation density is most often inferred from a measure of strength associated with SSD density and not directly evolved, while the magnitude polar density is directly measured by the dislocation tensor. Since the magnitude of the statistical dislocation density never appears explicitly in any of these models, the models have "free" parameters with which to scale the contribution of the polar density to the total strength of the crystal.

Conceptually, this method relies on the assumption that the polar dislocations contribute additively to the statistical density, based on the physical arguments of Ashby (1970), and on the ability to distinguish polar dislocations from a sea of statistical densities. These arguments do not make a very strong case for adopting this method of incorporating an internal length scale. Namely, as shown in the evolution equations for the individual density species in Eq's.3.36 and 3.37, the polar dislocation density does not necessarily increase the mean density. Furthermore, it is impossible to distinguish a "polar" dislocation line from a "statistical" dislocation line in a sea of (possibly polarized) density; therefore it is similarly improper to assign a stronger response to that part of the density.

The first two proposals for directly modifying the dislocation velocity function attempted to increase the denominator of the $|\tau^a|/s^a$ ratio in Eq.'s 4.1and 4.2. The third option for introducing the effects of a polarity of dislocation density into the average dislocation velocity function is to reduce the numerator (applied resolved shear stress) through a back stress. Unlike the statistical dislocation density, polar dislocations are associated with long range stress fields (Hurtado and Weertman,

1995). The stress field of a single dislocation decays with $1/r$, where r is the distance from the dislocation. The stress field of a dislocation dipole decays with $1/r^3$, and the stress fields associated with higher-order statistical multi-poles decay more rapidly than dipoles. The long range stress fields of polar dislocations drive polar densities to organize into twist and tilt boundaries so as to lower their long range stress fields; alternatively, in the presence of an applied stress, the polar dislocations can organize into pile-ups to establish internal stresses that oppose the applied stresses.

The stress fields associated with the polarity of the dislocation density are independent of the level of statistical dislocation density. The back stress associated with polar densities piling up is blind to the level of the mean density, just as the forest obstacle strength as determined by the strength interaction matrix is, on average, blind to the dislocation polarity. Including the effects of the dislocation polarity in a back stress doesn't necessitate an additive polar density. The effect of the back stress is independent of any change in the mean value of dislocation density that may result from the flux divergence of the density species. Furthermore, the back stress doesn't depend on the ability to distinguish a "polar" dislocation from a "statistical" dislocation because it depends on a field property of the density, and not on the interaction between any single dislocation with another.

Two indirect methods of incorporating a material length-scale-dependence could both affect the evolution of the statistical dislocation density in the presence of a density polarity. The average segment length could be made shorter in the presence of a polar density, or the capture radii could become smaller in the presence of a polar density. Both methods would have the effect of increasing the rate of accumulation of statistical dislocations per unit dislocation flux, relative to the rate of accumulation in a homogeneously-deforming crystal, and thus increasing the hardening rate of the crystal. The thermodynamic restrictions of including the material length-scale-dependence in the hardening equations (in this case, the evolution equations of the mean density level) have been investigated by Acharya and Shawki (1996).

The average-segment-length interaction matrix, $H^{\xi\zeta}$, could be polarized in the same fashion as the strength interaction matrix discussed earlier. Just as in the

previous case, a polarization of the average segment length interaction matrix would lead to a difference in the segment lengths between the positive and negative species of a density with same character. Two dislocation densities with the same mean could have different average segment lengths, depending on the level of polarity. A crystal with no polarity of density would lead to the segment lengths being the same for all dislocation densities with the same character on the same slip system. A polarized dislocation density state would lead, in the model, to one density having a shorter segment length and the other having a longer segment length, both compared to the unpolarized crystal with the same total dislocation density. Just as in the analysis of the polarized strength interaction matrix, the longer and shorter segment lengths would tend to offset each other, resulting in a small (if any) net difference in the rate of generation of statistical density in polarized crystals compared to unpolarized crystals.

Another possibility is to associate smaller mobile segment lengths in the presence of polar dislocations by assigning larger interaction coefficients to the absolute polar density than the statistical dislocation density in the average segment length functional form. The modification to the average mobile segment length function could take the form

$$\bar{l}^{\xi}_{(m)} = \frac{1}{\sqrt{H^{\xi\zeta}\left[\left(\bar{\rho}^{\zeta} - \frac{1}{2}|\rho^{\zeta}_{\pm}|\right) + \frac{w}{2}|\rho^{\zeta}_{\pm}|\right]}}\,, \tag{5.17}$$

where w is a coefficient greater than one. The shorter segment lengths in the polarized crystal (compared to the unpolarized crystal) would lead to an increase in the rate of generation of dislocation dipoles in the polarized crystal compared to that in the unpolarized crystal. During the course of plastic deformation, a greater mean density would be present for a given amount of plastic strain in a non-homogeneously deforming crystal than in a homogeneously deforming crystal, and it would appear as though the presence of polar density increased the total dislocation density. This method is analogous to attributing stronger strength interactions to the polar density than to the statistical dislocation density, and it depends on the same assumptions as the previous case; namely, that the polar dislocations are additive and that individual

dislocations can be distinguished as either polar or statistical.

A final possibility is to make the capture radii decreasing functions of polarity. The result of such a function would lead to an increase in the hardening as the polarity increased and to a higher saturation level of dislocation density. For example, a possible functional form of the capture radii could be

$$R_e = R_{e0} - w\sqrt{|\rho_{e\pm}|}b^2 \tag{5.18}$$

$$R_s = R_{s0} - w\sqrt{|\rho_{s\pm}|}b^2 \ , \tag{5.19}$$

where w is a positive coefficient. Although such a functional form could be constructed, there appears to be no good physical argument for making the capture radii functions of polarity. The polarity of the reaction is already present in the two densities that multiply the radius, and the magnitudes of the capture radii are related to the ability of the edge dislocations to climb and of the screw dislocations to cross-slip, respectively. The strongest functional dependence of the capture radii should be on the homologous temperature of the crystal, since the both climb and cross-slip are thermally activated processes.

Including a back stress associated with the polar dislocation density seems to be the most logical method for incorporating the material length scale dependence in the dislocation density-based internal state variable model. Dislocation density pile-ups are related to the spatial variation of the polar dislocation density. A rigorous description of the influence of pile-ups would require investigating the gradients (or more appropriately the curl) of the Nye's tensor throughout the crystal. For computational efficiency as well as modeling simplicity, the contribution of polar dislocation pile-ups will be treated "effectively" (both definitions of the word are intended)[†], based on a simple scaling argument, without using the gradients of the polarity explicitly.

[†]**effectively** (adv.) : 1. In a way producing an intended or expected effect 2. efficiently from The American Heritage Dictionary of the English Language, Third Edition, 1994

The new functional form proposed for the average dislocation velocity becomes

$$\bar{v}^a_{e+} = \bar{v}^a_{e-} = v_{e0} \exp\left[-\frac{\Delta F_e}{k\theta}\left(1 - \left(\frac{|\tau^a_{eff}|}{s_{ep} + s_{ed}}\right)^{p_e}\right)^{q_e}\right] \tag{5.20}$$

$$\bar{v}^a_{s+} = \bar{v}^a_{s-} = v_{s0} \exp\left[-\frac{\Delta F_s}{k\theta}\left(1 - \left(\frac{|\tau^a_{eff}|}{s_{sp} + s_{sd}}\right)^{p_s}\right)^{q_s}\right] , \tag{5.21}$$

where τ^a_{eff} is the effective resolved shear stress, and the rest of the terms are the same as in Eq.'s 4.1 and 4.2. The effective resolved shear stress is related to the applied stress, $\bar{\mathbf{T}}$, and the polar dislocation back stress, $\mathbf{B}$, through the following expression

$$\tau^a_{eff} \doteq \left(\bar{\mathbf{T}} - \mathbf{B}\right) \cdot (\mathbf{m}^a_0 \otimes \mathbf{n}^a_0) \ , \tag{5.22}$$

where the back stress, $\mathbf{B}$, is defined in the intermediate configuration, the same configuration as the second Piola-Kirchhoff stress measure, $\bar{\mathbf{T}}$.

The functional dependence of the polar back stress is motivated by the stress field associated with a single dislocation pile-up. The stress associated with a single pile-up of edge dislocations (from Hirth and Lothe (1982)) is

$$\boldsymbol{\sigma} = \frac{\mu\,|\mathbf{b}|}{2\,(1-\nu)}\frac{N}{L}\left(\mathbf{m}^a_0 \otimes \mathbf{n}^a_0 + \mathbf{n}^a_0 \otimes \mathbf{m}^a_0\right) \ , \tag{5.23}$$

where $\boldsymbol{\sigma}$is the remote value of stress required to get N (polar) dislocations to pile up within a length L, and ν is Poisson's ratio. The ratio L/N can be interpreted as the average spacing between polar dislocation lines, and this spacing can be further related to the magnitude of the dislocation polarity such that Eq. 5.23 could rewritten as a function of the polarity:

$$\boldsymbol{\sigma} = \frac{\mu\,|\mathbf{b}|}{2\,(1-\nu)}\sqrt{|\rho_{e\pm}|}\left(\mathbf{m}^a_0 \otimes \mathbf{n}^a_0 + \mathbf{n}^a_0 \otimes \mathbf{m}^a_0\right) \ . \tag{5.24}$$

In polar dislocation pile-ups, the direction of the pile-up, in terms how the polar dislocations are arranged in the pile-up, determines the direction of the shear stress field. The magnitude of the polarity doesn't contain any information about the gradient of the polar dislocation field. Without considering the polar gradients,

the pile-ups can be assumed to be organized in such a fashion that they oppose the applied stress field. Pile-ups that did not oppose the applied stress would quickly disappear. Also, the form of Eq. 5.24 assumes that all of the polarity organizes into dislocation pile-ups, but the polar dislocations may also form twist boundaries (screw densities), tilt boundaries (edge densities), or other energy minimizing structures, and not form pile-up structures at all. These two considerations lead to the final form of the back stress, $\mathbf{B}$, such that

$$\mathbf{B} \equiv \frac{\mu\,|\mathbf{b}|}{2\,(1-\nu)} \sum_a \sqrt{c\,|\rho^a_{e\pm}|}\,(\mathbf{m}^a_0 \otimes \mathbf{n}^a_0 + \mathbf{n}^a_0 \otimes \mathbf{m}^a_0)\;\; sign\left(\mathbf{m}^a_0 \cdot \bar{\mathbf{T}}\mathbf{n}^a_0\right) \tag{5.25}$$

where c is a "free" parameter setting the fraction of the total polar density leading to a back stress. Since the applied stress, $\bar{\mathbf{T}}$, enters into the expression for the back stress, the model is only valid for monotonic loading histories.

The rest of the constitutive equations follow the same form as the constitutive equations used in the simulation of the aluminum single crystals. The dislocation resistance takes the form of Eq. 4.4, but now, with only two interaction coefficients, G_0 and G_1. The coefficient G_0 quantifies the interactions between gliding density and dislocations on parallel slip planes with the same Burgers vector. The coefficient $G_1 = g_1 \left|\mathbf{n}^\xi_0 \cdot \mathbf{t}^\zeta_0\right|$ quantifies the interactions of the gliding dislocation density with density on the other slip plane. In this simplified double-slip geometry, the screw dislocations are the only dislocations which pierce the slip planes; therefore, there will be no resistance contribution from the out-of-plane edge densities.

The same functional form will be used to capture the average segment length in this idealized geometry as was used in the simulation of aluminum single crystals. The functional form of Eq. 4.5 requires the definition of two interaction coefficients, H_0 and H_1. The coefficient H_0 quantifies the dependence of the average segment length on the in-plane dislocation density, and the coefficient $H_1 = h_1 \left|\mathbf{n}^\xi_0 \cdot \mathbf{t}^\zeta_0\right|$ quantifies the dependence of the average segment length on the out-of-plane dislocation density. As with the strength interaction matrix, the average segment length has no dependence on the out-of-plane edge density because the latter do not pierce the slip plane.

The capture radii will take simple functional forms as in the simulations conducted for aluminum single crystals, again. Since the simulations are conducted at room temperature, and isothermal conditions are imposed, the capture radii will be modeled as constants. The radius R_e will be used to scale the annihilation rate of edge dislocations, and the radius R_s will be used to to scale the annihilation rate of screw dislocations.

Since the back stress associated with the polarity of the dislocation density was treated in an effective manner by relating the magnitude of the dislocation polarity to an internal stress level, instead of by developing a more rigorous functional form based on appropriate gradients of the polarity, the size of the representative volume element (RVE) must be sufficiently large so that the mean value of density is much larger than the polarity of the density. Although the polarity of the dislocation density is not assumed to be additive to the total dislocation density, the method relies implicitly on the ability to distinguish collections of polar dislocations from collections of statistical dislocations in a volume.

5.3 Finite Element Implementation of Non-Local Constitutive Model

Unlike the finite element implementation of the local constitutive model that the necessitated the development of a user-material subroutine (UMAT) for ABAQUS/ Standard, the finite element implementation of the non-local constitutive model requires the development of a user-element subroutine (UEL) for ABAQUS/Standard (Hibbitt et al., 1998). The development of a user-element is needed because the calculation of the polar accumulation/loss equations depends on the plastic activity at multiple material points, and the ABAQUS UMAT interface does not contain information about the state at other material points.

A modified 8-node iso-parametric reduced integration (CPE8R) element was developed for the length-scale-dependent simulations. The development of a UEL can

be broken into two components: the non-local material definition, and the calculation of the nodal forces and the element stiffness matrix from the stress state and material jacobian at the material points. The procedure of the second component is standard in finite element calculations (Bathe, 1996); therefore, the discussion will concentrate on the non-local material definition.

The time integration procedure for the non-local material model follows basically the same procedure as the time integration procedure developed for the local material model in Section 4.3.1. The difference is in the incorporation of the equations leading to the polarity of dislocation density. The technique for evaluating $\dot{\mathbf{A}}^{\xi}$ from the rates of plastic deformation at the material points in the element adopted in the simulation was developed by Dai (1997). The calculation method involves using the finite element shape functions to map the time rate of change of the plastic deformation gradient from the four Gaussian integration points to the corner nodes of the element, then using the derivatives of the shape functions to find $\dot{\mathbf{A}}^{\xi}$ at the center of the element. The time rate of change of Nye's tensor is approximated to be constant within the element so the value of $\dot{\mathbf{A}}^{\xi}$ calculated at the center of the element is transferred to the four Gaussian integration points, and then the time rate of change of the dislocation density state is calculated at each of the four Gaussian integration points. The calculation scheme is illustrated in Figure 5-6.

The approximation of a constant value of $\dot{\mathbf{A}}^{\xi}$ leads to a constant polarity of the edge dislocation densities within an element. The mean edge dislocation density at a material point is not constrained by the mean edge densities at the other material points within the element. The constant polarity leads to a constant level of the back stress as calculated through Eq. 5.25; therefore, the calculation of the back stress is done explicitly, and is not included in the implicit iterative solution of the crystallographic dislocation density state and stress.

The calculational procedure for the crystallographic density state, $\rho^{\xi}(\tau)$, Cauchy stress $\mathbf{T}(\tau)$, and the plastic deformation gradient, $\mathbf{F}^{\mathrm{p}}(\tau)$ at time $\tau = t+\Delta t$, given the the crystallographic density state, $\rho^{\xi}(t)$; Cauchy stress, $\mathbf{T}(t)$; the plastic deformation gradient, $\mathbf{F}^{\mathrm{p}}(t)$; the total deformation gradient, $\mathbf{F}(t)$, all at time t, as well as the total

deformation gradient, $\mathbf{F}(\tau)$, is outlined as follows:

Step 1 Using Eq. 4.17, calculate $\bar{\mathbf{T}}^{tr}$ and $\mathbf{C}^{a}$. With Eq. 5.25, calculate $\mathbf{B}_{\text{old}} = \mathbf{B}(t)$ using $\rho^{\xi}(t)$ and $\bar{\mathbf{T}}(t)$. Make initial guesses for $\bar{\mathbf{T}}(\tau)$ and $\rho^{\xi}(\tau)$ using Eq.'s 4.26 and 4.27, respectively.

Step 2 Calculate $\bar{\mathbf{T}}(\tau)$ and $\rho^{\xi}(\tau)$ through Eq. 4.23 using the backward Newton method. The calculation is performed on all the material points within an element simultaneously so as to include the polar accumulation/loss terms in the crystallographic density evolution. Note: the partial derivatives of the average dislocation velocity with respect to the polarity of the dislocation density in the back stress are not included in the $\mathcal{F}$-matrix.

Step 3 Using the values of $\bar{\mathbf{T}}(\tau)$ and $\rho^{\xi}(\tau)$ calculated in Step 2, calculate a new value for the back stress, $\mathbf{B}_{\text{new}}$. If the difference between $\mathbf{B}_{\text{new}}$ and $\mathbf{B}_{\text{old}}$ is larger than a tolerance level, set $\mathbf{B}_{\text{new}}$ to $\mathbf{B}_{\text{old}}$ and repeat Step 2, else proceed to Step 4.

Step 4 Update the state. Using Eq. 4.12, calculate $\mathbf{F}^{\text{p}}(\tau)$. Using Eq. 3.1, calculate $\mathbf{F}^{\text{e}}(\tau)$. Finally, using Eq. 3.6, calculate $\mathbf{T}(\tau)$.

The non-local material jacobian is approximated by the local material jacobian outlined in Section 4.3.2. The partial derivatives of the average dislocation velocity with respect to the dislocation polarity associated with the back stress are not included in the material jacobian.

5.4 Selection of Material Parameters

The material constants of the idealized double slip crystal were chosen in such a way as to capture the evolution of the mechanical properties and dislocation density of a real crystal during plastic deformation. The crystal that was chosen was aluminum since it was the focus of the simulations conducted with the "local" model in Chapter 4, and the parameter space of the three-dimensional model provided a starting point for the reduced parameter space in this simple two-dimensional model.

In the three-dimensional model, the material parameters were found by fitting the anisotropic stress/strain behavior in the plastic deformation from four different initial orientations. A similar procedure will be used to fit the parameters of the simplified double slip model.

The double slip geometry has a limited set of orientations that can be related to the stress/strain behavior of the three-dimensional crystal. The $\phi = 0°$ and the $\phi = 90°$ orientations (with respect to a T_{22} tensile stress) are the only orientations in which both slip systems are equally active in tension. Furthermore, both orientations yield the same stress/strain curve because of the plane strain boundary conditions. The rest of the orientations lead to one slip-system being favored over the other. To span all of the stress/strain space of the real crystal with the double slip crystal, the plastic behavior of the 0° orientation of the double-slip model was fit to the plastic behavior of the $< 111 >$-oriented single crystal, and the plastic behavior of the 15° orientation of the double-slip model was fit to the plastic behavior of the $< 123 >$-oriented single crystal. The 15° orientation of the double slip model maximizes the Schmid factor on one of the slip-systems leading to single-slip behavior like the $< 123 >$-oriented single crystal.

As in the local model, the edge and screw dislocation densities were assumed to have the same mobility. Furthermore, the same values of $\bar{v}_0$, ΔF, p, q, and s_p will be used in this two-dimensional crystal as were used in the three-dimensional simulations. The anisotropic elastic constants were also taken from the three-dimensional simulations, leaving as "free" parameters the strength interaction coefficients, average segment length interaction coefficients, the capture radii, and the dislocation pile-up fraction, c.

The strength interaction coefficients, average segment length interaction coefficients, and the capture radii control the plastic evolution of the bulk crystal as demonstrated in Chapter 4. These parameters were determined by fitting the two orientations of the planar crystal corresponding to multi-slip and single slip to the stress/strain behavior of the $< 111 >$- and $< 123 >$-oriented crystals, respectively, while simultaneously evolving the reduced density basis over four orders of magnitude

to achieve statistical density levels representative of real crystals. The results of the fitting can be found in Figure 5-5 in terms of the stress/strain response of the model compared to the experimental values for the two orientations.

Both the strength and average-segment-length interaction coefficients in real crystals are restricted in magnitude to be less than unity. A strength coefficient equal to one entails that the gliding dislocation line is unable to cut through an obstacle and must therefore loop completely around the obstacle to pass, leaving a dislocation loop around the uncut obstacle in the process. In this idealized two-dimensional crystal, the restrictions on the interaction coefficients must be relaxed so that the stress and density levels in the real crystal can be achieved. The capture radii must be decreased also so that individual dislocation densities in the reduced basis can reach greater levels than the crystallographic densities in the real crystal, leading to comparable total dislocation density measures. Although there are no planes in this limited geometry for the screw dislocations to cross-slip on, cross-slip is nonetheless assumed to occur as a mechanism for screw dislocation annihilation, while climb occurs for edge dislocation annihilation, leading to a larger capture radius for the screw dislocation density than the edge dislocation density.

The final material parameter which must be set is the polar dislocation density pile-up fraction, c. The value of this parameter is restricted to lie between zero and unity. A value of zero indicates all of the polar dislocation density organizes spatially into low energy structures like tilt and twist boundaries that carry no long range stress field. A value of unity indicates that all of the polar dislocation density piles-up and leads to long-range stresses in the material. In general, the c parameter will depend on the kinetics of the deformation: the ability of polar dislocations to organize into low energy structures while interacting with the overwhelmingly (in number) statistical dislocation density that frustrates their organization. Since no spatial information of the polar density is supplied in the finite element framework adopted in this study, a constant value for the polar dislocation density pile-up fraction was chosen that led to a magnitude of material length-scale-dependence in the stress/strain behavior of the idealized crystal that was comparable to the dependence found in experimental

observations.

The constants used to model the behavior of thin single-crystal beams in bending can be found in Table 5.1. Along with the material parameters, the initial conditions which must be set for the simulation are the initial dislocation density profile, the temperature, and the orientation angle ϕ.

5.5 Simulation of Plane Strain Bending

Plane strain bending of single crystals was simulated to investigate the length-scale-dependence of crystal plasticity, and the interaction between the statistical dislocation density and the polarity of the dislocation density. Six different beam thicknesses were simulated: 12.5μm, 25μm, 50μm, 100μm, 200μm, and 400μm. Along with those six simulations, a baseline simulation was conducted that did not incorporate any material length-scale dependence. Labeled "Local Theory," this simulation did not calculate the dislocation polarity (thereby setting $\rho_{\pm} = 0$), and it is equivalent to calculating the response of an infinitely thick beam.

The simulation was conducted on a beam discretized into 864 user-defined finite elements as shown in Figure 5-7. The boundary conditions placed on the beams imposed a condition of pure bending in the beam section. The left boundary of the section was required to remain vertical, but allowed to contract as required by the plane strain deformation. The bottom left node was pinned to prevent rigid body translation of the beam section. The right side of the beam section was subject to a user-defined multi-point constraint (Hibbitt et al., 1998). The applied boundary condition required all of the nodes on the right side to be co-linear along a line with a specified slope but with an unspecified y-intercept. The imposed boundary conditions lead to a stress state with a net bending moment and with no net force at the ends of the beam section.

To maintain the geometric and dynamic similarity of the bending beams over the length scales spanned by the simulations, the deformation was applied with a constant surface strain rate of $\dot{\epsilon} = 0.001$ s^{-}1 to a level of ten percent surface strain.

The time rate of curvature change in the beams increased with decreasing beam thickness, but the strain rates across the sections of the beam remained unchanged as the beam thickness decreased. Therefore, the rate dependence of the stress/strain response did not augment the length scale dependence in the simulations. In the experiments conducted by Stölken and Evans (1998), there is no report that such care was taken to maintain dynamically similar deformation paths in their thin beam bending experiments other than commenting that the "die was displaced slowly."

The initial material state of the beam as quantified by the density, the orientation, and temperature was similar to the state adopted in the aluminum simulations. The total initial density was $\rho_0 = 10^{12}\ \mathrm{m}^{-2}$, and it was split evenly among the eight discrete dislocation densities in the model. Half of the density was of edge character and the other half was of screw character, as in the aluminum simulations, and furthermore, there was no initial polarity in the crystal, meaning that the positive and negative species of each dislocation type had the same initial densities. The distribution of the dislocation density in the crystal was homogeneous. The crystal was oriented symmetrically with respect to the tension/compression loading in the bending beam. According to the slip system geometry given in Figure 5-2 and the coordinate axis given in Figure 5-7, the angle ϕ for the simulations was 90°. The simulations were conducted at ambient temperatures of 298 K, and isothermal conditions were assumed during the course of the deformation of the beams.

5.6 Results and Discussion

The length-scale-dependent mechanical response of the beam subject to plane strain bending is shown in Figure 5-8 for beams ranging in thickness from 12.5 μm to 400 μm. The bending moments calculated are normalized in the same manner found in Stölken and Evans (1998), where the bending moment is divided by the beam thickness squared and the tensile yield strength of the $< 111 >$ orientation, $s_0 = 5$ MPa, of the crystal. A curve labeled "Local Theory" is also included, representing the mechanical behavior of an infinitely thick beam. This baseline curve is the normalized

moment/surface strain response that would be predicted without incorporating any material length scale dependence. As shown in Figure 5-8, the normalized moment at a given value of the surface strain increases as the beam thickness decreases.

A benefit of the simulation is that the limiting behavior for infinitely thick beams can be easily calculated. The experimentalists do not have this ability, but with the direct availability of the baseline value, an alternate normalization that isolates the length-scale-dependence from the bulk behavior can be performed. Consider Figure 5-9 in which the bending strength has been normalized with respect to the baseline bending strength determined by the local theory. The plot shows the same pattern as in Figure 5-8, in which the thinner beams are predicted to have stronger responses. The 12.5 μm beam shows a sixteen percent increase in bending strength over the behavior of the beam calculated with the local theory.

By incorporating the beam thickness in the vertical scale, all of the normalized bending strength curves in Figure 5-9 can be collapsed onto a single master curve as shown in Figure 5-10. The length-scale-dependence can be reduced to a simple function of the form:

$$\left(\frac{M/h^2 - M_o/h_o^2}{M_o/h_o^2}\right)\left(\frac{h}{|\mathbf{b}|}\right)^{\frac{1}{2}} = f(\epsilon_s) \ , \tag{5.26}$$

where M is the bending moment for a beam of thickness h, M_o/h_o^2 is the bending strength in the infinite limit of thickness, and ϵ_s is the surface strain. The expression in Eq. 5.26 can be rearranged into a more familiar Hall-Petch (Hall, 1951; Petch, 1953) type expression:

$$\sigma = \sigma_o + kh^{-m} \ , \tag{5.27}$$

with

$$\sigma = M/h^2$$

$$\sigma_o = M_o/h_o^2$$

$$k = fM_o/h_o^2|\mathbf{b}|^{\frac{1}{2}}$$

$$m = \frac{1}{2} .$$

Incorporating the length-scale-dependence by appealing to polar dislocation pile-ups naturally leads to a Hall-Petch exponent $m = 1/2$ that remains constant with decreasing beam thickness. In the model, the exponent is fixed because the back stress associated with the dislocation pile-ups is proportional to the square root of the polarity of the dislocation density, and the polarity scales linearly with the beam curvature.

Figure 5-10 shows that the thinnest beams simulated, 12.5 μm and 25 μm, follow the trend of the calculations conducted for the thicker beams, but there is quite a bit of noise in the calculated response. Comparing Figure 5-8 and Figure 5-10, the noise that appears in the first figure does not appear to be large in magnitude compared to the value of normalized bending moment, but the subsequent normalization magnifies the noise by normalizing the bending strengths with respect to the local theory calculation. An explanation for the noise will be offered later in the section when contour plots of the bent beams are presented and discussed.

The length-scale-dependence calculated in these simulations can be understood better by inspecting the dislocation density evolution in the deforming beams in gross measures of statistical density and polarity. Figure 5-11 depicts the average dislocation density in the beams as a function of the surface strain. The average density was calculated by summing all of the "crystallographic" densities at every material point in the crystal, and then calculating a body average from the material point totals. As argued Section 5.2, the total density at a given accumulated dislocation flux may not change appreciably as a result of increasing polarity. The total density scales with the accumulated strain, which is the same for all of the beam thicknesses simulated, as in the aluminum simulations.

Weertman (1996) has argued that the redundant (SSD) density evolution is connected to the non-redundant (GND) density state of the crystal. Through questionable physical arguments about the mobility of the non-redundant density state of the crystal, Weertman argues that the redundant density must always be greater than

the non-redundant density in the crystal. Despite the physical reasoning, it is the only instance in the literature where the evolution of the of the statistical density is considered to be a function of the polarity in the crystal. Within the framework of the present model, the accumulation rate of statistical density could have been augmented by making either the average segment lengths or the capture radii decreasing functions of dislocation polarity. Currently there are no clear physical justifications, Weertman's arguments notwithstanding, for including such a dependence in the average segment length or capture radius functions.

Figure 5-12 depicts the magnitude of the polarity of the dislocation density, as a function of surface strain, for the six beam thicknesses simulated. The average dislocation density polarity was calculated in a manner similar to the average dislocation density. The magnitudes of the polarity in both "crystallographic" edge densities were summed at each material point, and then a body average was calculated from the material point totals. For each of the beams the dislocation polarity increases linearly with surface strain. All of the lines in Figure 5-12 have a y-intercept of zero since the initial conditions were set with no initial polarity. The slopes of lines increase with decreasing beam thickness. If the average dislocation polarity is plotted against the beam curvature as shown in Figure 5-13, the dislocation polarity for all of the beams collapses onto one linear curve. As expected from Eq. 2.28, the dislocation polarity scales linearly with the curvature of the beam. As shown in Figure 5-11 the total density in the beams scales with the plastic deformation, parameterized by the surface strain in this measure.

Comparing average dislocation density with the dislocation polarity found in Figures 5-11 and 5-12, respectively, for the 12.5 μm beam, the dislocation polarity accounts for only 1.5% of the total dislocation density. The overwhelming majority of the density, 98.5%, is statistical in nature. Although the polar dislocations are dominated in number by the statistical density, their influence on the mechanical behavior is substantial. In fact, Figure 5-9 shows that the dislocation polarity that was only 1.5% of the total dislocation density led to a strengthening of 16% as measured by the normalized bending strength: a tenfold relative difference. If the Ashby model

of length-scale dependence had been adopted by considering the polar density as "additive" and "immobile", the difference in the normalized bending strength would be on the order of half the relative dislocation polarity, and definitely not ten times greater. The experimental literature that focuses on the length-scale-dependence of crystal plasticity found in the bending of thin films (Stölken and Evans, 1998), the torsion of thin wires (Fleck et al., 1994), or micro-indentation (Nix and Gao, 1998) does not support the small change in magnitude of the normalized strength measures that an obstacle-based incorporation of polar density would predict. The change in the magnitude of the normalized strengths measures observed in these experiments is much larger than half of the relative dislocation polarity.

The order of magnitude disparity between the relative magnitude of the dislocation polarity and its relative effect on the strength/strain evolution suggests that the SSD density and the GND density play different roles in the evolution of strength during plastic deformation. Indeed, Hurtado and Weertman (1995) suggest that the SSD's should be distinguished from the GND's like "apples from oranges" because of their differing influences on mechanical behavior. Again, it is impossible to assign a label, SSD or GND, to any one dislocation that is part of a larger density, but on the density level, it is clear that the density mean and the density polarity must be treated differently to model the material length-scale effects observed in the plastic deformation of crystals on the micron scale.

Figure 5-14 contains a contour plot of the von Mises equivalent stress in the 12.5 μm beam after 10% surface strain. The contour plot shows that the largest stresses are found in the outer surfaces of the beam where the most plastic deformation occurs. The stresses not only vary through the thickness of the beam, as expected in homogenous bending, but also vary along the length of the beam. The variation along the length of the beam is larger on the compressive side of the beam than on the tensile side.

A similar variation can be seen in the total dislocation density. Figure 5-15 contains a contour plot of the total dislocation density in the 12.5 μm beam after 10% surface strain. The largest densities are found on the outer surfaces where the most

plastic deformation occurs. Through the thickness of the beam, the dislocation density spans over two orders of magnitude at the end of the simulation. The dislocation density was homogeneously distributed through the crystal at the onset of the simulation. At the end of the simulation, the density varies both through the thickness and across the length of the beam. The variation of density along the thickness is due to the difference in the magnitude of the plastic deformation of the beam. The variation along the length of the beam is due to a corresponding variation in the plastic deformation along the length.

The contour plot of the magnitude of the dislocation polarity in the 12.5 μm beam after 10% surface strain can be found in Figure 5-16. The non-homogeneous distribution of the density polarity is more striking than the total dislocation density contour. The polarity of the dislocation density scales with the plastic curvature of the beam, and not with the (surface) level of plastic deformation in the beam. The average polarity is directly proportional to the average curvature of the beam, as shown in Figure 5-13, but the polarity is not homogeneously distributed through the section. The non-homogeneity is more pronounced in the part of the crystal under compression than in the part of the crystal under tension. The two-dimensional crystal under compression breaks a material symmetry, like certain orientations of the three-dimensional aluminum simulations in tension.

The two slip systems in the planar model are separated by an acute angle of 60° and an obtuse angle of 120°. The initial orientation of the crystal was such that the acute angle between the slip-systems was bisected by the beam direction, and the obtuse angle between the slip-systems was bisected by the thickness direction. This particular symmetric orientation is stable in tension but unstable in compression. In tension, if one slip-system has more slip activity than the other, then the crystal rotates so as to increase the Schmid factor on the less active system and decrease the Schmid factor on the more active system. In compression, the opposite is true. If one slip-system has more slip activity than the other, then the crystal rotates so as to increase the Schmid factor on the more active system, and decrease the Schmid factor on the less active system.

The non-homogeneous distribution of stress and density across the length of the beam is due to the compressive instability of the double slip geometry. The boundary conditions of the bending deformation imposed don't allow for a single slip deformation mode to propagate globally through the crystal, but locally the slip activation on the two systems may differ leading to the behavior seen. The noise that appears in the bending strength found in Figure 5-9 corresponds to the initiation of these events in the part of the crystal under compression.

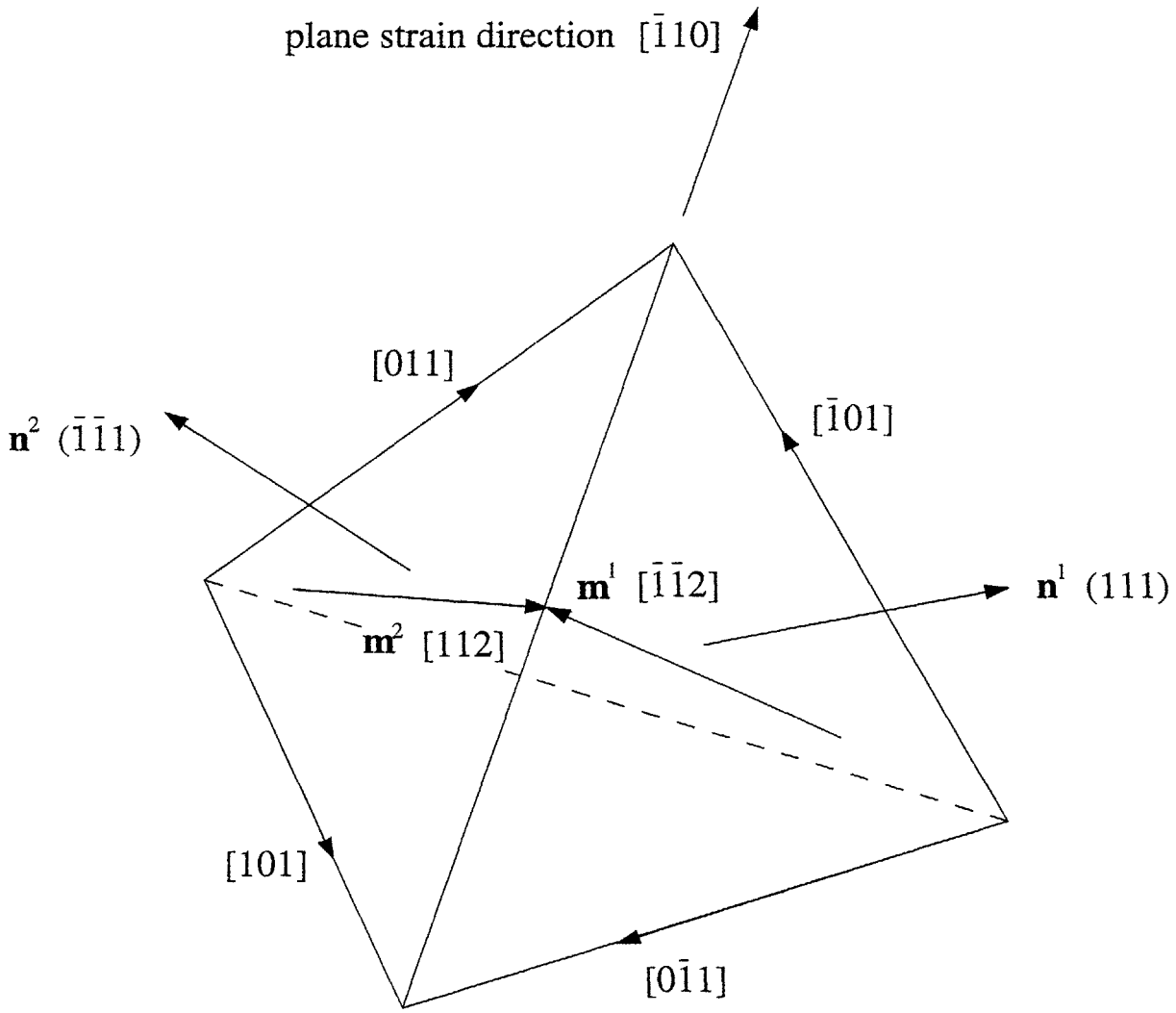

Figure 5-1: The special orientation of FCC crystals that leads to adoption of two effective slip-systems in the idealized plane strain model.

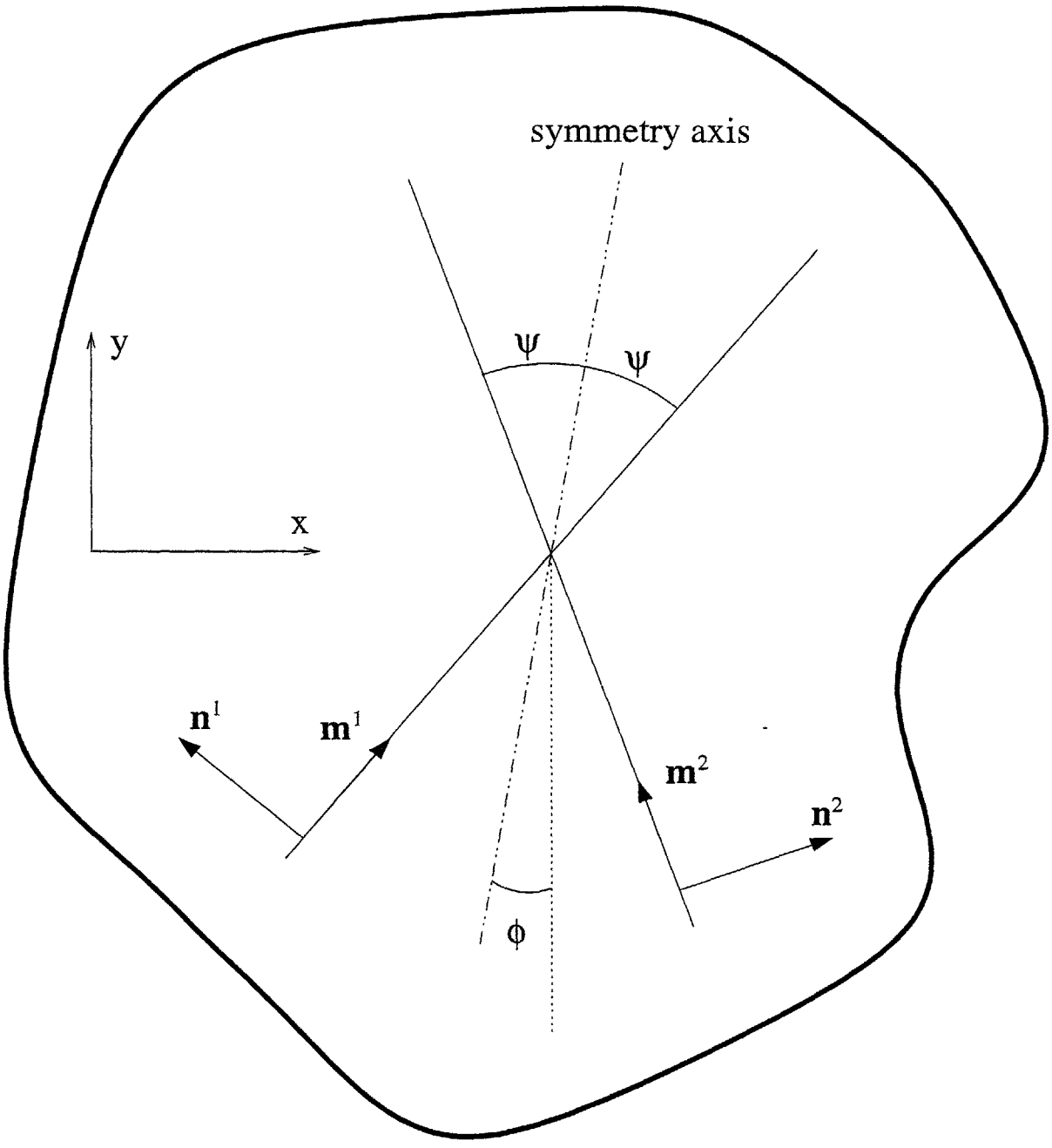

Figure 5-2: A schematic depicting the orientation angle ϕ, and the orientation of the two slip-systems in the model relative to that angle.

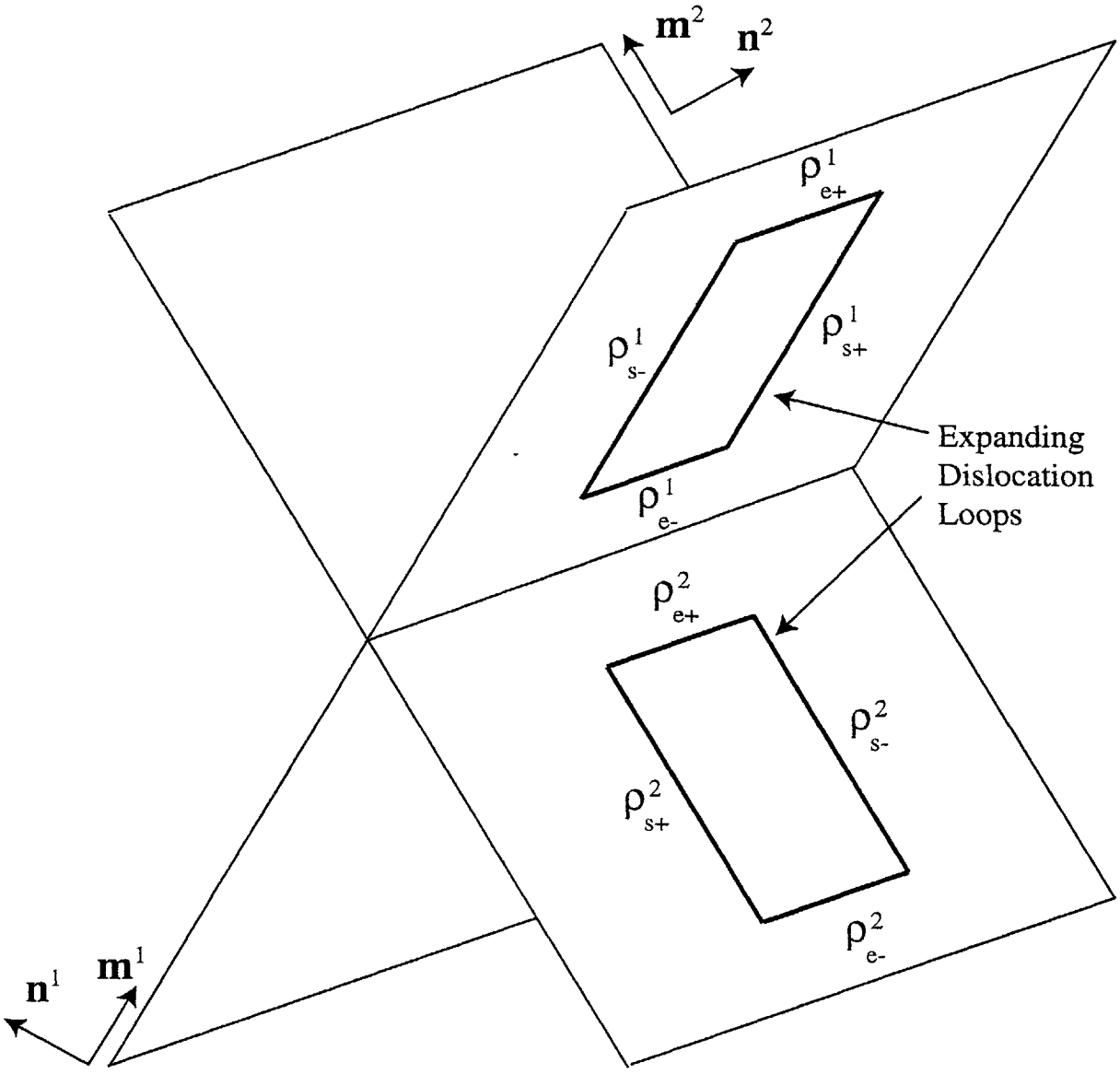

Figure 5-3: The dislocation density geometries included in the plane strain double-slip geometry.

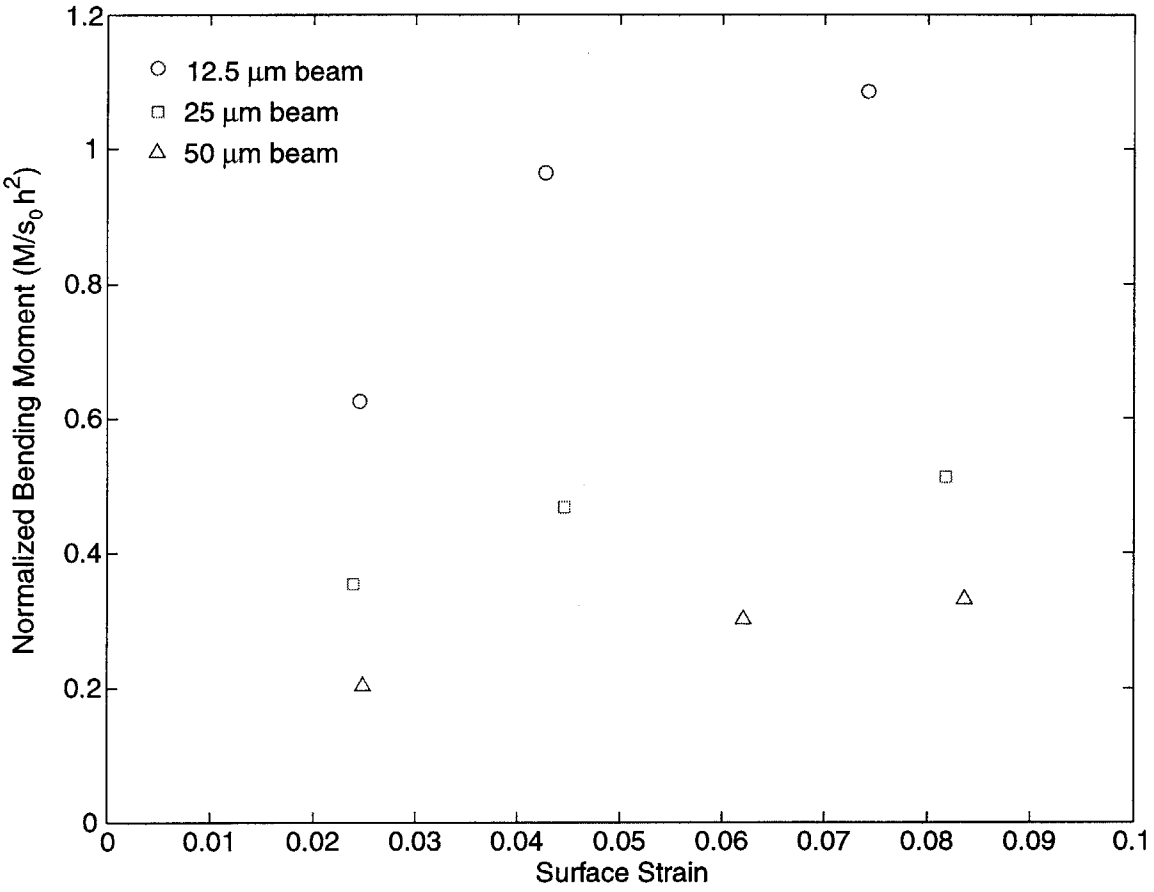

Figure 5-4: Normalized bending moment versus surface strain from the experimental study of Stölken and Evans (1998) on thin films of nickel polycrystals.

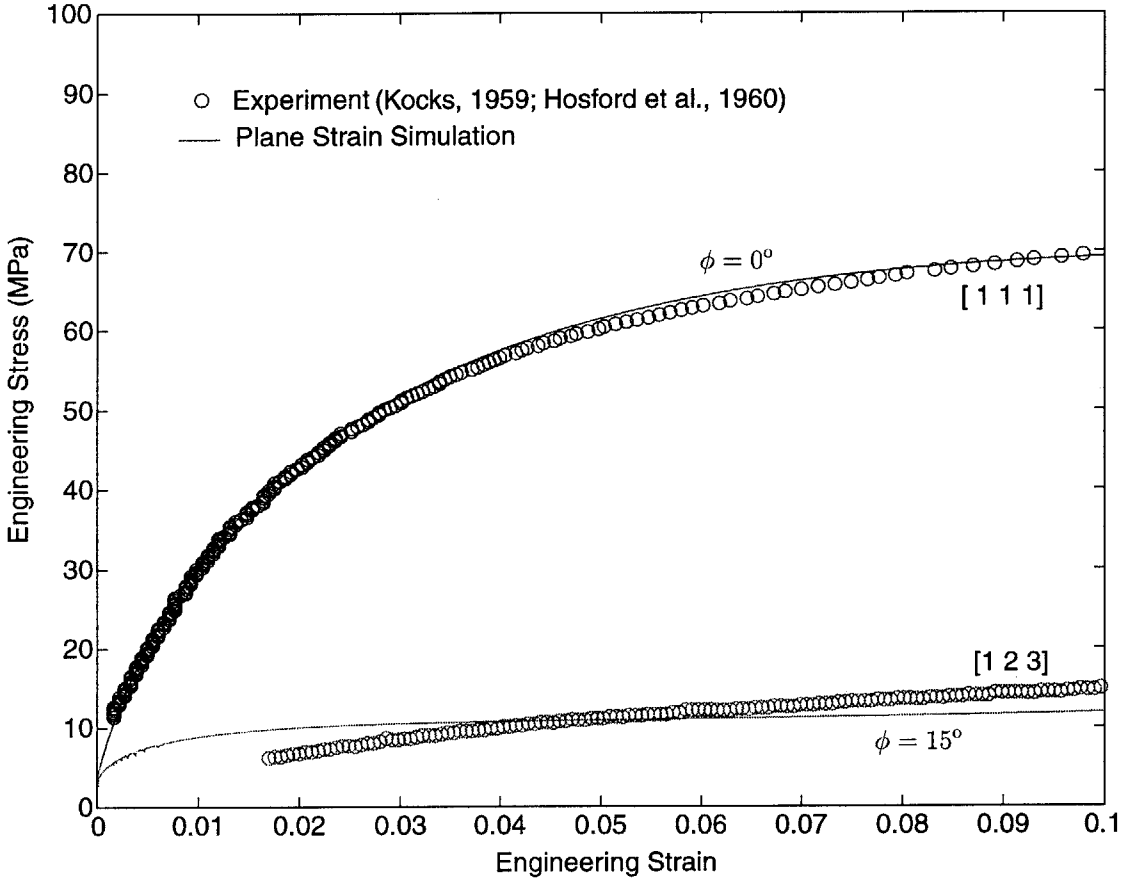

Figure 5-5: Stress/strain fit of two orientations of the double-slip model with the experimentally determined values of $< 111 >$- and $< 123 >$-oriented single crystals in tension.

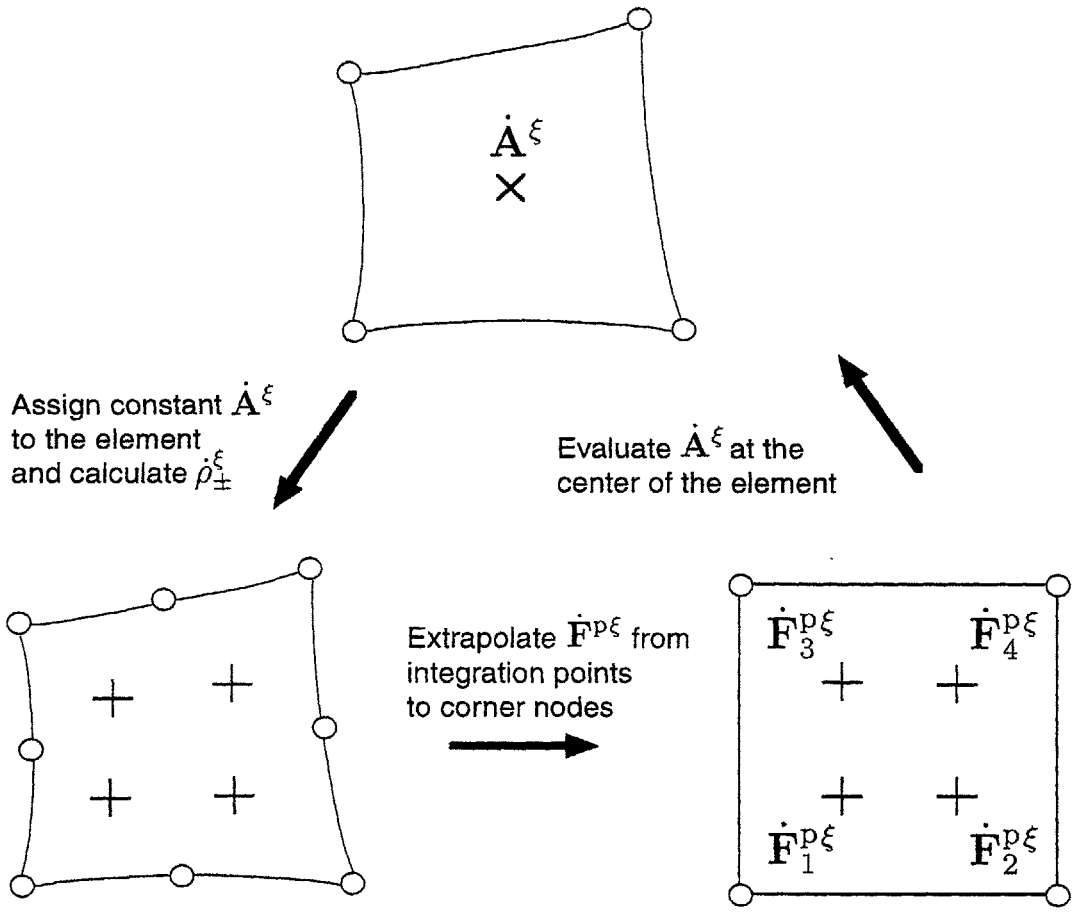

Figure 5-6: Schematic of the computational procedure for calculating the polarity of the dislocation density based on the interpolation of the species components of the time rate of change of the plastic deformation gradient using a modified 2-D isoparametric brick element with reduced integration.

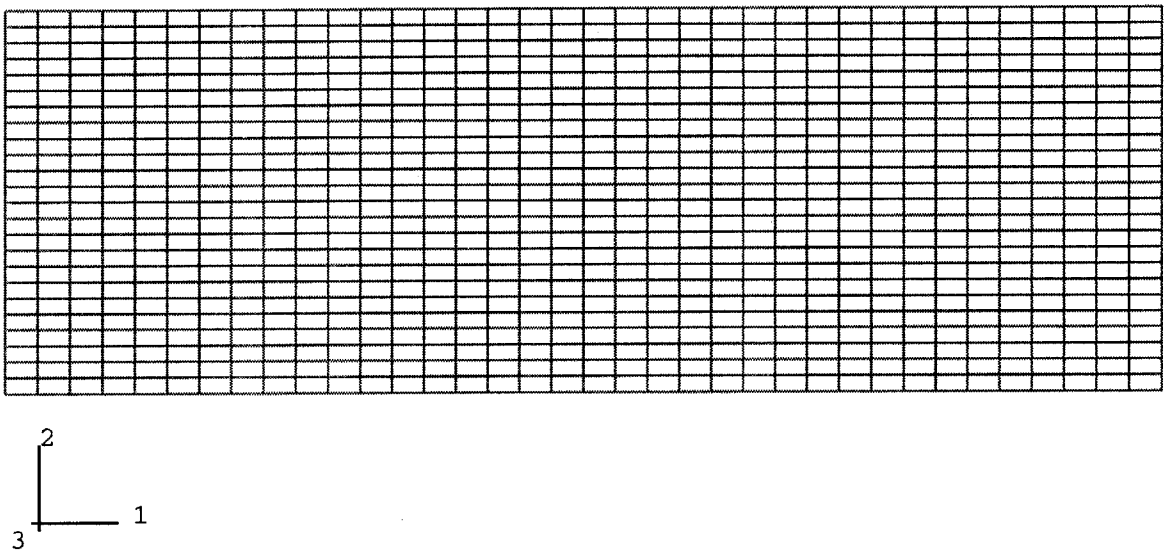

Figure 5-7: Finite element discretization of a planar single crystal beam used to simulate the material length-scale dependence in the plane-strain bending behavior of thin beams.

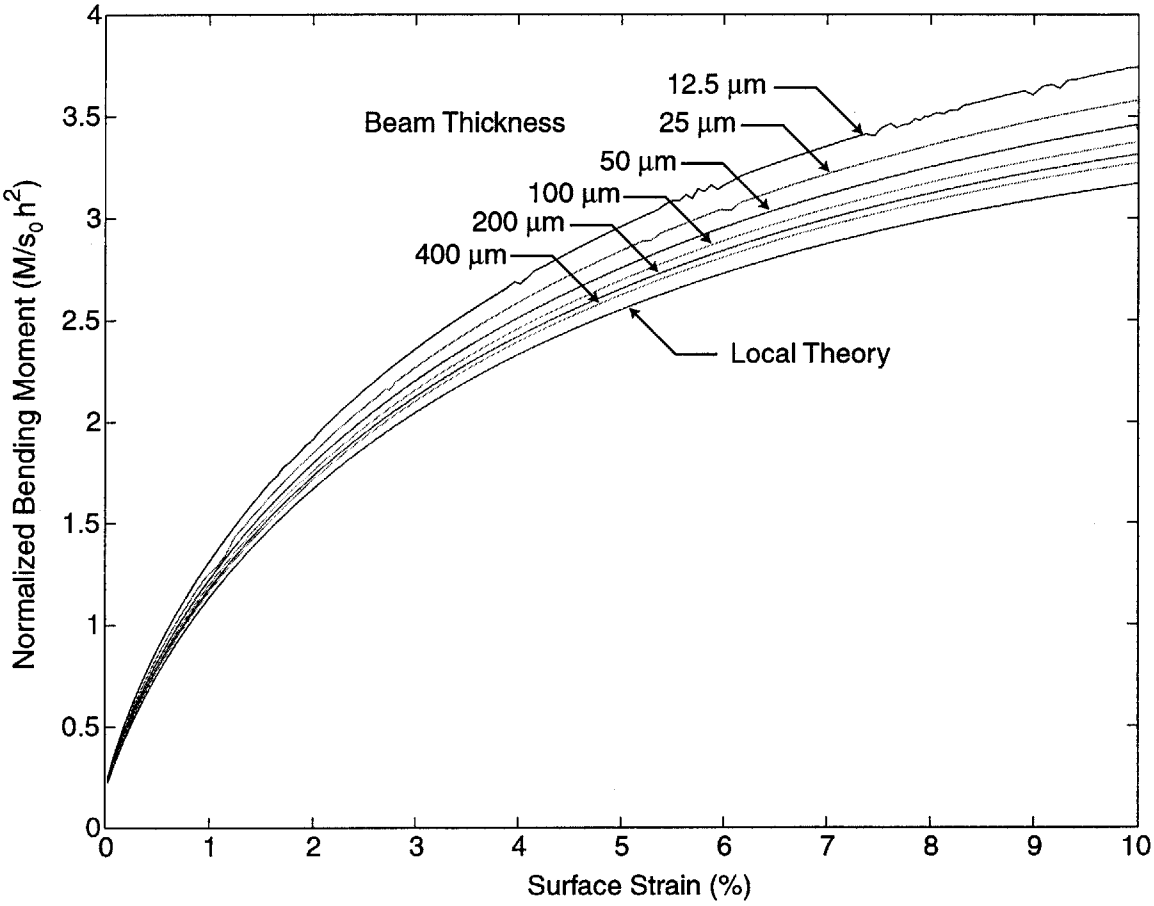

Figure 5-8: Normalized bending-moment showing the material length-scale-dependence observed in thin beam bending. No length-scale-dependence would lead to a single normalized bending-moment/surface-strain curve corresponding to the line labeled "Local Theory."

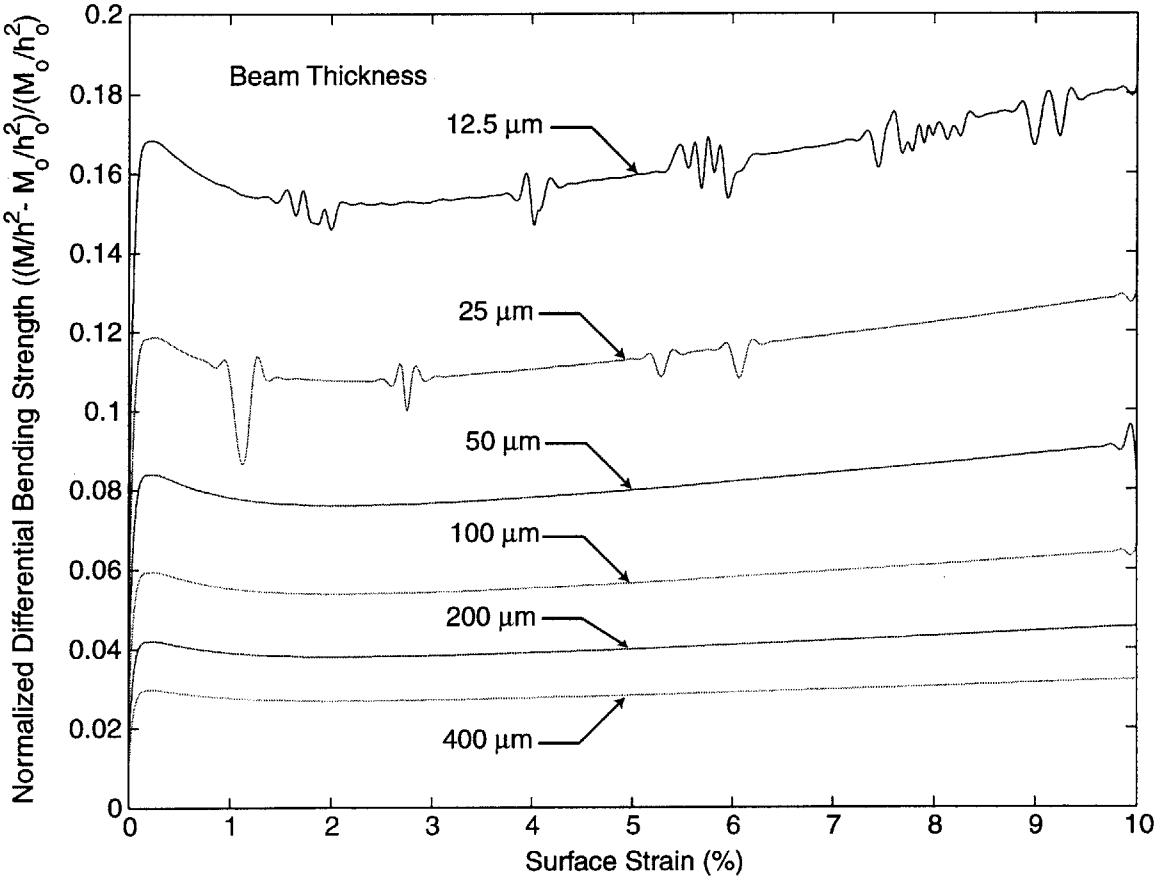

Figure 5-9: The bending moments simulated in beams varying in thickness from 12.5 μm to 400 μm, normalized with respect to the moment calculated by the local theory, as a function of the surface strain.

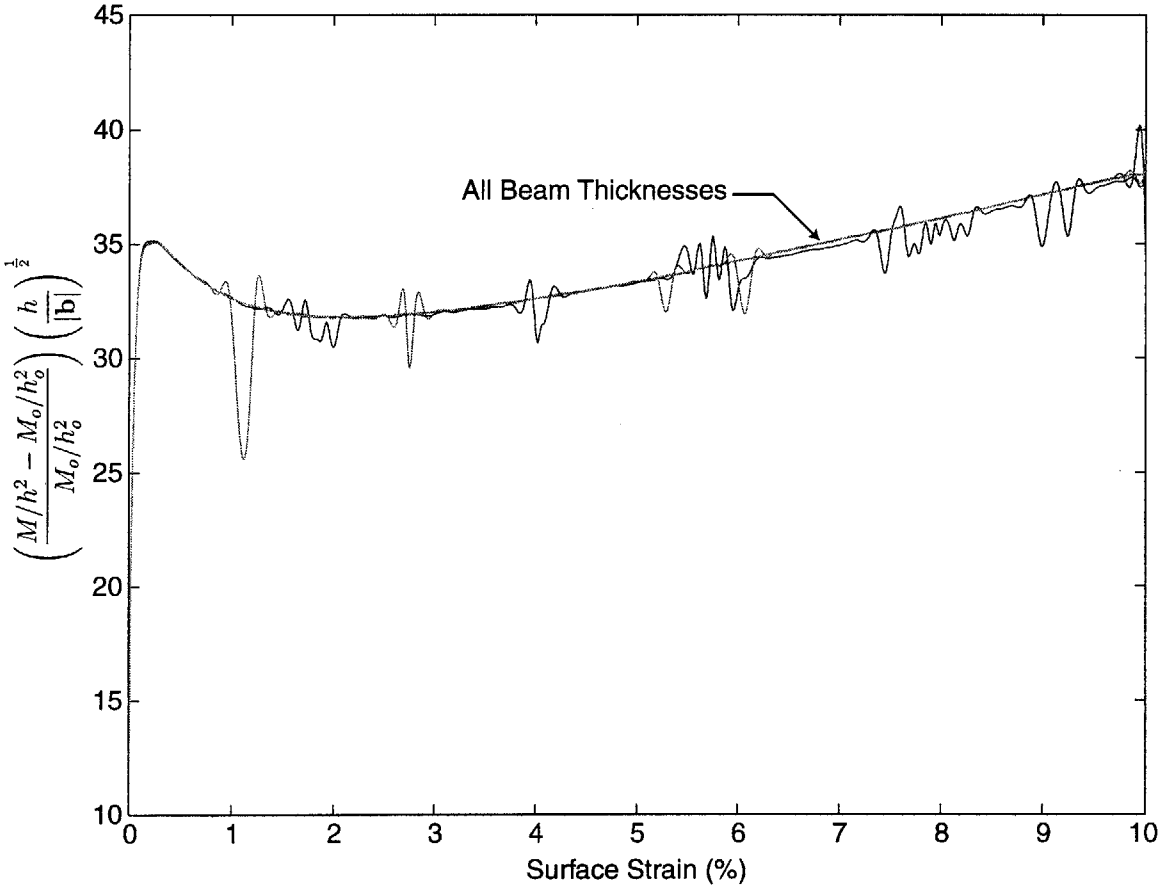

Figure 5-10: Plot of $(M/h^2 - M_0/h_0^2)/M_0/h_0^2(h/b)^{0.5}$ versus surface strain showing that the bending moments calculated for different thicknesses reduce to a generalized Hall-Petch type relationship.

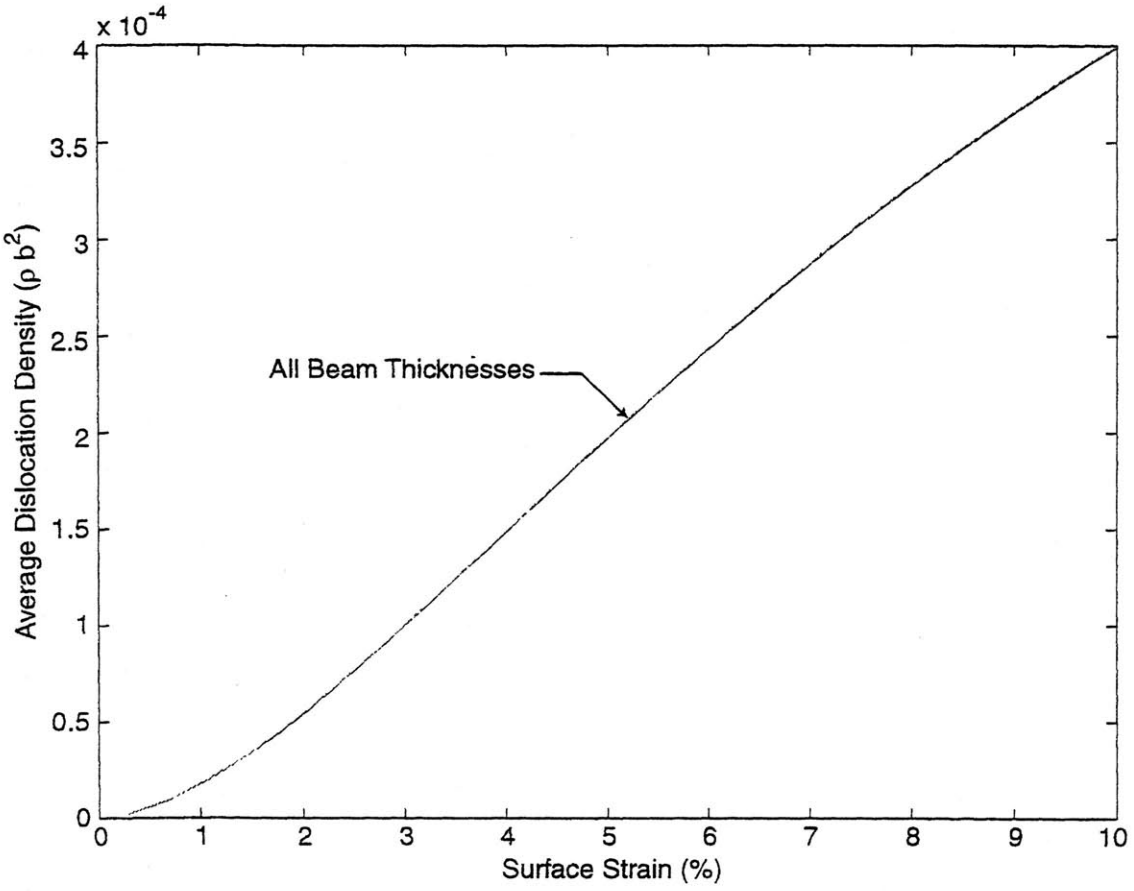

Figure 5-11: Average dislocation density as a function of surface strain for beams ranging in thickness from 12.5 μm to 400 μm.

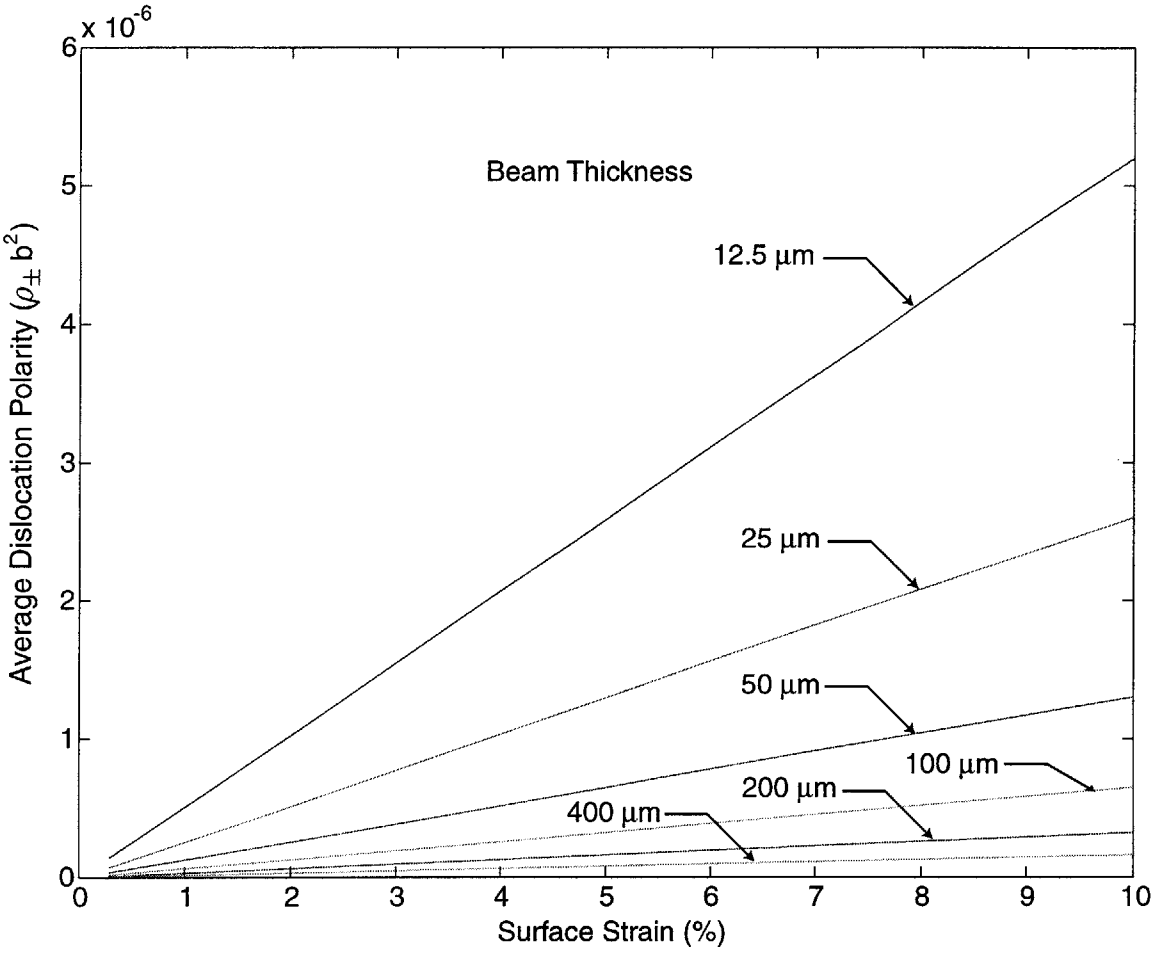

Figure 5-12: Average polarity of the dislocation density as a function of surface strain for beams ranging in thickness from 12.5 μm to 400 μm.

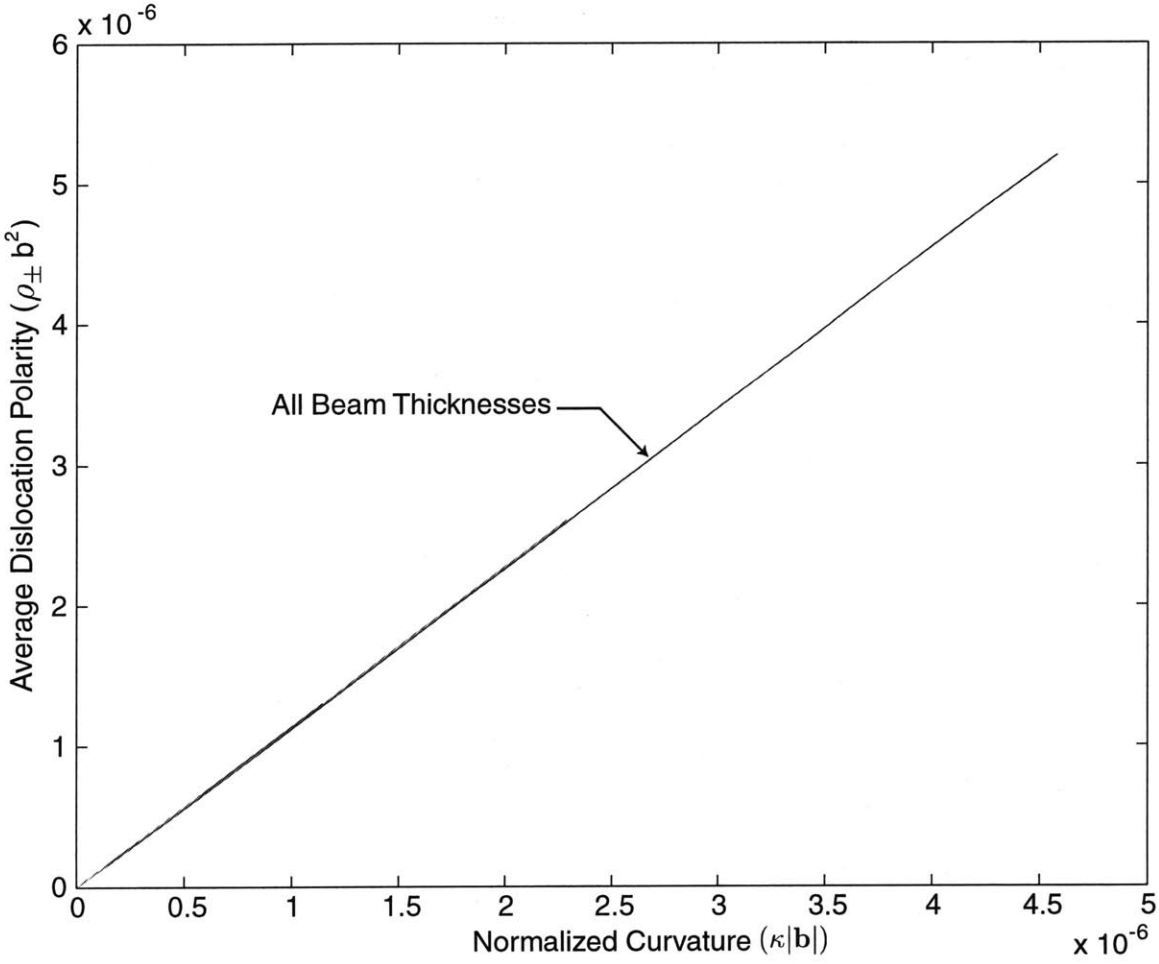

Figure 5-13: Total polarity of the dislocation density as a function of beam curvature ($\kappa|\mathbf{b}|$) for beams ranging in thickness from 12.5 μm to 400 μm.

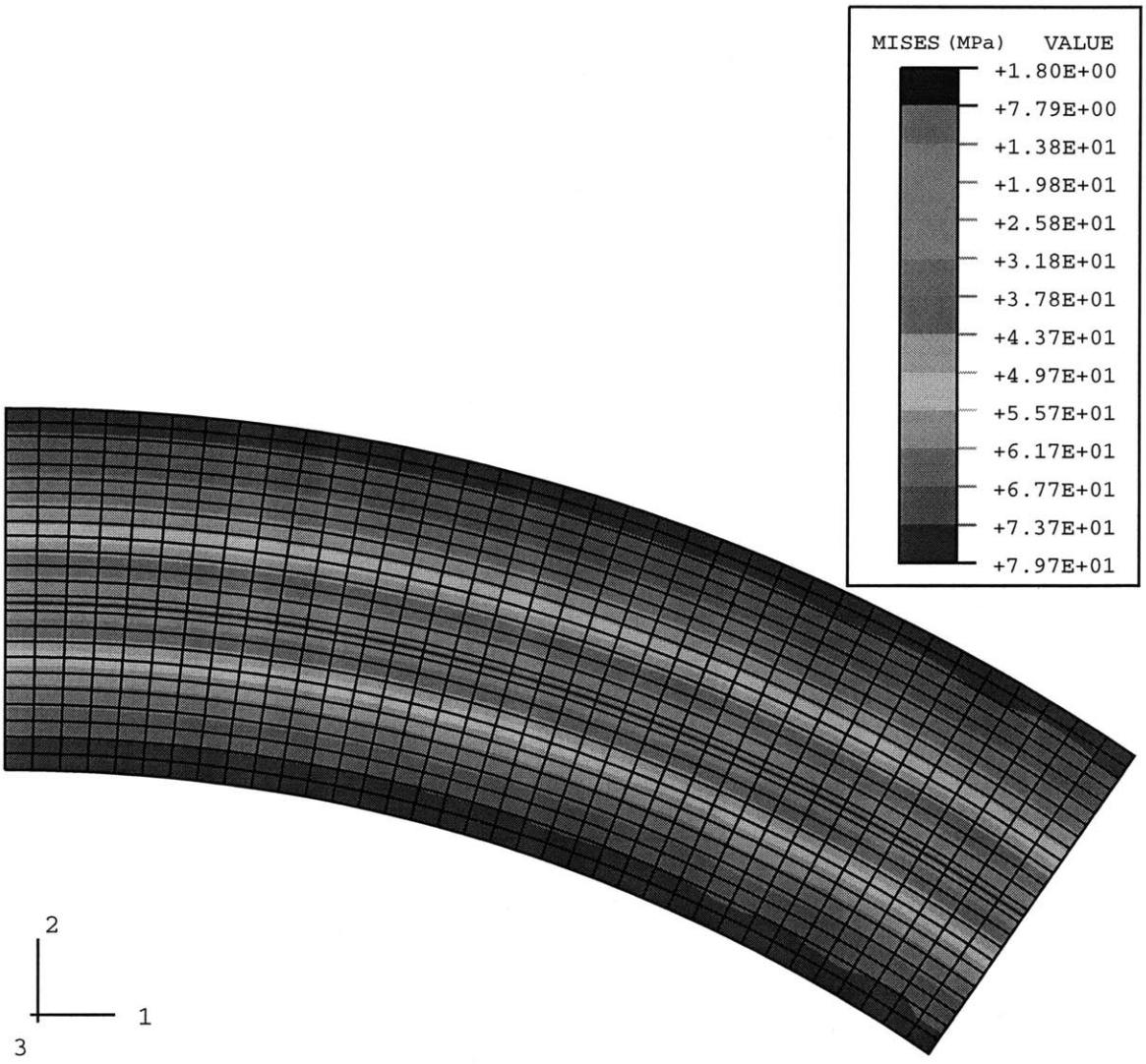

Figure 5-14: Contour plot of the equivalent Mises stress in the 12.5 μm thick beam after 10% surface strain.

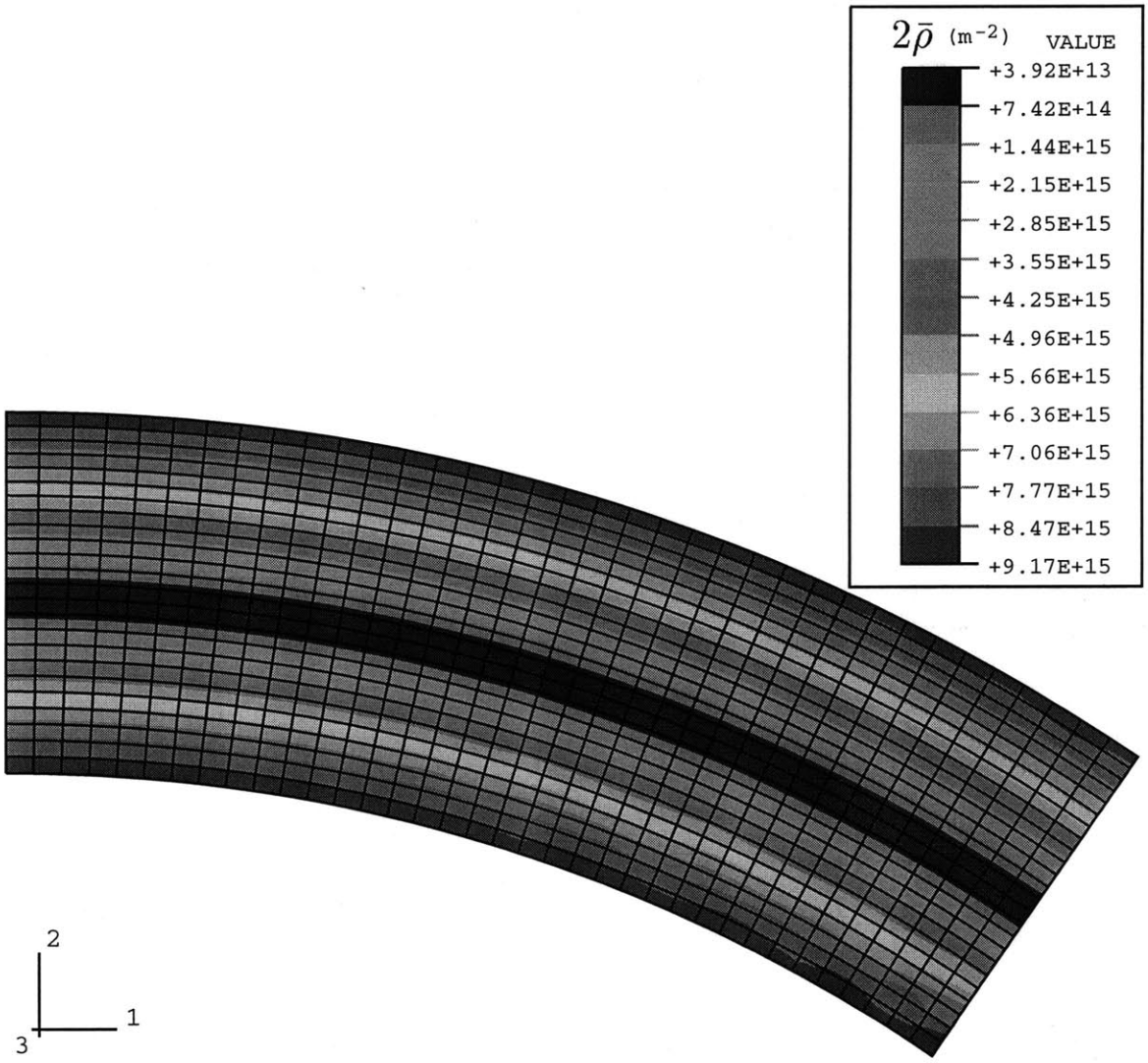

Figure 5-15: Contour plot of the total crystallographic dislocation density in the 12.5 μm thick beam after 10% surface strain.

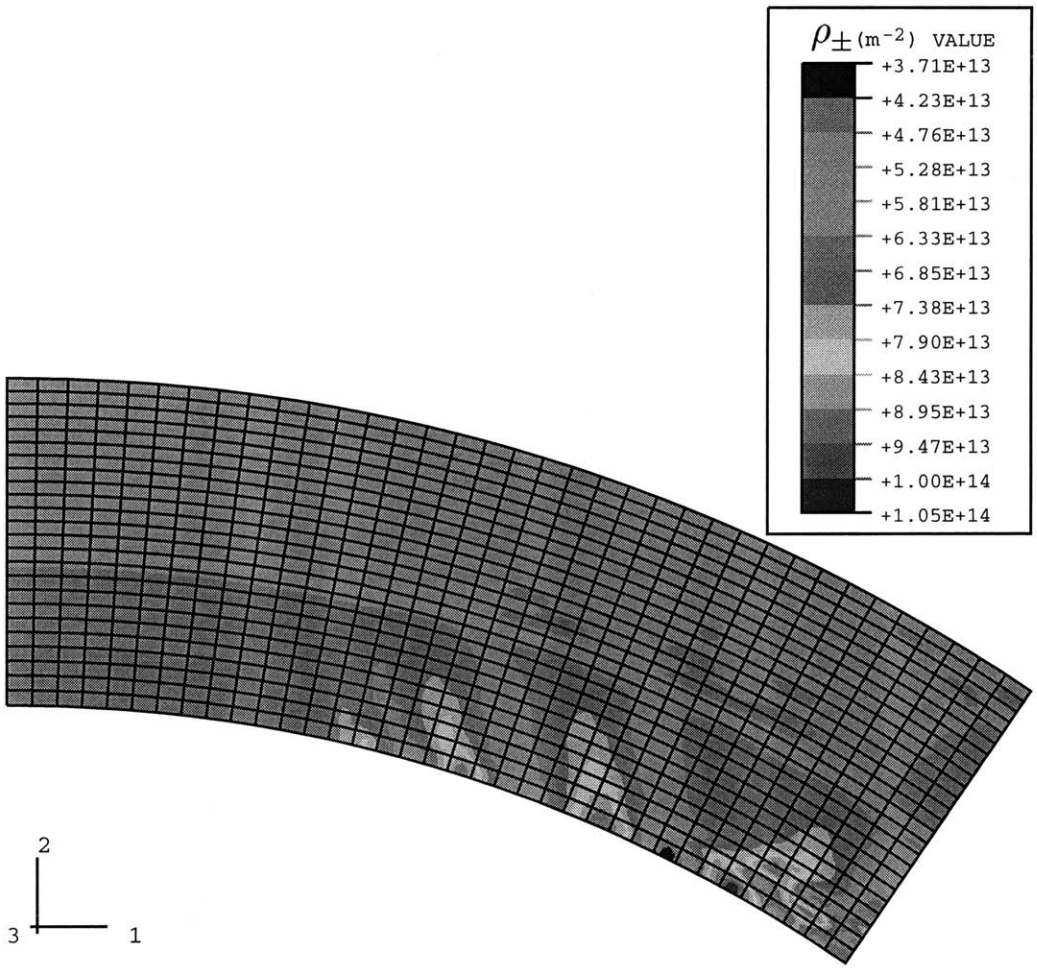

Figure 5-16: Contour plot of the total polarity of the dislocation density in the 12.5 μm thick beam after 10% surface strain.

Table 5.1: Material parameters used for idealized planar double-slip crystal.

Elastic Coefficients	C_{11}	=	108 GPa
	C_{12}	=	61.3 GPa
	C_{44}	=	28.5 GPa
	μ	=	25.0 GPa
	ν	=	0.345
Dislocation Mobility Coefficients	$v_{e0} = v_{s0}$	=	1 m/s
	$\Delta F_e = \Delta F_s$	=	3.0×10^{-19} J/atom
	$s_{ep} = s_{sp}$	=	2 MPa
	$p_e = p_s$	=	1.1
	$q_e = q_s$	=	0.141
Strength Interaction Coefficients	G_0	=	0.5
	g_1	=	1.732
Average Segment Length	H_0	=	0
Interaction Coefficients	h_1	=	0.577
Capture Radii	R_e	=	10.7 nm
	R_s	=	53.7 nm
Burgers Vector	$\|\mathbf{b}\|$	=	2.863 Å
Slip-System Half Angle	ψ	=	30°
Polar Dislocation Pile-up Fraction	c	=	0.1111

Chapter 6

Conclusions and Future Work

The focus of this work has been modeling the evolution of the underlying dislocation density in single crystals responsible for the mechanical response found in experimental observations. A continuum crystal plasticity model was developed within an internal state variable framework for finite plastic deformations. A discrete set of crystallographic dislocation densities were used as internal state variables to capture the material state. Unlike the slip-system resistance-based models and dislocation density-based models that have been previously employed to characterize the material state, the crystallographic dislocation densities in this formulation retained their geometric structure determined by their Burgers vector and tangent line directions.

The geometry of the crystallographic dislocation densities was the focus of Chapter 2. Dislocation arrangements were found that had lattice-geometric consequences and thus led to a non-zero Nye's tensor. Other dislocation arrangements were found that had no geometric consequences and thus led to a net zero Nye's tensor. The former were called geometrically-necessary dislocations (GND's), while the latter were labeled statistically-stored dislocations (SSD's). Since there were more independent crystallographic dislocation densities than unique entries in Nye's tensor, two minimization techniques were considered as methods for determining the geometric dislocation density from a known value of Nye's tensor. General dislocation distributions, contained in representative volume elements (RVE's) within a non-homogeneously deforming crystal, would contain both SSD and GND populations simultaneously,

and individual dislocations could not be distinguished as belonging to either the SSD or GND populations.

The non-homogeneous plastic deformation in crystals can yield detailed dislocation density information; however, the evolution of dislocation density associated with the homogeneous plastic deformation of single crystals was not as well understood, leading to the adoption of resistance-based internal state variables in most continuum models. The focus of Chapter 3 was the development of evolution equations for crystallographic dislocation density. The generation of density was based on the expansion of dislocation loops. The annihilation of density was based on the frequency of interaction between positive and negative species of the same character. The accumulation/loss of polar dislocation density was based on the species flux divergence of each crystallographic dislocation density. With the evolution equations in place, a phenomenological hardening model in strength was replaced with evolution equations based on density kinematics.

Instead of developing phenomenological constitutive equations for the evolution of the slip-system resistances, the density evolution equations required the development of three constitutive functions: the average dislocation velocity, the average dislocation segment length, and the critical capture radius for annihilation. With these three constitutive functions, the stress/strain evolution as well as the underlying dislocation density evolution could be captured.

The accumulation/loss equations for the polar dislocation density on the species level showed that the geometrically-necessary dislocation density did not necessarily increase the total dislocation density found in non-homogeneously deforming bodies compared to the density found in homogeneously deforming bodies. Since the dislocation density in a non-homogeneously deforming crystal (bending) compared to the density in a homogeneously deforming crystal was approximately the same, the theory that the length-scale-dependence in crystal plasticity, in which crystals have been observed to exhibit greater strength in the presence of strong plastic strain gradient fields, was due to an increase in the forest obstacle density was refuted. Within the dislocation density framework used to describe the behavior of single crystals,

various techniques were evaluated for including the material length scale dependence in crystal plasticity. The most promising method was determined to be the addition of a long range (back) stress associated with the polarity in a dislocation density distribution.

A local version of the model that included only the generation and annihilation parts of the dislocation evolution equations, but not the polar accumulation/loss equations, was implemented into a finite element scheme and was used to capture the anisotropic plastic behavior of aluminum single crystals. The state variable model captured not only the tensile stress/strain behavior for different orientations of the aluminum single crystals, but also captured the evolution of the underlying dislocation density responsible for the mechanical behavior observed. The model was able to capture the predominance of edge dislocation density during single slip and the differences between the deformation behavior of the $< 111 >$-oriented crystal and the $< 100 >$-oriented crystal. The interaction between dislocations of different character, screw and edge, as well as the interaction between the gliding density and different types of forest density, proved to be crucial to understanding the underlying mechanisms leading to the stress/strain observations. The dislocation density description of the state was also consistent with the experimental microscopy of slip traces conducted on the deformed samples.

The set of dislocation density state variables used to quantify the material state was 18-dimensional. The set of slip-system-resistance state variables typically used to quantify the material state is typically only 12-dimensional. A slip-system resistance was calculated from the dislocation density state as part of the average dislocation velocity constitutive equations, and although a rate form of the slip-system resistance could be derived as a function of the density and its time rate of change, as done by Franciosi and Zaoui (1982), the form is not invertible, so a hardening matrix cannot be found explicitly. The higher dimension of the crystallographic dislocation density, resulting from the quantification of dislocation character, prevents the inversion, and as presented in Chapter 4, the dislocation character evolves with deformation history and cannot be taken to be constant for arbitrary deformation histories, as was

assumed by Cuitiño and Ortiz (1992).

A non-local version of the model using a simplified planar double-slip geometry was implemented into a finite element scheme and was used to simulate the length-scale dependence observed in thin beam bending. The modes of interaction between the statistical density and the polarity of the dislocation density within the model framework were discussed, and results of the simulations showed that a relatively small polarity (1.5%) in the dislocation density could nonetheless significantly increase the strength levels (16%), compared to the local theory. Adoption of a consistent obstacle-based method for modeling the length scale dependence in crystal plasticity would have led to a much smaller increase in the strength than is found in the experimental observations of Stölken and Evans (1998). The length scale dependence of the new model was found to fit a Hall-Petch type relationship with a constant exponent $m = 1/2$.

The advantages of adopting a dislocation density framework for continuum crystal plasticity are clear. The dislocation density description can be used to investigate the validity of assumptions used in strength-based constitutive models. The role of dislocation polarity in the length scale dependence of plasticity is an excellent example of this. The structure and geometry associated with dislocations enables the use of simpler constitutive equations instead of increasing the complexity of phenomenological hardening equations to capture the mechanical response of crystalline materials. The evolution of the plastic deformation in the $< 100 >$-oriented crystal is an excellent example of the need to include both edge and screw dislocation densities to capture the dislocation mechanisms that lead to the observed behavior.

The potential of using a dislocation-density-based model for single crystal plasticity within a multi-scale modeling framework is the most promising aspect of the model. The constitutive inputs to the model are couched in terms of statistical information of dislocation densities such as the average mobility, and average segment length of lines in a deforming crystal, as well as junction strengths, and radii of capture. In principle, all of this information could be determined by carrying out detailed investigations of dislocation dynamics simulations. By varying the initial dislocation

density profile as well as the loading history of the dislocation dynamics simulation cells, the constitutive space of the three functional inputs to the density-based model could be spanned. After the density-based continuum model, whose constitutive functions have been determined from simulations at smaller length scales, has been experimentally verified through comparisons of simulation results with controlled single crystal experiments, simulations of polycrystalline aggregates on the order of fifty grains could be conducted. By varying the grain orientations, grain neighbors, initial density state and loading history, the density-based model could be used to construct anisotropic yield loci to be used in a coarser polycrystal model, that could be used to model engineering structures. The density-based single crystal plasticity model presented in this thesis is able to efficiently translate information on the dislocation mechanics level to information on the macroscopic strength and plastic deformation level.

Obviously, there remains an abundance of work to be done in the area, on varying levels of complexity. Perhaps the easiest refinement that could be considered would be to include more dislocation annihilation reactions than the self-annihilation interaction considered in this thesis. In FCC crystals, an interaction between two coplanar dislocations with different Burgers vectors will create a dislocation with the third Burgers vector in the plane, and can reduce the total dislocation density of the system. Including such annihilation reactions would permit a reduction of the magnitude of the capture radii used in the aluminum simulations, and lead to increased evolution of dislocation density on inactive slip-systems. In the aluminum simulations, the dislocation density evolved mainly on the active systems, while the dislocation density profile on the inactive systems remained roughly unchanged. Including more dislocation reactions would lead to richer evolution histories of the crystallographic dislocation densities within the discrete set considered thus far. With the addition of annihilation reactions between dislocations on different slip-planes, a single-slip deformation mode could possibly increase the piercing density on the slip plane with little or no activity on other slip-planes.

Another avenue of interest could be the effects of expanding the discrete dislo-

cation density space to include more tangent line vectors. The expansion of planar loops was the motivation for the generation evolution equations in this thesis. The loop geometry was idealized as a rectangle consisting of edge and screw dislocation line segments. The dislocation tangent space could also be discretized in hexagonal or octagonal loops consisting of dislocation line segments with mixed character. The expanded space would approximate more closely the real crystal, and more annihilation reactions would need to be investigated other than just the simple self-annihilation reactions considered here.

More research must also be conducted to determine if the constitutive functions used in the thesis accurately describe the material behavior. The dislocation mechanics based evolution equations appealed to the geometric aspects of the density, and all of the kinetics were placed into the three constitutive functions for average dislocation velocity, average segment length, and capture radius. The constitutive equations adopted in the thesis were based on physical arguments of slip activation and simple scaling laws. Parameterization of dislocation dynamics results with respect to the three constitutive functions could lead to better constitutive functions for continuum simulations, as well as a deeper understanding of the evolution of material state predicted by dislocation dynamics.

The model could also be applied to different crystal systems in which the need to model dislocations of different character is more important than in FCC crystals. Screw dislocations in BCC metals can possibly cross-slip on three lattice planes, and there is a large difference in the mobility of screw dislocations compared to edge dislocations. The edge dislocations may have mobilities that are two orders of magnitude greater than the screw mobility in BCC crystals. Most continuum models of BCC crystals have largely focused on the rate-limiting motion of screw dislocations, with little or no attention to the edge density. In fact, the physics of slip activation in these systems has been based on the nucleation and migration of kinks on screw dislocations (Kothari and Anand, 1998), but the density evolution equations presented in Chapter 3 show close ties between the motion of edge dislocations and generation of screw density. The behavior of edge dislocation density in BCC crystals

has been largely ignored in the literature, but the framework developed in this thesis shows that the evolution of edge and screw dislocation densities is strongly coupled, and the presence and behavior of edge dislocation density should not be ignored.

The directions of further research discussed in the last four paragraphs are the most conservative directions for constitutive development. They represent refinements of the current constitutive framework that should yield better understanding of the processes controlling the plastic deformation in crystals, leading to simulations that resemble the behavior of real materials more closely. More ambitious directions of research lie in the length-scale-dependence of crystal plasticity. The treatment of the dislocation polarity in this thesis employed assumptions about the organization of dislocation density and simplified calculation techniques to estimate the level of polarity at a material point within the finite element. A more rigorous treatment of the dislocation density is needed to capture the correct behavior of dislocation densities on the micron level. The ultimate goal of such increased rigor is not simply to capture the length-scale-dependence in thin-beam bending, thin-wire torsion, or micro-indentation, but to capture the internal forces leading to the locally inhomogeneous organization of dislocation density into walls and dense tangles during the macroscopically homogeneous deformation of crystals.

The dislocation density evolution equations provide insight into dislocation pattern formation process on a density level, but more work must be done to determine the interaction forces between densities that cause stable patterns to develop. Based on the results of this thesis, my belief is that the dislocation polarity and its spatial gradients are the key to solving this complex problem. The evolution equation for Nye's tensor found in Eq. 3.47 includes a term which leads to an exponential growth rate of the dislocation polarity. The last term in the equation states that a homogeneous dislocation flux through a dislocated (polarized) lattice will lead to an increase in the polarity, but the initial polarity must be in the forest density, with Burgers vectors projecting out of the slip plane. This observation leads to the conclusion that multiple slip-systems on different glide planes must be active for an exponential growth in the polarity to occur.

Secondly, because the dislocation polarity most likely leads to long range stress fields associated with the non-homogeneous distribution of polarity in the crystal, a relatively small fraction of polar density, relative to the total dislocation population, can lead to strong internal stress fields. The lowest energy state for the polar density is not a pile-up but an organized tilt or twist boundary, and although the density would prefer to organize in such structures so as to minimize the internal dislocation interaction energy (Kuhlmann-Wilsdorf, 1999), such an organization is frustrated by the interaction of the polar density with the statistical forest density. The polar pile-up must be bound by a high density of dislocations, as found in cell walls, to provide an almost impenetrable barrier that the dislocations can pile-up against. The profile of a pile-up leads to a similar stress/density relationship used to model the length-scale-dependence found in thin-beam bending, in which the stress is directly proportional to the number of dislocations in the pile-up and inversely proportional to its length. If the number of dislocations in the pile-up remains constant, then the length of the pileup will decrease as the macroscopically applied stress increases, leading to the observation that dislocation cells decrease in size as the stress increases (Godfrey and Hughes, 2000).

The effects of the polar dislocation density were treated in an "effective" manner by simply scaling a back stress with the square root of the magnitude of the polarity. A more rigorous treatment of the back stress would involve a function that depended on the magnitude of the polarity at a point and its gradients. The gradients of the polarity give more information as to arrangement of the polar density, and whether or not pile-up structures exist in the crystal. The gradients of Nye's tensor have the greatest potential for describing the back-stresses in a non-homogeneously deforming crystal. Gurtin (2000) has developed a constitutive framework in which the Laplacian of the plastic deformation gradient leads to micro-forces within the crystal. It is my belief that the curl of Nye's tensor is the proper measure of the dislocation polarity that will lead to micro-forces within the crystal (Menzel and Steinmann, 2000). The divergence of Nye's tensor is identically zero since Nye's tensor is defined as the curl of another tensor field, but the curl of Nye's tensor contains information about the

change in the polarity in the directions that describe pile-ups. For example, the curl operation determines the change in polarity of an edge dislocation density in the direction of its Burger's vector, and returns a tensor that is simply a magnitude multiplied by the Schmid tensor of the edge density's slip system.

Evaluation of the curl of Nye's tensor using the finite element method requires that dislocation density be kept as field variables and not as internal state variables. Within the finite element framework, the dislocation density would be described as nodal degrees of freedom, and the finite element shape functions could be used to evaluate Nye's tensor and its curl at the material integration points. Describing the dislocation density as a nodal degree of freedom also leads to dislocation density flux in and out of the finite elements, necessitating a mixed Lagrangian-Eulerian description of the plastic deformation of crystals and the incorporation of higher-order boundary conditions on the dislocation flux. This more rigorous description of effects of polarity in the crystal is more computationally intensive than the computations done in this thesis; however, low order linear elements could perhaps be used instead of the isoparametric elements used in Chapter 5.

Appendix A

Parameter Study of the Three-Dimensional Local Model

The three-dimensional "local" model that was implemented to simulate the orientation-dependence in the stress/strain behavior of single crystal aluminum introduced many parameters whose influences were not fully investigated in Chapter 4. The purpose of this Appendix is to provide more insight into the overall behavior of the model, and the manner in which the material constants might be altered to capture the behavior of other FCC crystals (e.g., copper). The most important feature of the model that was not able to be manipulated was the ability of the screw dislocations to cross-slip. The ability of the screw dislocations to do so was deeply embedded in the UMAT subroutine; however, other features of the model were more amenable to manipulation.

The study will focus on the crystal orientations relative to the tensile axis which had the most slip systems active: the $< 111 >$ and $< 100 >$ orientations. The $< 111 >$-oriented crystal will be used to show the effect that different parameters have on the magnitude and shape of the stress/strain response of the model. The $< 100 >$-oriented crystal will be used to show the effect of different parameters on the activation of slip systems during deformation. Since the scale of the stress/strain response will be considered in the $< 111 >$-oriented crystal, the initial alignment of the crystal with the tensile axis will be perfect, leading to symmetric activation of all

six potentially-active slip-systems. The < 100 >-oriented crystal was misaligned by 1° and given the same initial orientation as in Chapter 4 to break the initial symmetry of the slip-systems with the tensile axis.

In each of the parameter studies that were conducted, the reference point of the material constants was the set of material constants listed in Tables 4.2 and 4.3 used to simulate single crystal aluminum. When any part of the material parameters were modified in a controlled fashion, the rest of the material parameters held values at the reference point. The stress-strain curves will be plotted on a normalized axis along with the experimental data for the aluminum single crystals of Kocks (1959) and the experimental data for copper single crystals of Takeuchi (1975) serving as reference.

Before the parameter study is presented, a series of simulations showing the effects of different strain rates and temperatures on the stress-strain response of the model. Figure A-1 depicts the effect that different strain rates have on the response of this model, and Figure A-2 depicts the effect that different temperatures have on the behavior of this model. The constitutive model is both rate and temperature dependent, although the temperature can only be included isothermally in the model's present form. The temperature dependence of the stress/strain response of aluminum single crystals at low temperatures has been experimentally investigated by Hosford et al. (1970), and the magnitude of the response simulated at low temperatures is representative of the magnitude measured in the experiments.

In Section 4.6.2, the behavior of aluminum was contrasted to that of copper, and several reasons as to the differences were given in the text. Several of the reasons given in the text can be investigated by changing different material parameters and quantifying their effects, even though the biggest difference, the activation of cross-slip, cannot be directly investigated. Figure A-3 shows the effect of increasing the strength interaction matrix. Changing all of the coefficients by a factor of two led to 40% increase in the stress, while the general shape of the curve remained similar. With the factor of two change in the interaction matrix, the strength of the Lomer-Cottrell lock (strongest junction) was still less than unity. The underlying dislocation density evolution remained unaffected by the changes in the interaction matrix. Figure A-4

shows the effect of changing the average segment length interaction matrix by simple scalar multiplication. Changing this interaction matrix does change the evolution of the dislocation density. A decrease in $H^{\xi\zeta}$ will cause the dislocation density to accumulate slower than the reference point value $H_A^{\xi\zeta} l$. Conversely, an increase in $H^{\xi\zeta}$ will cause the dislocation density to accumulate at a greater rate than the reference point value. The changes in the rate of accumulation result in changes of the initial slopes of the stress/strain curves. The changes also affect the saturation level of the dislocation density and, therefore, the stress levels reached at larger strains. The changes in the overall shape of the stress/strain response due to changing average segment length interaction matrix are similar to the changes in the stress/strain response due to changing the strength interaction matrix. In Figure A-5, the effects of changing the average mobility of the dislocation density on the stress/strain response was probed. The mobility was altered by modifying the pre-exponential reference velocity for both the edge and screw densities uniformly. The results show that sluggish densities need greater stresses compared the stresses needed to move dynamic densities at the same strain rate. As with the changes in the strength interaction matrix, changes in the reference velocity do not change the evolution of the dislocation density.

The changes in the stress/strain behavior due to changes in the dislocation resistance, average segment length, and dislocation mobility all look very similar and do not make the aluminum-like behavior of the simulation look any more copper-like. The changes appear as though they could be offset by changing the value of the shear modulus to an effective value so as to recover the reference (aluminum) behavior. The curvature of the different stress/strain curves appears to scale with the magnitude of stress levels reached by the different simulations. Decreasing the capture radii as depicted in Figure A-6 does modify the behavior of the model to appear more copper-like. The two capture radii in the model were decreased simultaneously while keeping the ratio between the two radii constant. Decreasing the capture radii decreases the curvature of the stress/strain curve without significantly changing the initial slope of the stress/strain curve. The evolution of the dislocation density is also affected by the

changing capture radius, and as the capture radius decreases, the saturation level of density increases. The results of decreasing the capture radii change the shape of the stress/strain curve from an aluminum-like behavior to a more copper-like behavior.

The effect of decreasing capture radii on the stress/strain behavior of the $< 100 >$-oriented crystal is not as large as the effect was on stress/strain behavior of the $< 111 >$-oriented crystal. Figure A-7 depicts the response of the stress/strain curves to changes in the capture radii of the material. The radii were decremented in the same manner as in the study on the $< 111 >$ orientation. Decreasing the capture radii has the effect of changing the terminal slope of the stress/strain curve as discussed earlier. The slope of the stress/strain curve of the $< 100 >$-oriented crystal at 10% strain is much smaller than the slope of the stress/strain curve of the $< 111 >$-oriented crystal at the same level of strain. The change in the slopes of the two curves due to the decreasing capture radii follow the same behavior.

As discussed in Chapter 4, the strength of the Hirth lock junction was very important in controlling the stress/strain behavior exhibited by the $< 100 >$-oriented crystal. The low strength of this junction enabled the crystal to change its mode of deformation from activation of all eight to activation of four slip-systems. Figure A-8 shows the effects of increasing the strength of the Hirth lock, g_4, on the stress/strain behavior of the $< 100 >$-oriented crystal. The plot shows that there is a 60% increase in the stress level for an 88% increase in the strength of the lock. Whereas a 100% increase in the whole strength interaction matrix resulted only in a 40% increase in the stress levels of the $< 111 >$-oriented crystal (Figure A-3), changing only one of the strength parameters had a significant effect of the stress levels achieved in the $< 100 >$-oriented crystal.

Inspection of the crystallographic strain rates on the eight potentially-active slip-systems, found in Figure A-9, shows why this one material parameter has such a significant effect on the stress/strain behavior the crystal in this orientation. The two plots show the crystallographic plastic strain rates on the eight systems during the course of the simulations for two different values of g_4. With the addition of Figure 4-11, which shows the behavior for $g_4 = 0.16$, the underlying reason for the importance

of the Hirth-lock to the deformation path of the $< 100 >$-oriented crystal can be explained. An increase in the strength of the Hirth-lock leads to a more symmetric plastic deformation mode in which all eight potentially-active slip-systems equally contribute to the total plastic deformation of the crystal in this orientation.

Figure A-10 depicts the effects of decreasing the capture radii in the same manner as discussed earlier on the $< 100 >$-oriented crystal with $g_4 = 0.30$. As in Figure A-7, a reduction of the capture radii does not have a large effect on the stress/strain behavior in this orientation. Certainly, the effect is not as large as it is on the $< 111 >$-oriented crystal depicted in Figure A-6.

Although the ability of the screw density to cross-slip was not modified, the effects of preventing cross-slip can be discussed within the model framework. There would be little difference in the behavior of the constitutive model for crystal orientations that led to single slip behavior; however, there would significant changes in the behavior of the crystal orientations that favored activation of multiple slip-systems during deformation. The six active slip-systems in the $< 111 >$-oriented crystal come in the form of three cross-slip pairs, and the eight active slip systems in the $< 100 >$-oriented crystal come in the form of four cross-slip pairs. Disallowing cross-slip would reduce the mobile density on each slip-system because unlike the case here the dislocation density on one slip-system would not be able to affect the plastic deformation on another. A reduction of the mobile density would lower the rate of accumulation of density and change the character of the density. Also, a lower mobile density would necessitate greater stresses to reach the same plastic strain rates compared to the stresses that were needed to activate slip with cross-slip allowed. All of these effects would lead to stress/strain curves that would approximate the behavior of copper single crystals, especially with the changes in the material parameters discussed earlier.

The last two parameter studies were conducted on the ratio between the edge and screw capture radii and on the ratio between the edge and screw reference velocities. As discussed in Section 4.6.2, these ratio control the overall character of the density in the simulations. Unlike other dislocation density-based models, the current model can distinguish between edge and screw density on a slip system, and the ratio of

edge density to screw density can be easily controlled. Consider Figure A-11 which depicts the effect that the ratio between the edge and screw capture radii has on the character of the density. In this study, the average of the two capture radii was held constant as the ratio between them was modified. The simulations were conducted on the $< 111 >$ orientation, and the plot is of the total edge dislocation density found at one material point divided by the total dislocation density found at that same material point. As shown in Figure A-11, the capture radii can be used to control the profile of the density, but the character, here defined as the edge/screw ratio, develops over the length of the simulation towards steady state values.

A more powerful method for controlling the character of the density is to allow disparate mobility in the edge and screw density. Figure A-12 depicts the effects of varying the ratio between the reference velocities of the edge and screw densities on the character of the density. As in the previous case, the simulations were conducted on the the $< 111 >$-oriented crystal. The geometric mean of the two reference velocities was held constant as the ratio between them was varied. A difference in the mobility of edge and screw densities has a much stronger effect on the character of the density. In this case the slower density is more prevalent than the faster density. The character develops at lower strain levels than the capture radii could affect. Although overall the character of the dislocation density may not be important in FCC crystals, the character of the dislocation density can play an integral role in the behavior of BCC metals in which there may be a great difference in the mobility of the edge and screw dislocation densities.

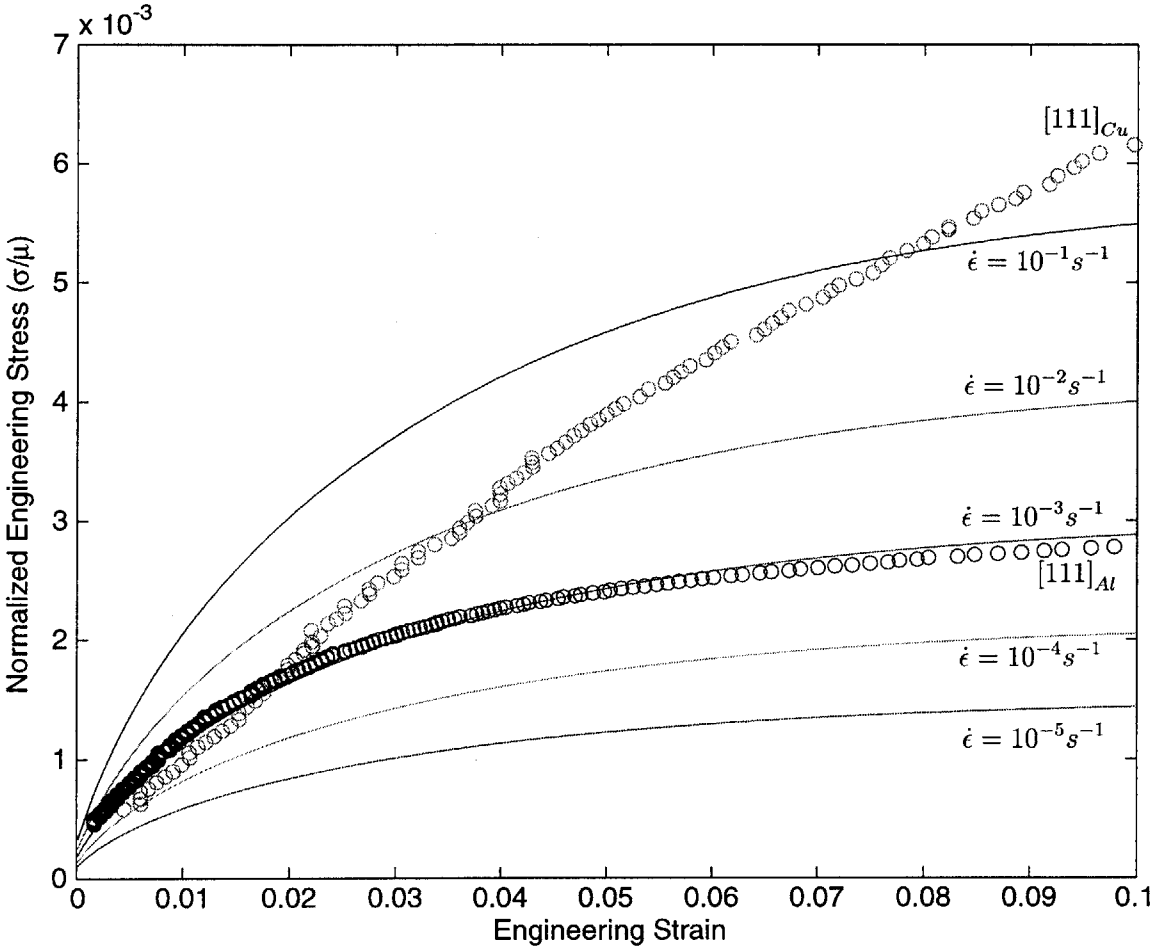

Figure A-1: Effect of different strain rates on the stress/strain response of a perfectly-oriented aluminum single crystal with the $< 111 >$ along the tensile axis.

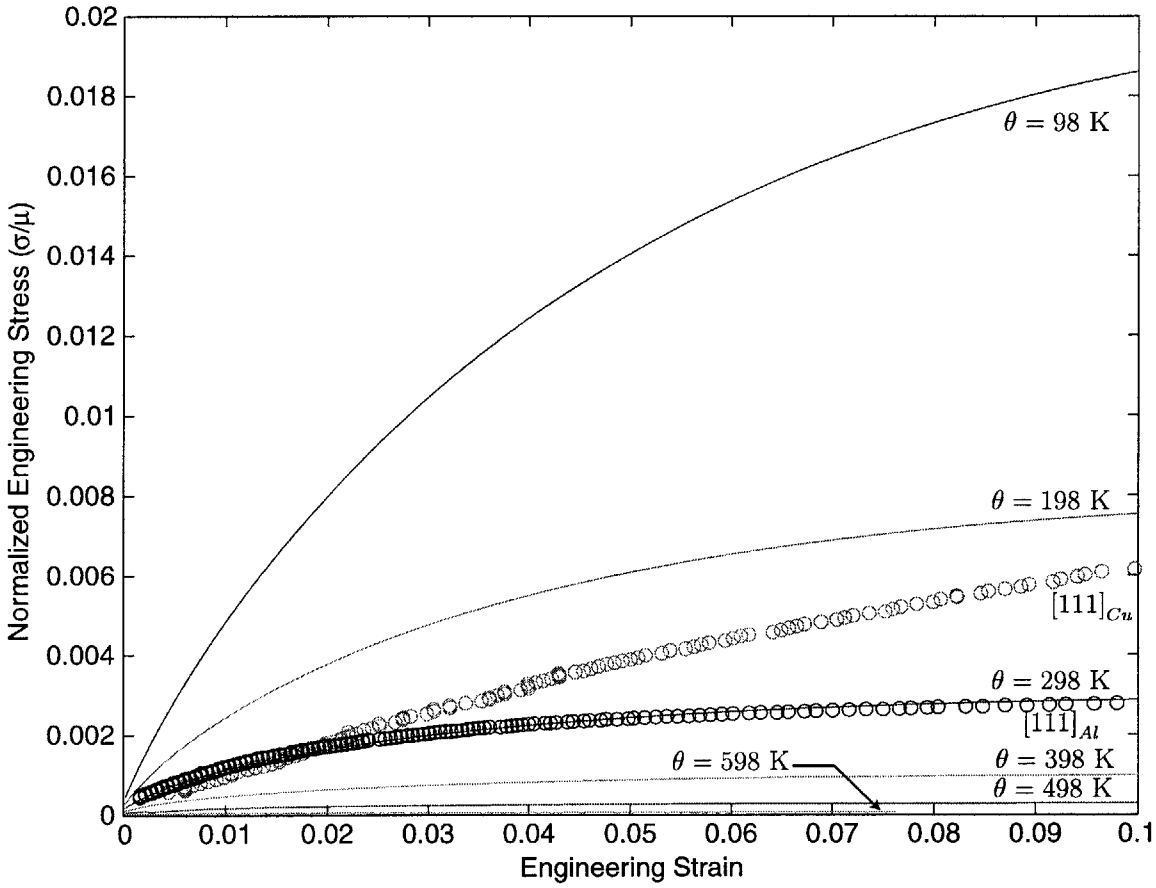

Figure A-2: Effect of different temperature on the stress/strain response of a perfectly-oriented aluminum single crystal with the $< 111 >$ along the tensile axis.

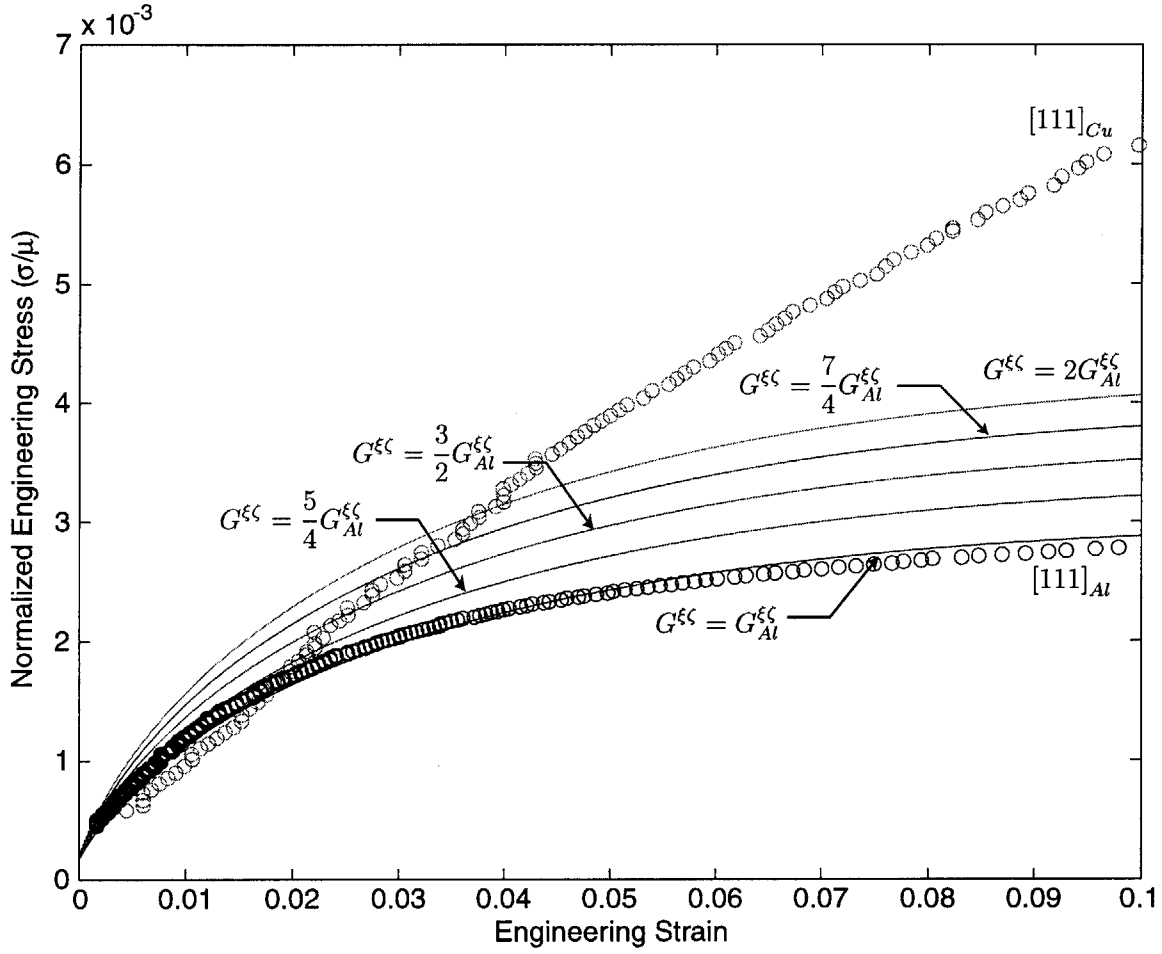

Figure A-3: Effect of increasing the magnitude of the strength interaction matrix on the stress/strain response of the constitutive model for the < 111 >-oriented crystal.

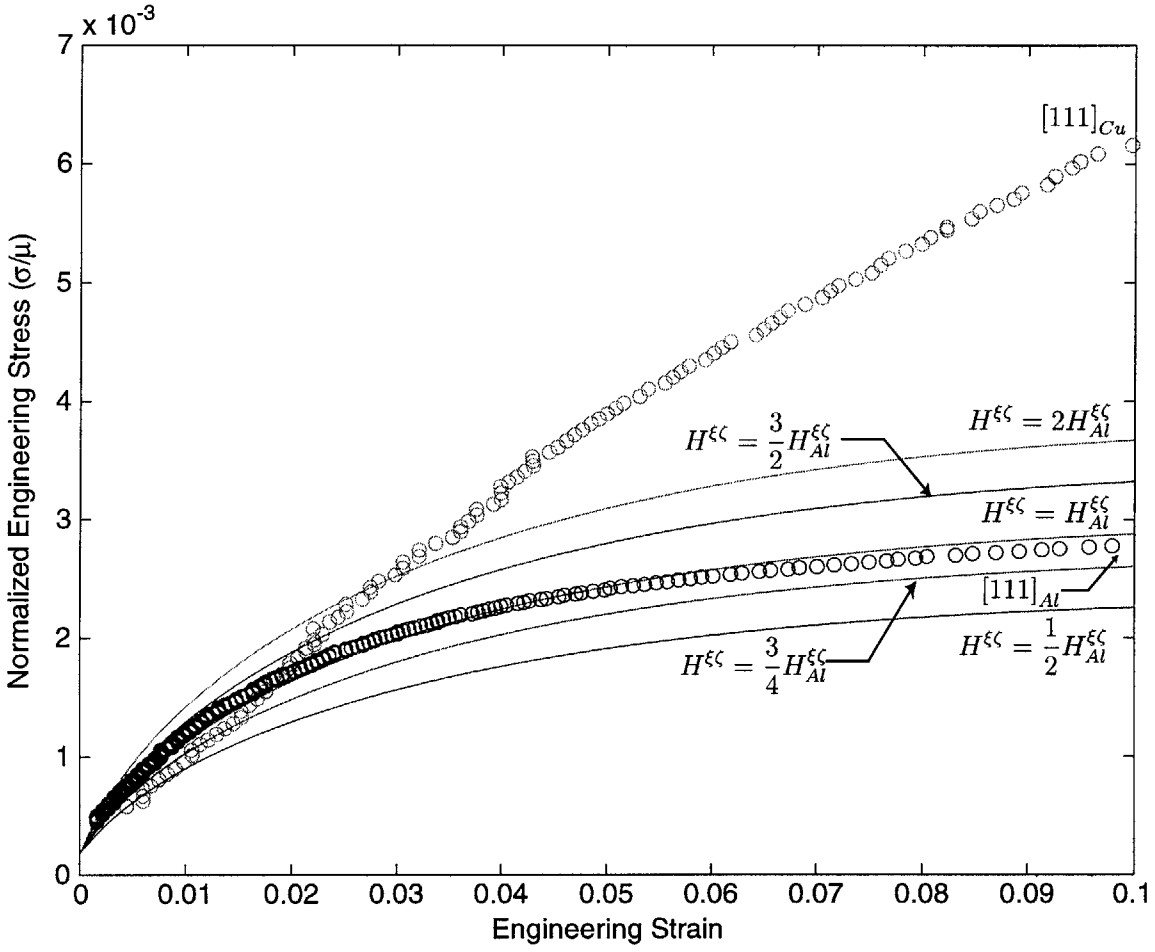

Figure A-4: Effect of changing the average segment length interaction matrix on the stress/strain response of the constitutive model for the $< 111 >$-oriented crystal.

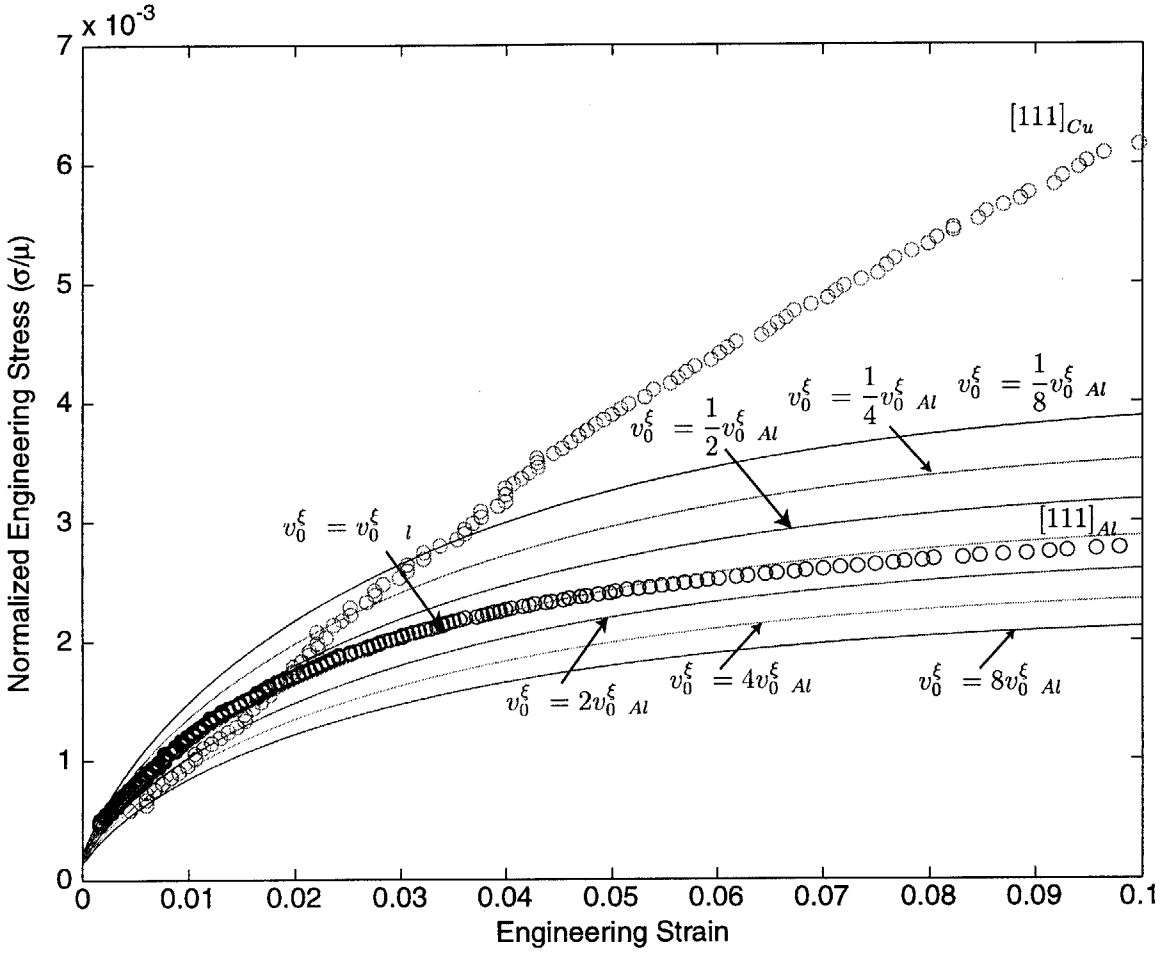

Figure A-5: Effect of changing the pre-exponential reference velocity on the stress/strain response of the constitutive model for the < 111 >-oriented crystal.

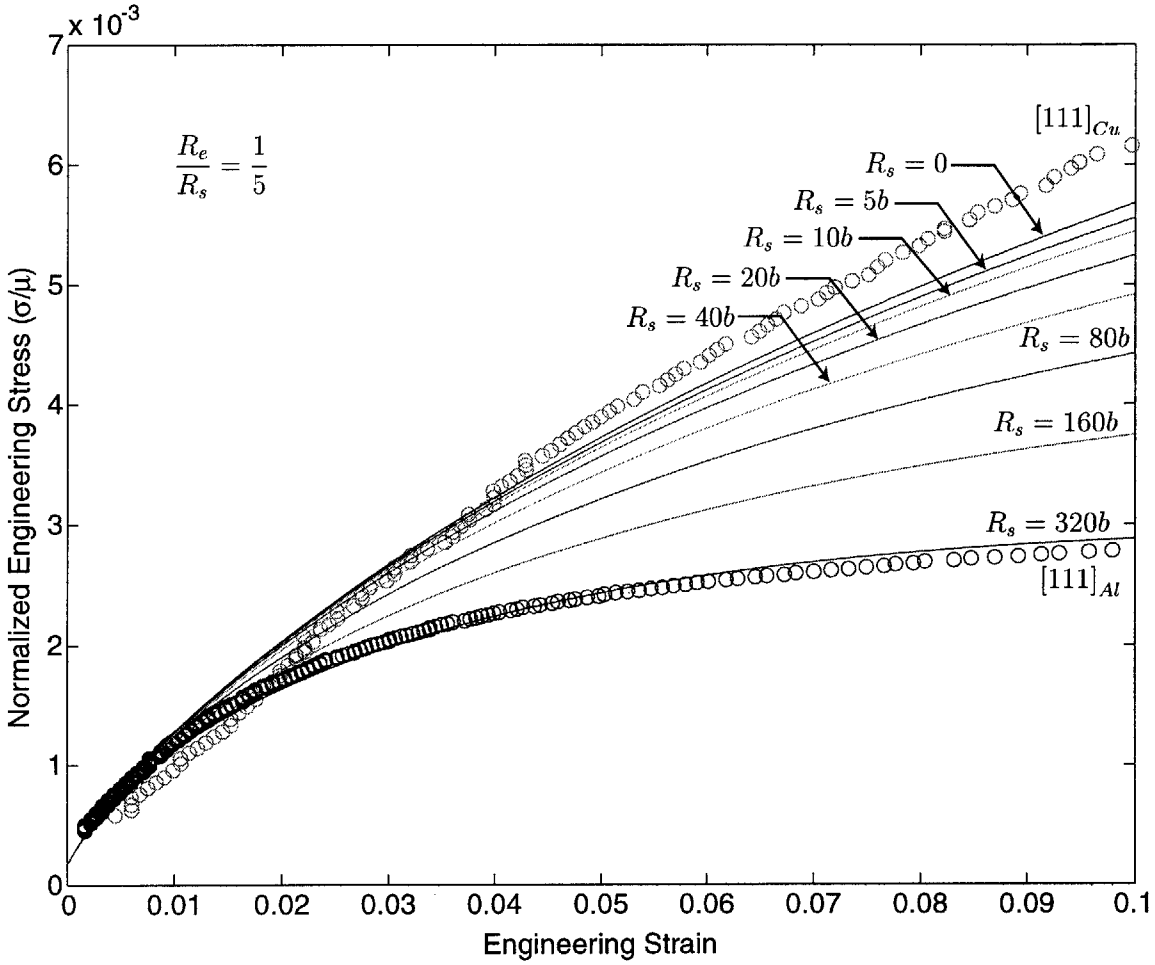

Figure A-6: Effect of decreasing the capture radii of the dislocation density on the stress/strain response of the constitutive model for the < 111 >-oriented crystal.

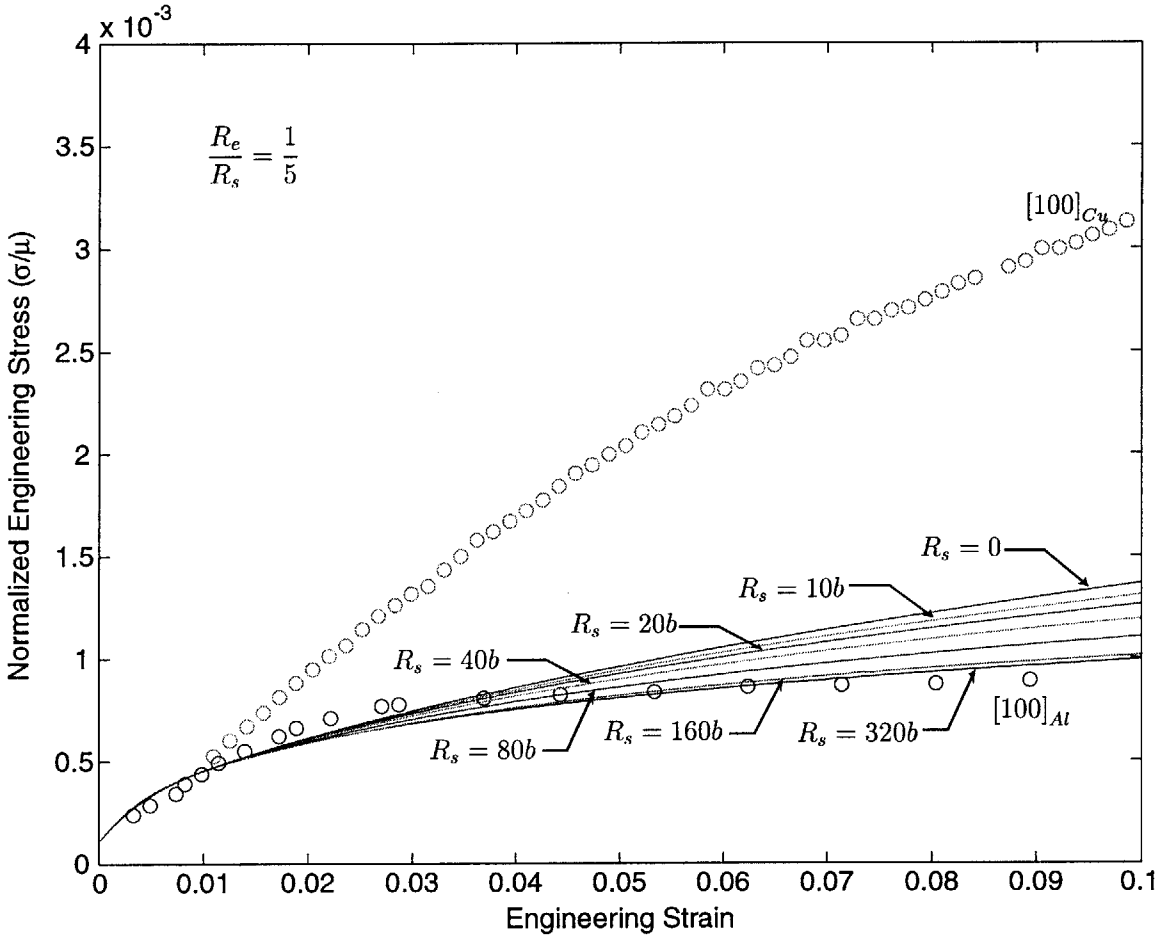

Figure A-7: Effect of decreasing the capture radii of the dislocation density on the stress/strain response of the constitutive model for the < 100 >-oriented crystal.

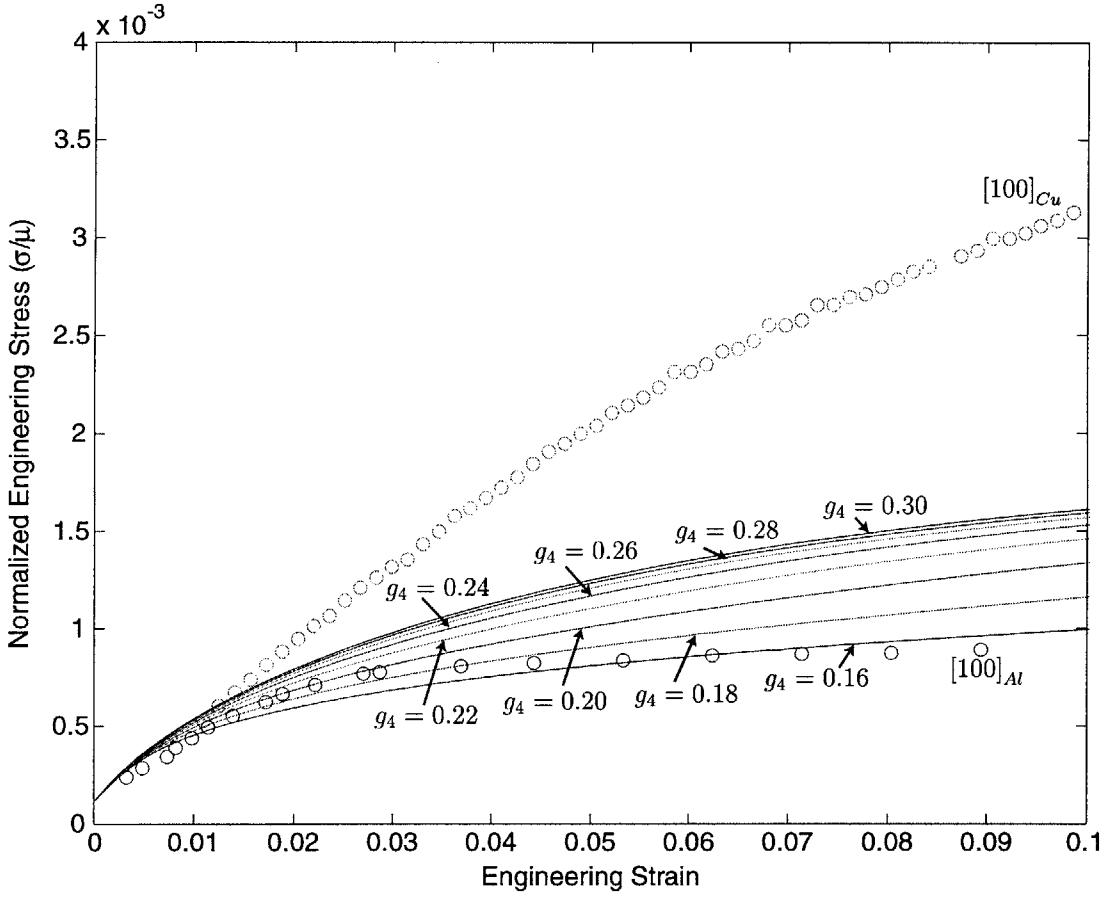

Figure A-8: Effect of increasing the junction strength of the Hirth lock, g_4 on the stress/strain response of the constitutive model for the $< 100 >$-oriented crystal.

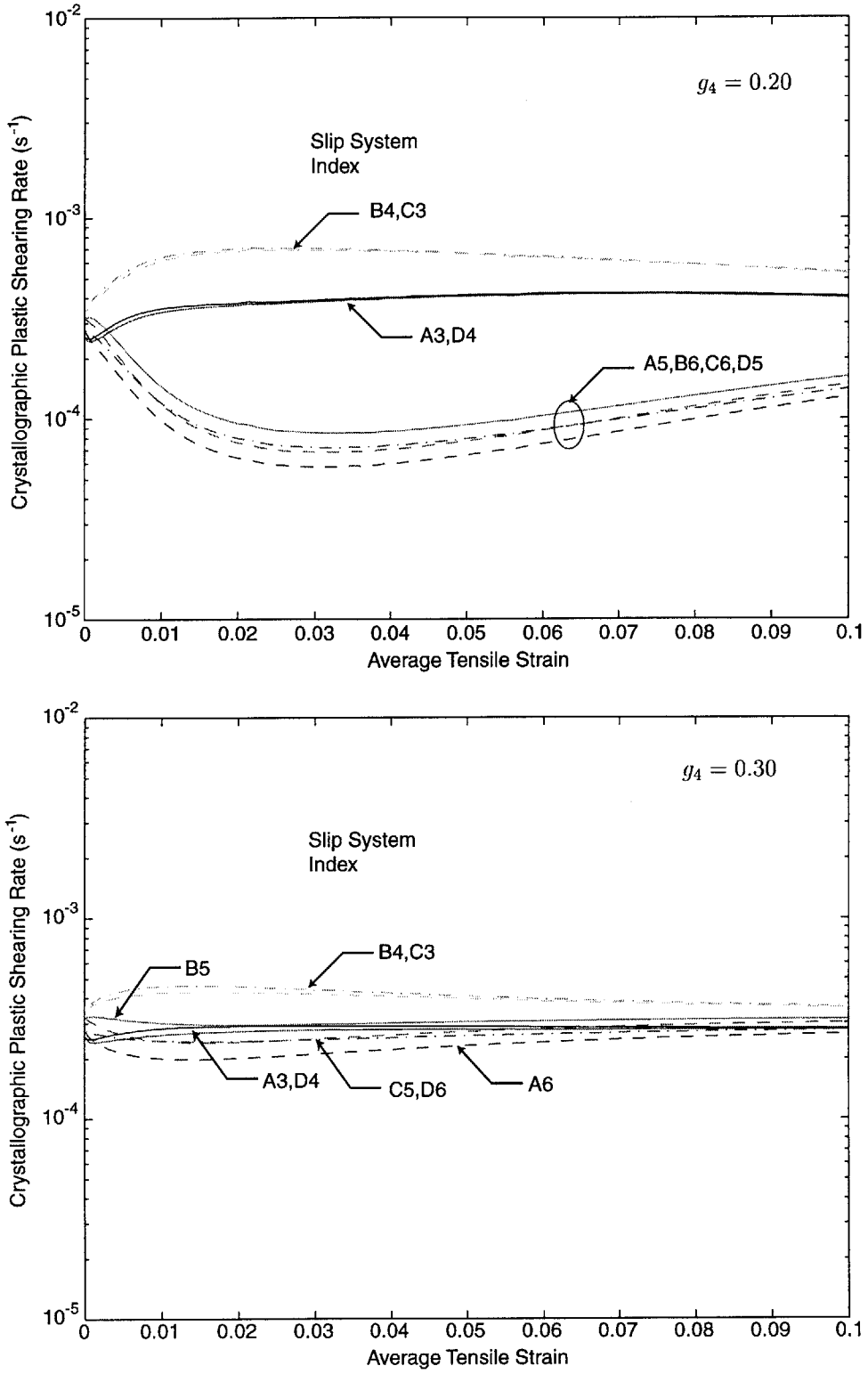

Figure A-9: Effect of increasing the junction strength of the Hirth lock, g_4 on the plastic response of the eight potentially-active slip-systems in the $< 100 >$-oriented crystal.

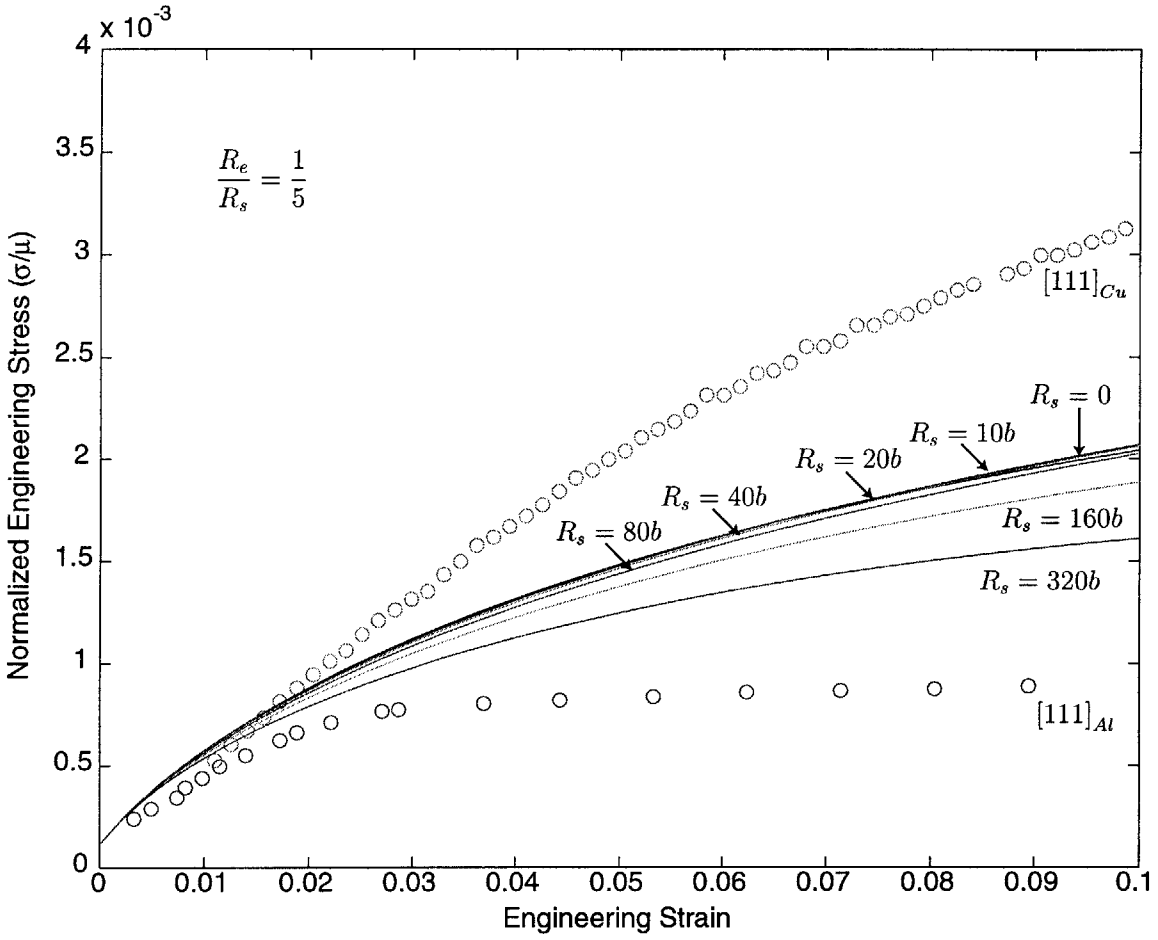

Figure A-10: Effect of decreasing the capture radii for a material with a Hirth lock strength of $g_4 = 0.30$ on a $< 100 >$-oriented crystal.

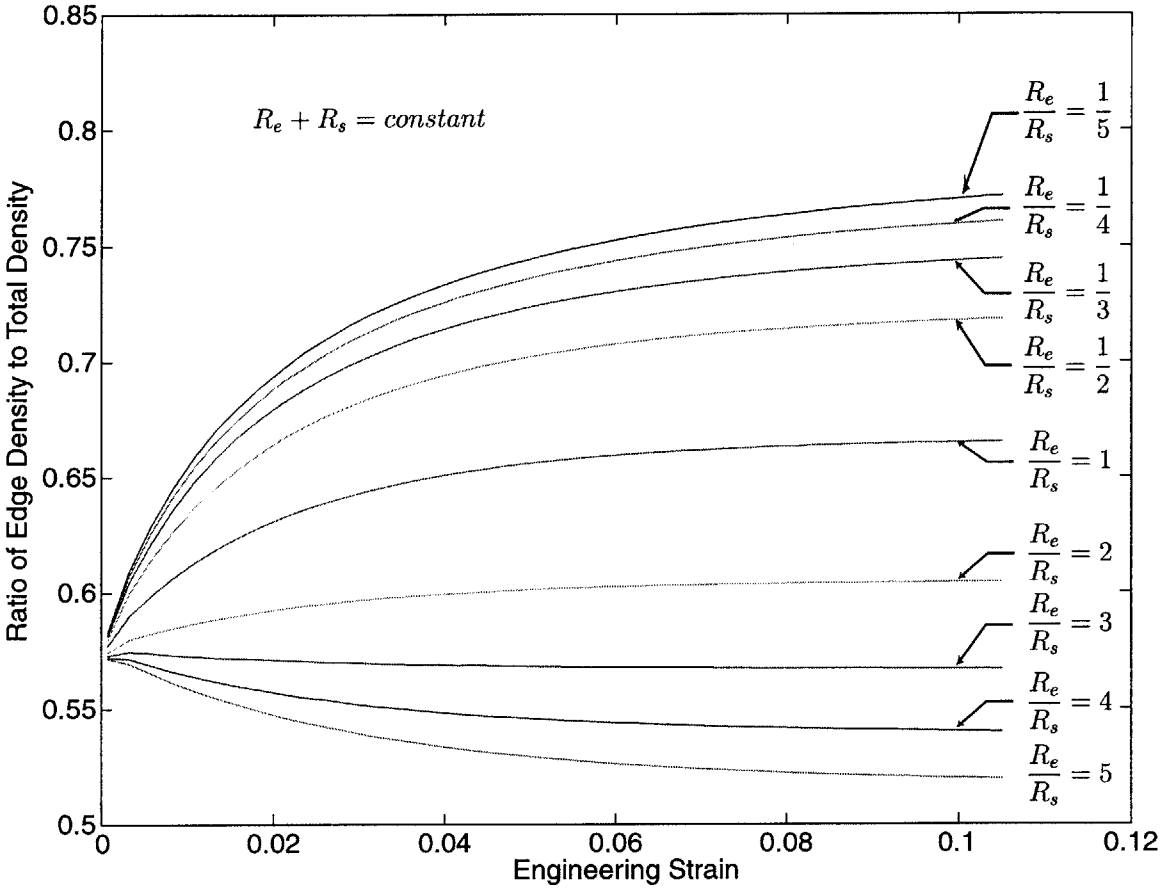

Figure A-11: Effect of changing the ratio between the edge and screw capture radii on the character of the dislocation density in the < 111 >-oriented crystal.

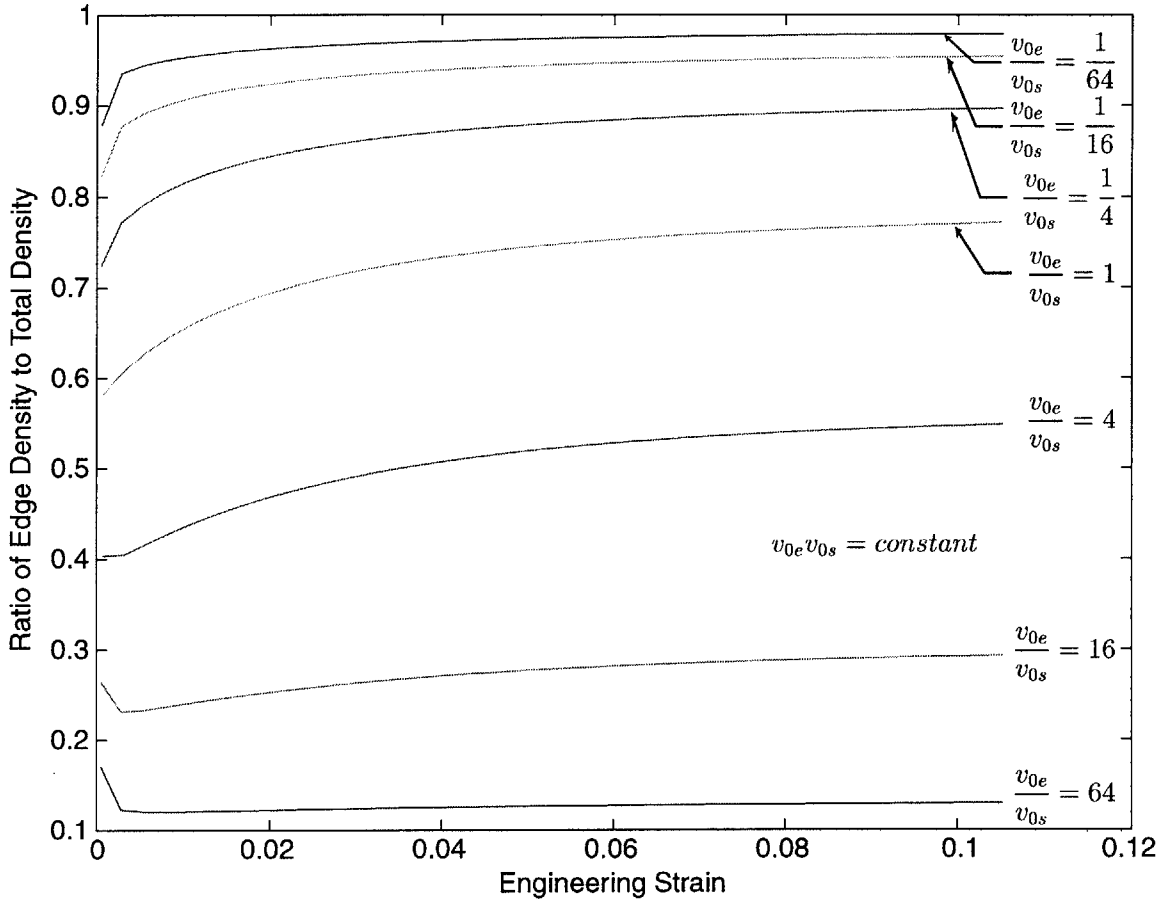

Figure A-12: Effect of changing the ratio between the edge and screw mobility on the character of the dislocation density in the $< 111 >$-oriented crystal.

Bibliography

Acharya, A. and Bassani, J. L. (2000). Lattice incompatibility and a gradient theory of crystal plasticity. *Journal of the Mechanics and Physics of Solids*, 48:1565–1595.

Acharya, A. and Beaudoin, A. (2000). Grain-size effect in viscoplastic polycrystals at moderate strains. *Journal of the Mechanics and Physics of Solids.*

Acharya, A. and Shawki, A. G. (1996). Thermodynamic restrictions on constitutive-equations for 2nd-deformation-gradient inelastic behavior. *Journal of the Mechanics and Physics of Solids*, 43:1752–1771.

Adams, B. L., Wright, S. I., and Kunze, K. (1993). Orienation imaging - the emergence of a new microscopy. *Metallurgical Transactions A: Physical Metallurgy and Materials Science*, 24:819–831.

Amelinckx, S. (1964). *The Direct Observation of Dislocations.* Academic Press.

Argon, A. S. (1969). *Physics of Strength and Plasticity*, chapter A statistical theory for easy glide II, pages 217–244. MIT Press.

Argon, A. S. (1996). Mechanical properties of single-phase crystalline media: deformation at low temperatures. In Cahn, R. W. and Haasen, P., editors, *Physical Metallurgy*, chapter 21, pages 1878–1955. Elsevier Science, 4th edition.

Arsenlis, A. and Parks, D. M. (2000). Three-dimensional modeling of the grain size dependent inelastic behavior of polycrystals. *to appear in International Journal of Plasticity.*

Asaro, R. (1979). Geometrical effects in the homogeneous deformation of ductile single crystals. *Acta Metallurgica*, 27:445–453.

Asaro, R. J. and Rice, J. R. (1977). Strain localization in ductile single crystals. *Journal of the Mechanics and Physics of Solids*, 25:309–338.

Ashby, M. F. (1970). The deformation of plastically non-homogeneous alloys. *Philosophical Magazine*, 21:399–424.

Balasubramanian, S. and Anand, L. (2000). Elasto-viscoplastic constitutive equations for polycrystalline fcc materials at low homologous temperatures. *to be published.*

Basinski, S. J. and Basinski, Z. (1979). Plastic deformation and work hardening. In Nabarro, F. R. N., editor, *Dislocations in Solids*. North-Holland.

Bassani, J. L. and Wu, T. Y. (1991). Latent hardening in single crystals ii. analytical characterization and predictions. *Proceedings of the Royal Society of London*, A435:21–41.

Bathe, K. (1996). *Finite Element Procedures*. Prentice-Hall, Upper Saddle River, New Jersey.

Beaudoin, A. J., Dawson, P. R., Mathur, K. K., Kocks, U. F., and Korzekwa, D. A. (1994). Application of polycrystal plasticity to sheet forming. *Computer Methods in Applied Mechanics and Engineering*, 117:49–70.

Becker, R. and Panchanadeeswaran, S. (1995). Effects of grain interactions of deformation and local texture in polycrystals. *Acta Metallurgica et Materialia*, 43:2107–2719.

Bishop, J. F. W. and Hill, R. (1951a). A theoretical derivation of the plastic properties of a polycrystalline face-centered metal. *Philosophical Magazine*, 42:1298–1307.

Bishop, J. F. W. and Hill, R. (1951b). A theory of plastic distortion of a polycrystalline aggregate under combined stresses. *Philosophical Magazine*, 42:414–427.

Bronkhorst, C. A., Kalidindi, S. R., and Anand, L. (1992). Polycrystalline plasticity and the evolution of crystallographic texture in FCC metals. *Philosophical Transactions of the Royal Society of London A*, 341:443–477.

Cottrell, A. H. (1958). Theory of brittle fracture in steel and similar materials. *Transactions of the American Institute of Mining Engineers*. 212:192–203.

Cuitiño, A. M. and Ortiz, M. (1992). Computational modelling of single crystals. *Modelling and Simulation in Materials Science and Engineering*, 1:225–263.

Cuitiño, A. M. and Ortiz, M. (1993). Consitutive modeling of $L1_2$ intermetallic crystals. *Materials Science and Engineering*, A170:111–123.

Dai, H. (1997). *Geometrically-Necessary Dislocation Density in Continuum Plasticity Theory, FEM Implementation and Applications*. PhD thesis, Massachusetts Institute of Technology.

Dai, H., Parks, D. M., and Nielson, G. N. (2000). Geometrically-necessary dislocation density in continuum crystal plasticity theory and FEM implementation. *to be published.*

Davis, R. S., Fleisher, R. L., Livingston, J. D., and Chalmers, B. (1957). Effect of orientation on the plastic deformation of aluminum single crystals and bicrystals. *Transactions of the AIME*, 209:136–140.

El-Azab, A. (2000). The boundary value problem of dislocation dynamics. *Modelling and Simulation in Materials Science and Engineering*, 8:37–54.

Fleck, N. A. and Hutchinson, J. W. (1993). Phenomenological theory for strain gradient effects in plasticity. *Journal of the Mechanics and Physics of Solids*, 41:1825–1857.

Fleck, N. A. and Hutchinson, J. W. (1997). Strain gradient plasticity. *Advances in Applied Mechanics*, 33:295–361.

Fleck, N. A., Muller, G. M., Ashby, M. F., and Hutchinson, J. W. (1994). Strain gradient plasticity: theory and experiment. *Acta Metallurgica et Materialia*, 42:475–487.

Follansbee, P. S. and Kocks, U. F. (1988). A constitutive description of the deformation of copper based on the use of the mechanical threshold stress as an internal state variable. *Acta Metallurgica et Materialia*, 36:81–93.

Franciosi, P. and Zaoui, A. (1982). Multislip in FCC crystals: a theoretical approach compared with experimental data. *Acta Metallurgica*, 30:1627–1637.

Gao, H., Huang, Y., Nix, W. D., and Hutchinson, J. W. (1999). Mechanism-based strain gradient plasticity - I. theory. *Journal of the Mechanics and Physics of Solids*, 47:1239–1263.

Godfrey, A. and Hughes, D. A. (2000). Scaling of the spacing of deformation induced dislocation boundaries. *Acta Materialia*, 48:1897–1905.

Gurtin, M. E. (2000). On the plasticity of single crystals: free energy, microforces, plastic-strain gradients. *Journal of the Mechanics and Physics of Solids*, 48:989–1036.

Hall, E. O. (1951). The deformation and aging of mild steel: III. discussion of results. *Proceedings of the Physical Society of London*, B64:747–753.

Hibbitt, Karlsson, and Sorensen, Inc. (1998). *ABAQUS Reference Manuals*. Pawtucket, RI.

Hirth, J. and Lothe, J. (1982). *Theory of Dislocations*. Wiley, New York, 2nd edition.

Hirth, J. P. (1961). On dislocation interactions in the fcc lattice. *Journal of Applied Physics*, 32:700–706.

Hosford, W. F. J., Fleischer, R. L., and Backofen, W. A. (1960). Tensile deformation of aluminum single crystals at low temperatures. *Acta Metallurgica*, 8:187–199.

Huang, Y., Gao, H., Nix, W. D., and Hutchinson, J. W. (2000). Mechanism-based strain gradient plasticity - II. analysis. *Journal of the Mechanics and Physics of Solids*, 48:98–128.

Huntington, H. B. (1958). The elastic constants of crystals. *Solid State Physics*, 7:213–351.

Hurtado, J. A. and Weertman, J. (1995). Non-redundant dislocation density field of a circular bar deformed in torsion and the stress gradient hardening effect. *Physica Status Solidi A*, 149:173–186.

Kocks, U. F. (1959). *Polyslip in single crystals of face-centered cubic metals.* PhD thesis, Harvard University.

Kocks, U. F., Argon, A. S., and Ashby, M. F. (1975). Thermodynamics and kinetics of slip. *Progress in Materials Science*, 19.

Kocks, U. F. and Brown, T. J. (1966). Latent hardening in aluminum. *Acta Metallurgica*, 14:87–98.

Kothari, M. and Anand, L. (1998). Elasto-viscoplastic constitutive equations for polycrystalline metals: application to tantalum. *Journal of the Mechanics and Physics of Solids*, 46:51–83.

Kröner, E. (1962). Dislocations and continuum mechanics. *Applied Mechanics Review*, 15:599.

Kubin, L. P., Canova, G., Condat, M., Devincre, B., Pontikis, V., and Brechet, Y. (1992). Dislocation microstructures and plastic flow: a 3D simulation. *Solid State Phenomena*, 23 & 24:455–472.

Kubin, L. P., Devincre, B., and Tang, M. (1998). Mesoscopic modeling and simulation of plasticity in fcc and bcc crsytals: Dislocation intersections and mobility. *Journal of Computer-Aided Materials Design*, 5:31–54.

Kuhlmann-Wilsdorf, D. (1999). The theory of dislocation-based crystal plasticity. *Philosophical Magazine A*, 79:955–1008.

Kumar, A. and Dawson, P. R. (1998). Modeling crystallographic texture evolution with finite elements over neo-eulerian orientation. *Computer Methods in Applied Mechanics and Engineering*, 153:259–302.

Kumar, A. V. and Yang, C. (1999). Study of work hardening models for single crystals using three dimensional finite element analysis. *International Journal of Plasticity*, 15:737–754.

Lardner, R. W. (1974). Dislocation dynamics and the theory of the plasticity of single crystals. *Zeitschrift fur Angewadte Mathematik und Physik*, 20:514–529.

Lomer, W. M. (1951). A dislocation reaction in the face-centered cubic lattice. *Philosophical Magazine*, 42:1327–1331.

Ma, Q. and Clarke, D. R. (1995). Size dependent hardness in silver single crystals. *Journal of Materials Research*, 10:853–863.

Marin, E. B. and Dawson. P. R. (1998). On modelling the elasto-viscoplastic response of metals using polycrystal plasticity. *Computer Methods in Applied Mechanics and Engineering*, 165:1–21.

Mathur, K. K. and Dawson, P. R. (1989). On modeling the development of crystallographic texture in bulk forming processes. *International Journal of Plasticity*, 5:67–94.

Menzel, A. and Steinmann, P. (2000). On the continuum formulation of higher gradient plasticity for single and poly-crystals. *Journal of the Mechanics and Physics of Solids*, 48:1777–1796.

Mühlhaus, H. B. and Aifantis, E. C. (1991). A variational principle of gradient plasticity. *International Journal of Solids and Structures*, 28:845–857.

Nakanishi, K. and Suzuki. H. (1974). Analysis of the grain size dependence of the yield stress in Cu-Al and Cu-Ni alloys. *Transactions of the Japan Institute of Metals*, 15:435–440.

Needleman, A. (1995). Discrete dislocation plasticity - a simple planar model. *Modelling and Simulation in Materials Science and Engineering*, 3:689–735.

Nemat-Nasser, S., Ni, L. Q., and Okinaka, T. (1998a). A constitutive model for fcc crystals with application to polycrystalline ofhc copper. *Mechanics of Materials*, 30:325–341.

Nemat-Nasser, S., Okinaka, T., and Ni, L. Q. (1998b). A physically-based constitutive model for bcc crystals with application to polycrystalline tantalum. *Journal of the Mechanics and Physics of Solids*, 46:1009–1038.

Nix, W. D. and Gao, H. (1998). Indentation size effects in crystalline materials: a law for strain gradient plasticity. *Journal of the Mechanics and Physics of Solids*, 46:411–425.

Nye, J. F. (1953). Some geometrical relations in dislocated crystals. *Acta Metallurgica*, 1:153–162.

Orowan, E. (1934). Zur kistallplastizität III. über den mechanismus des gleitvorganges. *Zeitschrift für Physik*, 89:634–659.

Orowan, E. (1940). Problems in plastic gliding. *Philosophical Transactions of the Royal Society of London A*. 52:8–22.

Petch, N. J. (1953). The cleavage strength of polycrystals. *Journal of the Iron and Steel Institute*, 174:25.

Polanyi, M. (1934). Gitterstörung die einen kristall plastisch machen könnte. *Zeitschrift für Physik*, 89:660–664.

Qin, Q. and Bassani, J. L. (1992). Non-associated plastic flow in single crystals. *Journal of the Mechanics and Physics of Solids*. 40:813–833.

Schwarz, K. W. (1999). Simulation of dislocations on the mesoscopic scale: I. Methods and examples. *Journal of Applied Physics*, 85:108–119.

Shenoy, V. B., Kukta, R. V., and Phillips, R. (2000). Mesoscopic analysis of structure and strength of dislocation junctions in fcc metals. *Physics Review Letters*, 84:1491–1494.

Shu, J. Y. and Fleck, N. (1998). The prediction of a size effect in micro-indentation. *International Journal of Solids and Structures*, 35:1363–1383.

Shu, J. Y. and Fleck, N. (1999). Strain gradient crystal plasticity: size-dependent deformation of bicrystals. *Journal of the Mechanics and Physics of Solids*, 47:297–324.

Sluys, L. J. and Estrin, Y. (2000). The analysis of shear banding with a dislocation based gradient plasticity model. *International Journal of Solids and Structures*, 37:7127–7142.

Smyshlyaev, V. P. and Fleck, N. (1996). The role of strain gradients in the grain size effect for polycrystals. *Journal of the Mechanics and Physics of Solids*, 44:465–495.

Stelmashenko, N. A., Walls, M. G., Brown, L. M., and Milman, Y. V. (1993). Microindentation on W and Mo oriented single crystals: an STM study. *Acta Metallurgirca et Materialia*, 41.

Stölken, J. S. and Evans, A. G. (1998). A microbend test for measuring the plasticity length scale. *Acta Materialia*, 48:5109–5115.

Sun, S., Adams, B. L., and King, W. E. (2000). Observations of lattice curvature near the interface of a deformed aluminium bicrystal. *Philosophical Magazine A*, 80:9–25.

Takeuchi, T. (1975). Work hardening of copper single crystals with multiple glide orientations. *Transactions of the Japan Institute of Metals*, 16:629–640.

Taylor, G. I. (1934). The mechanism of plastic deformation of crystals part I.- theoretical. *Proceedings of the Royal Society of London*, A145:362–387.

Taylor, G. I. (1938). Plastic strain in metals. *Journal of the Institute of Metals*, 62:307–324.

Volterra, V. (1907). *Annales Ecole Nationale Superieure de Mechanique*, 24:400.

Weertman, J. (1996). *Dislocation Based Fracture Mechanics.* World Scientific, River Edge, NJ.

Wickham, L., Schwarz, K., and Stölken, J. (1999). Rules for forest interactions between dislocations. *Physical Review Letters*, 83:4574–4577.

Zbib, H. and Aifantis, E. C. (1989). A gradient-dependent flow theory of plasticity: Application to metal and soil instabilities. *Applied Mechanics Review*, 42:295–304.

Zbib, H. M., Rhee, M., and Hirth, J. P. (1998). On plastic deformation and the dynamics of 3D dislocations. *International Journal of Mechanical Sciences*, 40:113–127.